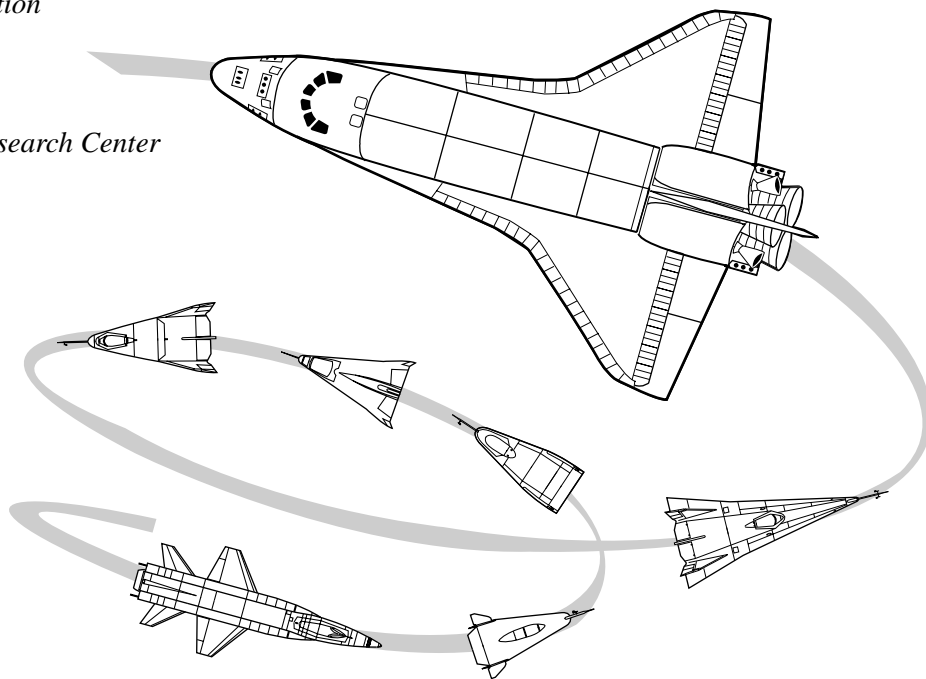# Aerodynamic Assessment of Flight-Determined Subsonic Lift and Drag Characteristics of Seven Lifting-Body and Wing-Body Reentry Vehicle Configurations

Edwin J. Saltzman
Analytical Services & Materials
Edwards, California

K. Charles Wang
The Aerospace Corporation
El Segundo, California

Kenneth W. Iliff
NASA Dryden Flight Research Center
Edwards, California

The NASA STI Program Office…in Profile

Since its founding, NASA has been dedicated to the advancement of aeronautics and space science. The NASA Scientific and Technical Information (STI) Program Office plays a key part in helping NASA maintain this important role.
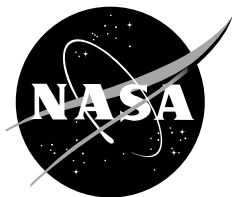
The NASA STI Program Office is operated by Langley Research Center, the lead center for NASA's scientific and technical information. The NASA STI Program Office provides access to the NASA STI Database, the largest collection of aeronautical and space science STI in the world. The Program Office is also NASA's institutional mechanism for disseminating the results of its research and development activities. These results are published by NASA in the NASA STI Report Series, which includes the following report types:

- TECHNICAL PUBLICATION. Reports of completed research or a major significant phase of research that present the results of NASA programs and include extensive data or theoretical analysis. Includes compilations of significant scientific and technical data and information deemed to be of continuing reference value. NASA's counterpart of peer-reviewed formal professional papers but has less stringent limitations on manuscript length and extent of graphic presentations.

- TECHNICAL MEMORANDUM. Scientific and technical findings that are preliminary or of specialized interest, e.g., quick release reports, working papers, and bibliographies that contain minimal annotation. Does not contain extensive analysis.

- CONTRACTOR REPORT. Scientific and technical findings by NASA-sponsored contractors and grantees.

- CONFERENCE PUBLICATION. Collected papers from scientific and technical conferences, symposia, seminars, or other meetings sponsored or cosponsored by NASA.

- SPECIAL PUBLICATION. Scientific, technical, or historical information from NASA programs, projects, and mission, often concerned with subjects having substantial public interest.

- TECHNICAL TRANSLATION. English-language translations of foreign scientific and technical material pertinent to NASA's mission.

Specialized services that complement the STI Program Office's diverse offerings include creating custom thesauri, building customized databases, organizing and publishing research results…even providing videos.

For more information about the NASA STI Program Office, see the following:

- Access the NASA STI Program Home Page at ***http://www.sti.nasa.gov***

- E-mail your question via the Internet to help@sti.nasa.gov

- Fax your question to the NASA Access Help Desk at (301) 621-0134

- Telephone the NASA Access Help Desk at (301) 621-0390

- Write to:
  NASA Access Help Desk
  NASA Center for AeroSpace Information
  7121 Standard Drive
  Hanover, MD 21076-1320

Aerodynamic Assessment of Flight-Determined Subsonic Lift and Drag Characteristics of Seven Lifting-Body and Wing-Body Reentry Vehicle Configurations

Edwin J. Saltzman
Analytical Services & Materials
Edwards, California

K. Charles Wang
The Aerospace Corporation
El Segundo, California

Kenneth W. Iliff
NASA Dryden Flight Research Center
Edwards, California

November 2002

Available from the following:

CONTENTS

TABLES

FIGURES

ABSTRACT

This report examines subsonic flight–measured lift and drag characteristics of seven lifting-body and wing-body reentry vehicle configurations with truncated bases. The seven vehicles are the full-scale M2-F1, M2-F2, HL-10, X-24A, X-24B, and X-15 vehicles and the Space Shuttle *Enterprise*. Subsonic flight lift and drag data of the various vehicles are assembled under aerodynamic performance parameters and presented in several analytical and graphical formats. These formats are intended to unify the data and allow a greater understanding than individually studying the vehicles allows. Lift-curve slope data are studied with respect to aspect ratio and related to generic wind-tunnel model data and to theory for low-aspect-ratio planforms. The definition of reference area is critical for understanding and comparing the lift data. The drag components studied include minimum drag coefficient, lift-related drag, maximum lift-to-drag ratio, and, where available, base pressure coefficients. The influence of forebody drag on afterbody and base drag at low lift is shown to be related to Hoerner's compilation for body, airfoil, nacelle, and canopy drag. This feature might result in a reduced need of surface smoothness for vehicles with a large ratio of base area to wetted area. These analyses are intended to provide a useful analytical framework with which to compare and evaluate new vehicle configurations of the same generic family.

NOMENCLATURE

a_l	longitudinal acceleration, g
a_n	normal acceleration, g
A	aspect ratio, $A = b^2/S$
A_b	base area, ft^2
A_c	maximum projected cross-sectional area, ft^2
A_w	wetted area, ft^2
b	span, ft
c	base pressure profile factor, $c = C_{D_b}/C_{D_b}{}^*$
cf	compressibility factor
$c/4$	quarter chord of wing
C_D	drag coefficient, $C_D = D/\bar{q}S$
$C_D{}'$	drag coefficient based on reference area S'
C_{D_b}	base drag coefficient, using derived base pressure profile (reference area is A_b for equations (11) and (12); reference area is S for equations (14), (15), and (16))

$C_{D_b}{}^*$	base drag coefficient, assuming "flat" base pressure profile (reference area is S)
$C_{D_{fore,\,b}}$	forebody drag coefficient referenced to A_b
$C_{D_{fore,\,S}}$	forebody drag coefficient referenced to S
C_{D_i}	lift-related drag coefficient
$C_{D_{min}}$	minimum drag coefficient at vertex of drag polar (reference area S for equation (11))
$C_{D_{min}}'$	minimum drag coefficient based on reference area S'
C_{D_0}	zero-lift drag coefficient (when zero-lift drag corresponds to minimum drag)
C_F	turbulent boundary-layer skin-friction coefficient (over wetted surfaces)
C_{F_e}	equivalent skin-friction coefficient (includes all drag components at $C_{D_{min}}$)
$C_{F_{e,\,fore}}$	equivalent skin-friction coefficient of the forebody only
C_L	lift coefficient, $C_L = L/\bar{q}S$
C_L'	lift coefficient based on reference area S'
$C_{L_{min}}$	lift coefficient for minimum drag coefficient
C_{L_α}	lift-curve slope (with respect to α), $\deg^{-1}$ or rad^{-1}
c_n	normal force coefficient for local fuselage station
C_{N_A}	normal force coefficient of complete vehicle, $C_{N_A} = N/\bar{q}S$
C_{N_F}	normal force coefficient of fuselage (reference area is maximum fuselage cross section)
C_{P_b}	base pressure coefficient, $C_{P_b} = (p_b - p)/\bar{q}$
(C_{P_b})	estimated base pressure coefficients before adjusting for effects of lower forebody drag
d	diameter
d_{eff}	effective diameter, $d_{eff} = \sqrt{4A_c/\pi}$
D	drag force along flightpath, lbf
D_{min}	minimum drag at vertex of drag polar, lbf
f	equivalent parasite drag area, ft^2
F	planform parameter, $F = A\dfrac{\sqrt{1-(M\cdot\cos\Lambda)^2}}{0.9\cos\Lambda}$

2

g	gravitational acceleration
K	base pressure factor (numerator coefficient in Hoerner's equation for three-dimensional configurations)
l	longitudinal length of a vehicle, ft
L	lift force normal to the flightpath, lbf
LC	lift-curve slope parameter, $LC = 10 C_{L_\alpha} \dfrac{\sqrt{1-(M \cdot \cos\Lambda)^2}}{\cos\Lambda}$ (where C_{L_α} in deg^{-1} units)
L/D	lift-to-drag ratio
$(L/D)_{max}$	maximum lift-to-drag ratio
M	free-stream Mach number
N	force normal to vehicle longitudinal axis, lbf
p	ambient pressure, lbf/ft^2
p_b	base static pressure, lbf/ft^2
p_{local}	local surface static pressure, lbf/ft^2
$\bar{q}$	free-stream dynamic pressure, lbf/ft^2, $\bar{q} = 0.7 p M^2$
r	local fuselage radius, ft
R	maximum fuselage radius, ft
R_l	Reynolds number based on body length
S	representative (revised) planform reference area, ft^2 (for HL-10 and X-24B vehicles, $S = S'$)
S'	published reference area requiring revision for the M2-F1, M2-F2, X-24A, and X-15 vehicles and the Space Shuttle *Enterprise*, ft^2
W	vehicle weight, lb
x	distance from fuselage apex to a specific fuselage station, ft
α	angle of attack, deg
α^*	$\alpha - (\alpha$ at $C_L = 0)$, deg

δA_B — aileron bias, deg (X-24A and X-24B vehicles)

δBF — body flap bias, deg (*Enterprise*)

δ_{ef} — elevon flap bias, deg (HL-10 vehicle)

δe_L — lower flap deflection, deg (X-24A and X-24B vehicles)

δe_U — upper flap deflection, deg (X-24A vehicle)

δL_B — lower flap bias, deg (X-24A vehicle)

δR_B — rudder bias, deg (X-24A and X-24B vehicles)

δSB — speed-brake surface bias, deg (*Enterprise*)

δ_{uf} — upper flap bias, deg (M2-F2 and M2-F3 vehicles)

δU_B — upper flap bias, deg (X-24A and X-24B vehicles)

δw — wedge angle, deg, $\delta w = \left|\delta e_L\right| + \left|\delta U_B\right|$ or $\left|\delta e_U\right| + \left|\delta L_B\right|$

Δ — uncertainty or increment of quantity

ΔC_D — increment in drag coefficient

$\Delta C_{D_{gear}}$ — increment of drag coefficient caused by extended landing gear

$\Delta C_D / \Delta C_L{}^2$ — drag-due-to-lift factor

$\Delta C_{F_{e,base}}$ — equivalent skin-friction coefficient of the vehicle base for 0° wedge angle

$\Delta C_{F_{e,lee}}$ — equivalent skin-friction coefficient of the lee side of the body flaps

$\Delta C_{F_{e,total}}$ — total equivalent skin-friction coefficient of the body flaps

$\Delta C_{F_{e,windward}}$ — equivalent skin-friction coefficient of the windward side of the body flaps

Δf_{gear} — increment of parasite drag area caused by extended landing gear

ε — Oswald lifting-efficiency factor

θ — counterclockwise angle from the lower centerline (viewed from the front), deg

Λ — wing sweep angle, deg

INTRODUCTION

Renewed interest has been shown in controlled reentry from low-Earth orbit and the Earth's upper atmosphere. This interest has been motivated by several factors: a growing commercial space launch market and its desire for a low-cost, reusable means of space access; the need for a crew return and rescue vehicle from the International Space Station; and the potential for future military space operations. Fundamental studies by the NACA[*] and NASA in the late 1950's and early 1960's described three basic methods of atmospheric reentry: ballistic reentry, winged reentry, and wingless lifting-body reentry. The ballistic reentry approach necessitates the use of parachutes to land, but the lifting-body and winged-body approaches provide the possibility of horizontal landings. Flight examples of these latter two approaches include the M2-F1, M2-F2, HL-10, X-24A, X-24B, and X-15 vehicles and the Space Shuttle.[†] Most lifting reentry configurations are attractive because of their crossrange and downrange capability and low-speed handling qualities. In addition to their volumetric efficiency, wingless lifting bodies benefit from peak decelerations that are lower than those of ballistic reentry, and peak heating rates that are lower than those of winged reentry vehicles. Because of the current interest in lifting reentry shapes, this report reexamines lift and drag characteristics of the seven aforementioned vehicles during subsonic unpowered flight, and presents a unified analysis of their subsonic aerodynamic performance that enables meaningful comparisons with future lifting reentry designs.

The vehicles examined in this report; the M2-F1, M2-F2, HL-10, X-24A, X-24B, and X-15 vehicles and the Space Shuttle *Enterprise*; comprise a unique class of aircraft. Not only were the vehicles all lifting reentry shapes, they were all piloted and capable of routine unpowered horizontal landings. Each of these vehicles also had a truncated afterbody or blunt base, which resulted in base drag being a significant component of the total vehicle drag. In terms of planform design, all of the aforementioned vehicles had low aspect ratios, with published values between 0.6 and 2.5. The lift and drag data of the vehicles presented herein were obtained during subsonic, unpowered, coasting flights performed at Edwards Air Force Base (California) between 1959 and 1977. The primary organizations involved were the NASA Dryden Flight Research Center[‡] (Edwards, California) and the Air Force Flight Test Center; the U. S. Navy was a partner in the X-15 program.

The purpose of this study is to assemble flight-measured lift and drag data from these vehicles under common aerodynamic performance parameters or metrics (that is, the data from all seven vehicles are plotted together) in an attempt to unify the results for this class of vehicles. This array of data is intended to collectively yield information that might otherwise escape notice if the vehicles were individually studied. To accomplish this study, the performance parameters of the subject vehicles have been related, or exposed, to data formats and standards that are based on theory and concepts that range from several decades to a century old (for example, the concepts of Jones; Allen and Perkins; Helmbold; Krienes; Oswald; and ultimately, Prandtl and Lanchester). Works explicitly used are referenced.

---

[*]The National Advisory Committee for Aeronautics (NACA) became incorporated into the National Aeronautics and Space Administration (NASA) in October 1958.

[†]The Space Shuttle *Enterprise* referenced in this report is a nonorbiting version of a Space Shuttle Orbiter vehicle. The Space Shuttle Orbiter referenced is the operating space vehicle *Columbia*. (The *Enterprise* was launched from a special modified 747 "carrier" airplane and was used to obtain subsonic performance and handling qualities data during subsequent coasting flight.)

[‡]NASA Dryden was called the NASA Flight Research Center at the time of the subject flight experiments for the five lifting bodies and the X-15 vehicle. The center was renamed the NASA Dryden Flight Research Center prior to the *Enterprise* flights.

The innovative and intuitive concepts cited above were intended for vehicle configurations that are quite different than the subject vehicles. For example, the relevant Jones work applied to sharp-edged, low-aspect-ratio wings; Allen's and Perkins' related work addressed high-fineness-ratio bodies of revolution; and the concepts of the others applied to moderate-, high-, and even infinite-aspect-ratio wings. Although some of the concepts and standards employed herein were not originally intended to apply to the subject vehicles, several such theoretical relationships and standards have been used as a means of organizing and assessing the flight results considered.

This study is ultimately intended to provide a useful database and analytical framework with which to compare and evaluate the subsonic aerodynamic performance of new vehicle configurations of the same generic family: low-aspect-ratio lifting reentry shapes with truncated bases. The results can also be used as a first-order design tool to help airframe designers define the outer mold lines of future related configurations as well as assess the predictive techniques used in design and development.

HISTORICAL BACKGROUND

At a NACA conference held in March of 1958, manned satellites and methods of reentering the Earth's atmosphere were comprehensively studied (ref. 1). Three different methods of reentry from Earth orbit were considered and discussed within the first four papers. The three methods were ballistic reentry (ref. 2), the wingless lifting body (ref. 3), and winged configurations (ref. 4). Reference 3 advocates the lifting body mainly on the basis that its hypersonic lift-to-drag ratio of approximately 0.5 would provide a maximum tangential reentry deceleration of approximately 2 g, low enough to allow a pilot to intervene in the control of the vehicle during this portion of the reentry. (For a pure ballistic, nonlifting reentry, the peak tangential deceleration would be approximately 8 g.)

The first lifting-body concepts included but were not limited to very blunt half-cone shapes (refs. 3 and 5). Those concepts later evolved into cone shapes that had higher fineness ratios (refs. 6–8), and the capability of achieving conventional (although unpowered) horizontal landings was discussed. Numerous wind-tunnel tests were performed on models of candidate versions of the half-cone shape and shapes with flattened bottom surfaces. In 1962, Reed demonstrated unpowered horizontal landings and controllable flight with a miniature, lightweight, radio-controlled model of an M2 half-cone configuration (ref. 9). This demonstration was followed by the construction of a lightweight M2 craft large enough to carry a pilot. This unpowered M2-F1 vehicle demonstrated controllable flight and horizontal landings for a maximum lift-to-drag ratio of 2.8 for subsonic flight. The M2-F1 lift, drag, and stability and control characteristics were published in 1965 (refs. 10–11).

A heavier and modified version of the M2 shape was built and began flying in 1966. The resulting lift and drag data from subsonic flight were published in 1967 (ref. 12). Other lifting-body configurations (all capable of unpowered horizontal landings) were developed and flight-tested as well. The lift and drag characteristics from subsonic flights have previously been reported for the HL-10 (ref. 13), X-24A (ref. 14), and X-24B (ref. 15) lifting bodies. More information on the evolution and flight testing of the lifting bodies is available (refs. 9 and 16–18). Much of the remaining discussion will concern the data contained in these and related references.

The M2-F1 and subsequent lifting bodies were not the pioneer vehicles for performing unpowered ("dead-stick") landings, but they were the first vehicles with very low aspect ratios (less than 1.5) to

routinely land without power. The early rocket-powered research vehicles (the X-1, X-2, and D-558-II aircraft) were also designed for unpowered landings, but they had higher aspect ratios (between 6.0 and 3.6). Later, the X-15 hypersonic research aircraft, which had a published aspect ratio of 2.5 (between those of the early rocket-powered vehicles and the lifting bodies), made routine dead-stick landings. Confidence in the X-15 aircraft being able to land unpowered (ref. 19) was based on the successful experience of the earlier rocket-powered aircraft that had the higher aspect ratios and on a series of special landing investigations using low-aspect-ratio fighter-type airplanes (ref. 20). This study investigated subsonic approach and landings at lift-to-drag ratios of 2 to 4 and used extended gear and speed brakes to increase the drag. Lift and drag data for the X-15 aircraft have previously been published (refs. 19 and 21).

Despite the success of the X-15 unpowered landing experience, the early planning for the Space Shuttle considered "pop-out" auxiliary engines to ensure safe horizontal landings. Thompson, an X-15 and lifting-body research pilot, argued that the X-15 and lifting-body experience rendered landing engines for the Space Shuttle as an unnecessary weight and payload penalty (ref. 22). The Space Shuttle ultimately was designed to make unpowered landings, and thus became the heaviest of the reentry-type vehicles to use routine dead-stick landings. (The *Enterprise* was 120 times the weight of the M2-F1 vehicle.) The low-speed lift and drag characteristics of the *Enterprise* have previously been published (ref. 23). Results have been reported for the *Enterprise* with and without a tailcone (ref. 23). Only the truncated configuration—that is, without a tailcone—is subjected to the same tools of analysis that are used on the other six vehicles. Only slight use is made of results from the *Enterprise* with the tailcone attached. Those data are used when they help explain a concept or reveal a finding that merits documentation.

Currently, new lifting reentry vehicles are being developed for rescue missions from space and to serve as reusable launch vehicles. These vehicles have much in common with the lifting bodies described herein and, if aspect ratio is somewhat increased, with the X-15 aircraft and the *Enterprise*. This report presents the subsonic lift and drag characteristics of the M2-F1, M2-F2, HL-10, X-24A, X-24B, and X-15 vehicles and the Space Shuttle *Enterprise* under unifying performance parameters and formats, with the intent of aiding the definition of exterior mold lines of future candidate reentry vehicles that perform horizontal landings.

As was mentioned in the "Introduction" section, some of the unifying metrics depend on borrowed concepts and standards that are several decades old and were originally intended for application on winged vehicles of high or moderate aspect ratio. The authors acknowledge that some readers may disagree with how the borrowed concepts and standards are applied herein. The formats, concepts, and standards that have been used, and the information that may be derived therefrom, are offered as a beginning in the quest for understanding the general nature of lift and drag for this unique class of vehicles. This "beginning" could not have occurred but for the seven flight research programs addressed herein and the dedicated technical personnel who processed, analyzed, and carefully documented the lift and drag data. The present authors are indebted to these earlier investigators for their attention to detail and comprehensive reporting.

The following information is included for the purpose of orientation and perspective.

Earliest flight:	June 8, 1959	X-15 vehicle
Last flight:	October 26, 1977	*Enterprise*
Most number of flights:	199	X-15 vehicle
Least number of flights:	5	*Enterprise*
Lightest vehicle:	1250 lb	M2-F1 lifting body
Heaviest vehicle:	150,900 lb	*Enterprise*

The seven vehicles completed a combined total of 424 flights. Data from 6 to 7 percent of those flights were used for this report.

METHODS OF ANALYSIS

This section assembles methods and metrics (performance parameters) used in the analysis of the subject lift and drag data. The primary metrics of aerodynamic performance include lift-curve slope; a modified Oswald lifting-efficiency factor; the drag-due-to-lift factor; maximum lift-to-drag ratio; and for minimum drag analysis, equivalent parasite drag area, equivalent skin-friction coefficient, base pressure coefficient, base drag coefficient, and forebody drag coefficient.

Lift-Curve Slope

Trimmed lift-curve slope data for the subject vehicles are related to potential flow standards for finite-span wings. The most exact theoretical solution for unswept, rectangular wings at incompressible conditions is considered to be that derived by Krienes (ref. 24). Krienes' relationship for lift-curve slope, C_{L_α}, and aspect ratio, A, is well-represented by the following relationship from Helmbold (ref. 25) as expressed by Polhamus (ref. 26), where C_{L_α} is represented in rad^{-1}:

$$C_{L_\alpha} = \frac{2\pi A}{\sqrt{A^2 + 4} + 2} \qquad (1)$$

As A approaches infinity, C_{L_α} approaches 2π. At the lowest aspect ratios $(A < 1.0)$, equation (1) merges with the linear relationship of Jones (ref. 27):

$$C_{L_\alpha} = \frac{\pi A}{2} \qquad (2)$$

Equations (1) and (2) represent lift caused by circulation. Neither of these relationships account for leading-edge vortex lift, such as is developed by highly-swept delta wings (ref. 28), nor lift generated by vortices resulting from crossflow over the forebody (refs. 29–31). The relationships represented by equations (1) and (2) are each oblivious to the effects of trim. Although all seven vehicles violate the

limitations of equations (1) and (2), as generally does any aircraft during trimmed conditions, these equations are considered to be rational standards for evaluating the relative lifting capability of the subject configurations. The slopes for the lift curves of the present study were obtained over the lift coefficient range extending from the lowest lift coefficient achieved for a given maneuver to a lift coefficient somewhat greater than that required to obtain maximum lift-to-drag ratio.

Lift-Related Drag

The metrics used to evaluate the lift-related drag of the subject vehicles are the drag-due-to-lift factor, $\Delta C_D / \Delta C_L{}^2$; and the Oswald lifting-efficiency factor, ε (ref. 32), which is a measure of the span-wise distribution of lift. Equations (3)–(5) show how these metrics are related. Reference 31 and other sources indicate that for wing-body combinations flying at subsonic Mach numbers, the total vehicle drag coefficient may be expressed as

$$C_D = C_{D_0} + C_{D_i} \tag{3}$$

where

$$C_{D_i} = \frac{C_L{}^2}{\pi A \varepsilon} \text{, or } \Delta C_D = \frac{\Delta C_L{}^2}{\pi A \varepsilon} \tag{4}$$

Equation (4) defines the lift-related drag coefficient when the minimum drag occurs at zero lift. Thus, the Oswald lifting efficiency factor is defined as

$$\varepsilon = \frac{1/\pi A}{\Delta C_D / \Delta C_L{}^2} = \frac{1/\pi A}{C_{D_i}/C_L{}^2} = \frac{C_L{}^2}{\pi A (C_D - C_{D_0})} \tag{5}$$

Although these definitions of lift-related drag and lifting efficiency were originally intended to apply to vehicles having high to modest aspect ratios (for example, $A \geq 4$), the authors are borrowing these metrics for use on configurations of very low aspect ratio. Lift-related drag for winged configurations can be dependent on several geometric factors such as span, taper ratio, sweep, wing twist, fuselage effects, longitudinal control deflections for trim, and other configuration variables. A detailed accounting of all of these variables when they are present would require a more complex equation for the lift-related drag coefficient, C_{D_i}. Because of the relative simplicity of the subject vehicles, however, where many of the above noted variables are absent, equations (4) and (5) will be used for the two subject vehicles that have lift-drag polars where minimum drag coefficient occurred at zero lift.

For the remaining configurations studied herein, minimum drag coefficient did not occur at zero lift—that is, the vertex of the nearly parabolic curve occurred at a positive value of lift coefficient. For these lift-drag polars, the Oswald factor is modified as proposed by Wendt (ref. 33) as follows:

$$\varepsilon = \frac{(C_L - C_{L_{min}})^2}{\pi A (C_D - C_{D_{min}})} \tag{6}$$

In this modified form of Oswald's efficiency factor, $C_{L_{min}}$ and $C_{D_{min}}$ are the values of lift coefficient and the minimum drag coefficient at the vertex of the parabolic or nearly parabolic relationship of lift coefficient as a function of drag coefficient (that is, the drag polar), which does not necessarily occur at zero lift. This condition exists for five of the seven vehicles considered in this study. Both lift-related drag factors, $\Delta C_D / \Delta C_L^2$ and ε, represent lift coefficients extending to greater than that required to obtain maximum lift-to-drag ratio.

Maximum Lift-to-Drag Ratio

The maximum lift-to-drag ratio, $(L/D)_{max}$, achieved by each of the subject vehicles at subsonic speeds is presented as a function of b^2 / A_w. This form of aspect ratio is referred to as the "wetted aspect ratio" (ref. 34). This presentation includes a reference framework consisting of a family of curves representing constant values of equivalent skin-friction coefficient or equivalent viscous drag coefficient, C_{F_e}, which is a form of minimum drag coefficient, $C_{D_{min}}$ (which includes both forebody and base drag). Thus, if

$$C_{D_{min}} = \frac{D_{min}}{\bar{q} S} \tag{7}$$

then

$$C_{F_e} = C_{D_{min}} \frac{S}{A_w} \tag{8}$$

Although C_{F_e} is called the "equivalent skin-friction coefficient," the important word is "equivalent" because C_{F_e} is composed of base drag, separation losses, interference drag, protuberance drag, and other losses in addition to skin friction. The family of reference curves is analogous to that employed by Stinton (ref. 35), and the curves are defined by the following often-used expression from Loftin (ref. 36):

$$(L/D)_{max} = \frac{1}{2} \sqrt{\frac{\pi A \varepsilon}{C_{D_{min}}}} \tag{9}$$

Minimum Drag of the Vehicle

Minimum drag is considered in several formats. If the lift coefficient and drag coefficient are based on vehicle planform reference area, the minimum drag coefficient can be defined as in equation (7). The discussion on maximum lift-to-drag ratio also revealed that another metric for minimum drag coefficient is the equivalent skin-friction coefficient (eq. (8)), which is obtained by basing the minimum drag coefficient on the wetted area, A_w. The wetted area for each vehicle is considered to be the wetted area of the respective forebody, which includes the body and wings or fins, and thus is the sum of all outer mold-line surfaces ahead of an associated base or trailing edge.

Another format for comparing minimum drag for various configurations is the equivalent parasite drag area, f. This metric is related to equation (7) but eliminates controversy regarding the choice of reference area by being defined as follows:

$$f = C_{D_{min}} S = \frac{D_{min}}{\bar{q}} \tag{10}$$

Use of equivalent skin-friction coefficient, C_{F_e} (eq. (8)), and equivalent parasite drag area, f (eq. (10)), is common among aircraft designers. An early example of their use is given in reference 37.

Minimum drag has been represented as $C_{D_{min}}$, where the reference area is the vehicle planform area, S, which is sometimes defined subjectively; C_{F_e}, where the reference area is the forebody wetted area, A_w, which can be defined objectively and accurately; or as f, where reference area is eliminated as a factor. Despite any confusion that might result from such names as "equivalent skin-friction coefficient" and "equivalent parasite drag area" (which have been commonly used for many years), each of the metrics presented above for minimum drag should be understood to include all losses caused by the forebody (that is, body plus fins, protuberances, control surfaces, and, if applicable, wings) as well as the drag caused by all base surfaces. Mathematically speaking, the following exists:

$$C_{D_{min}} = C_{D_{fore,\, S}} + C_{D_b} \frac{A_b}{S} \tag{11}$$

and

$$C_{F_e} = C_{F_{e,\, fore}} + C_{D_b} \frac{A_b}{A_w} \tag{12}$$

where $C_{D_{fore,\, S}}$ is the forebody drag coefficient referenced to S, $C_{F_{e,\, fore}}$ is the equivalent skin-friction coefficient caused by the forebody only, C_{D_b} is the coefficient of base drag, and A_b is the base area.

Minimum Forebody Drag

Significant forebody drag losses exist in addition to the losses caused by skin friction. One method to quantify the sum of these losses is to compare the measured minimum drag of a vehicle with the sum of the measured base drag and the calculated skin-friction drag for completely attached, turbulent, boundary-layer flow. The difference that results from this comparison represents losses from multiple sources, which are designated "excess forebody drag." The calculated, idealized sum of the base drag and skin-friction drag for each vehicle is obtained from the following:

$$C_{F_e} = C_F + \left| C_{P_b} \right| \frac{A_b}{A_w} c \tag{13}$$

where C_F is the turbulent boundary-layer skin-friction coefficient (calculated) of the forebody and c is a base pressure profile factor.

The values of C_F, representing idealized forebody losses, have been calculated for each of the vehicles at the various flight conditions; adjusted for compressibility effects by the reference temperature method as applied by Peterson (ref. 38); and adjusted for form factor (three-dimensionality) by the coefficient, 1.02, as recommended for conical flow (ref. 39). The value of C_F used to calculate the reference curves presented herein is 0.0023, which is the average value of C_F for the various vehicles at the flight conditions reported herein. The constant, $c = 0.92$, is a base pressure profile factor that will be explained in the following section.

Base Pressure Profile Factor

A common practice by wind-tunnel and flight experimenters has been to define a base drag coefficient increment as

$$C_{D_b} = \left| C_{P_b} \right| \frac{A_b}{S} \tag{14}$$

where the base pressure coefficient, C_{P_b}, is obtained from a few scattered pressure measurements within the confines of the base surface. Thus, equation (14) is based on the assumption that the base pressure profile (consisting of the average of the pressures measured within a specific base region) was flat to the very edge of the base. However, the pressure profile is known to be somewhat rounded along the edges. Nevertheless, the flat profile approximation was usually used, mainly because making the numerous measurements required to define the profile was not practical. The factor c is used here to account for the rounded edges of the pressure profiles.

For example, the base drag increments for the X-15 vehicle (ref. 21) are derived from the base pressure data (ref. 40) using the flat profile assumption. When the resulting "flat profile" base drag increment is subtracted from the total zero-lift drag, however, the resulting forebody drag coefficient, based on wetted area, is approximately 0.0011 for Mach 0.65. For forebody drag, this increment is clearly

too small, being only approximately one-half of what the turbulent boundary-layer skin-friction coefficient should be for the given flight conditions.

The X-15 flight experience had shown that no significant regions of laminar flow existed. Considering, therefore, overall turbulent flow for surfaces ahead of each base element and accounting for the skin temperature at subsonic speeds following coast-down from hypersonic speeds (refs. 41–43), the friction drag component has been calculated for the Mach numbers and Reynolds numbers of interest here (refs. 38–39). The drag of the blunt leading edges and the several protuberances that were exposed to the flow at subsonic speeds was estimated using guidelines from reference 31. The resultant—more realistic—forebody drag is the sum of the friction drag, the leading-edge drag, and the protuberance drag for low-lift coefficients. The more correct base drag coefficient can now be defined as

$$C_{D_b} = C_{D_0} - C_{D_{fore, S}} \tag{15}$$

where each factor is based on reference area, S, and C_{D_b} is representative of the real (natural) base pressure profile. The former base drag coefficient, based on an assumed flat base pressure profile, is now designated as $C_{D_b}^*$.

From these analyses, a base pressure profile factor, c, can be defined as

$$c = \frac{C_{D_b}}{C_{D_b}^*} = 0.92 \tag{16}$$

This constant, c, is the same constant that appears in equation (13) for calculating the base drag component of C_{F_e}, as used in the description of excess forebody drag. How well this profile factor represents the other vehicles is not known, but $c = 0.92$ was used to calculate the base drag of all of the vehicles because it is the only profile factor known to be available for full-scale vehicles. The X-15 configuration serves as a nearly ideal vehicle for defining the base pressure profile factor by the means described because of its known overwhelmingly turbulent boundary layer, the small projected boattail area, and the precisely defined base area that does not change with variations in longitudinal control deflection. In contrast, for most of the lifting-body vehicles, longitudinal control variations can cause significant changes in base area.

Base Pressure Coefficients

Flight-measured base pressure coefficients; base pressure coefficients derived from published incremental drag attributed to the base; and estimated base pressure coefficients derived from those of a closely related, afterbody-base configuration are compared with two analytical equations developed by Hoerner (ref. 31). These equations were derived from wind-tunnel experiments of small-scale models. Hoerner's equation for three-dimensional axisymmetric bodies of revolution is as follows:

$$-C_{P_b} = \frac{K}{\sqrt{C_{D_{fore,\,b}}}} \tag{17}$$

where $K = 0.029$. Hoerner's equation for quasi-two-dimensional base flow conditions that generate the well-known Kármán vortex street is:

$$-C_{P_b} = \frac{0.135}{\sqrt[3]{C_{D_{fore,\,b}}}} \tag{18}$$

Lift and Drag Coefficients

The flight-measured lift and drag coefficients (C_L and C_D) for all seven vehicles were obtained by the accelerometer method (refs. 44 and 45). The relationships for unpowered, gliding flight are:

$$C_L = (a_n \cos\alpha + a_l \sin\alpha)\frac{W}{\bar{q}S} \tag{19}$$

$$C_D = (a_n \sin\alpha - a_l \cos\alpha)\frac{W}{\bar{q}S} \tag{20}$$

where a_n and a_l are the normal and longitudinal accelerations, α is the angle of attack, W is the vehicle weight, $\bar{q}$ is the free-stream dynamic pressure, and S is the reference area.

DATA UNCERTAINTY

The accurate definition of lift and drag characteristics from flight data requires high-quality sensors and careful attention to detail in sensor calibration and use. In general, lift-and-drag determination is most sensitive to error in the measurement of thrust, longitudinal and normal acceleration, angle of attack, static pressure, Mach number, vehicle weight, and an accounting of control deflections. For the seven vehicles considered herein, thrust is not a factor because the data were obtained during coasting flight; thus, a major source of uncertainty is avoided. Some of the problems associated with the measurement of these quantities, and their relative importance, are discussed in reference 45.

Uncertainty information has been published for four of the subject aircraft: the M2-F1, M2-F2, HL-10, and X-15 vehicles. For the three lifting bodies, the sources provide estimated measurement errors from sensors (that is, the standard deviation) and the contribution of individual sensors to error in C_L and C_D. Then the combined contribution of the sensors to uncertainty of C_L and C_D is given in the form of the square root of the sum of the errors squared (refs. 10, 12, and 13). References 21 and 40 provide errors for the X-15 aircraft for Mach numbers higher than those considered herein. Uncertainty in C_L and C_D for the X-15 aircraft therefore has been prepared based on unpublished data and through adjustments to the errors shown in references 21 and 40 for the effects of Mach number and dynamic pressure. Uncertainty in base pressure coefficient is available only for the M2-F1 and X-15 vehicles. Table 1 shows the uncertainties that are available from these four vehicles.

Table 1. Data uncertainties.

Vehicle	$\Delta C_L / C_L$, percent	$\Delta C_D / C_D$, percent	$\Delta C_{P_b} / C_{P_b}$, percent
M2-F1	±3.0	±5.5	±7.0
M2-F2	±1.7	±3.2	Not available
HL-10	±3.2	±3.9	Not available
X-15	±4.3	±3.9	±6.4

These uncertainties represent the square root of the sum of the squares for each of these coefficients when plotted as individual data points. Because these coefficients (as used in this report) are obtained from curves faired through numerous data points, the uncertainty of the coefficients resulting from faired data and other metrics should be smaller than those shown in table 1.

Corresponding uncertainties are not available for the X-24A and X-24B lifting bodies and the Space Shuttle *Enterprise*; however, airdata system calibration procedures similar to those used on the other four vehicles are known to have been used on these three. In addition, lift and drag were obtained by the accelerometer method for all seven vehicles. Although table 1 cannot be established as representing the uncertainties for the latter three vehicles, expecting their uncertainties to be relatively close to those listed is not unreasonable.

RESULTS AND DISCUSSION

The primary results of the current study are presented and discussed under four subheadings: "Lift-Curve Slope," "Lift-Related Drag," "Lift-to-Drag Ratio," and several metrics of "Minimum Drag." Formats for collectively presenting the data were chosen in the hope that one or more formats will yield a greater understanding of the data than would likely occur by individually studying the subject vehicles.

The aerodynamic performance metrics mentioned above, as applied to the subject vehicles, primarily have been reported in reference 46. Some of the metrics considered in reference 46 are examined in greater detail in this report, and the increment of drag caused by landing gear deployment has been added. In addition, appendix A provides authentic copies of the "root-source" plots of drag polars and lift-curve slopes from which the analyses contained herein were performed (refs. 10, 12–15, 21, and 23). These copies are presented, despite their nonuniform formats, so that readers can easily refer to the same root sources that were used herein and thereby challenge or verify the authors' interpretation of the basic data.

Appendix B provides an alternate presentation of the root-source data in appendix A. For user convenience, the root-source data of appendix A were electronically scanned and replotted using a consistent set of formats for all seven vehicles and their various configurations. The data in appendix B are not root-source data, but are only *based on* root-source data, with small (although generally negligible) differences caused by transmission variations during fairing, tracing, scanning, and replotting of the root-source data.

To compare representative aerodynamic data between vehicles, appendix C presents a consistent set of basic lift and drag plots in which one flight condition or configuration of each of the seven vehicles is represented on each plot. Only one flight condition or configuration of each vehicle is used in appendix C (that is, seven curves for each plot, one curve for each vehicle) to clarify and simplify comparison.

Appendix D provides flight data and supporting references that are important for understanding the contributions of fuselage forebody lift to the total lift of a winged vehicle. Appendix E is a reproduction of previously unpublished base pressure data from the M2-F3 vehicle, and appendix F outlines the procedure used for estimating base pressure coefficients for the X-24A and X-24B vehicles at Mach numbers less than 0.8.

Lift-Curve Slope

This section attempts to unify the lift capabilities of the seven flight vehicles previously discussed. The lift-curve slope data for subsonic flight of these vehicles have been assembled from references 10, 12–15, 21, and 23. Data were obtained during gradual pushover/pullup maneuvers (consequently trimmed for the respective maneuvers) over a range of lift coefficients extending to somewhat greater than that required to achieve the maximum lift-to-drag ratio. These data are compared to generic wind-tunnel model data and to theory for very low and moderately low aspect ratios. Figure 1 shows three-view drawings of each of the seven vehicles and the M2-F3 lifting body. Schematic illustrations of control surfaces whose deflections influence base area are also shown for four lifting bodies (fig. 1(i)).

Table 2 shows the data to be considered as derived from their respective references. The C_{L_α} and aspect-ratio values shown first are subject to the values of the reference area that were used in the various referenced documents. Use of the appropriate reference area and the actual tip-to-tip span is important towards achieving understanding of how the lifting characteristics of the various configurations relate to each other, to wind-tunnel data for generic models, and to theory.

Figure 2(a) shows the lift-curve slope data (the solid symbols) as published in the respective references plotted as functions of aspect ratio for five of the seven vehicles. Figure 2(a) also shows the relationships of C_{L_α} to aspect ratio as defined by Helmbold (eq. (1)) and, for the lowest aspect ratios, the linear relationship of Jones (eq. (2)). Neither of these relationships accounts for lift from crossflow over the bodies or from vortices generated by sharp, highly-swept leading edges. Stated another way, equations (1) and (2) apply where the flow does not separate from leading or swept lateral edges (that is, these equations represent lift generated by circulation).

The lift-curve slopes for each of the flight vehicles were expected to occur below the Jones and Helmbold relationships, which represent maximum efficiency for medium- or low-aspect-ratio configurations that obtain their lift from circulation. However, the results from both M2 vehicles and the X-24A vehicle, as shown by the solid symbols in figure 2(a), considerably exceed these expectations. The X-15 solid-symbol lift-curve slope also greatly exceeds the Helmbold relationship. These comparisons of lift-curve slope data to the Jones and Helmbold expressions raise at least four questions:

16

Table 2. Lift-curve slope data.

Vehicle	M	Configuration remarks	As published					Revised					α at $C_L = 0$,
			S', ft^2	b, ft	A	C_{L_α}, deg^{-1}	C_{L_α}, rad^{-1}	S, ft^2	b, ft	A	C_{L_α}, deg^{-1}	C_{L_α}, rad^{-1}	deg
M2-F1	0.15	Exposed gear	139.0	9.50	0.649	0.0225	1.289	152.4	14.17	1.318	0.0205	1.175	−7.89
M2-F2	0.45	$\delta_{uf} = -11.5°$	139.0	9.95	0.712	0.0217	1.243	160.0	9.95	0.619	0.0189	1.083	−9.00
	0.62	$\delta_{uf} = -11.5°$	139.0	9.95	0.712	0.0216	1.238	160.0	9.95	0.619	0.0188	1.076	−9.68
HL-10	0.60	$\delta_{ef} = 0.0°$	160.0	13.60	1.156	0.0230	1.318	(160.0)	(13.60)	(1.156)	(0.0230)	(1.318)	2.93
	0.60	$\delta_{ef} = -3.0°$	160.0	13.60	1.156	0.0210	1.203	(160.0)	(13.60)	(1.156)	(0.0210)	(1.203)	3.68
	0.60	$\delta_{ef} = -30.0°$	160.0	13.60	1.156	0.0200	1.146	(160.0)	(13.60)	(1.156)	(0.0200)	(1.146)	2.40
X-24A	0.50	$\delta L_B = 0.0°$	162.0	10.00	0.617	0.0239	1.369	195.0	13.63	0.953	0.0199	1.138	−3.86
	0.50	$\delta U_B = -13.0°$	162.0	10.00	0.617	0.0263	1.507	195.0	13.63	0.953	0.0218	1.252	−2.34
	0.50	$\delta U_B = -21.0°$	162.0	10.00	0.617	0.0220	1.261	195.0	13.63	0.953	0.0183	1.047	−3.28
X-24B	0.50	$\delta U_B = -13.0°$	330.5	19.14	1.108	0.0217	1.243	(330.5)	(19.14)	(1.108)	(0.0217)	(1.243)	1.50
	0.50	$\delta U_B = -20°$	330.5	19.14	1.108	0.0217	1.243	(330.5)	(19.14)	(1.108)	(0.0217)	(1.243)	1.05
	0.60	$\delta U_B = -20°$	330.5	19.14	1.108	0.0188	1.076	(330.5)	(19.14)	(1.108)	(0.0188)	(1.076)	−0.48
X-15	0.65	$\Lambda, c/4, \approx 25.6°$	200.0	22.36	2.500	0.0649	3.719	307.0	22.36	1.629	0.0423	2.423	0.75
	0.72	$\Lambda, c/4, \approx 25.6°$	200.0	22.36	2.500	0.0662	3.793	307.0	22.36	1.629	0.0431	2.471	1.02
Enterprise	0.40	$\Lambda, c/4, \approx 36.0°$	2690.0	78.07	2.266	0.0446[*]	2.556	3816.0	78.07	1.597	0.0314	1.799	−0.45
	0.50	$\Lambda, c/4, \approx 36.0°$	2690.0	78.07	2.266	0.0437	2.504	3816.0	78.07	1.597	0.0308	1.765	−0.30

[*]The lift-curve slope at Mach 0.4 with the tailcone on is 0.0449 deg^{-1} for $S' = 2690$ ft^2.

Parentheses indicate that revision was not required for these two vehicles.

- To what extent is reference area a factor that contributes to the apparent anomalies?

- Do wind-tunnel data exist for very low–aspect–ratio models that would support or refute the lifting-body slopes that exceed the Jones expression?

- To what extent are compressibility effects a factor contributing to the apparent anomalies?

- To what extent is sweep angle a factor for the two winged vehicles?

These questions have been addressed, and some of the results are represented by the open symbols in figure 2(a). Representative reference areas have been assigned for five of the seven vehicles; the other two vehicles were already assigned representative reference areas, as published. Table 2 shows the revised reference areas and the resulting lift-curve slopes. Figure 2(a) also shows wind-tunnel results for low-aspect-ratio models (refs. 47–48).

The five vehicles for which reference areas were revised were those whose previously published reference areas did not accurately reflect the total planform area (projected onto the longitudinal-lateral plane), but were simply the commonly accepted value in conventional use during the specific flight program. For the M2-F1 vehicle, the value of $S' = 139$ ft^2 formerly was used (ref. 10), which is the planform area of the lifting body itself. However, the elevons that laterally extend beyond the body increase the span by approximately 4.7 ft and represent 13.4 ft^2 of additional area. To qualitatively determine its contribution to the lift of the M2-F1 vehicle, the elevon planform area should be included in the reference area and accounted for in the definitions of force coefficients and aspect ratio. Similarly, for the M2-F2 and the X-24A data (the open symbols), actual projected planform areas as defined in references 12, 49, and 50 have been applied instead of the conventional program values that were used in references 12 and 14.

As figure 2(a) shows for the M2-F2 vehicle, the revised data still show the lift-curve slope, C_{L_α}, greater than the relationships of Jones and Helmbold for low aspect ratios. However, application of the revised (more representative) reference areas causes the data for the M2-F1 and the X-24A vehicles to fall below the theoretical relationships of equations (1) and (2). A literature search for the lifting characteristics of model shapes having aspect ratios less than 1.0 reveals that such elevated lift-curve slopes as shown for the M2-F2 vehicle may be expected. Results from wind-tunnel tests (shown in figure 2(a) as open right triangles) represent slender half-cone (ref. 47) and elliptical cone (ref. 48) shapes.

The reason that the M2-F2 vehicle and the slender model shapes (that is, those having aspect ratios less than 1.0) have relatively high lift-curve slopes may be related to well-developed forebody vortices caused by crossflow as reported by Allen and Perkins (ref. 29) and Hoerner (refs. 30–31). Because the model data (refs. 47–48) were untrimmed, their lift-curve slopes were expected to be optimistic. The half-cone shapes, having lateral edges with a small radius, were expected to produce vortex lift. However, the elliptical cone shape with the most slender planform (the lowest aspect ratio) also has a high slope compared to potential theory. Thus, the conjecture that well-developed vortices (resulting from body crossflow) may provide an extra component of lift is afforded credence even if sharp lateral edges are absent.

Because of this evidence that crossflow (counter-rotating vortex pair) effects may significantly contribute to the lift of the slender forebody portions of lifting bodies, considering that the forebodies of

the X-15 aircraft and the *Enterprise* may likewise generate significant amounts of crossflow lift is appropriate. For these winged vehicles, therefore, the forebody planform area and the wing area projected to the vehicle centerline will now be considered to be the reference area. Perhaps the most direct evidence supporting this definition for reference area (regarding lift coefficient or the lift-curve slope) is provided by comparing slopes for the *Enterprise* with the blunt base and with the tailcone (ref. 23). These lift-curve slopes are listed for Mach 0.4 and with *S'* as the reference area in table 2 and as a footnote to table 2 for the blunt configuration and the tailcone configuration, respectively. Note that the tailcone was ineffective in providing lift and represented a weight penalty of approximately 5900 lb. The failure of the tailcone to generate lift combined with the fact that the tailcone planform area is primarily aft of the wing trailing-edge station (fig. 1(h)) is in accord with the proposed definition for reference area. Additional information related to this subject is included as a footnote[§] and in appendix D. The reduction in drag provided by the tailcone is included in following sections.

The consequences of the revised reference areas for the X-15 aircraft and the *Enterprise* are represented in figure 2(a) by the respective open symbols. The revisions of reference area and aspect ratio affect the subject data for all vehicles except the HL-10 and X-24B vehicles, both of which already had proper, representative, reference areas as published. Note that a substantial reduction in lift-curve slope exists for the X-15 aircraft and the *Enterprise* in figure 2(a) when solid symbols are compared with open symbols (that is, lift-curve slope is reduced when the more representative reference area is used). Note also that when the area and span effects of the M2-F1 elevons are applied, the datum shifts to a much higher aspect ratio and below the Helmbold curve. In addition, the X-24A data are no longer greater than the theoretical curves, because of revision of area and span dimensions compared to the values originally used.

As noted earlier, the lift-curve slope data from the half-cone (ref. 47) and elliptical cone (ref. 48) models tend to confirm the M2-F2 flight results, which exceed the Jones relationship. The values for the elliptical cone models at aspect ratios greater than 1, however, have lift-curve slopes that are significantly lower than both the Helmbold and Jones relationships (eqs. (1) and (2), respectively). For the elliptical cone shapes having the highest aspect ratios (that is, clearly nonslender), a lift component caused by circulation dominates and some degree of crossflow additionally exists; whereas at the lowest aspect ratios, the crossflow component of lift is more dominant (refs. 30–31).

Regarding compressibility effects, table 2 shows that the lift-curve slope data obtained from the vehicles represent a range of subsonic Mach numbers. Compressibility effects may be approximately accounted for by applying the often-used Prandtl-Glauert factor, $(1 - M^2)^{0.5}$. Both Gothert (ref. 51) and Hoerner (ref. 30) believe that for the low aspect ratios, the exponent *n* in $(1 - M^2)^n$ should be less than 0.5. Nevertheless, compressibility effects are approximated here by use of the more common exponent of 0.5. Figure 2(b) shows the lift-curve slopes from figure 2(a) for the seven vehicles, based on the more

---

[§]Because the revisions of reference area for the X-15 and Space Shuttle vehicles are a departure from convention, and because two separate concepts are involved, additional discussion and supporting data are justified. Inclusion of the forebody planform area with the wing-panel area is justified in part on the basis of the crossflow lift experienced by lifting bodies (ref. 29–31; 47–48). In addition, appendix D presents fuselage normal force data obtained in flight from two aircraft that establish that fuselage lift is significant. The second concept, which rejects fuselage planform area aft of the wing trailing edge for inclusion as reference area, conforms to reference 27 (pgs. 59 and 63), which postulates that for pointed shapes, "sections behind the section of maximum width develop no lift." This theory, the lack of tailcone-lift effectiveness observed from the *Enterprise,* and flight data from the X-1 airplane shown in appendix D, all taken together, constitute the rationale for this second concept.

representative reference area and adjusted for compressibility effects. The purpose here is to show that, for the vehicles having data at two Mach numbers (the M2-F2, X-24B, and the X-15 vehicles and the *Enterprise*), accounting for compressibility effects places the affected data approximately in alignment with the relationships of equations (1) and (2).

This example of realignment of data in accord with compressibility effects suggests that it would be appropriate to also consider a format such as developed by Diederich (ref. 52), which was formulated as a means to correlate the lifting characteristics of finite-span wings approximating the effects of aspect ratio, wing sweep, and Mach number for subcritical Mach numbers. Hoerner, in reference 30, chapter 15, provides a simplified version of Diederich's formulation. This simplified format has been applied to the subject vehicles, and figure 2(c) shows the results.

Whether leading-edge or quarter-chord angle of sweep should be applied in the calculation of the lift-curve slope and planform parameters, LC and F, is arguable. Hoerner uses what he calls "the effective angle of sweep," which approximates the effect of a wing neutral angle (the sweep angle for a given aspect ratio where the lift-curve slope would be maximized) occurring at a modest sweep of positive value.[¶] In figure 2(c), the effects of sweep angle are only considered for the X-15 and *Enterprise* vehicles, the two winged vehicles. Both the "effective" sweep angle and that of the quarter chord have been used herein. Application of the quarter-chord sweep angle clearly elevates the X-15 and *Enterprise* values of parameter LC relative to the "effective angle of sweep" and the family of curves representing Helmbold's equation. The lowest values of parameters LC for the HL-10, X-24A and X-24B vehicles represent longitudinal control deflections that form a large "wedge angle," or flared afterbody, that also increases the base area. Thus, these large wedge angles represent the transonic control modes and therefore are nonoptimum configurations for subsonic flight. The level of the highest slopes for the HL-10 and the X-24B vehicles exceed 70 percent of the Helmbold curve transformed to accommodate the respective axis parameters of figure 2(c). The highest value of LC for the X-24A low wedge angle during subsonic flight is approximately 85 percent of Helmbold's transformed relationship. The corresponding *Enterprise* values vary from 80 percent to approximately 85 percent of the theoretical curve, depending on the definition of sweep angle; and the X-15 data are above the Helmbold boundary.

Sweep angle was not considered in calculating the parameters for the lifting bodies. The rationale for this decision partly arises from the fact that the X-15 and *Enterprise* vehicles have forebodies related to lifting-body planforms. Of course, wing sweep and not forebody sweep was assigned to the former vehicles for the presentation of figure 2(c). In addition, as figure 3 shows, the effects of wing sweep are drastically diminished at low aspect ratios representative of lifting bodies (ref. 53). Note that the authors of references 30 and 52 did not intend that the Diederich derivation should be used for lifting bodies. The formulation, however, was intended to include very low–aspect–ratio wings. The low-aspect-ratio vehicles considered herein, the wind-tunnel data for slender-body shapes in references 47–48, and references 30–31 all indicate that slender bodies and low-aspect-ratio wings each experience various combinations of crossflow vortex lift and circulation lift. On this basis, the decision was made to include a form of the Diederich formulation as a tool to relate lifting characteristics of the various vehicles to theory.

The major factor that contributed to greater order for the lift-curve slope data developed in figure 2 was the application of the more representative reference areas and application of actual tip-to-tip span for

---

[¶]That is, the wing neutral angle occurs at a modest value of aft sweep, between 5° and 10° according to references 30 and 31.

calculating aspect ratio. Adjustment of the data for compressibility effects and wing sweep angle had less influence for the vehicles considered here. Together, these factors did not provide an impressive coalescence of the flight results; however, that casually chosen reference areas can confound understanding and result in misleading conclusions has been established. Also of interest, based on the M2-F2 data and the slender-body data from references 47 and 48, is that a very low–aspect–ratio lifting reentry vehicle may have a lift-curve slope somewhat greater than the Jones relationship. This possibility is also supported by data and reasoning contained in references 28–31.

Lift-Related Drag

The data array of lift-related drag characteristics for the subject vehicles uses a format employed by Hoerner in chapter 7 of reference 31. Figure 4 shows these data as drag-due-to-lift factor $(\Delta C_D/\Delta C_L{}^2)$ plotted as a function of the reciprocal of aspect ratio $(1/A)$. Included as a reference framework is a family of lines representing the theoretical relationship for an ideal elliptical span loading, wherein $\varepsilon = 1.0$, and for significantly less optimal load distributions represented by $\varepsilon < 1.0$ (refs. 31 and 32), which are expected for the vehicles reported here.

The derivation of drag-due-to-lift factor and lifting-efficiency factor normally would include obtaining $\Delta C_D/\Delta C_L{}^2$ from their linear relationship, and deriving ε from Oswald's equation for a polar plot of C_L as a function of C_D in which the minimum drag is at zero lift (eq. (5)). For several of the subject vehicles, however, the minimum drag did not occur at zero lift. For these vehicles, their polars were displaced, and $C_{D_{min}}$ occurred at a nonzero lift coefficient defined as $C_{L_{min}}$, which is the lift coefficient at the vertex of the parabolic (or nearly parabolic) polar. A transformation (eq. (6)) is proposed by Wendt (ref. 33) that accounts for the displacement of the vertex for polars of this type.

Application of Wendt's transformation should be straightforward enough; however, for some low-aspect-ratio vehicles, analysis of the available flight data still presents a challenge. Low-aspect-ratio vehicles often have polars that are quite shallow—that is, the vertex, where minimum drag coefficient occurs on the parabolic curve, is not as easily identified as it is for higher-aspect-ratio aircraft. In addition, for some polars in this study, the curve is incomplete and whether the lift coefficient for the vertex has been reached is not readily apparent; or the vertex is judged to not have been defined by the range of the data. For all of these cases herein, the authors' judgement has been exercised and equation (6) has been applied. Figure 4(a) shows the results of this approach. The ε factors thereby derived are tabulated in the legend of the figure and are also evident by the relative positions of the data points (of $\Delta C_D/\Delta C_L{}^2$ from table 3) in the plot with respect to the theoretical reference lines. The $\Delta C_D/\Delta C_L{}^2$ and ε columns noted in table 3 with the superscript ‡ incorporate the Wendt transformation.

Figure 4(a) shows a dashed line intersecting the ordinate at approximately 0.16 that represents a drag increment, separate and above the induced drag associated with the induced angle of attack. Note that this line is parallel to the line for $\varepsilon = 1.0$ and therefore, where applicable, this drag increment is additive to the line corresponding to $\varepsilon = 1.0$. This increment is defined as $1/2\pi$; and according to reference 31,

Table 3. Drag characteristics data.

Vehicle	M	Configuration remarks	$C_{D'_{min}}$ ¶	f, ft²	A_w, ft²	C_{F_e}	A_b, ft²	A_b/A_w, percent	C_{P_b} †	$\left(\dfrac{\Delta C_D}{\Delta C_L^2}\right)$ ‡	ε ‡	$\left(\dfrac{\Delta C_D}{\Delta C_L^2}\right)$ §	ε §	$(L/D)_{max}$	$\dfrac{C_{F_e}}{C_F}$	$\dfrac{C_{F_{e,fore}}}{C_F}$	W, nominal lb
M2-F1	0.15	Exposed gear	0.0860	11.95	431.0	0.0277	30.84	7.16	–0.103	0.689	0.351	0.497	0.486	2.80	10.05	7.62	1250
		"Clean"	0.0618	8.59		0.0199	30.84	7.16	–0.103					3.44	7.22	4.79	
M2-F2	0.45	$\delta_{uf} = -11.5°$	0.0650	9.04	459.0	0.0197	22.51	4.90	–0.198	0.946	0.544	0.667	0.772	3.13	8.13	4.46	6000
	0.62	$\delta_{uf} = -11.5°$	0.0680	9.45		0.0206	22.51	4.90	–0.209	0.870	0.592	0.609	0.844	3.16	9.01	4.90	
HL-10	0.60	$\delta_{ef} = 0.0°$	0.0496	7.94	460.5	0.0172	14.83	3.22	–0.110	0.571	0.482	0.512	0.538	3.60	7.24	5.89	6000
	0.60	$\delta_{ef} = -3.0°$	0.0558	8.93		0.0194	16.98	3.69	–0.110	0.554	0.497	0.541	0.509	3.33	8.16	6.57	
	0.60	$\delta_{ef} = -30.0°$	0.0895	14.32		0.0311	29.13	6.33	N/A	0.475	0.579	0.535	0.515	2.48	13.09	N/A	
X-24A	0.50	$\delta_{L_B} = 0.0°$	0.0400	6.48	590.0	0.0110	11.78	2.00	–0.129	0.623	0.536	0.535	0.624	4.25	4.70	3.67	6360
	0.50	$\delta_{U_B} = -13.0°$	0.0480	7.78		0.0132	18.12	3.07	–0.157	0.500	0.668	0.395	0.845	4.17	5.39	3.59	
	0.50	$\delta_{U_B} = -21.0°$	0.0605	9.80		0.0166	25.36	4.30	–0.194	0.629	0.531	0.501	0.667	3.28	7.10	3.80	
X-24B	0.50	$\delta_{U_B} = -13.0°$	0.0252	8.33	948.4	0.0088	18.79	1.98	–0.145	0.500	0.575	0.500	0.575	4.50	3.97	2.79	8500
	0.50	$\delta_{U_B} = -20.0°$	0.0285	9.42		0.0099	25.64	2.70	–0.178	0.495	0.577	0.495	0.577	4.28	4.39	2.44	
	0.60	$\delta_{U_B} = -20.0°$	0.0312	10.31		0.0109	25.41	2.68	–0.184	0.524	0.557	0.524	0.557	3.96	5.04	2.96	
	0.80	$\delta_{U_B} = -40.0°$	0.0702	23.20		0.0245	38.05	4.01	–0.287	0.628	0.458	0.628	0.458	2.39	10.81	6.13	
X-15	0.65	$\Lambda, c/4, \approx 25.6°$	0.0645	12.90	1186.0	0.0109	33.00	2.78	–0.333	0.360	0.543	0.360	0.543	4.05	5.22	1.15	15,000
	0.72	$\Lambda, c/4, \approx 25.6°$	0.0680	13.60		0.0115	33.00	2.78	–0.346	0.296	0.661	0.296	0.661	4.20	5.51	1.25	
Enterprise	0.40	$\Lambda, c/4, \approx 36.0°$	0.0610#	164.09#	11,833.0	0.0139#	449.60	3.80	–0.230	0.332	0.600	0.290	0.687	4.70	7.43	3.10	150,900
	0.50	$\Lambda, c/4, \approx 36.0°$	0.0604	162.48		0.0137	449.60	3.80	–0.230	0.351	0.567	0.292	0.683	4.69	7.37	3.06	

N/A = not available

† C_{P_b} } For the M2-F1, M2-F2/F3, and X-15 vehicles; Space Shuttle, and X-24B vehicle at Mach 0.8; the base pressures were measured.
For the HL-10 vehicle, base pressure was derived from published base drag data.
For the X-24A and X-24B vehicles at Mach numbers less than 0.8, base pressures were estimated based on data from the X-24B vehicle at Mach 0.8.

‡ $\Delta C_D/\Delta C_L^2$ and ε based on Wendt transformation.

§ $\Delta C_D/\Delta C_L^2$ and ε derived from linear portion of relationship without concern for vertex of polar.

¶ Note that reference area for $C_{D'_{min}}$ is published value from respective reference sources: all remaining force metrics are based on representative reference areas.

\# The corresponding values of $C_{D'_{min}}$, f, and C_{F_e} with tailcone on are 0.0275, 73.98, and 0.0063, respectively. If the estimated ΔA_w of the tailcone (2078 ft²) is added to A_w for the truncated *Enterprise*,

C_{F_e} = 0.0053.

the additional drag is analogous to that resulting from the loss of leading-edge suction and the associated losses from flow separation and reattachment. For lifting bodies, an analogy may involve drag associated with the flow separation over the upper body caused by crossflow as well as the lack of a conventional leading edge. Note that only the winged vehicles, the X-15 vehicle and *Enterprise*, have drag-due-to-lift factors below this line, although one configuration of the X-24A vehicle is "borderline." Figure 4(a) shows a qualitative interpretation of the relative lifting efficiency of the subject vehicles.

Having acknowledged that the presentation of figure 4(a) is subject to the authors' judgment, offering another approach that yields numbers that are virtually free of such judgment is appropriate. Therefore, figure 4(b) has been included in which the slopes of ΔC_D with respect to ΔC_L^2 are recorded for the linear portion of these relationships, irrespective of where the polar vertex (minimum drag) might occur. Thus, for these cases the lifting-efficiency factor is simply:

$$\varepsilon = \frac{1/(\pi A)}{\Delta C_D / \Delta C_L^2}$$

Although this presentation results in some values of ε that are believed to be beyond the reach of this class of vehicle, these data are presented as a less subjective (albeit a less rational) alternative to the approach used for figure 4(a). All slopes of $\Delta C_D / \Delta C_L^2$ shown in both parts of figure 4 and in table 3 are based on the revised reference areas used and discussed in the "Lift-Curve Slope" section, which are listed in table 2. Dimensional analysis of the above equation indicates that the resulting lifting-efficiency factor, ε, is not influenced by the choice of reference area. The $\Delta C_D / \Delta C_L^2$ and ε columns of figure 4(b) are noted in table 3 with the superscript §.

Maximum Lift-to-Drag Ratio

Figure 5 shows maximum lift-to-drag ratio as a function of the ratio of span-squared to wetted area for each of the vehicles in subsonic flight. This format is commonly used by designers of conventional subsonic aircraft because at subsonic speeds, air vehicle efficiency is most directly influenced by span and wetted area. Raymer (ref. 34) refers to this abscissa function as the "wetted aspect ratio."

For the lifting bodies, the X-15 vehicle, and the *Enterprise*, all of which have significant amounts of base drag, recognizing the "base" effects by assigning base drag to the equivalent skin-friction coefficient parameter, C_{F_e}, is necessary. Consequently, figure 5 also shows a reference framework consisting of a family of constant values of C_{F_e} as employed by reference 35. This family of curves is derived from the often-used expression that relates maximum lift-to-drag ratio to the minimum drag coefficient (here expressed as C_{F_e}); aspect ratio; and the lifting-efficiency factor ε (equation (9)). The range of the family of C_{F_e} curves shown in figure 5 covers the range of values experienced by the subject vehicles. Thus, the format used will accommodate this class of vehicles whose minimum drag consists of a large component of base drag as well as friction drag. A lifting-efficiency factor, ε, of 0.6 was assigned to these curves because this value is approximately the average for the subject vehicles as a group. The dashed curve for

the equivalent skin-friction coefficient is included because it represents a nominally clean modern aircraft that does not have a truncated body, and is constrained to an ε factor of 0.6. Note in figure 5(a) that when the *Enterprise* had its blunt base covered with a tailcone, the maximum lift-to-drag ratio increased to 7.5, relatively close to the dashed curve. The tailcone partially qualifies this configuration as approximating "nominally clean." However, the intentionally roughened surface of the *Enterprise* simulating a thermal protection system obviously violates "nominally clean" requirements. As previously noted, the tailcone did not contribute to lift; hence, the increase in maximum lift-to-drag ratio can only be attributed to a significant reduction in minimum drag. This reduction will be briefly addressed in a following section.

All M2-F1 lift and drag data were obtained as flown, with gear exposed. The value shown in figure 5(a) is adjusted for retracted gear, based on the estimated gear drag increment obtained from reference 10. The discussion that follows applies to the highest values of maximum lift-to-drag ratio at subsonic conditions obtained for each vehicle. Although figure 5(a) shows the highest values for each vehicle, table 3 also includes maximum lift-to-drag ratios for each vehicle for less efficient control deflections or conditions.

The highest values of maximum lift-to-drag ratio at subsonic conditions for five of the vehicles and their collective relationship to the reference framework of curves form an array (a band of $(L/D)_{max}$ over a range of b^2/A_w) that should be a useful reference source with which to relate future reentry-type vehicles. A fairing through this data band (as related to the dashed curve) would indicate that this class of vehicles has maximum lift-to-drag ratios that are approximately 55 percent of those for nominally clean vehicles, having an ε value of 0.6, without truncated bodies (that is, the dashed curve) for a given aspect ratio. The M2-F1 and HL-10 lifting bodies, which are less efficient, should be no less useful to the degree their apparent lesser efficiency is understood. In the case of the M2-F1 vehicle, the outboard elevons again seem to be negative components in this data format because they add drag; are inefficient in providing lift (and were not intended to provide lift); and displace the datum to a higher b^2/A_w value of the abscissa by a factor of approximately 2. The HL-10 lifting efficiency, ε, is somewhat low, and its equivalent skin-friction parameter, C_{F_e}, is quite high, although the HL-10 vehicle has a relatively modest component of base drag for the subsonic control position configuration.

Assigning the derived base pressures to the projected area of all aft sloping body surfaces normal to the flight path does not account for the flight-determined value of C_{F_e} for the HL-10 vehicle. This value suggests that if all aft sloping surfaces experienced separated flow, the resulting drag would not produce the observed equivalent friction drag coefficient. Therefore, considering compressibility effects, trim drag, and outboard fin drag caused by canceling fin sideloads (not vehicle sideloads) as possible contributors to the high C_{F_e} values for the HL-10 vehicle at $C_{D_{min}}$ conditions is reasonable. A combination of these factors and some separated flow over the aft sloping surfaces of the upper body are speculated to cause the HL-10 maximum lift-to-drag ratio to be displaced below the aforementioned band represented by the M2-F2, X-24A, X-24B, and X-15 vehicles and the *Enterprise* in figure 5(a).

24

The intermediate maximum lift-to-drag ratios for the HL-10, X-24A, and X-24B vehicles listed in table 3 represent the effects of increased longitudinal control deflections (that is, larger wedge angles). The lowest values of maximum lift-to-drag ratio for the HL-10 and the X-24B vehicles represent the large wedge angles used when traversing the transonic region. The lowest value for the M2-F1 vehicle in table 3 (also less than 3) was measured for this vehicle with exposed landing gear.

The flight values of maximum lift-to-drag ratio shown in figure 5(a) and the corresponding large symbols shown in figure 5(b) are the same. In figure 5(b), the large symbols represent the flight results and the corresponding smaller symbols represent values calculated from equation (9) using the values of ε and C_{F_e} shown in the figure legend. Agreement between the flight-measured and calculated values is relatively good for the X-15 and the X-24B vehicles. For the other vehicles, the calculated value is low, relative to the measured value, ranging from 12 percent (*Enterprise*) to 43 percent (M2-F2 lifting body) lower. The X-15 and X-24B vehicles were the only vehicles that had lift-drag polars with the vertex at $C_L = 0$. The discrepancy between the flight-measured and calculated values of maximum lift-to-drag ratio evidently is related to the degree of displacement for the respective polar vertex above zero lift. As is discussed in reference 54, page 12 and figures 25 and 26, accounting for this displacement through the use of equation (6) will provide a realistic, although harsh, definition of the lifting-efficiency factor, ε, because the vehicle is not credited therein with the increment of lift below C_L for $C_{D_{min}}$. Lift-to-drag ratio, however, accounts for this increment of lift. Thus, because flight-measured values of maximum lift-to-drag ratio include credit for this increment; and equation (9) uses a value of ε which does not account for this increment of lift; the discrepancies noted in figure 5(b) are expected.

Minimum Drag

Minimum drag is presented in several formats in order to better understand which components are dominant and to reveal the relationship of forebody and base drag. The metrics used, as defined earlier, include equivalent skin-friction coefficient (C_{F_e}) and equivalent parasite drag area (f); as previously mentioned, these forms of minimum drag include both base and forebody drag. Base drag is defined for each vehicle (using measurements for five of the vehicles and estimates for the other two) to allow separation of base drag and forebody drag components. The data from the vehicles are collectively presented in tabular and graphic formats to provide a greater understanding than would likely be achieved by studying the vehicles individually.

Table 3 shows the basic data along with some of the significant physical characteristics of the vehicles. The conventional minimum drag coefficients are tabulated as derived using the reference areas published by the respective reference authors. Although the revised reference areas are believed to be a rational improvement over the areas that they replace (as noted in the "Lift-Curve Slope" section), the format chosen here for graphically presenting the minimum drag eliminates the conventional reference area as a factor. Perkins and Hage (ref. 37), and subsequent others, have avoided the concern about reference area definition by multiplying the minimum drag coefficient by the reference area to define an equivalent parasite drag area, *f*, as shown in equation (10).

Figure 6 shows the equivalent parasite drag area for each of the subject vehicles as a function of total wetted area. Table 3 shows the range of equivalent parasite drag area for the subject vehicles is quite large, from 6.5 ft^2 to 164.0 ft^2. Total wetted area for each vehicle is defined as all outer mold-line or external surface areas ahead of a blunt base or any trailing edge. The definition thus assumes that the flow is attached over these surfaces. Separated regions ahead of the base, interference effects, vortex flow ahead of the base, and negative pressure coefficients over the base or aft sloping surfaces each represent drag increments in excess of the viscous drag generated by the actual wetted surfaces. Hence, this drag metric defines the sum of the drag sources (excluding lift) that include friction drag for turbulent flow conditions as well as drag components in excess of friction. Because even an ideal body will have friction drag, this metric is labeled as a "parasite" factor because the metric includes such parasitic losses.

The equivalent parasite drag area can also be interpreted in terms of an equivalent skin-friction coefficient, C_{F_e}, by noting the location of a datum point for a given vehicle relative to the family of constant equivalent skin-friction lines (fig. 6). The equivalent skin-friction coefficient is, of course, another metric that reveals the degree to which measured minimum drag of a vehicle exceeds the ideal minimum drag (that is, the skin-friction drag over the wetted area). The average skin-friction coefficient over wetted areas for all seven vehicles, assuming flat-plate, turbulent boundary-layer flow (adjusted by a form factor of 1.02) at flight Mach and Reynolds numbers, is $C_F = 0.0023$, which can also be considered as a reference value of C_{F_e} (see the dashed line in figure 6). Table 3 shows the explicit values of equivalent skin-friction coefficient for each of the subject vehicles at each flight condition considered herein. These values result from equation (8), as shown in the "Methods of Analysis" section.

Although table 3 shows more than one value of f or C_{F_e} for most of the vehicles, figure 6 shows only the lowest value for each vehicle. For some of the vehicles, drag coefficients exist that represent both the subsonic control configuration (the value shown in figure 6) and the less-efficient transonic configuration that requires larger control deflections. For the X-15 aircraft, the C_{F_e} included in figure 6 is the one for the lower Mach number, and thus is the one experiencing lower compressibility effects. In the case of the M2-F1 lifting body, which had a fixed landing gear, the estimated landing gear drag has been subtracted for the datum of figure 6. This estimate is from reference 10 and was based on information obtained from Hoerner (ref. 31). All data in figure 6 include the base drag for each vehicle.

A cursory summary of the data shown in figure 6 can be stated as follows:

- The early generations of lifting bodies, the M2 and the HL-10 vehicles, have equivalent skin-friction coefficients between 0.0170 and 0.0200 (in contrast to the average value of skin friction for all seven vehicles for turbulent flow, 0.0023).

- For the X-24A and X-15 vehicles, the corresponding equivalent skin-friction coefficients are approximately 0.011.

- The X-24B vehicle, the last of the lifting bodies, has an equivalent skin-friction coefficient slightly less than 0.009.

- The wetted surfaces of the *Enterprise* were purposely roughened to simulate the thermal protection tiles of operational vehicles to follow. In addition, this vehicle has a very large base area. Consequently, the *Enterprise* equivalent friction coefficient of approximately 0.014 is understandably higher than the three lowest values, and occupies the median position in the array of coefficients for the subject vehicles.

Note that the range of the lowest equivalent skin-friction coefficients for each of the seven vehicles, from approximately 0.009 to 0.020, is from 4 to slightly more than 8 times the skin-friction drag that would occur from an attached, turbulent boundary layer alone. This range in equivalent skin friction is of the same order as the range of values for older, propeller-driven aircraft having fixed landing gears (ref. 55). In the case of the seven vehicles, this range includes the base drag increment and upstream vortices not associated with the base, possible compressibility effects, interference, and local regions of separated flow that largely correspond to the drag penalties associated with exposed landing gears and the propulsion system (including cooling losses) for the small, more conventional aircraft. Figure 6 also shows in tabular form values of C_{F_e}/C_F for each data symbol on the graph, where C_F, the theoretical skin friction for turbulent flow at the flight condition of each vehicle, is calculated by the methods of reference 38 and adjusted for three-dimensional effects by the form factor of 1.02 from reference 39. Table 3 shows corresponding values of this ratio for every flight condition considered.

The preceding discussion revealed that the lowest of the equivalent skin-friction coefficients among the several vehicles was approximately 4 times greater than the associated turbulent boundary-layer skin-friction coefficient. As noted, when relating the equivalent skin-friction coefficients of the subject vehicles to that of propeller-driven aircraft having exposed landing gear, significant drag penalties exist in addition to the friction and base drag components, even at minimum drag conditions. These additional losses are designated as excess equivalent skin friction or as excess drag.

A family of relationships can be assembled representing the approximate level of equivalent skin-friction coefficient (C_{F_e}) corresponding to basic skin friction for turbulent flow over the forebody, variations in base pressure coefficient, and the ratio of base area to wetted area for the subject class of vehicles. Compared with measured data, this format should provide some understanding of how much the equivalent skin-friction coefficients for the subject vehicles exceed calculated levels based on friction drag for turbulent flow plus measured and estimated base pressures.

Figure 7 shows this comparison, in which the family of lines is calculated from equation (13) over a range of constant base pressure coefficients. All of the lines start at the reference average C_{F_e} value of $C_F = 0.0023$, such that each line represents a calculated level of C_{F_e} with basic (that is, the average) skin-friction drag and base drag for a specific value of A_b/A_w.

For the subject vehicles considered in this report, a vehicle-specific value of C_{F_e} can be calculated using vehicle-specific C_{P_b} values from table 3 (positioned as appropriate within the family of constant C_{P_b} lines) and vehicle-specific C_F values (instead of the average value of 0.0023).[#] These values are represented by the smaller symbol of each symbol pair, located at the lower end of the vertical line that connects to the corresponding larger symbol at the upper end (fig. 7).[**]

When the small symbols (fig. 7) are interpreted with respect to the ordinate scale, they approximate the equivalent skin-friction coefficient each subject vehicle should have if the vehicle experiences drag only from the friction resulting from a fully attached, turbulent boundary layer over the wetted surface and the base drag associated with the pressure coefficients indicated in table 3. The large symbol (fig. 7) at the upper end of a given vertical line is the in-flight–determined value of C_{F_e} for that vehicle as obtained from table 3. The increment of C_{F_e} represented by the length of the vertical line segment connecting a symbol pair quantifies the excess drag (that is, the amount that the actual drag exceeds the presumed or calculated drag at these minimum drag conditions). The authors speculate that the excess drag increments result from:

- local regions of separated flow upstream of base stations or any trailing edges.
- vortices generated by deflected control surfaces; body crossflow; and in some cases, unproductive side loads generated by outboard vertical or canted fins.
- interference drag.
- roughness and protuberance effects.
- compressibility effects.
- data uncertainty (see the "Data Uncertainty" section).

For example, note the M2-F2 lifting body (fig. 7; the circular symbol without a flag), which has a base area–to–wetted area ratio of 4.9 percent. If no excess drag sources existed for this vehicle, its calculated level of C_{F_e}, associated with the measured base pressure coefficient of –0.209 plus friction drag, would be 0.0117. However, the actual level of C_{F_e} for the M2-F2 vehicle (the larger circular symbols) is approximately 0.020. Apparently, this vehicle experiences significant excess drag beyond the skin-friction and base drag, even at minimum drag conditions. The M2-F1 and HL-10 vehicles experience even more excess drag.

The X-24B lifting-body vehicle is represented by the triangular symbols (fig. 7). Unfortunately, base pressure measurements were made for this vehicle only in the transonic configuration, wherein the very

---

[#]Upper and lower flap deflections necessary for calculating base area for the X-24A and X-24B vehicles were obtained from references 56 and 57, respectively.

[**]Because base pressure estimates for the X-24A and X-24B vehicles have been refined, the ordinate values of the smaller symbols for these vehicles are slightly different than they were in the corresponding figure in reference 46. These improved estimates also account for slight differences for these vehicles in figures 8–10, as well as changes that may be evident in table 3.

large upper and lower flap deflections created a flared afterbody (ref. 58). The sum of the upper and lower flap deflections was approximately 68°; refer to the schematic of body-flap angles in figure 1(i). This datum (the darkened triangle symbol) was obtained at Mach 0.8, whereas the other X-24B data presented in this paper were obtained at Mach 0.5 and Mach 0.6 with smaller flap deflections. The very large, excess drag increment noted between the large and small darkened triangular symbols shows the obvious effects of compressibility and of the large flare angles that produce high drag from both the windward surface and from reduced pressure on the leeward side (ref. 59).

This result, obtained at Mach 0.8, is included with the other data representing lower Mach numbers because it provides a base pressure coefficient reference datum that is used for estimating base pressure coefficients for the X-24A vehicle and the other X-24B data pairs. Appendix F contains the procedure used to estimate these pressure coefficients, based on the reference datum at Mach 0.8. The major portion of the base region for these two vehicles is the same; and the upper and lower body flaps, which influence the base area as they are deflected, are identical. Note that the X-24B vehicle had a very large increment of excess drag for the transonic configuration (fig. 7; the darkened triangles) as would be expected; however, the X-24B subsonic configurations experienced excess drag increments much smaller than those for the other lifting bodies. The excess drag of the X-24A vehicle at low lift is somewhat larger than that of the subsonic X-24B vehicle, but is still much smaller than those of the earlier lifting-body configurations (the M2-F1, M2-F2, and HL-10 vehicles).

The excess low-lift drag increment for the X-15 aircraft is very small. The likely reason for this small increment is the relatively high fineness ratio of the fuselage, thin wings, and horizontal stabilizer, which allows for small-angle aft-sloping surfaces. Therefore, these surfaces maintain a proverse pressure gradient that assures attached flow. These features greatly reduce compressibility effects.

Because the *Enterprise* had a roughened surface to simulate the thermal protection systems of the Space Shuttles to follow that would actually orbit, the value of C_F used to determine the position of the small symbol for the *Enterprise* (fig. 7) is too low for this vehicle. Consequently, the excess drag increment shown for the *Enterprise* in figure 7 is too large, but the magnitude of this discrepancy cannot be quantified based on the presently available data.[††]

Base Pressure Coefficients

Hoerner compiled base pressure data from projectiles, fuselage shapes, and other small-scale three-dimensional shapes (ref. 31) and derived therefrom an equation that related the base drag and base pressure coefficients to the forebody drag of the respective bodies (eq. (17)). Reference 31 also includes an equation that describes the analogous relationship for quasi-two-dimensional shapes that shed vortices in a periodic manner, the well-known Kármán vortex street (eq. (18)). Base pressure data from some of the subject vehicles will be compared on the basis of the Hoerner relationships and modifications to his equations (using different *K* values). The search for flight-measured base pressure data for the seven subject vehicles is somewhat disappointing, considering that each of these vehicles has a significant component of base drag. Table 4 shows the results of the literature search.

[††]According to reference 60, preflight estimates of thermal protection system drag indicated an additional increment of 0.00084 (based on wetted area) to the Space Shuttle friction drag. However, reference 60 also considered the estimate of thermal protection system drag to be too large after examining postflight data from an orbiting Space Shuttle (*Columbia,* mission STS-2).

Table 4. Base pressure sources.

Vehicle	C_{P_b} data	Reference number	Remarks
M2-F1	Yes	10	The base region was pressurized by turning the vanes.
M2-F3	Yes	Unpublished	The M2-F3 base pressure data (appendix E) were applied to the M2-F2 vehicle drag data.
HL-10	No		Base drag data have been published, but no explicit base pressure data were found.
X-24A	No		Base pressure coefficients were estimated using X-24B results (appendix F).
X-24B	Yes	58	Base pressure coefficients for Mach 0.5 and Mach 0.6 were estimated using Mach 0.8 results (appendix F).
X-15	Yes	40	
Space Shuttle	Yes	61	Base pressure data from the orbiting Space Shuttle *Columbia* have been applied to the drag data from the nonorbiting *Enterprise*.

Note from figures 1(b) and 1(c) that the M2-F3 vehicle is virtually the same as the M2-F2 vehicle. All configurational dimensions are the same except that a centerline upper vertical fin was added to the M2-F3 vehicle. For this reason, the unpublished base pressure data from the M2-F3 lifting body are accepted as representative of those of the M2-F2 lifting body. Consequently, the M2-F2 and the M2-F3 lifting bodies will be treated as if they were the same vehicle in the analysis to follow.

Because of Hoerner's convincing demonstration that base pressure is related to forebody drag, comparing the available base pressure coefficients from the subject vehicles to his equations is possible. Figure 8 shows these comparisons. Figure 8 also includes a shaded band for Hoerner's three-dimensional equation that is bounded by numerator coefficients, K, of 0.09 and 0.10. By modifying Hoerner's original equation with these K coefficients, the base pressure coefficients from the X-15, the M2-F3, and the Space Shuttle vehicles (which are obviously three-dimensional) are observed to fall within or relatively close to this band.

Figure 8 also shows that the flight data are relatively close to Hoerner's quasi-two-dimensional relationship (eq. (18)). The relatively higher (more negative) pressure coefficient from the X-24B vehicle (dark triangle) is caused by the large wedge angle, ahead of the base, formed by the upper and lower flaps that are used for control in pitch. The upper flap was deflected upward approximately 40°, and the lower flap was deflected downward approximately 28°. This geometry is known to produce more negative base pressure coefficients (ref. 59). The only measured base pressure data from the X-24B vehicle (ref. 58) unfortunately were obtained with a significantly larger wedge angle than existed for the subsonic control configurations. The X-24B polars for Mach 0.5 and Mach 0.6 were obtained using much smaller wedge angles.

The M2-F1 datum is somewhat unrepresentative of the subject class of vehicles in that the base region was pressurized to some extent by turning vanes (one on each side, below the rudders). Based on the available flight data, the vehicles considered herein (excepting the data for the M2-F1 vehicle and the X-24B transonic configuration) are best represented by the three-dimensional equation where $K = 0.09$ to 0.10, which means the base drag of blunt-based large-scale vehicles is much higher than predicted by Hoerner's original three-dimensional equation. Based on evidence from references 40 and 62 and figure 8, subsonic flow separating from a relatively large, sharp-edged, three-dimensional base can be argued to exhibit quasi-two-dimensional characteristics. In either case, the data indicate more negative base pressure coefficients than the unmodified three-dimensional equation ($K = 0.029$) would predict. Because of the large base drag component these base pressures represent, employing a method of pressurizing the base region may be advisable. Such methods are available, although their use necessarily complicates the afterbody design details. Considering the very large losses caused by the base region for this class of vehicles, such pressurizing devices deserve attention (refs. 31 and 63–70). Although "boat-tailing" would not ordinarily be considered for a reentry vehicle, the large reduction in low-lift drag provided to the *Enterprise* through use of the tailcone is worth noting (table 3 and ref. 23). This reduction in drag is almost 55 percent of the minimum drag for the *Enterprise* with the blunt base. Although that increment might seem large for a tailcone with a fineness ratio of approximately 1.3, related data from reference 31, represented in figure D-5 in appendix D, indicate such an improvement can occur.

Optimal Minimum Drag

Excluding the base pressure data from the M2-F1 and the X-24B vehicles for the reasons already given, the flight data from three other vehicles (M2-F3, X-15, and Space Shuttle vehicles) are believed to represent the generic blunt-based class of vehicles. More large-scale base pressure and overall minimum drag (and hence forebody drag) data must be obtained in flight to convincingly demonstrate their relationship. Defining this relationship for three or four values of forebody drag for the same outer mold-line shape would be most helpful. Until more flight data are obtained or a superior relationship is developed, the shaded region of figure 8, derived from the data of the latter three vehicles, is assumed to be a reasonable representation of the base pressure characteristics for this class of reentry craft. Therefore, a revised version of Hoerner's three-dimensional equation, $K = 0.10$, has been used to show the dependence of minimum drag on the relative size of the blunt base over a significant range of forebody drag.

Figure 9(a) shows this relationship, in which each of four curves shows how overall minimum drag coefficient varies with forebody drag coefficient for discrete ratios of base area to wetted area (2.5, 5.0, 7.5, and 10.0 percent). The salient feature of these curves is that each has what will be referred to as an optimal region of lowest overall minimum drag coefficient, C_{F_e}. This lowest value is called "optimal" here because "optimal" is more concise and less cumbersome than the repetitious use of "lowest minimum" or the "minimum of the minimum"; however, it is acknowledged that the term "optimal" would usually be used to signify the "ideal" in which a vastly more comprehensive range of factors that can influence performance is considered.

Note that for the 2.5-percent relationship, an optimal region (a drag "bucket") exists near the forebody drag coefficient value of 0.003. Because these coefficients are based upon the wetted area, and because

the smooth-skin turbulent friction coefficient for these Reynolds numbers (in the range of 10^7–10^8) would be close to 0.002, a configuration having a base area–to–wetted area relationship of 2.5 percent can afford only a minute amount of roughness, protuberance, interference, or separation drag over the forebody if the optimal C_{F_e} is to be achieved. Conversely, for the high base area–to–wetted area relationships, which more closely represent many reusable launch vehicle and reentry configurations, the optimal C_{F_e} (or drag bucket) occurs at significantly higher values of forebody drag coefficient, $C_{F_{e,fore}}$.

This characteristic should be of particular interest with regard to some emerging reusable launch vehicles that have relatively large base area–to–wetted area ratios (between 7.5 percent and 10.0 percent). This observation, of course, means that such configurations can afford (in fact, may benefit from) additional forebody drag in addition to the unavoidable smooth-skin turbulent friction. Thus, surface roughness that may accompany a thermal protection system may actually provide a reduction in overall C_{F_e} while increasing the forebody drag, if the upper body is shaped so as to maintain attached, high-energy flow.

Such a reduction would be the result of forebody roughness affecting the growth of the boundary layer from the nose to the edge of the base, which in turn affects the level of "vacuum" or suction at the base through a "jet-pump mechanism" as described by Hoerner (ref. 31). Thus, subject to the curves of figures 8 and 9, forebody roughness adds to the thickness of the boundary layer, thereby reducing the pumping (vacuuming) of the base and reducing the base drag. The drag bucket curves (fig. 9) are related to those seen in chapters 3, 6, and 13 of reference 31 for bodies, nacelles, canopies, and airfoils.

Figure 9(a) shows the relationship of C_{F_e} to forebody drag coefficient for the same vehicles as are represented in figure 8. The numbers adjacent to each data symbol indicate the base area–to–wetted area ratio (in percentage terms) of the respective vehicle at the specific flight condition. From these numbers, in relationship to the curves, note that the data from the vehicles designated by the open symbols (except the M2-F1 and HL-10 vehicles) are in qualitative accord with the semiempirical curves. As was stated earlier with regard to figure 8, the overall C_{F_e} for the M2-F1 vehicle is believed to be lower than the semiempirical curves suggest because turning vanes pressurized the base. For the X-24B vehicle (the dark triangle), the value of C_{F_e} is believed to be high because of the aforementioned large flare angle that produces high windward surface drag and lowers the lee-side pressures on the longitudinal control body flaps. This belief is not only supported by data from reference 59 but also by speed-brake data from the X-15 aircraft (the dark symbol) that represent a comparable flared, or wedge, angle (ref. 71).

With reference to the curves in figure 9, analytically determining the minimum, or "bucket" value of the equivalent skin-friction coefficient (C_{F_e}) and the associated forebody equivalent skin-friction coefficient ($C_{F_{e,fore}}$) for a given base area–to–wetted area ratio (A_b/A_w) is possible. The curves of figure 9 are defined by a revision of equation (13), repeated here:

$$C_{F_e} = C_F + |C_{P_b}| \frac{A_b}{A_w} c$$

Equation (13) was used to calculate C_{F_e} for a case where no forebody losses existed except for that of a fully attached, turbulent boundary over a smooth surface (hence, the term C_F on the right side of the equation). For the curves shown in figure 9, the abscissa values of $C_{F_{e,fore}}$ are substituted for C_F in equation (13), as follows:

$$C_{F_e} = C_{F_{e,fore}} + |C_{P_b}| \frac{A_b}{A_w} c \tag{21}$$

where $c = 0.92$, as derived from X-15 experience as a base pressure profile factor; and C_{P_b} is the Hoerner (ref. 31) expression given in equation (17):

$$-C_{P_b} = \frac{K}{\sqrt{C_{D_{fore,b}}}}$$

where $K = 0.10$, based on current analysis. Also,

$$C_{D_{fore,b}} = C_{F_{e,fore}} \frac{A_w}{A_b} \tag{22}$$

Substituting equation (22) into equation (17), and in turn, equation (17) into equation (21), gives the following:

$$C_{F_e} = C_{F_{e,fore}} + \frac{0.10}{\sqrt{C_{F_{e,fore}} \frac{A_w}{A_b}}} \frac{A_b}{A_w} 0.92 \tag{23}$$

To determine the coordinates for the bucket value of C_{F_e}, the above expression is differentiated with respect to $C_{F_{e,fore}}$. Setting the derivative to zero, the minimum C_{F_e} value occurs at

$$C_{F_{e,fore}} = 0.1284 \frac{A_b}{A_w} \tag{24}$$

Substituting back into equation (23), the minimum of C_{F_e} for a given base area–to–wetted area ratio is:

$$C_{F_e} = 0.3852 \frac{A_b}{A_w} \tag{25}$$

These expressions for optimal values of forebody drag and overall minimum drag coefficient are offered as tools for approximation until more definitive relationships are obtained. The present expressions define the coordinates for minima that are consistent with values obtained graphically from working plots; however, they and the families of curves of figure 9 are dependent on multiple assumptions. These assumptions include the validity of the Hoerner equation (eq. (17)) for three-dimensional flow, the assigned value of K for equation (17), and the validity of the base pressure profile factor of 0.92. Generally, improved values for such curves and the expressions for minima (eqs. (24) and (25)) can be generated as assumptions become based on a more comprehensive database or as a new superior relationship of the variables is formulated.

The Effect of Roughness on Drag

Lift and drag data from the actual X-24A vehicle, albeit from the 40- by 80-ft wind tunnel at NASA Ames Research Center (Moffett Field, California), show an increase in overall drag when the forebody was partially covered with roughness (ref. 49). The results from these wind-tunnel tests will be compared with X-24A flight results that have approximately the same body-flap deflections. Of the several X-24A vehicle configurations tested in the wind tunnel, configuration number 4 has been chosen for this study because it is the most similar to one of the X-24A flight configurations reported herein. Figure 9(b) shows the results of this examination of roughness effects for this vehicle.

For the longitudinal control flap deflections of configuration 4, the resulting base area is 4.3 percent of the wetted area. Therefore, in addition to the curves already shown in figure 9(a), figure 9(b) includes an additional curve corresponding to this area ratio. The X-24A data from the 40- by 80-ft wind-tunnel tests are included for both the smooth-skin case and with added roughness.

In order to define the forebody drag coefficient, $C_{F_{e, fore}}$, for these data from reference 49, subtracting base drag from the $C_{D_{min}}$ values for the smooth-skin configuration is necessary. Base drag was not determined during these wind-tunnel tests, nor were X-24A base pressures measured in flight. Consequently, estimating base pressure coefficients (see appendix F) based upon X-24B flight results (ref. 58) was necessary. The abscissa location of the datum for smooth skin (fig. 9(b); the solid squared diamond symbol) and its relationship to the forebody drag coefficient for the lowest portion of the curve (for 4.3 percent) indicate that a reduction in drag associated with added roughness should not be expected. Thus, the drag increase indicated by the flagged solid diamond symbol and reported in reference 49 for the roughened configuration is in accord with the associated semiempirical curve of figure 9(b). Note that the two symbols for the 40- by 80-ft wind-tunnel tests establish essentially the same slope as the curve for 4.3 percent.

The smooth-skin X-24A datum from the 40- by 80-ft wind tunnel, indicating a level of forebody drag coefficient that is greater than the abscissa value of the "bucket" for the associated semiempirical curve, is evidence that the upper-body aft-sloping surfaces experience low pressures and possibly body-tip fin interference that add considerably to the forebody drag, even at low lift conditions.[‡‡] This minimum forebody drag coefficient, based on wetted area, is approximately 3.7 times greater than the calculated

---

[‡‡]According to reference 49, flow-visualization studies during these wind-tunnel tests did not reveal any flow separation at low lift conditions, although some unsteadiness of the flow over the inboard, near-tip region of the outboard fins was evident.

turbulent skin friction over an aerodynamically smooth body experiencing attached flow throughout. Note in table 3, for the X-24A configuration having approximately the same flap wedge angle and $\delta U_B = -21°$, that the corresponding ratio of forebody drag to skin-friction drag is 3.80. Tuft flow–visualization data recorded during the full-scale wind-tunnel tests indicate that flow separation did not occur over the upper body at low and moderate angles of attack. This forebody drag coefficient thus represents attached flow, which is evidence that the upper-body surfaces of reentry-type vehicles may need to be relatively flat (not with an upper aft-sloping boat tail) so that the base and forebody drag combine favorably and approach the optimal C_{F_e} (the drag bucket) as postulated by the various curves shown in figure 9.

The Effect of Fineness Ratio on Drag

Truncated or blunt-based bodies, such as the subject vehicles, bear a familial relationship to the forward two-thirds or three-fourths of a classical body of revolution that has a fully boat-tailed afterbody (for example, Sears-Haack). Considering whether the forebody drag during subsonic flight of a blunt-based vehicle is dependent on fineness ratio, as is the drag of a fully boat-tailed body, is reasonable. To evaluate this relationship, figure 10 shows the forebody drag coefficients ($C_{F_{e, fore}}$) of the seven vehicles plotted with respect to effective fineness ratio (l/d_{eff}). The open symbols show a clear relationship between forebody drag and fineness ratio, although configurational differences other than fineness ratio are likely prominent for fineness ratios less than 3. As stated before for the discussion of figure 7, the solid triangle symbol representing the X-24B vehicle shows a much higher forebody drag coefficient than the other vehicles because of higher pressure on the windward surface of the body flaps, which are deflected to a large flare or wedge angle (fig. 10). The X-15 forebody drag for partially deflected speed brakes (the solid diamond symbol) is included here because it lends credence to the X-24B data, and discussion of same, in that the X-24B body flaps and the X-15 speed brakes experience related flow phenomenon.

Landing Gear Drag Increment

The increment of landing gear drag has been defined from flight measurements for five of the subject vehicles (all except the M2-F1 and the HL-10 vehicles). For the M2-F1 vehicle, gear drag was estimated and reported in reference 10. This estimated value will be included with the flight-measured values for the other vehicles in an effort to relate the increment of landing gear drag with vehicle weight. The flight-determined values were each obtained from the references that provided the subsonic lift and drag data reported herein, except for the X-15 gear drag, which was derived from reference 19.

Figure 11 shows the relationship of these increments of landing gear drag with the weight of the respective vehicles, where the drag increments are represented as parasite drag area from:

$$\Delta f_{gear} = \Delta C_{D_{gear}} S, \text{ft}^2$$

Thus, Δf_{gear} is the increment of parasite drag area caused by the exposed landing gear. The legend of figure 11 shows some distinguishing features relative to the landing gear of the several vehicles. Some of these features would complicate the weight-to-drag relationship portrayed here—for example; how much

would the parasite drag area increase if a 15,000-lb vehicle such as the X-15 vehicle had open main gear wells and doors during gear deployment? Furthermore, because the X-15 skids were exposed (albeit folded against the fuselage) before extension, the apparent extended gear drag increment is thereby diminished. Nevertheless, the vehicles considered establish a qualitative vehicle weight–to–gear drag relationship.
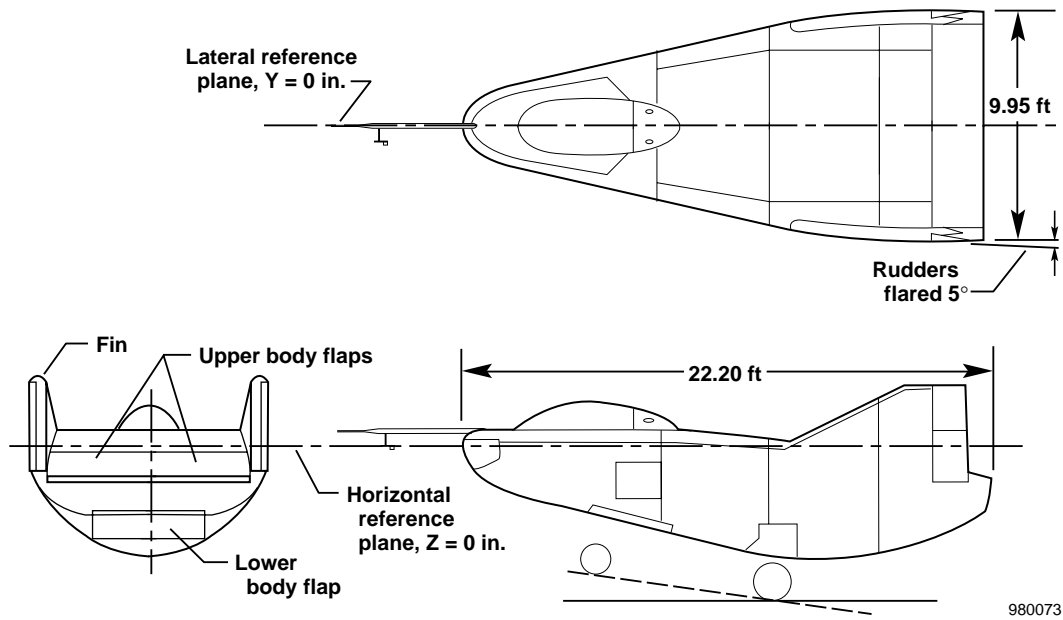
SUMMARY OF RESULTS

Flight-determined lift and drag characteristics from seven blunt-based lifting-body and wing-body reentry configurations have been compared and related to several standards of aerodynamic efficiency. For lift-curve slope, limited comparisons have been made with wind-tunnel results for generic models and the theoretical relationships of Jones and Helmbold. A summary of major results is as follows:

1. Base pressure coefficient data from the X-15, the M2-F3, and the Space Shuttle vehicles indicate that, to represent large-scale flight vehicles, Hoerner's equation relating base pressure to three-dimensional forebody drag requires a larger numerator coefficient than Hoerner used. A tentative range of values for the numerator coefficient is from 0.090 to 0.100 rather than Hoerner's value of 0.029, which is based on small-scale model data.

2. Evidence exists that subsonic flow separating from a relatively large, sharp-edged three-dimensional base can exhibit quasi-two-dimensional characteristics and base pressure coefficients.

3. The nature of the Hoerner base pressure–to–forebody drag relationship (regardless of whether the three-dimensional or two-dimensional equation is used, or the numerator coefficient value) causes base drag and forebody drag to combine to form an optimal minimum drag (a drag "bucket") over a small range of forebody drag. The magnitude of forebody drag coefficient that defines the bucket depends primarily on the ratio of base area to wetted area of the respective vehicle. A vehicle having a large base area–to–wetted area ratio and a relatively flat upper surface may benefit from surface roughness drag (such as that associated with a thermal protection system) at low lifting conditions; this combination of features may provide some favorable compensation for low-fineness-ratio vehicles having a relatively large base.

4. Conversely, a strong relationship between forebody drag and fineness ratio (favoring, of course, the high-fineness ratios) has been demonstrated to exist. This characteristic, in concert with the possibility of achieving the aforementioned drag bucket, underlines the importance of obtaining more large-scale, free-flight base pressure and forebody drag data. Such an investigation should either confirm the numerator coefficient band suggested herein for the three-dimensional equations ($K = 0.09$ to 0.10); confirm or refute the two-dimensional nature of the separating flow; or define a new numerator coefficient or a new superior relationship that will reliably define the nature of the drag bucket for general application.

5. Minimum equivalent parasite drag area values for the vehicles range from 6.5 ft^2 to 164.0 ft^2. Division of equivalent drag area by the associated wetted area provided equivalent parasite skin-friction coefficients ranging from approximately 0.009 to 0.020, excluding the less efficient body-flap configurations for transonic conditions (these coefficients include base drag). These minimum equivalent skin-friction values (for retracted landing gear) range from 4 to slightly more than 8 times the skin-friction drag for the attached, turbulent boundary layer alone.

6. When the base drag coefficient is subtracted from the minimum equivalent friction coefficient (thereby defining forebody drag coefficient), a considerable increment of excess drag (greater than that attributable to an attached, turbulent boundary layer) still exists for all of the vehicles except the X-15 vehicle. These equivalent skin-friction coefficients for forebodies with landing gear retracted ranged from approximately 1.2 to approximately 6.6 times the skin-friction drag for the attached, turbulent boundary layer alone. This extra increment of equivalent parasite friction drag, referred to as excess drag, is believed to result from the following:

   • local regions of separated flow upstream of base stations or any trailing edges.

   • interference effects.

   • vortices generated by deflected control surfaces; body crossflow; and in some cases, unproductive sideloads generated by the outboard fins.

   • roughness and protuberance effects.

   • compressibility effects.

7. Little order existed to the lift-curve slope data when lift coefficient was based on the reference areas used in the reports from which the data were obtained. Application of more representative reference areas (for five of the seven vehicles) and adjustment of the lift-curve slopes for compressibility provided improved order to the data. These data demonstrate that the choice of a physically meaningful (representative) reference area is of major importance.

8. The chosen definition for a physically meaningful reference area for lift parameters of a lifting body should include all of the planform area projected onto the longitudinal-lateral plane, including the projected area of canted tip or side fins. For wing-body combinations, the fuselage forebody is considered to perform as a lifting body. Therefore, the chosen reference area for these configurations includes the projection of all planform area ahead of the wing trailing edge (that is, forebody plus wing). This concept, which rejects projected body planform area aft of the wing trailing edge, is supported by full-scale flight measurements of lift-curve slope from the Space Shuttle *Enterprise* with the tailcone and with the truncated base, and by fuselage pressure distribution measurements from the X-1 research airplane.

9. The M2-F2 data demonstrate that the lift-curve slope of very low–aspect–ratio lifting bodies can exceed the lift-curve slope values represented by the relationships of Jones or Helmbold for aspect ratios less than approximately 1. The M2-F2 results are not believed to be an anomaly because they are afforded credence by generic model results, generic leading-edge vortex lift data from highly-swept wings, and crossflow (drag) lift data from bodies of revolution.

10. Excepting the M2-F1 and the HL-10 vehicles, the remaining five vehicles form an array (a band of the maximum lift-to-drag ratio over a range of the wetted aspect ratio) that should be a useful reference source with which to relate future reentry-type vehicles or reusable launch vehicles. A fairing through this band of data indicates that the maximum lift-to-drag ratio for this class of vehicles, where the lifting efficiency factor is limited to 0.6, is approximately 55 percent of those for nominally clean vehicles without truncated bodies for a given wetted aspect ratio.

Dryden Flight Research Center
National Aeronautics and Space Administration
Edwards, California, January 28, 2000

Body flap
9.50 ft
Rudder
Elevon
13°

14.167 ft

Horizontal reference plane (cone axis)

20.00 ft
13°
9.50 ft

980072

(a) The M2-F1 vehicle.

Lateral reference plane, Y = 0 in.
9.95 ft
Rudders flared 5°

Fin
Upper body flaps
Horizontal reference plane, Z = 0 in.
Lower body flap

22.20 ft

980073
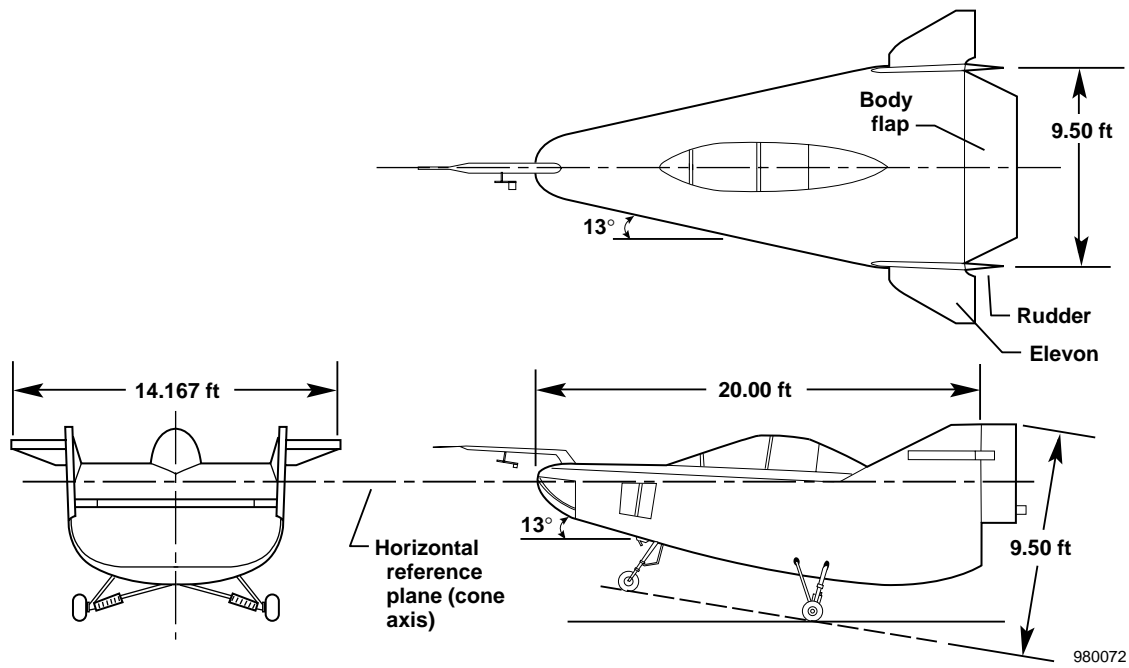
(b) The M2-F2 vehicle.

Figure 1. Three-view drawings of the subject vehicles.

Rudder

9.95 ft

Lateral
reference
plane

Rudder

Upper body flap

Horizontal
reference
plane

Lower
body flap

22.20 ft

980074

(c) The M2-F3 vehicle.

Cross section AA

Elevon
flaps

13.60 ft

Forward

Elevon

Rudders and
speed brakes

Inboard
Outboard

Tip-fin
flaps

Elevon
flaps

A

A

21.17 ft

Elevons

9.60 ft

Horizontal
reference
plane

980075
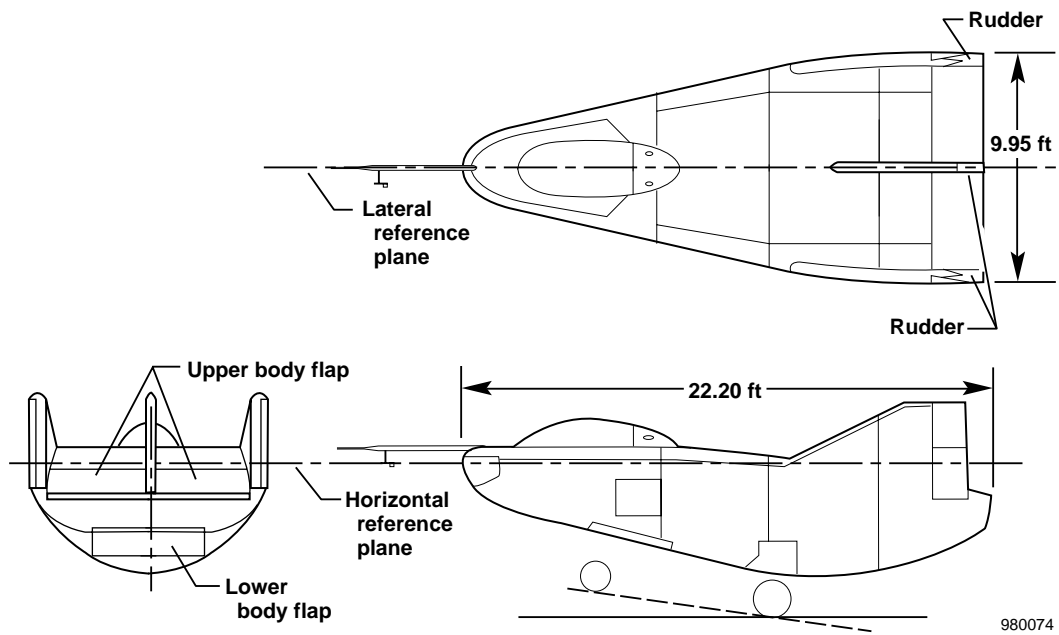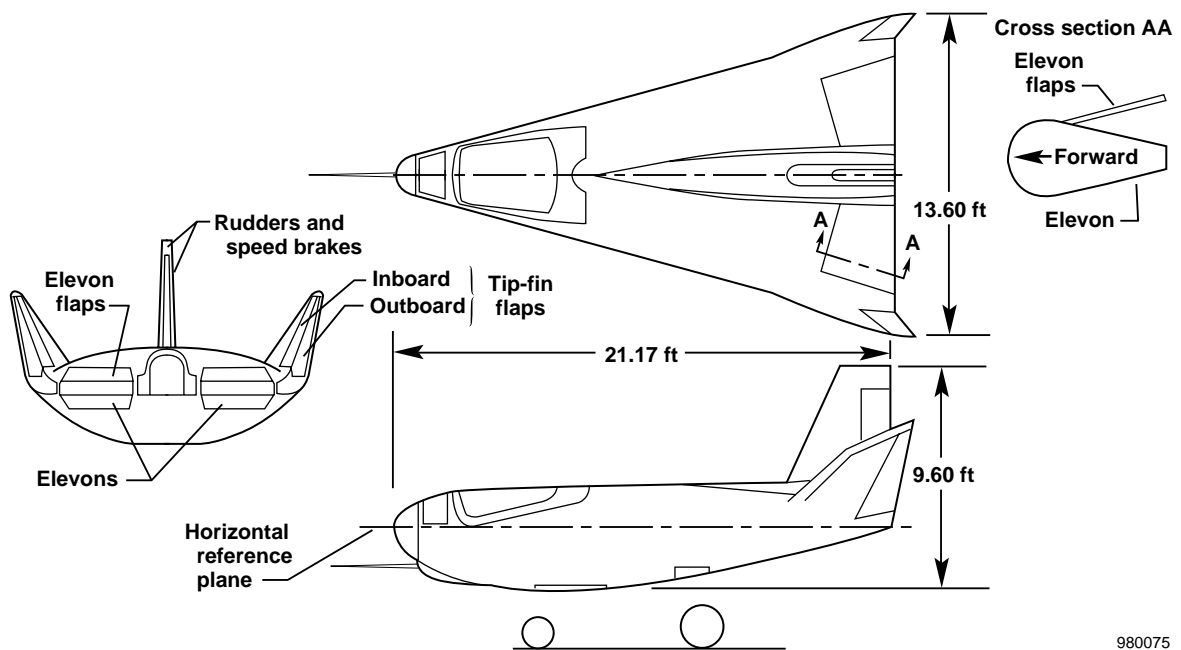
(d) The HL-10 vehicle.

Figure 1. Continued.
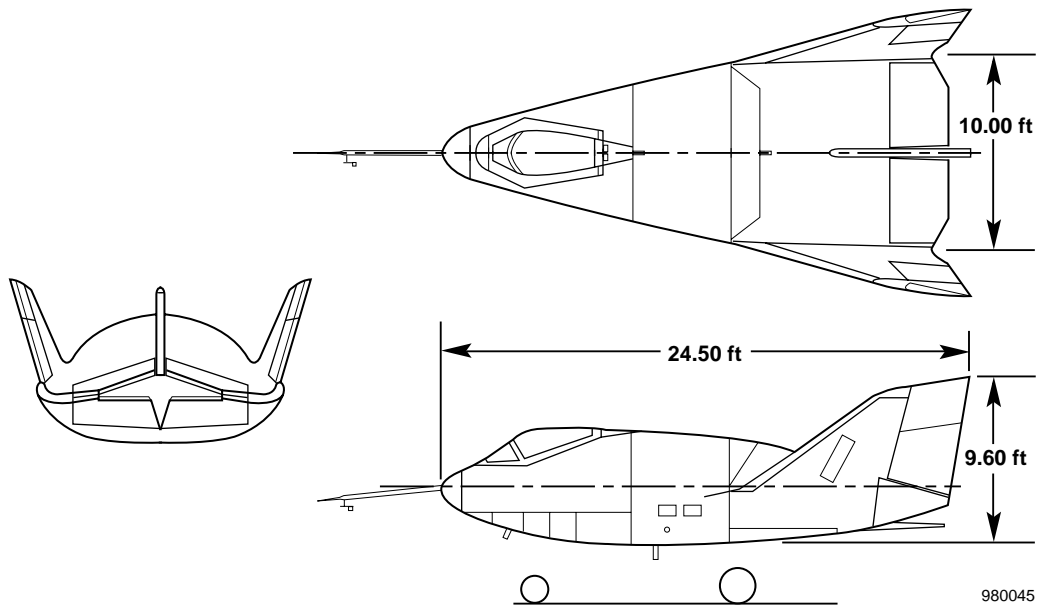
(e) The X-24A vehicle.
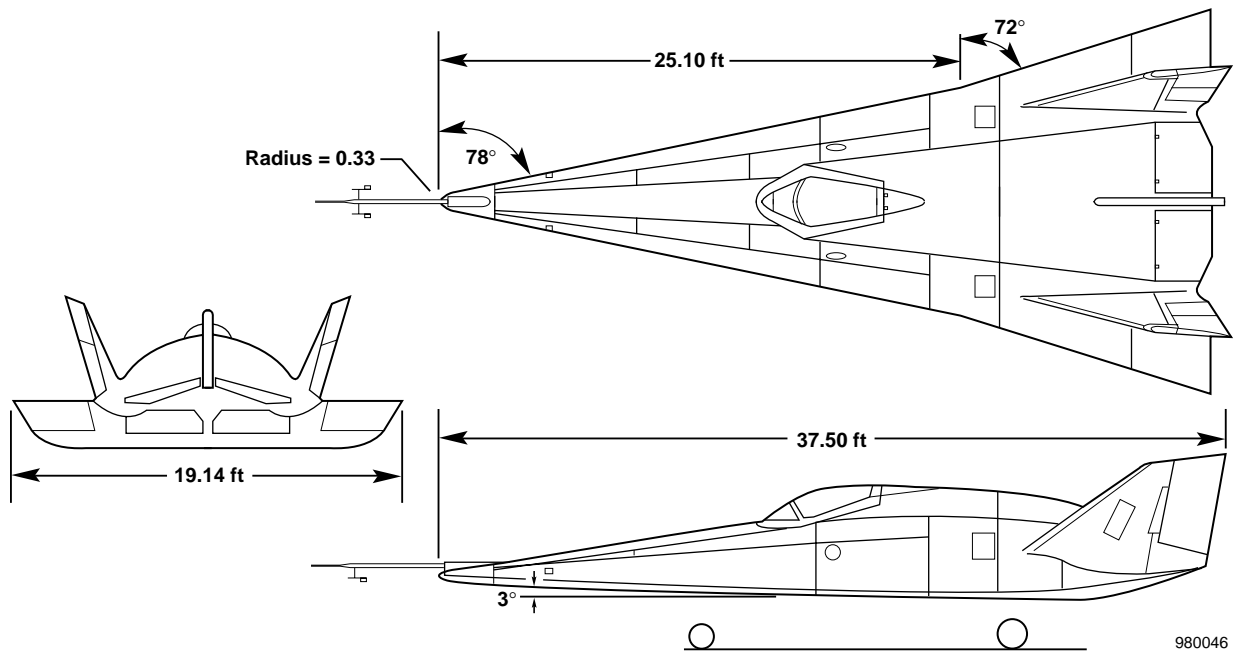
(f) The X-24B vehicle.

Figure 1. Continued.

Ailerons Horizontal stabilator

49.50 ft

18.08 ft

22.36 ft

Rudder Speed brakes

13.10 ft

Rudder

980546

(g) The X-15 vehicle.

Elevons

Tailcone (used only in earliest drop tests)

122.25 ft

Rudder

46.33 ft

56.58 ft

Body flap

78.07 ft

107.53 ft

980033
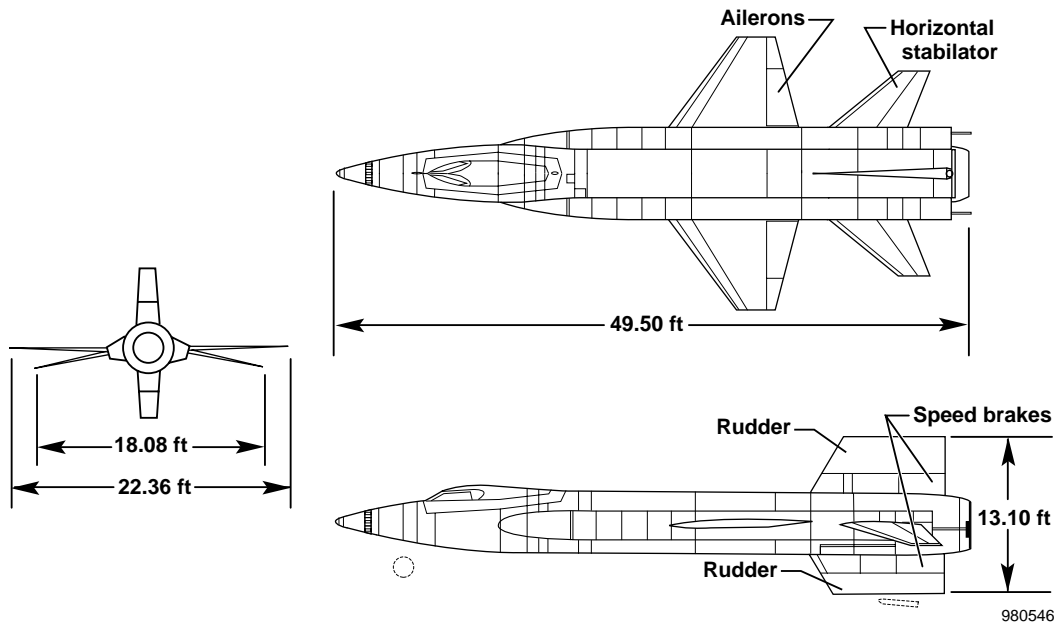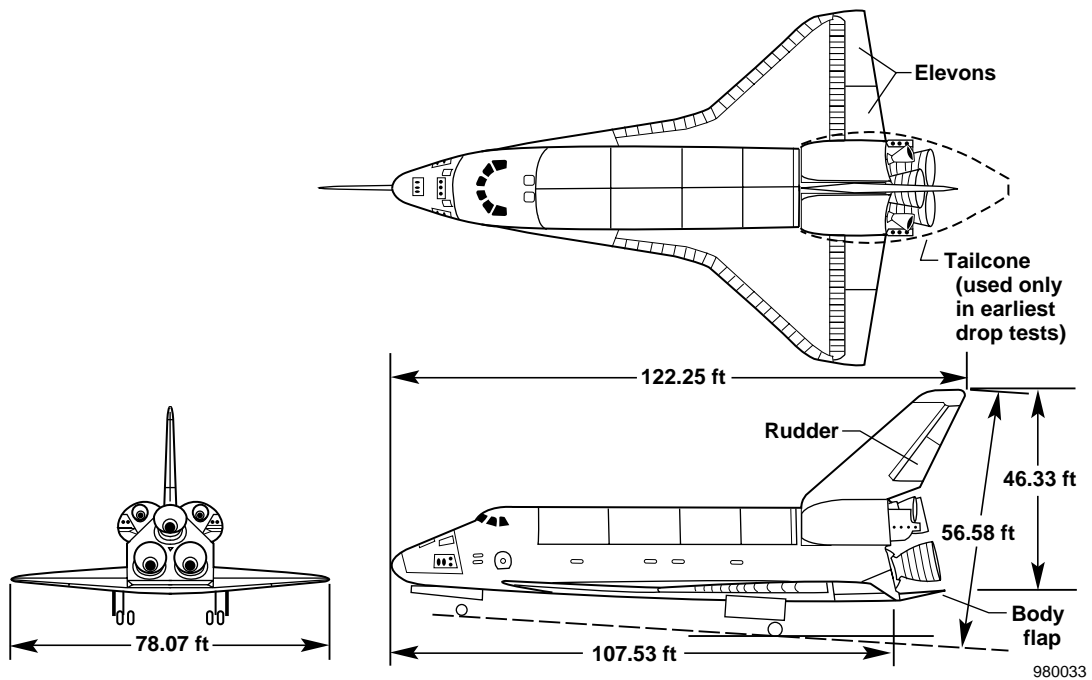
(h) The Space Shuttle.

Figure 1. Continued.

M2-F3 (M2-F2)

X-24A

HL-10

980547
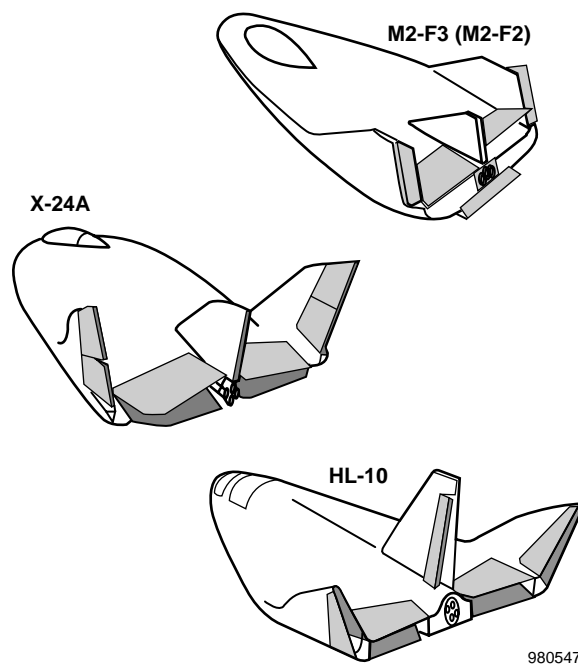
(i) Control surfaces that cause variable wedge angles. (Rudder and fin control surfaces are also shown.) The X-24A shaded items also apply to the X-24B lifting body.

Figure 1. Concluded.
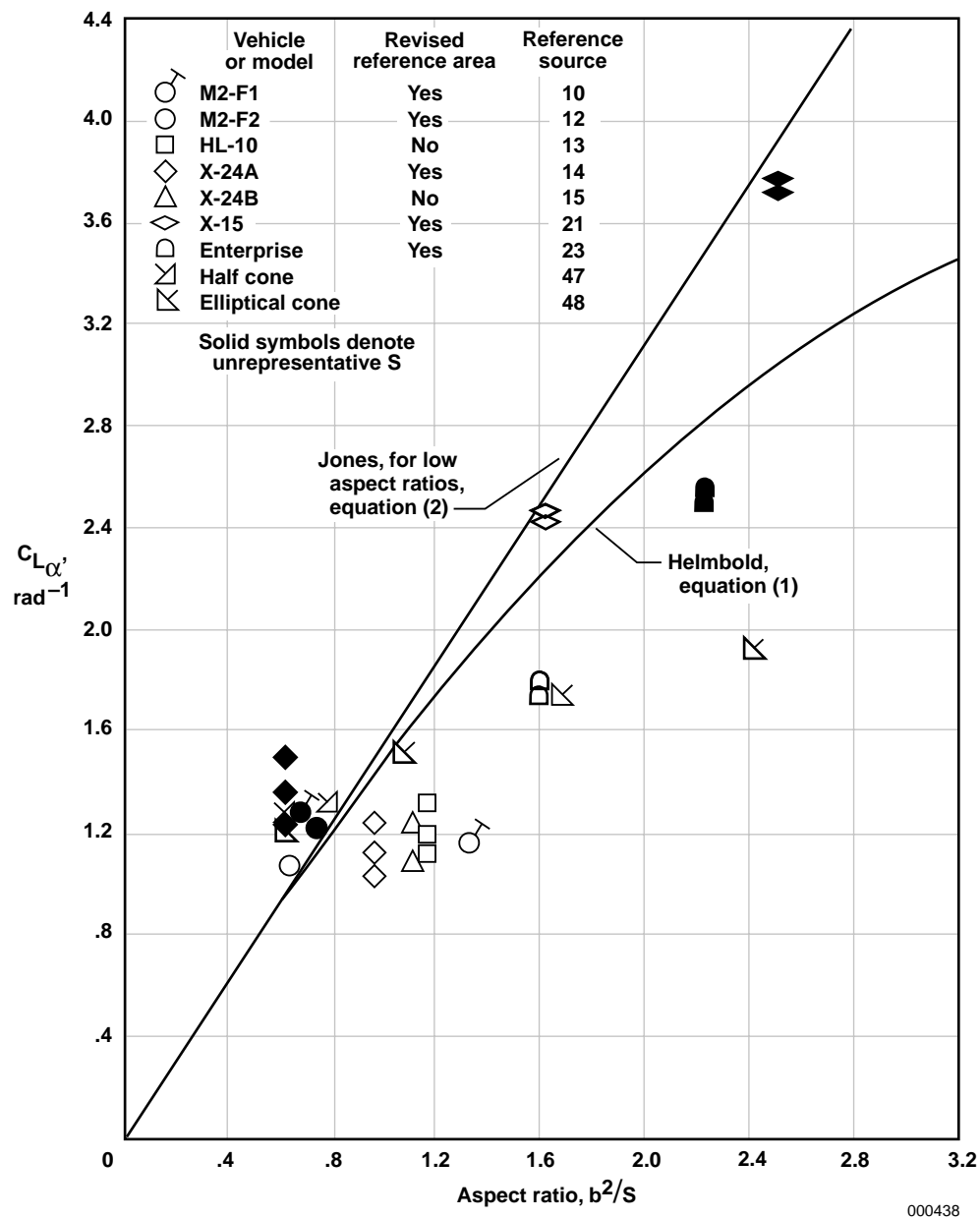
(a) Not adjusted for compressibility effects.

Figure 2. The relationship of lift-curve slope with aspect ratio as obtained in flight, from generic models, and from theories of Jones and Helmbold (Krienes).
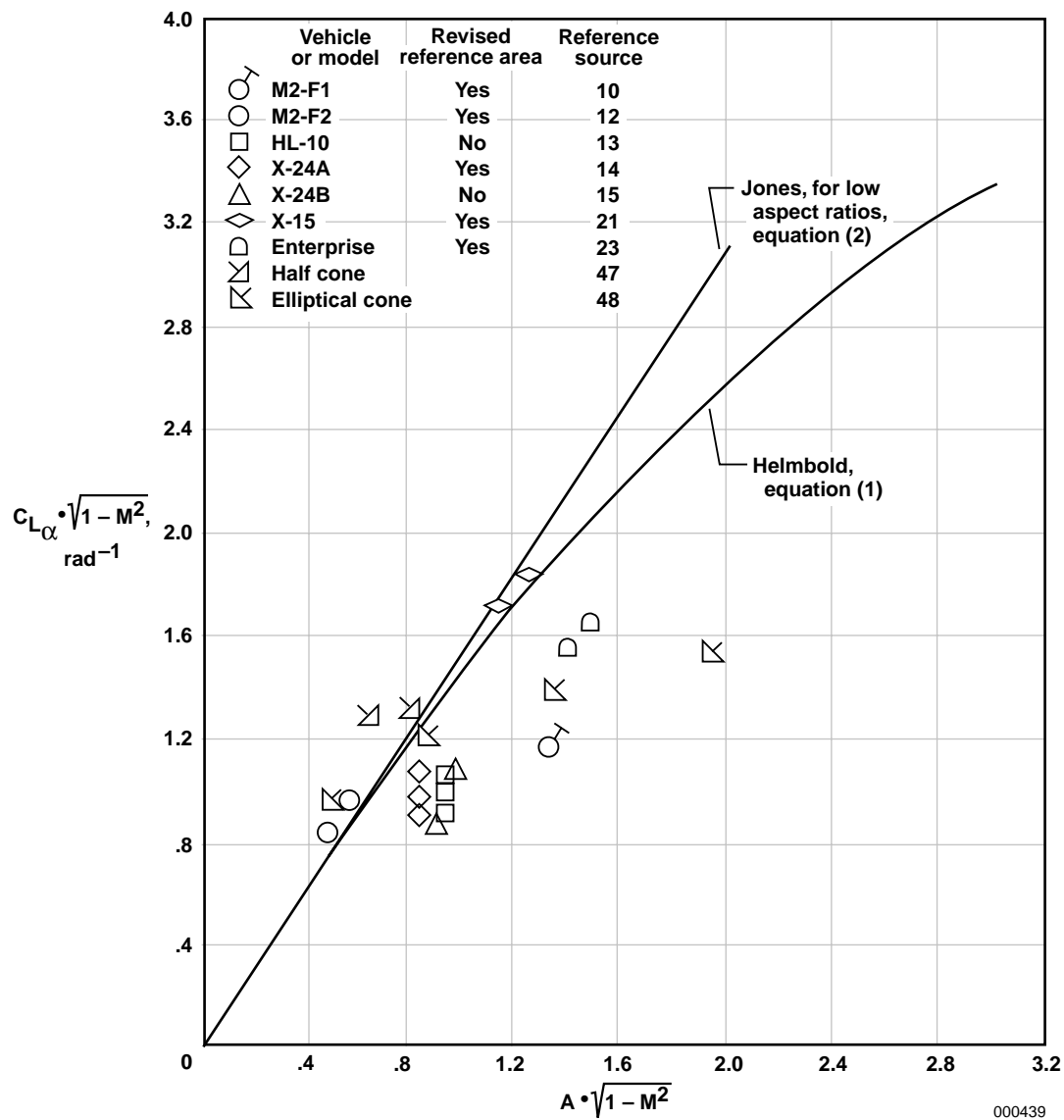
(b) Lift-curve slope and aspect-ratio values of figure 2(a) adjusted by applying revised reference areas and approximating for the effects of compressibility.

Figure 2. Continued.
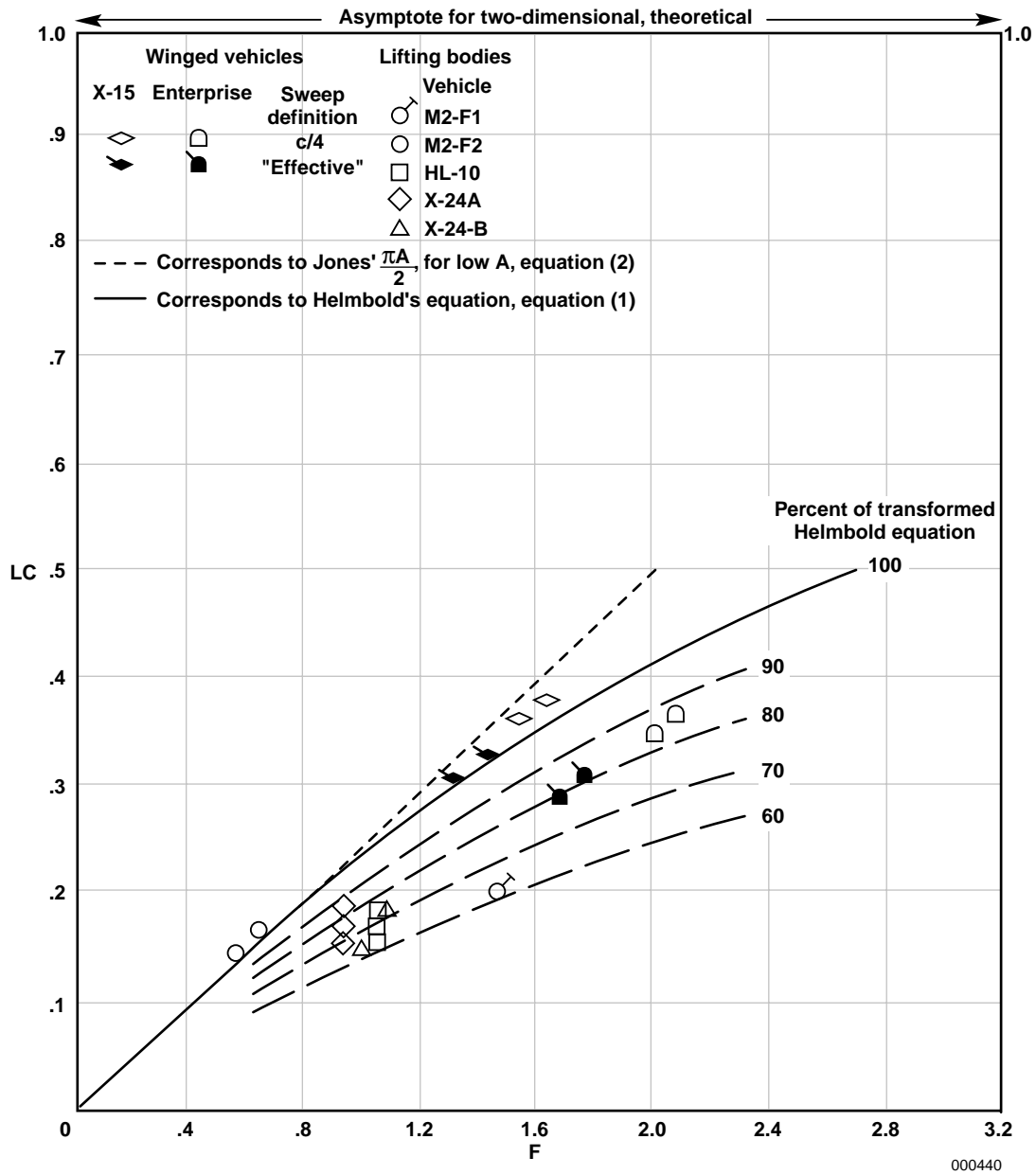
(c) Variation of lift-curve slope parameter, LC, with planform parameter, F, based on Hoerner relationship (ref. 30) after Diederich (ref. 52).

Figure 2. Concluded.

$$C_{L_\alpha} = \frac{\pi A}{2\,(57.3)}$$

$\Lambda = 0°$

$\Lambda = 45°$

$\Lambda = 60°$

C_{L_α}, deg^{-1}

Aspect ratio, b^2/S

980538
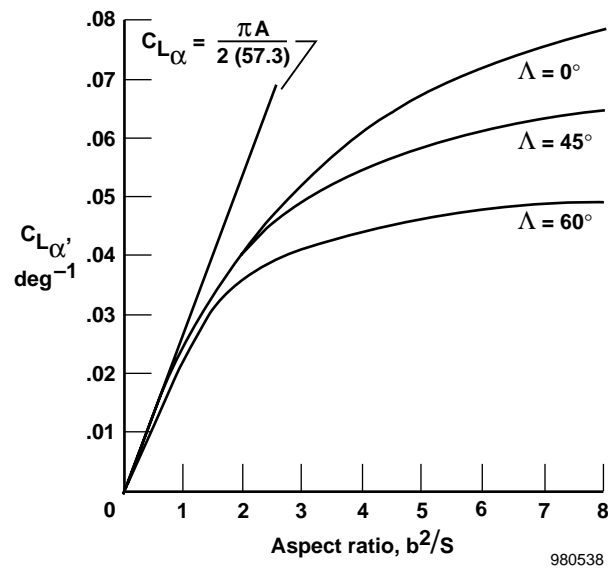
Figure 3. Variation of lift-curve slope with aspect ratio for various values of sweep angle (ref. 53).
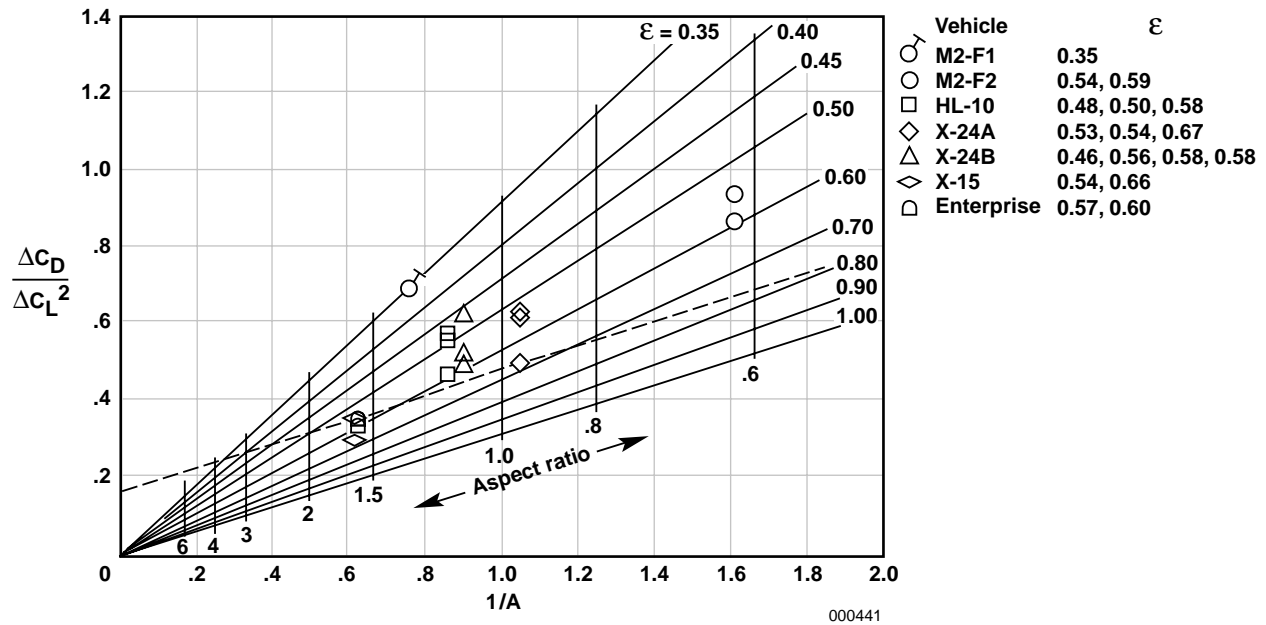
(a) Wendt adjustment applied for five vehicles having displaced polars.
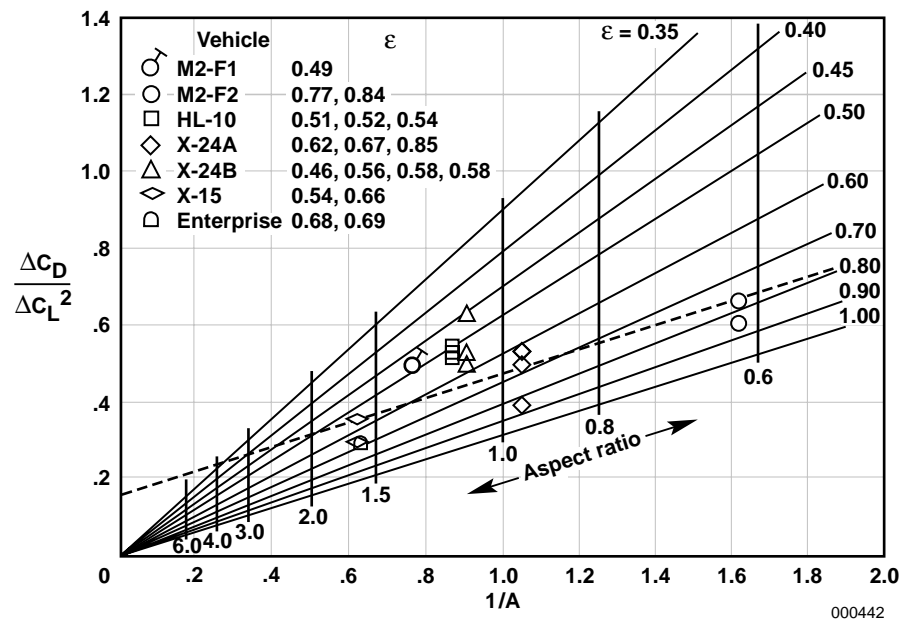
(b) $\Delta C_D / \Delta C_L^2$ derived from linear portion of relationship without concern about polar displacement.

Figure 4. The relationship of drag-due-to-lift factor with the reciprocal of aspect ratio.

47
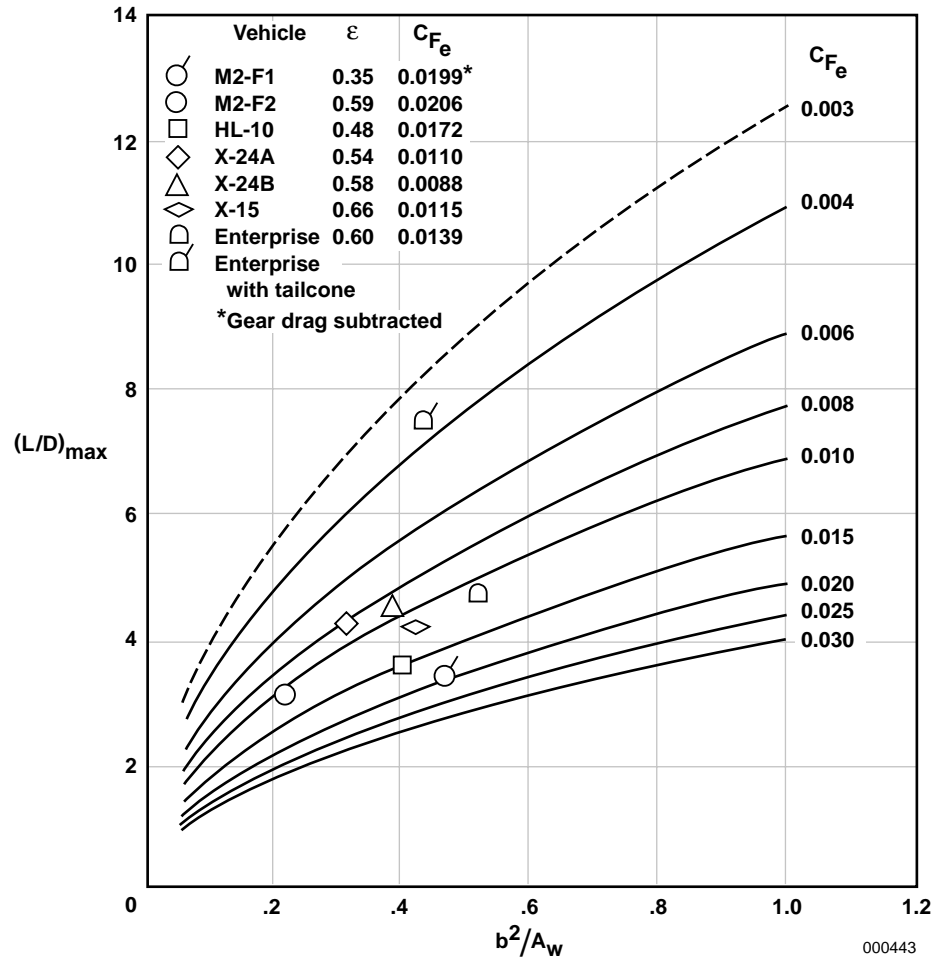
(a) Highest measured values of maximum lift-to-drag ratio for each vehicle.

Figure 5. The relationship of the maximum lift-to-drag ratio to wetted aspect ratio. The family of curves, at constant values of C_{F_e}, are derived using equations (8) and (9).

Vehicle	ε	C_{F_e}
M2-F1	0.35	0.0199*
M2-F2	0.59	0.0206
HL-10	0.48	0.0172
X-24A	0.54	0.0110
X-24B	0.58	0.0088
X-15	0.66	0.0115
Enterprise	0.60	0.0139

*Gear drag subtracted

Large symbol, flight data
Small symbol, from equation (9)
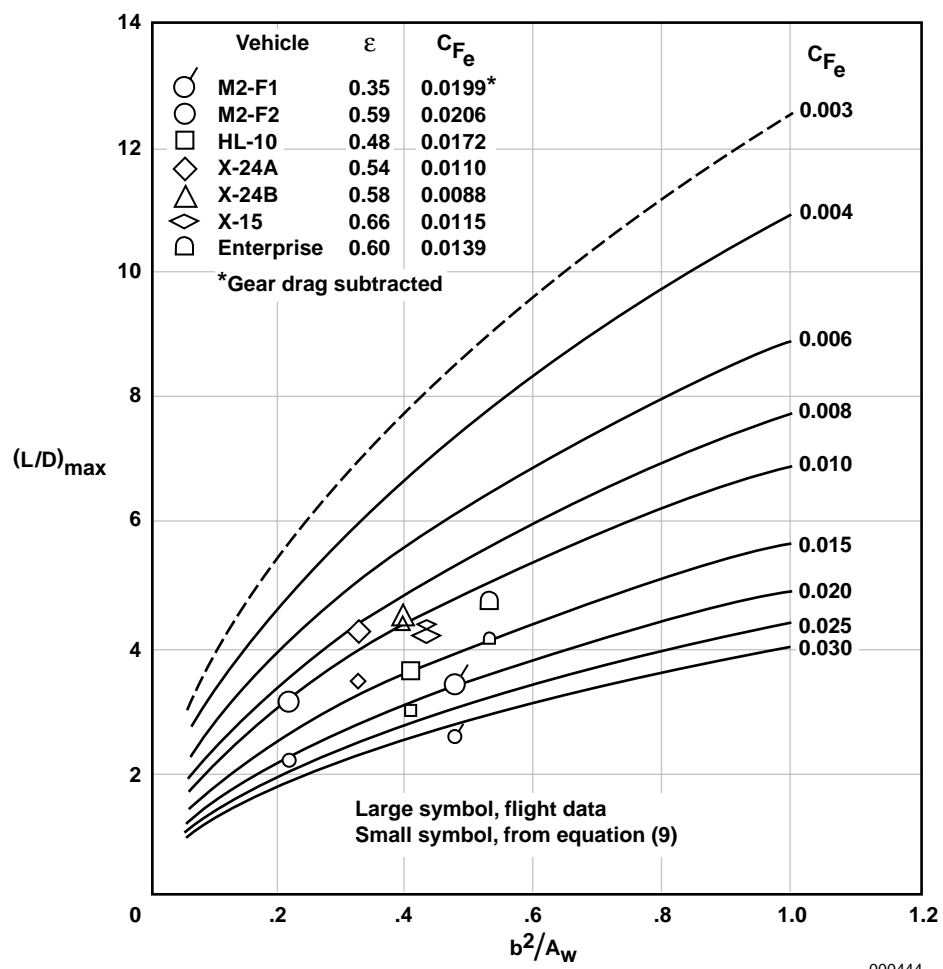
(b) Comparison of maximum lift-to-drag ratios from flight with values calculated from equation (9).

Figure 5. Concluded.
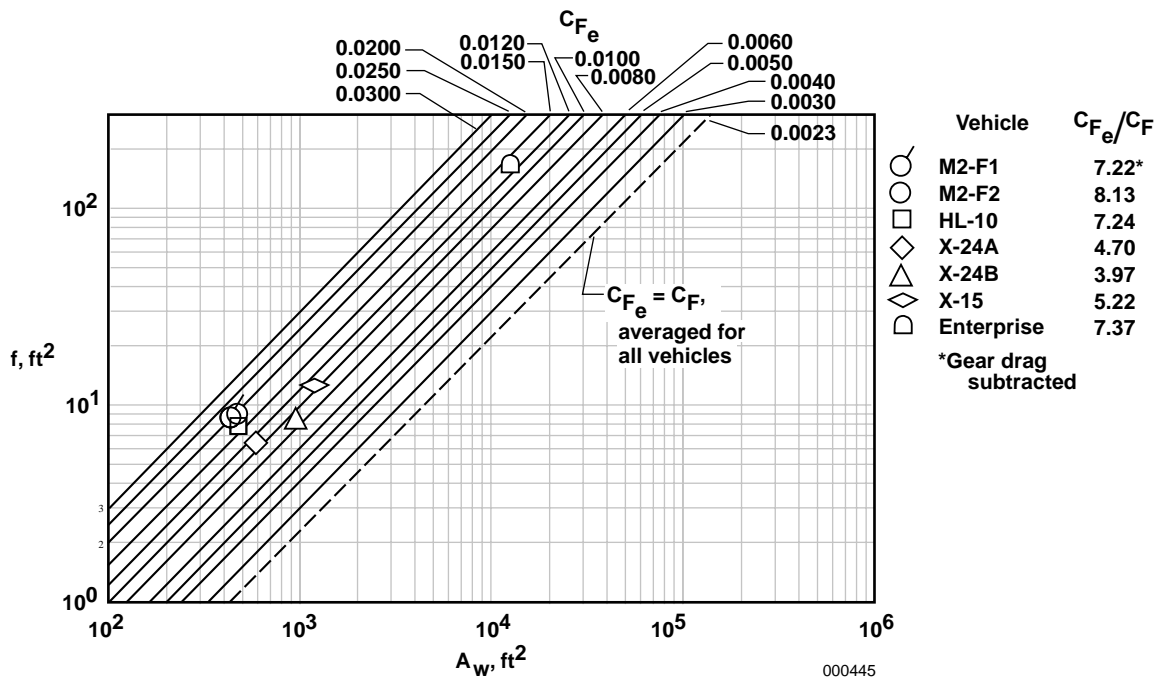
Figure 6. The relationship of equivalent parasite drag area and equivalent skin-friction coefficient to total wetted area.
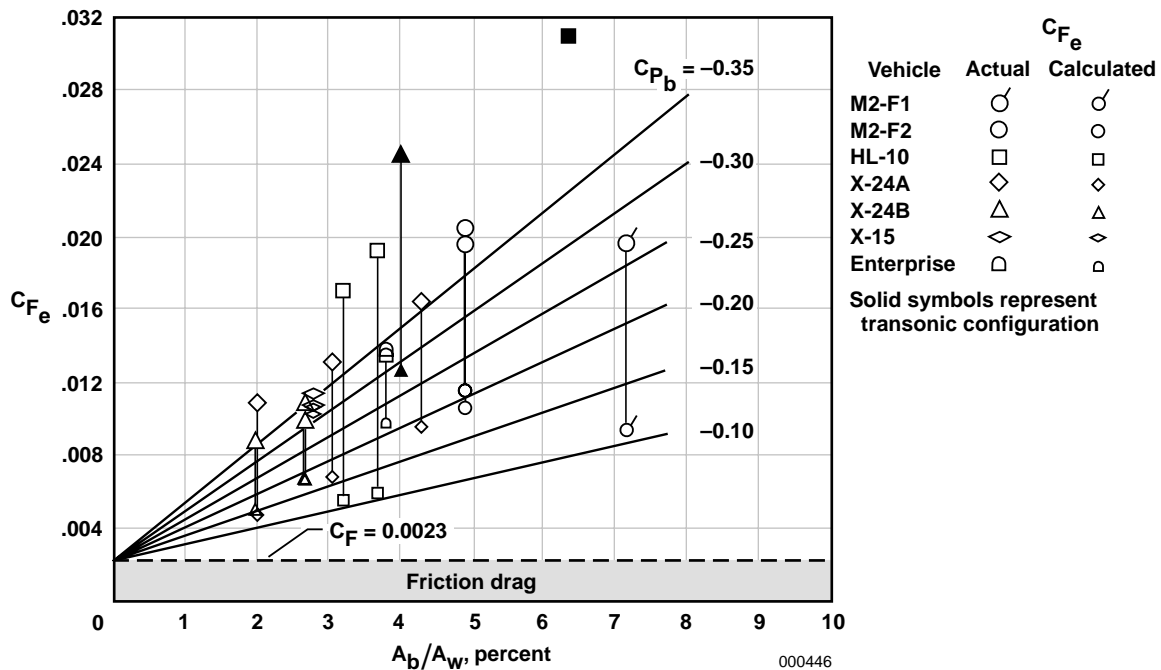
Figure 7. The relationship of equivalent skin-friction coefficient to the ratio of base area–to–wetted area.

Vehicle	C_{P_b} source	Remarks
M2-F1	Measured	Forebody drag includes gear: { turning vanes
M2-F1	Measured	Gear drag subtracted: { pressurize base
M2-F3	Measured	Forebody drag from M2-F2
HL-10	———	C_{P_b} derived from published base drag
X-24A	———	C_{P_b} estimates based on X-24B, ▲
X-24B	Measured	C_{P_b} for transonic configuration, M = 0.8
X-24B	———	C_{P_b} estimates based on X-24B, ▲
X-15	Measured	
Columbia	Measured	Forebody drag from Enterprise

000447

Figure 8. Comparison of base pressure coefficients for subject vehicles with Hoerner's two-dimensional relationship and with revised three-dimensional equation.
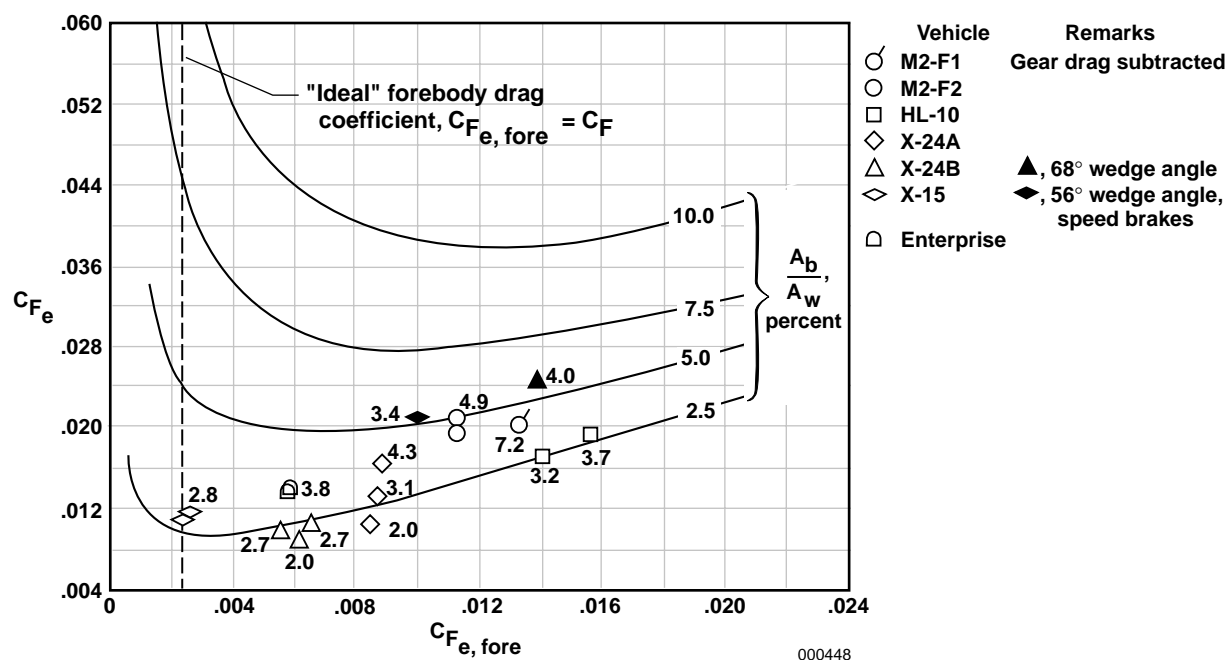
(a) Flight data (*Enterprise* with simulated thermal protection; other vehicles with natural "smooth" surfaces).
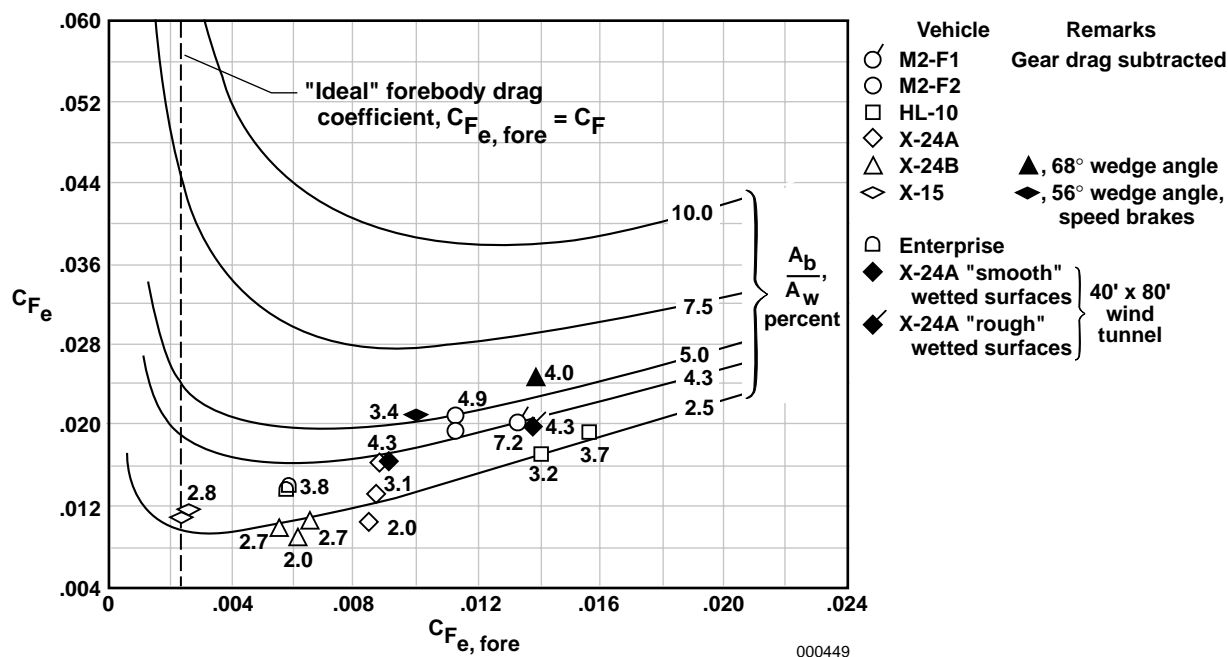
(b) Effects of roughness on X-24A vehicle included with figure 9(a) data.

Figure 9. The relationship of equivalent skin-friction coefficients for the complete vehicle and the forebody.
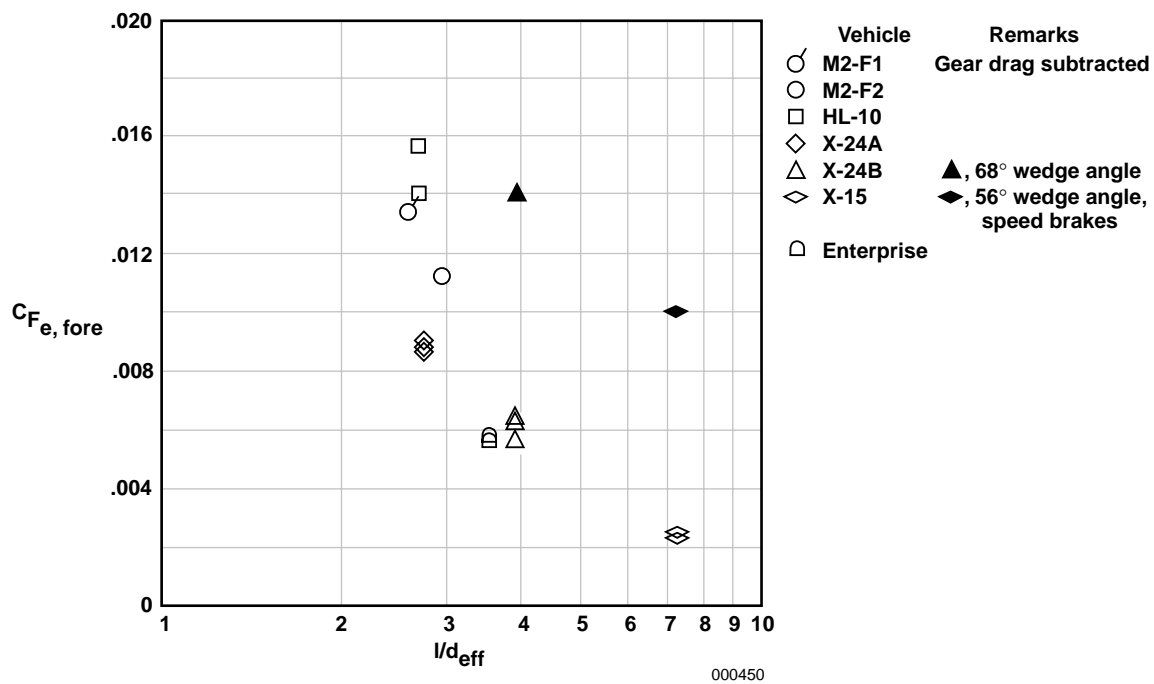
Figure 10. The relationship of forebody equivalent skin-friction coefficient with fineness ratio.
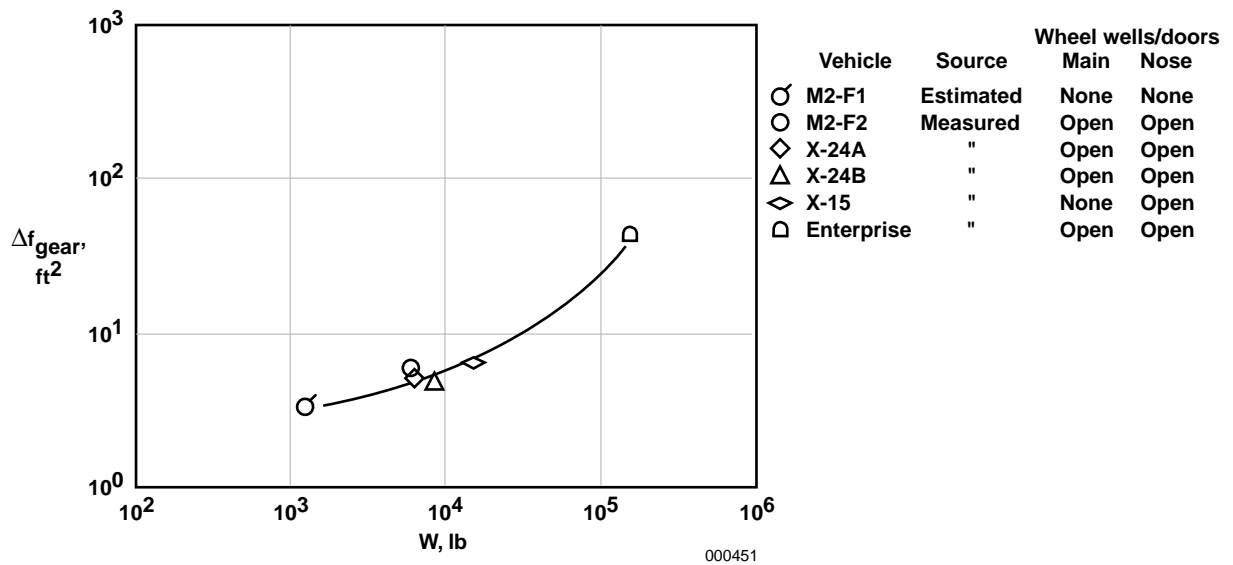
Figure 11. Relationship of landing gear drag area to vehicle weight.

53

APPENDIX A

ORIGINAL SOURCE DATA

The discussions of figures 2 and 4–10 and tables 2–3 are dependent on the author's interpretation of the flight data as reported in references 10, 12–15, 21, and 23. Other researchers may derive slightly different values from the basic lift-curve plots and polar plots contained in these references. Consequently, the pertinent "root-source" relationships from these references are reproduced here in their original published form.

Replotting the referenced data so as to provide uniform scales or a common format throughout originally was considered to be impractical (and more importantly, less reliable). Consequently, users will note a variety of formats and scales for the various vehicles in figures A-1–A-7 presented in this appendix. Although deriving the relationships of the lift coefficient to angle of attack and to the drag coefficient from the nonuniform formats is somewhat inconvenient, this approach provides the user with source data that are not influenced by the present authors' judgment. Note the values of the lift and drag coefficients for five of the vehicles (all except the HL-10 and the X-24B vehicles) are based on unrepresentative reference areas. Thus, according to the "Nomenclature" section, the labeling of these coefficients in appendix A should include a prime (that is, C_L' and C_D'). Because these coefficients as represented in appendix A are authentic reproductions from the original "root-source" references, the coefficients of concern are deceptive (relative to the designated nomenclature herein) unless the prime symbol is added to the affected symbols. Note that the subject prime symbols therefore have been added where appropriate.
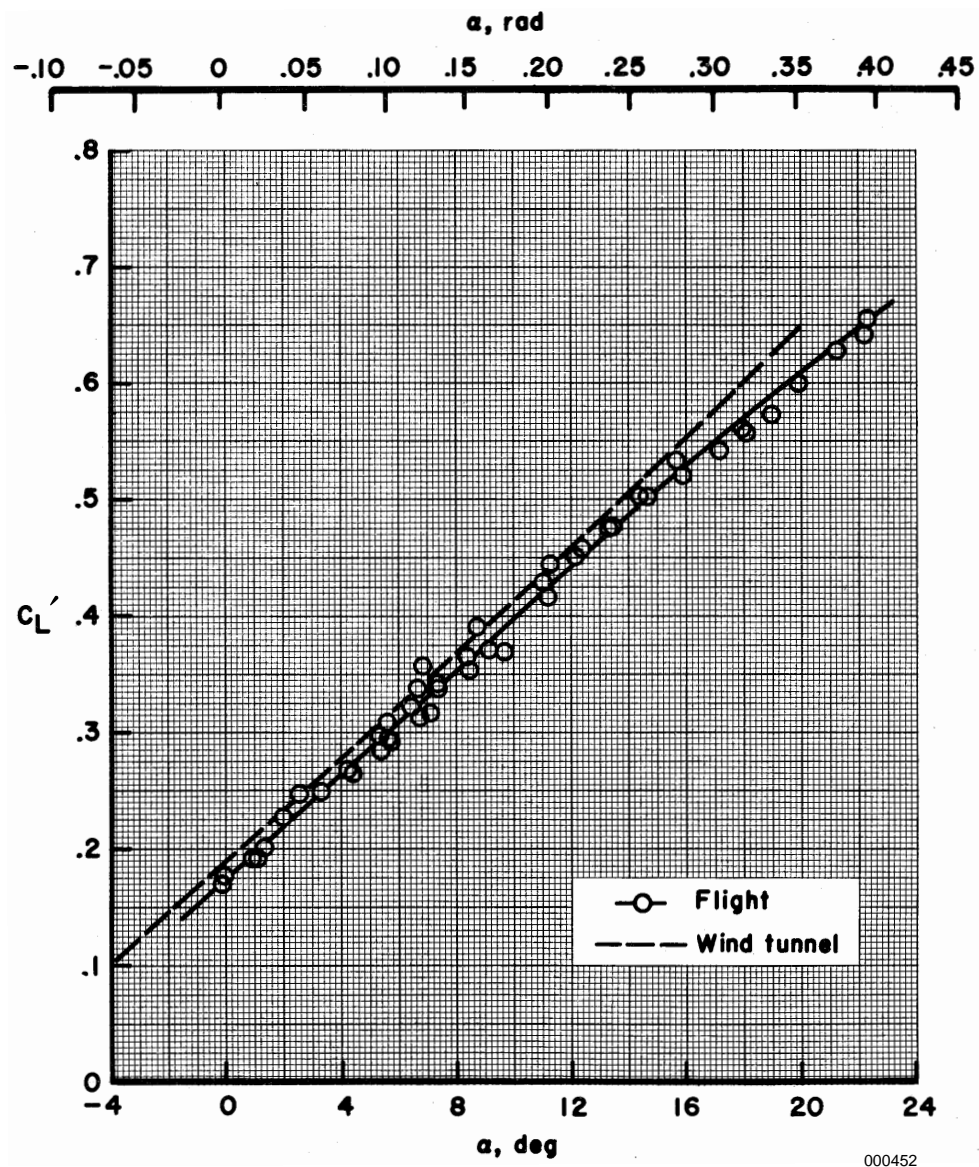
(a) Lift curve for the M2-F1 vehicle in trimmed, unpowered flight; $M = 0.15$; exposed landing gear.

Figure A-1. Photocopies of original published plots of lift-curves and drag polars for the M2-F1 vehicle from reference 10, pages 37–38.
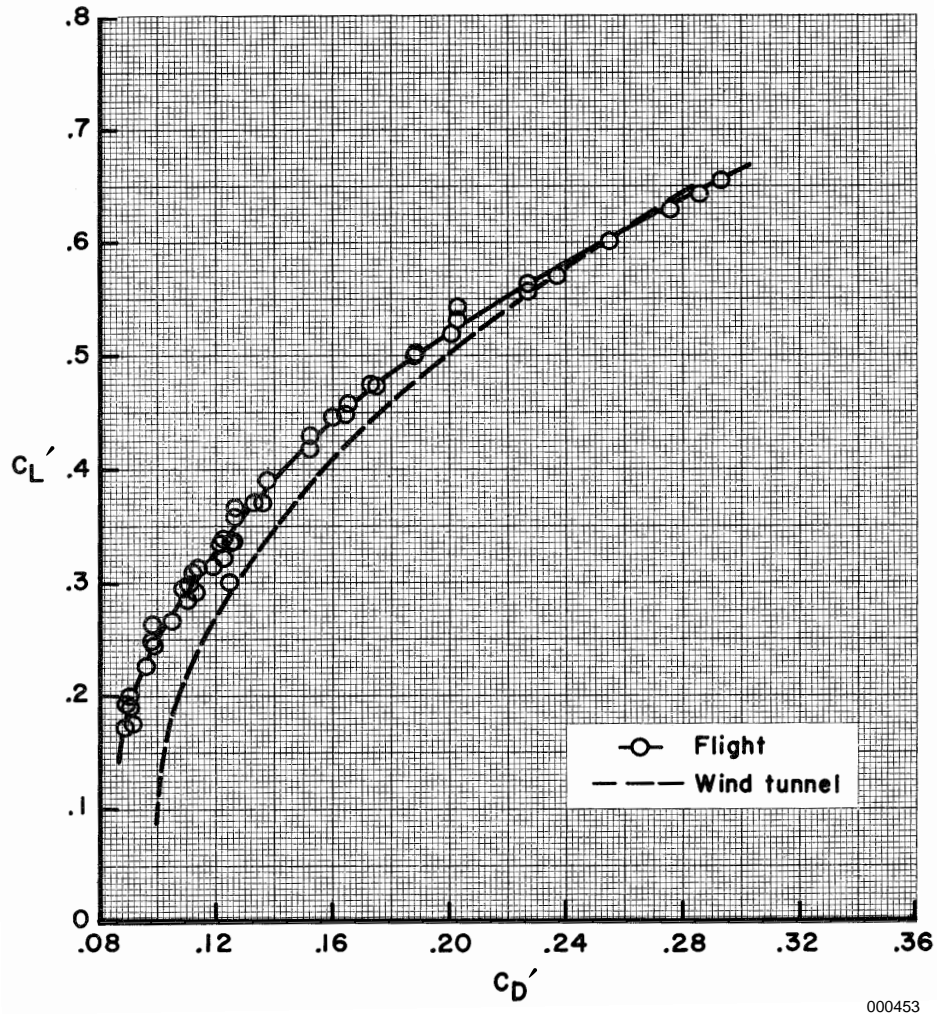
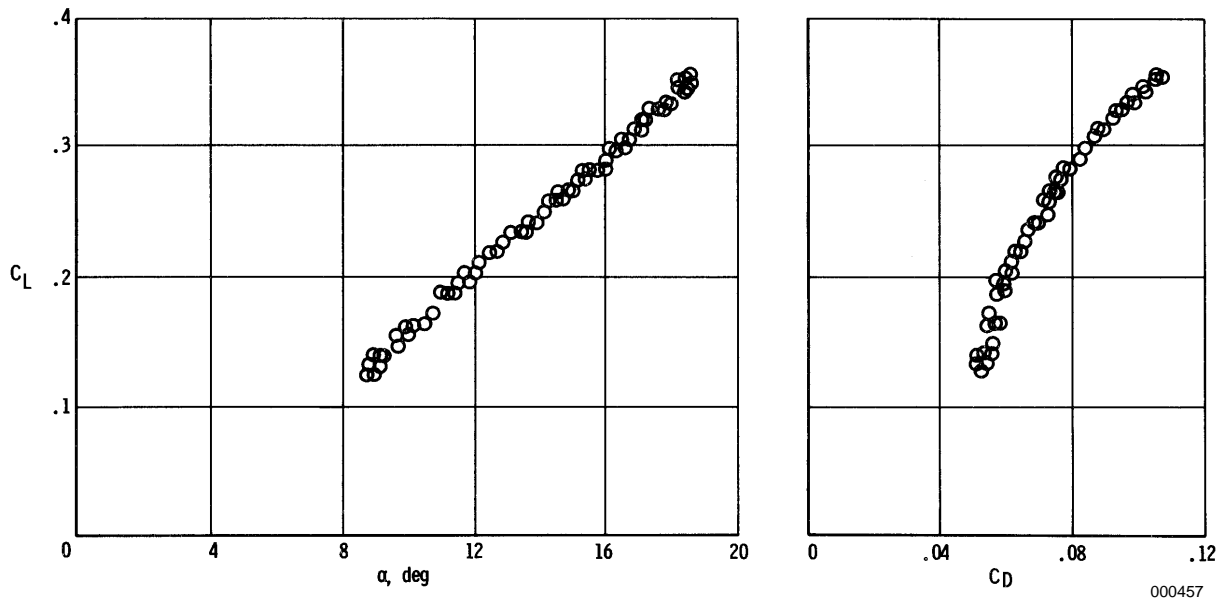(b) Drag polar for the M2-F1 vehicle in trimmed, unpowered flight; $M = 0.15$; exposed landing gear.

Figure A-1. Concluded.

000454
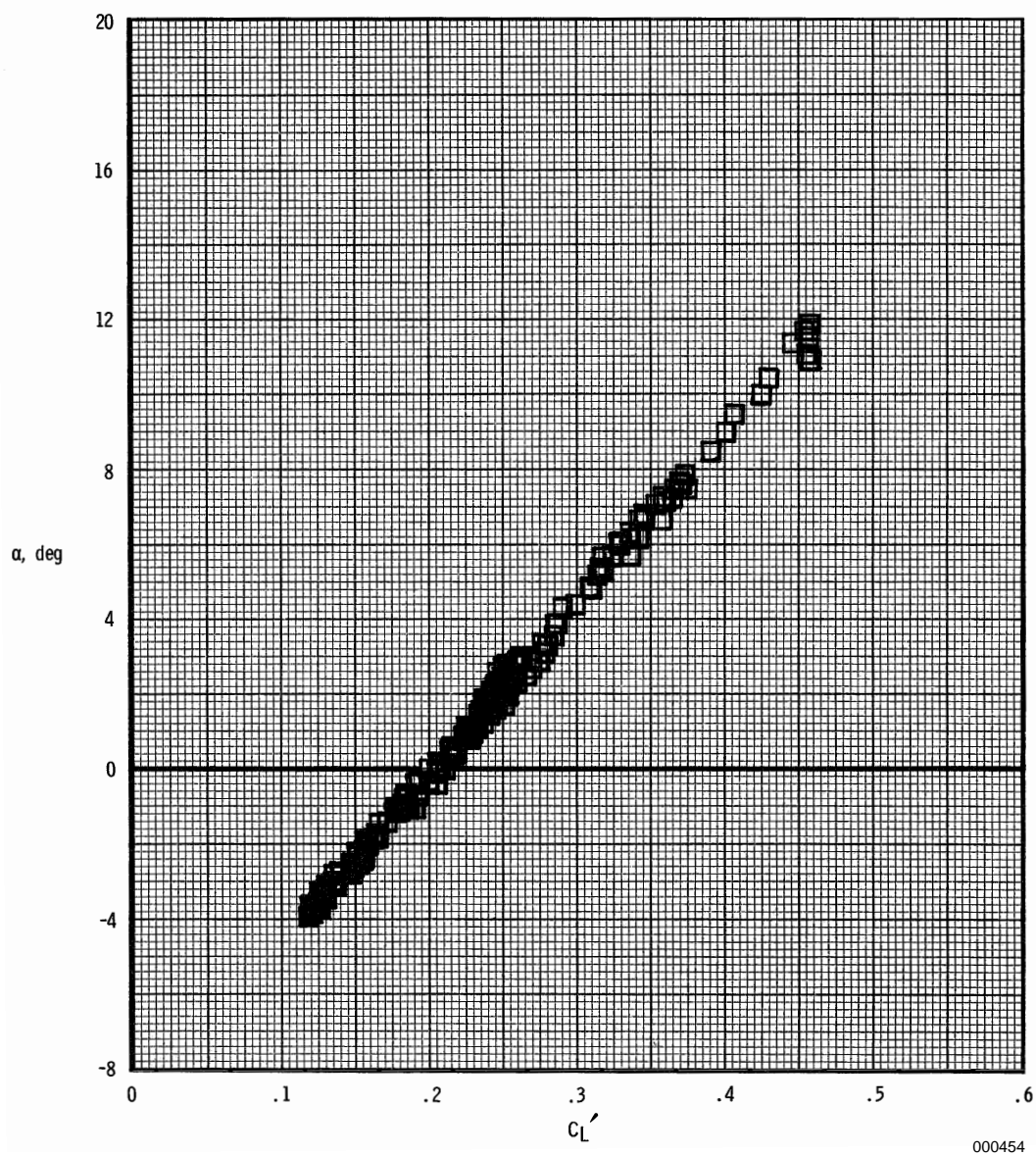
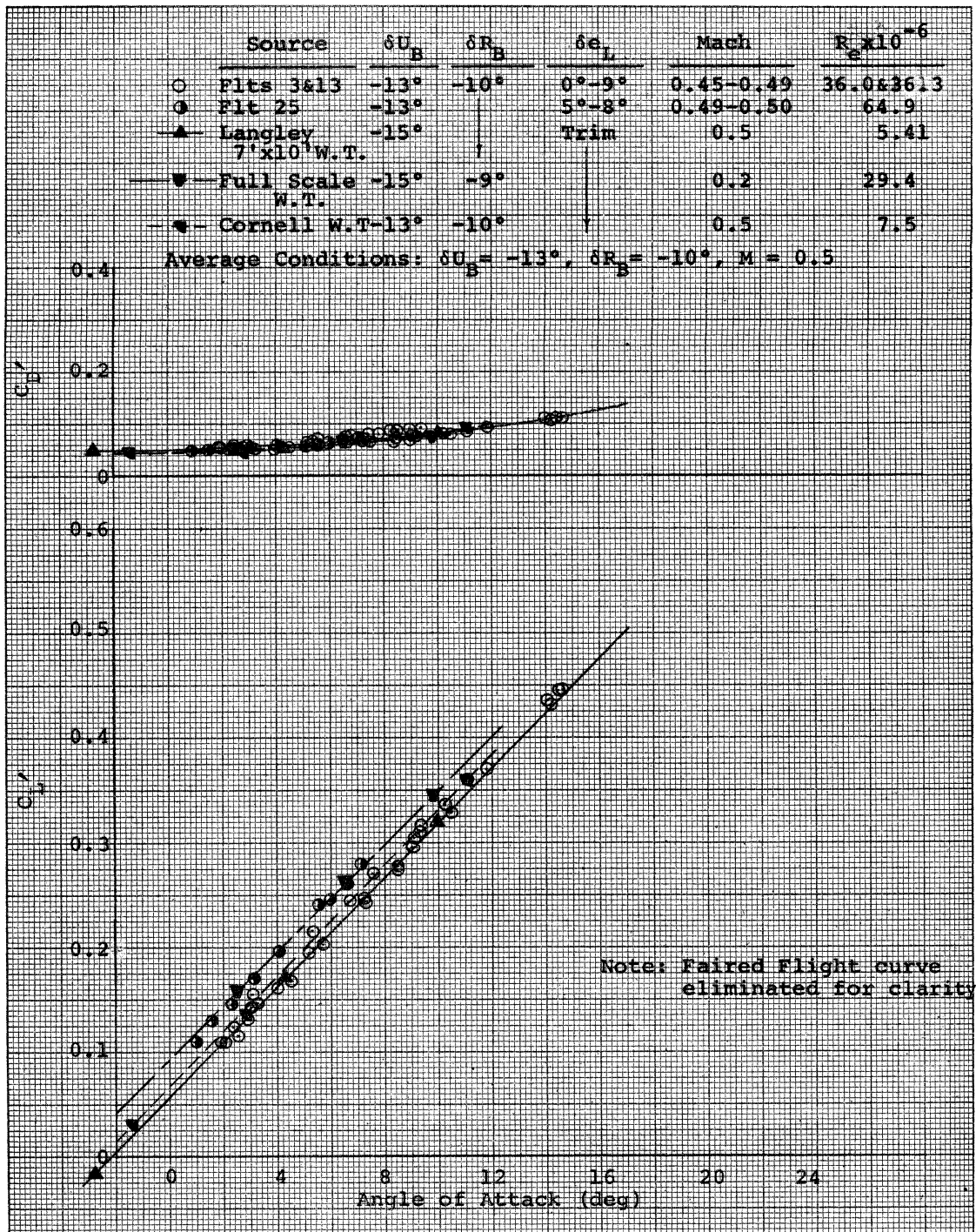(a) Lift curve for the M2-F2 vehicle in trimmed, unpowered flight; $M = 0.45$; $\delta_{uf} = -11.5°$.

Figure A-2. Photocopies of original published plots of lift-curves and drag polars for the M2-F2 vehicle from reference 12, pages 14–16.
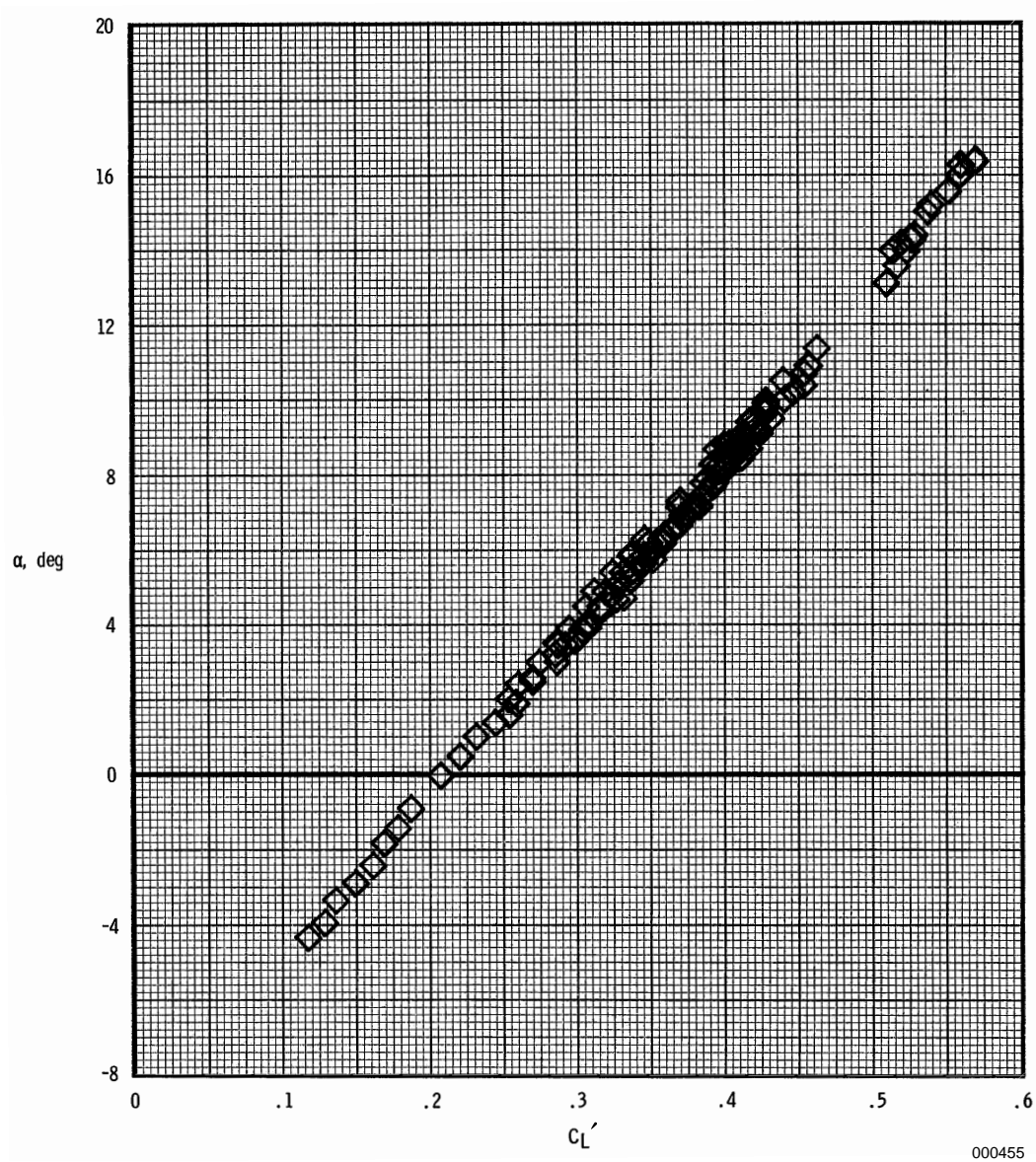
(b) Lift curve for the M2-F2 vehicle in trimmed, unpowered flight; $M = 0.62$; $\delta_{uf} = -11.5°$.

Figure A-2. Continued.

000456
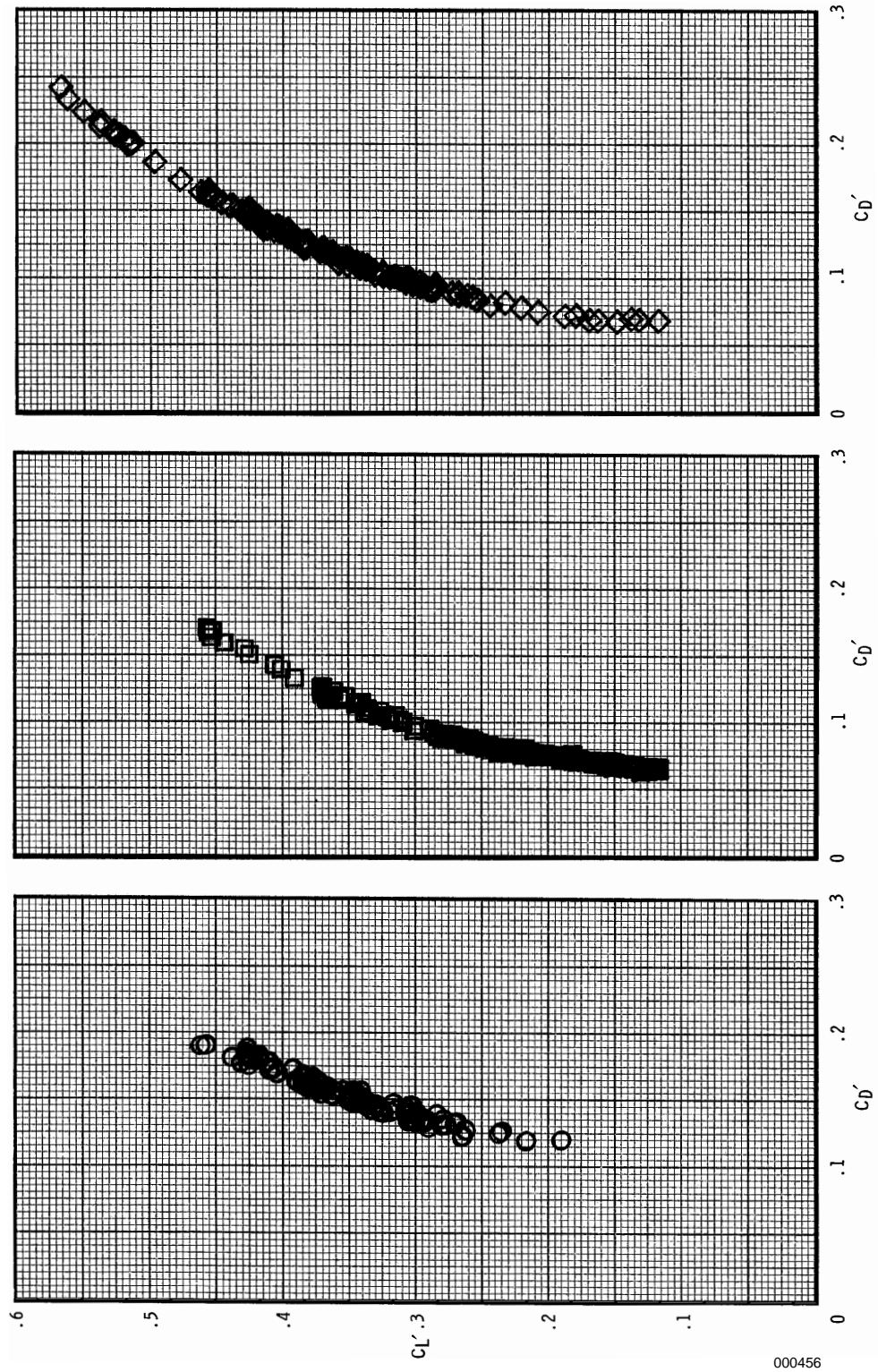
(c) Drag polars for the M2-F2 vehicle in trimmed, unpowered flight; $\delta_{uf} = -11.5°$.

Figure A-2. Concluded.

(a) Lift curve and drag polar for HL-10 vehicle (configuration B) in trimmed, unpowered flight; $M = 0.6$; $\delta_{ef} = 0°$.
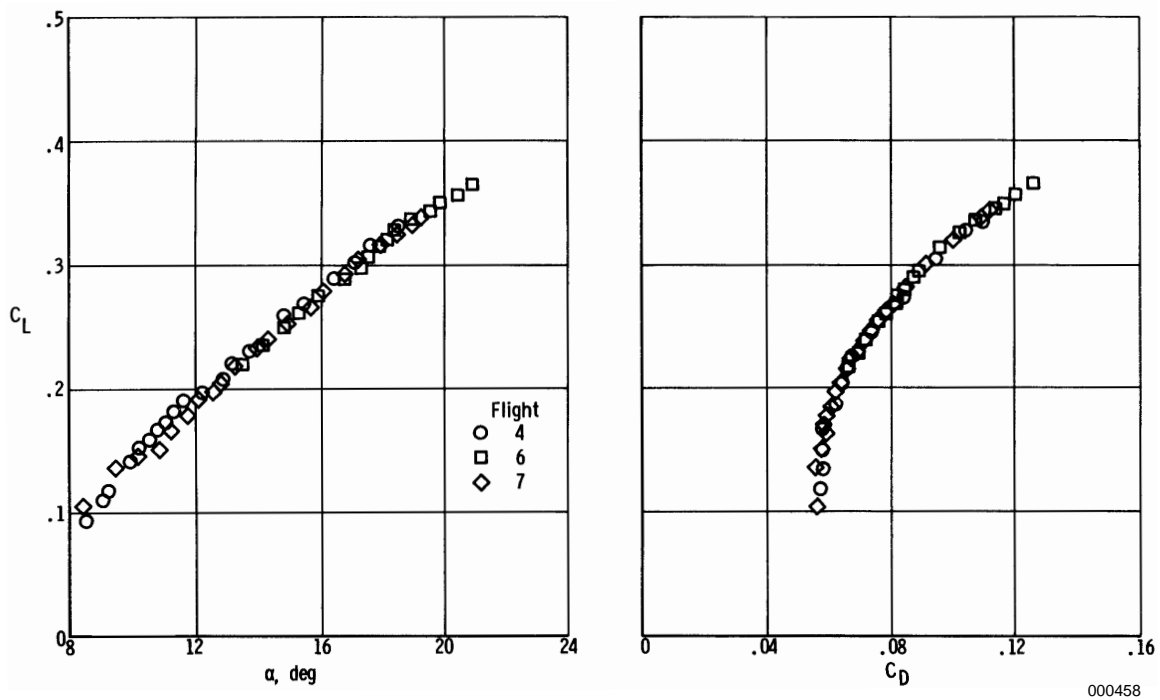
(b) Lift curve and drag polar for HL-10 vehicle (configuration C) in trimmed, unpowered flight; $M = 0.6$; $\delta_{ef} = -3°$.

Figure A-3. Photocopies of original published plots of lift-curves and drag polars for the HL-10 vehicle from reference 13, pages 14, 17, and 20.
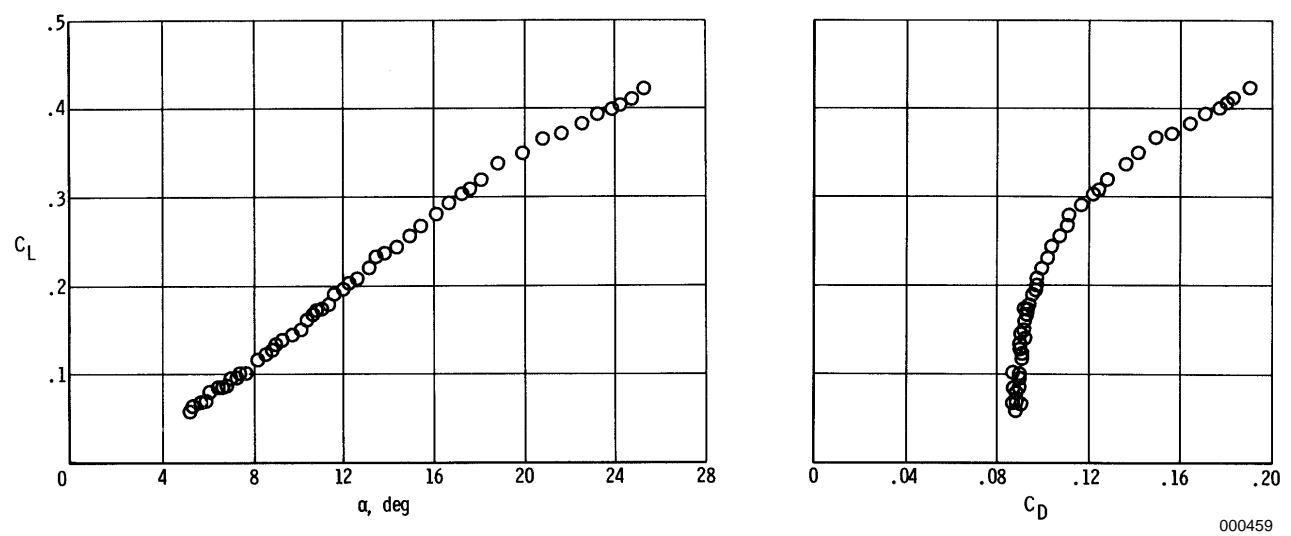
(c) Lift curve and drag polar for HL-10 vehicle (configuration D) in trimmed, unpowered flight; $M = 0.6$; $\delta_{ef} = -30°$.

Figure A-3. Concluded.
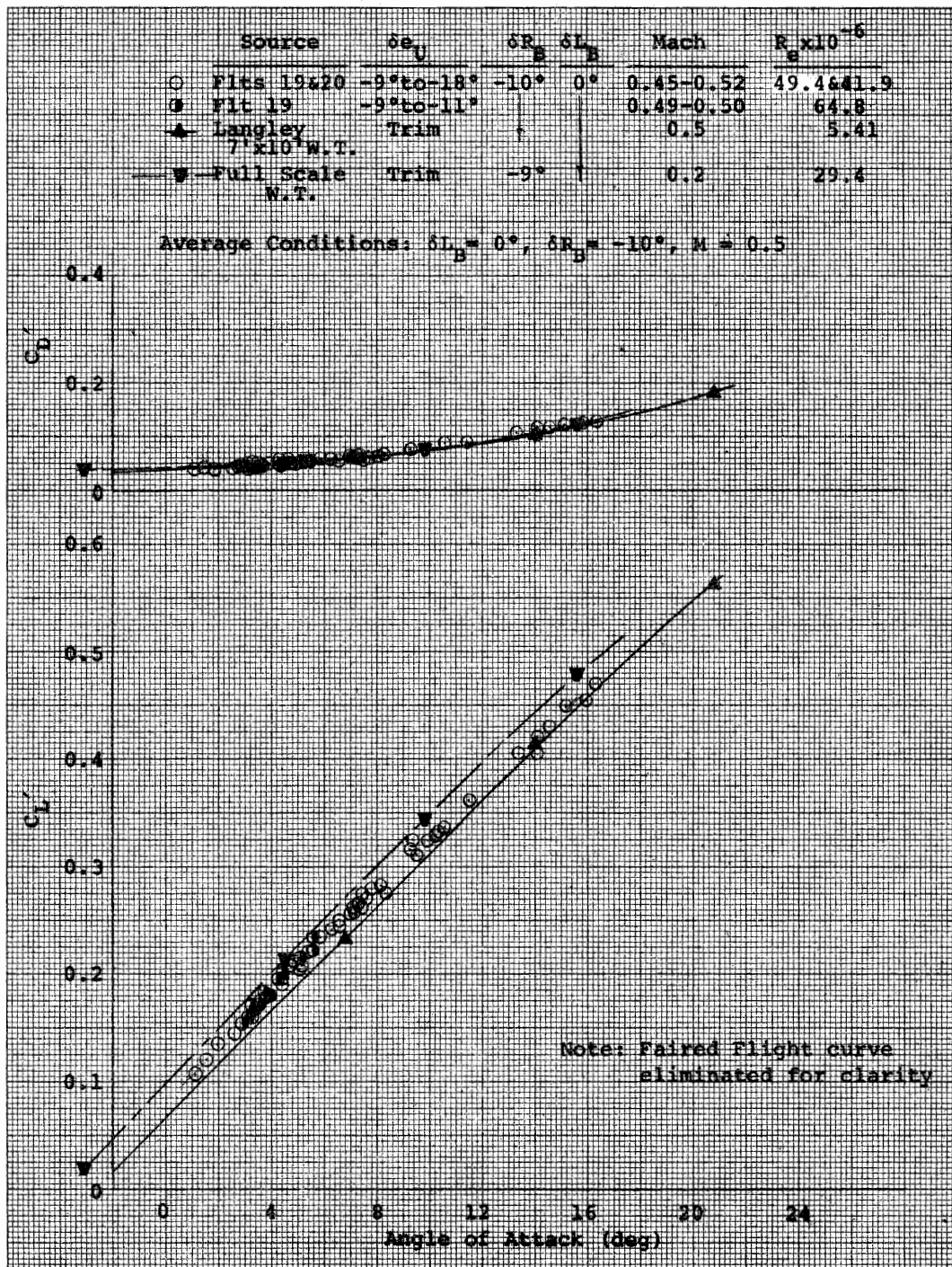
(a) X-24A vehicle trim flight test and wind-tunnel performance data; $M = 0.5$; $\delta L_B = 0°$.

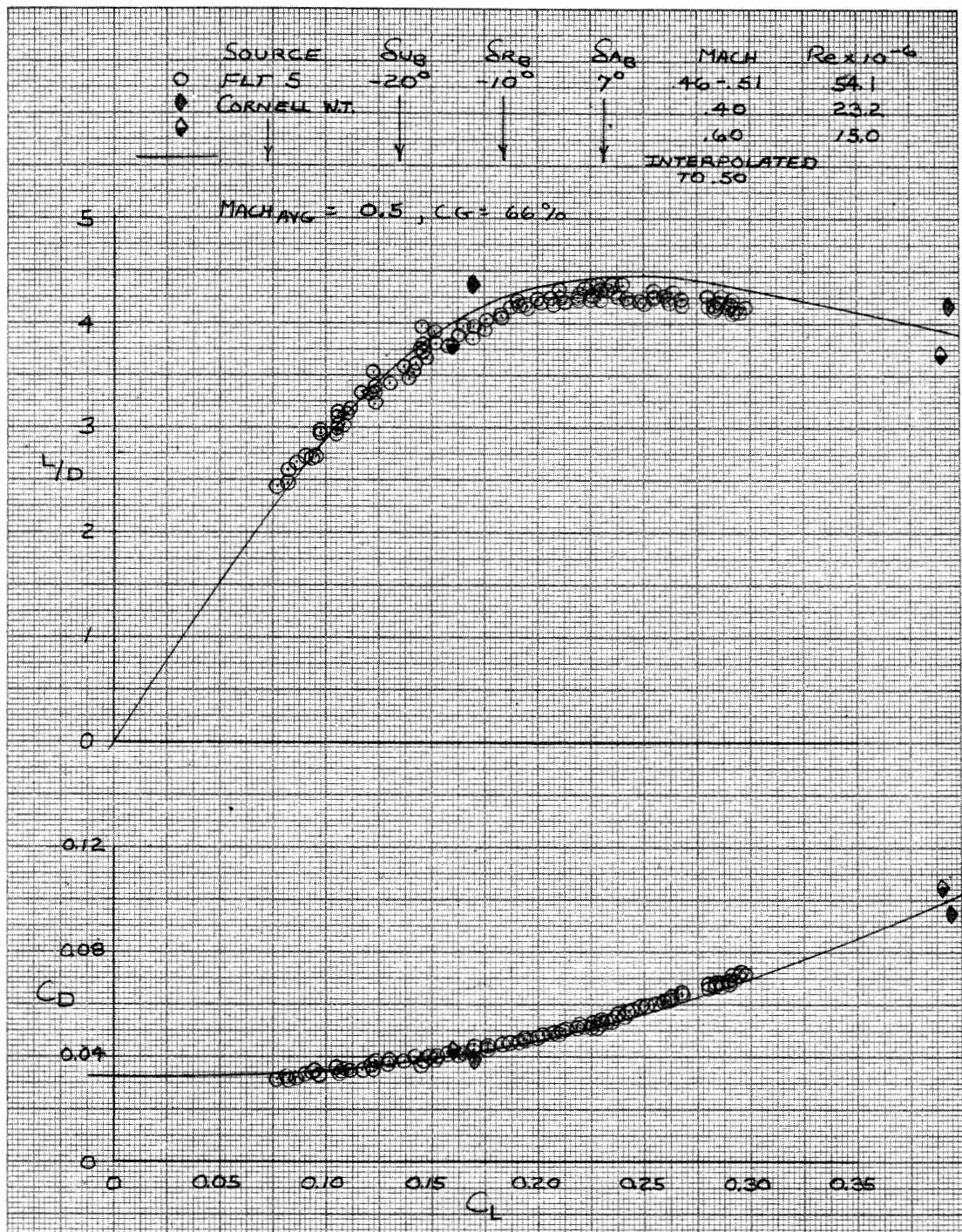Figure A-4. Photocopies of original published plots of lift-curves and drag polars for the X-24A vehicle from reference 14, pages 98–99 and 106–109.
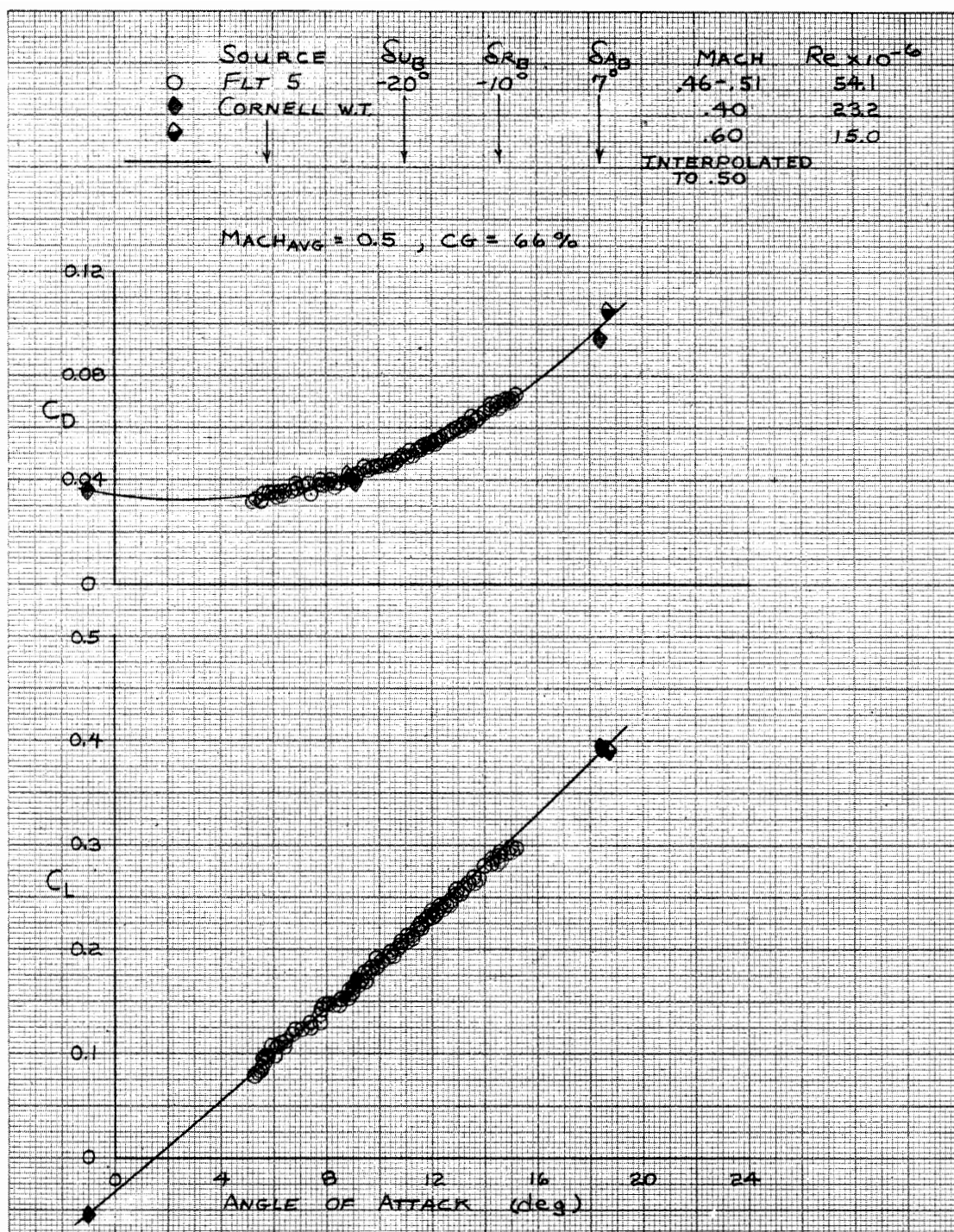
000523

(a). Concluded.

Figure A-4. Continued.

Source	δU_B	δR_B	δe_L	Mach	$R_e \times 10^{-6}$
○ Flts 3&13	-13°	-10°	0°-9°	0.45-0.49	36.0&36.3
● Flt 25	-13°		5°-8°	0.49-0.50	64.9
▲ Langley 7'x10' W.T.	-15°		Trim	0.5	5.41
▼ Full Scale W.T.	-15°	-9°		0.2	29.4
◆ Cornell W.T.	-13°	-10°		0.5	7.5

Average Conditions: $\delta U_B = -13°$, $\delta R_B = -10°$, $M = 0.5$

Note: Faired Flight curve eliminated for clarity
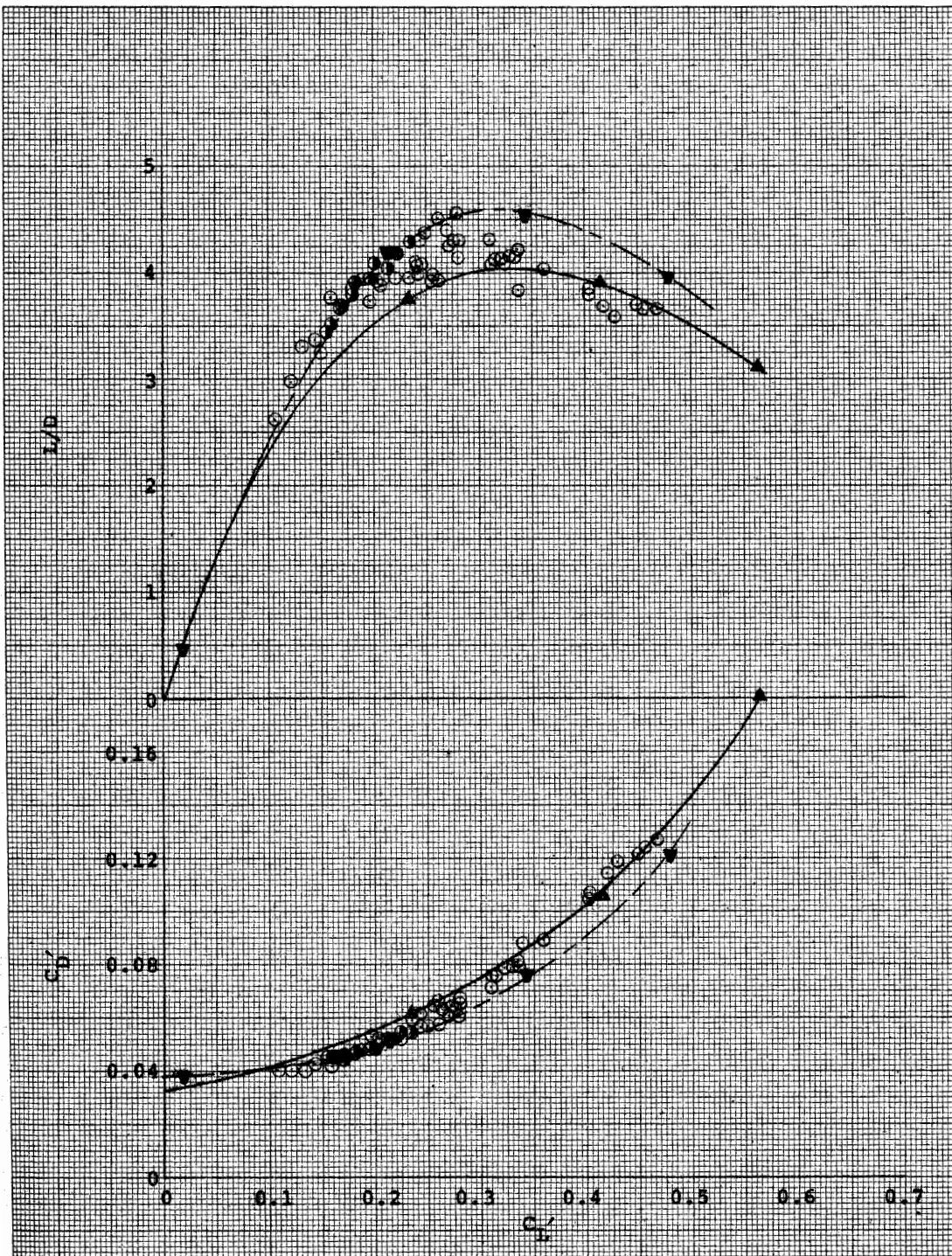
000461

(b) X-24A vehicle trim flight test and wind-tunnel performance data; $M = 0.5$; $\delta U_B = -13°$.

Figure A-4. Continued.

64

(b). Concluded.

Figure A-4. Continued.

Source	δU_B	δR_B	δe_L	Mach	$R_e \times 10^{-6}$
O Flt 2	-21°	-10°	10°-20°	0.48-0.54	39.9&45.5
▲ Langley 7'x10 W.T.	-20°	-10°	Trim	0.5	5.41
--- Faired Flight Data					

Average Conditions: $\delta U_B = -21°$, $\delta R_B = -10°$, $M = 0.5$
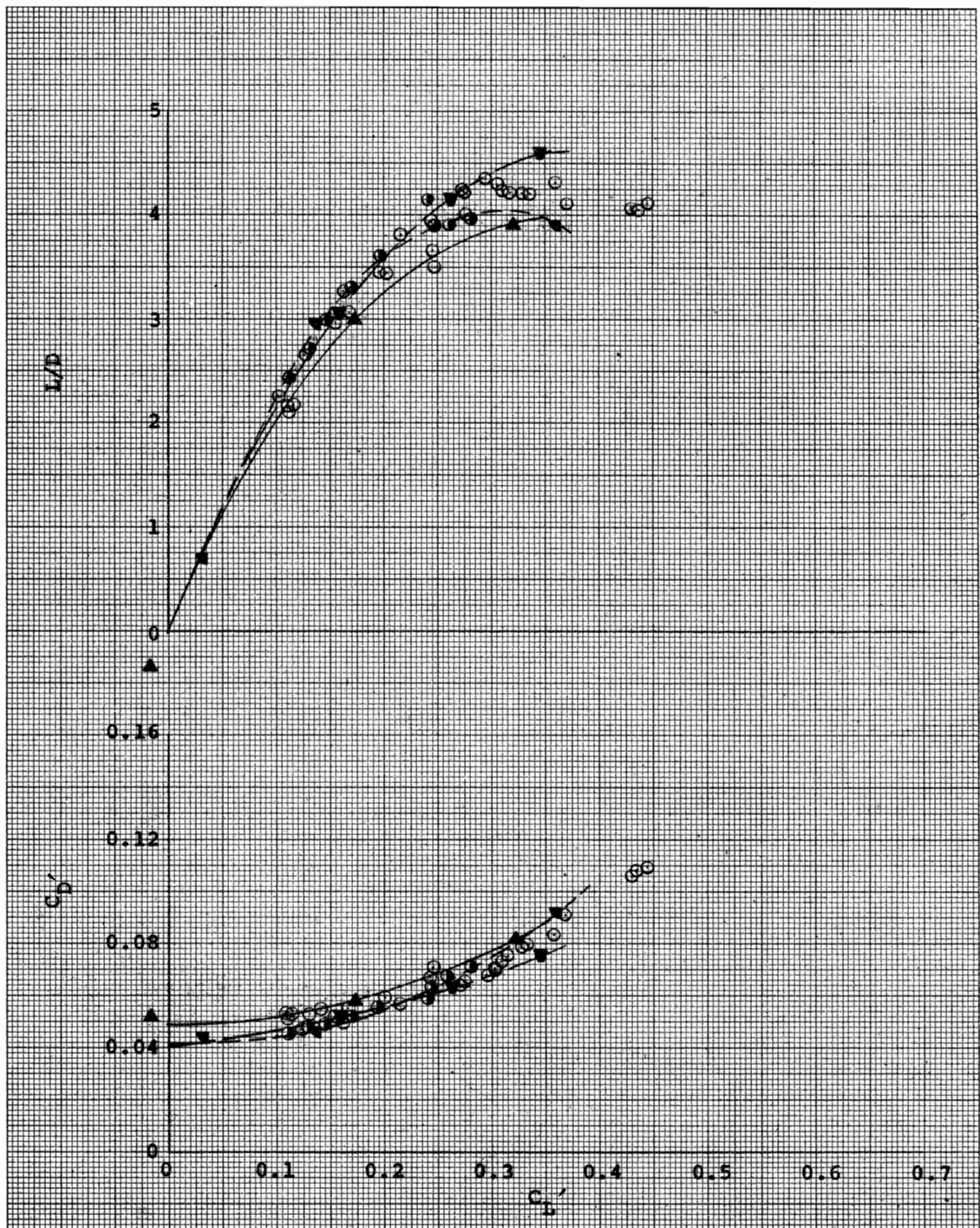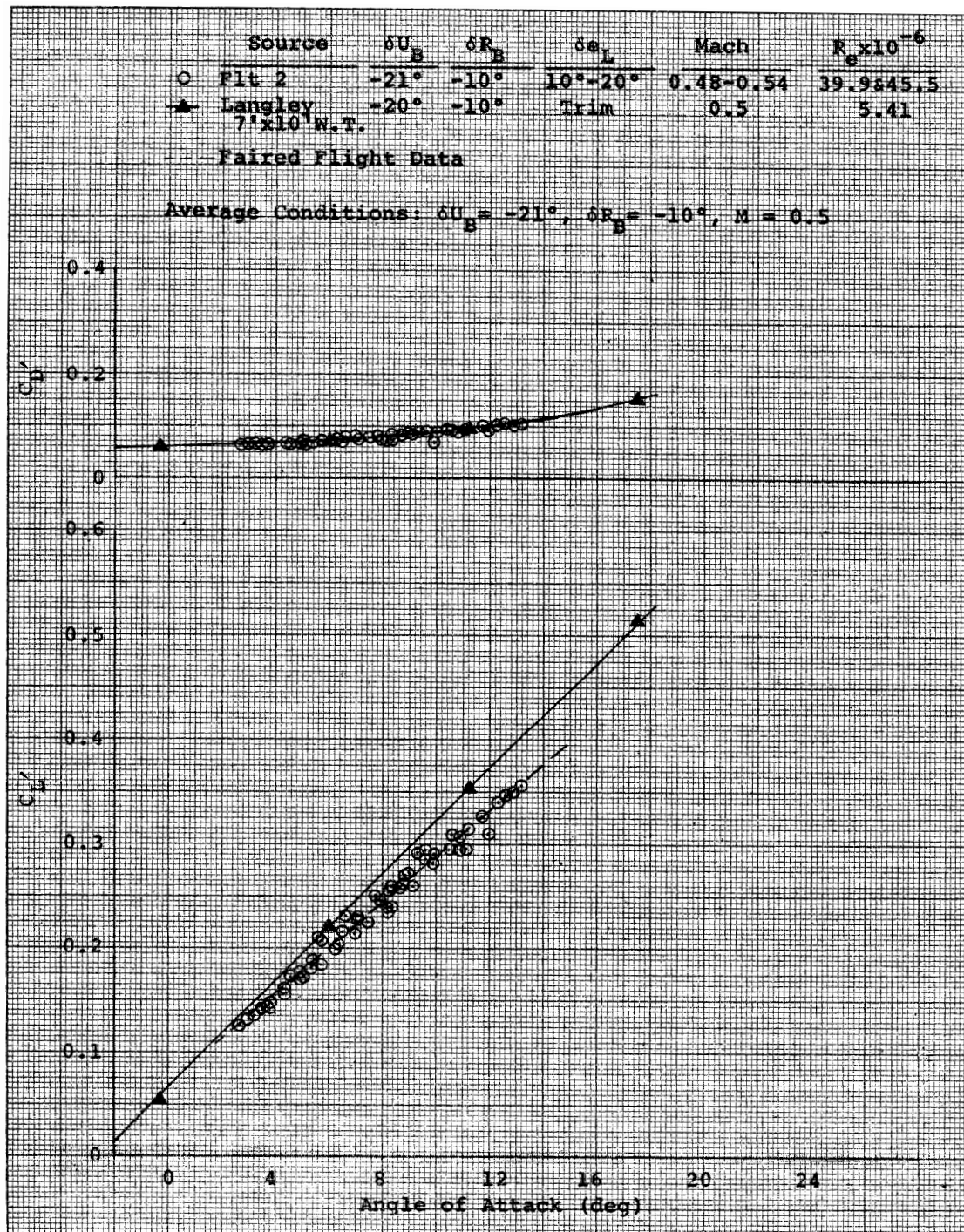
(c) X-24A vehicle trim flight test and wind-tunnel performance data; $M = 0.5$; $\delta U_B = -21°$.

Figure A-4. Continued.

66
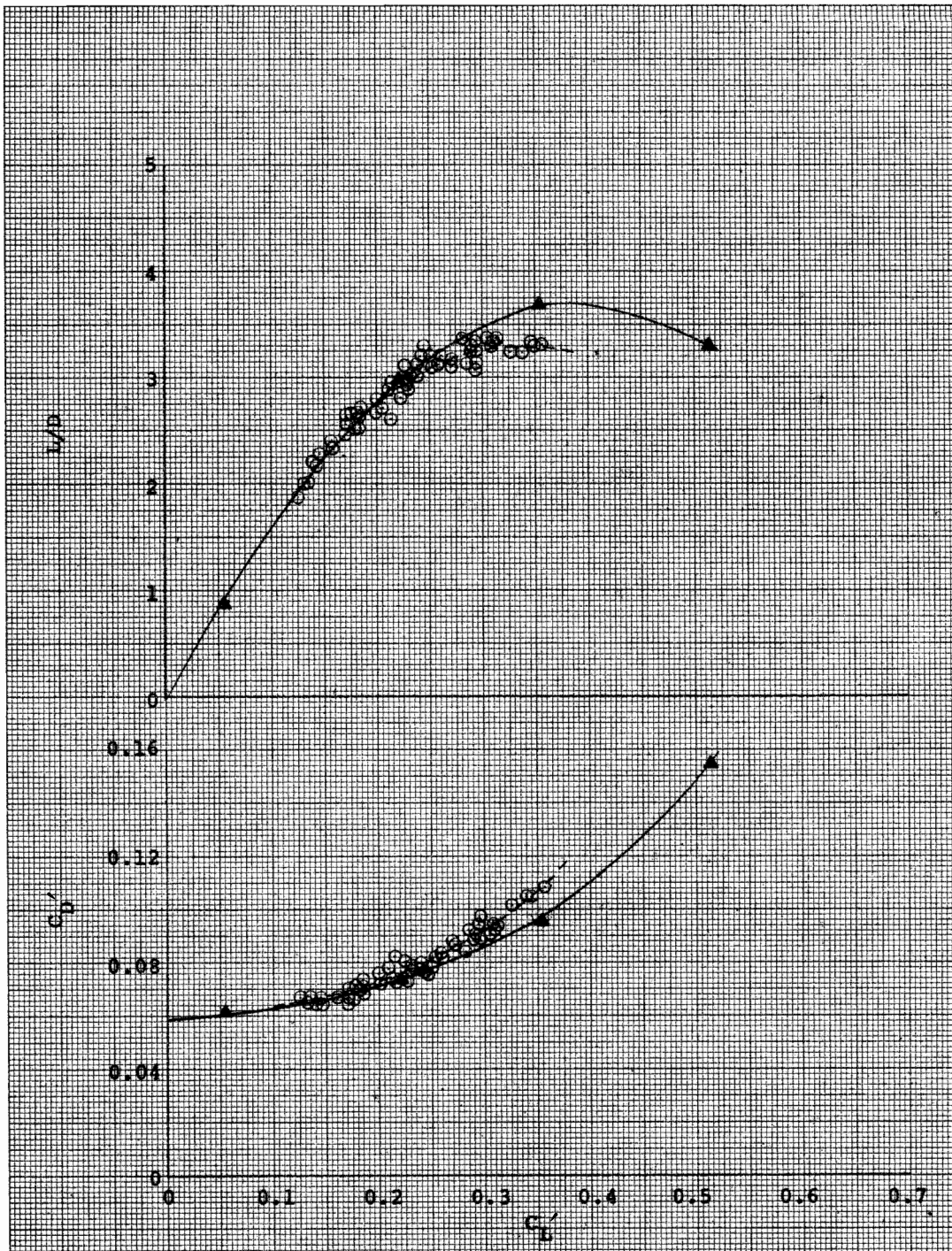
000525

(c). Concluded.

Figure A-4. Concluded.
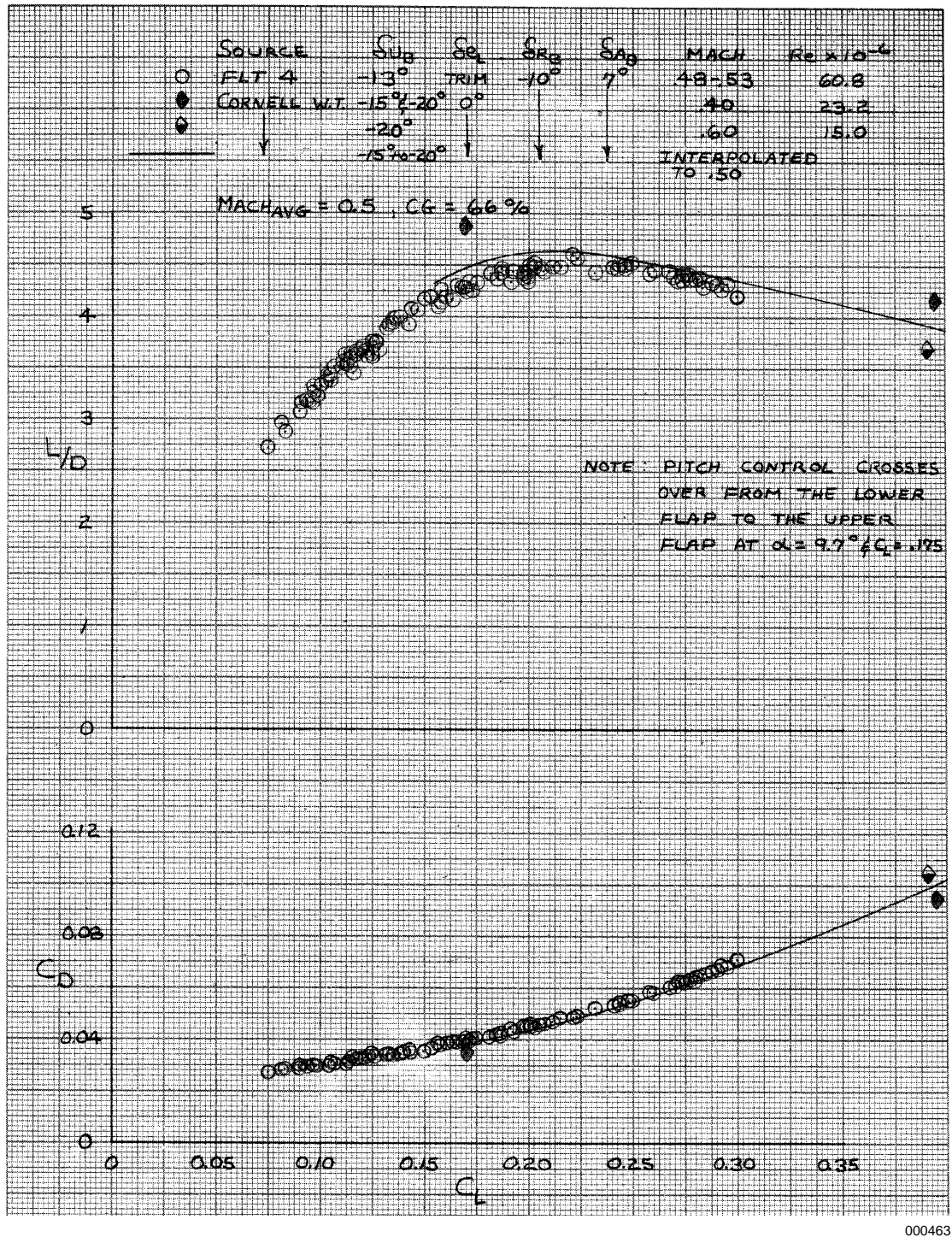
(a) X-24B vehicle trim performance data for $M = 0.5$ and $\delta U_B = -13°$.

Figure A-5. Photocopies of original published plots of lift-curves and drag polars for the X-24B vehicle from reference 15, pages 56–57, 94–97, and 102–103.
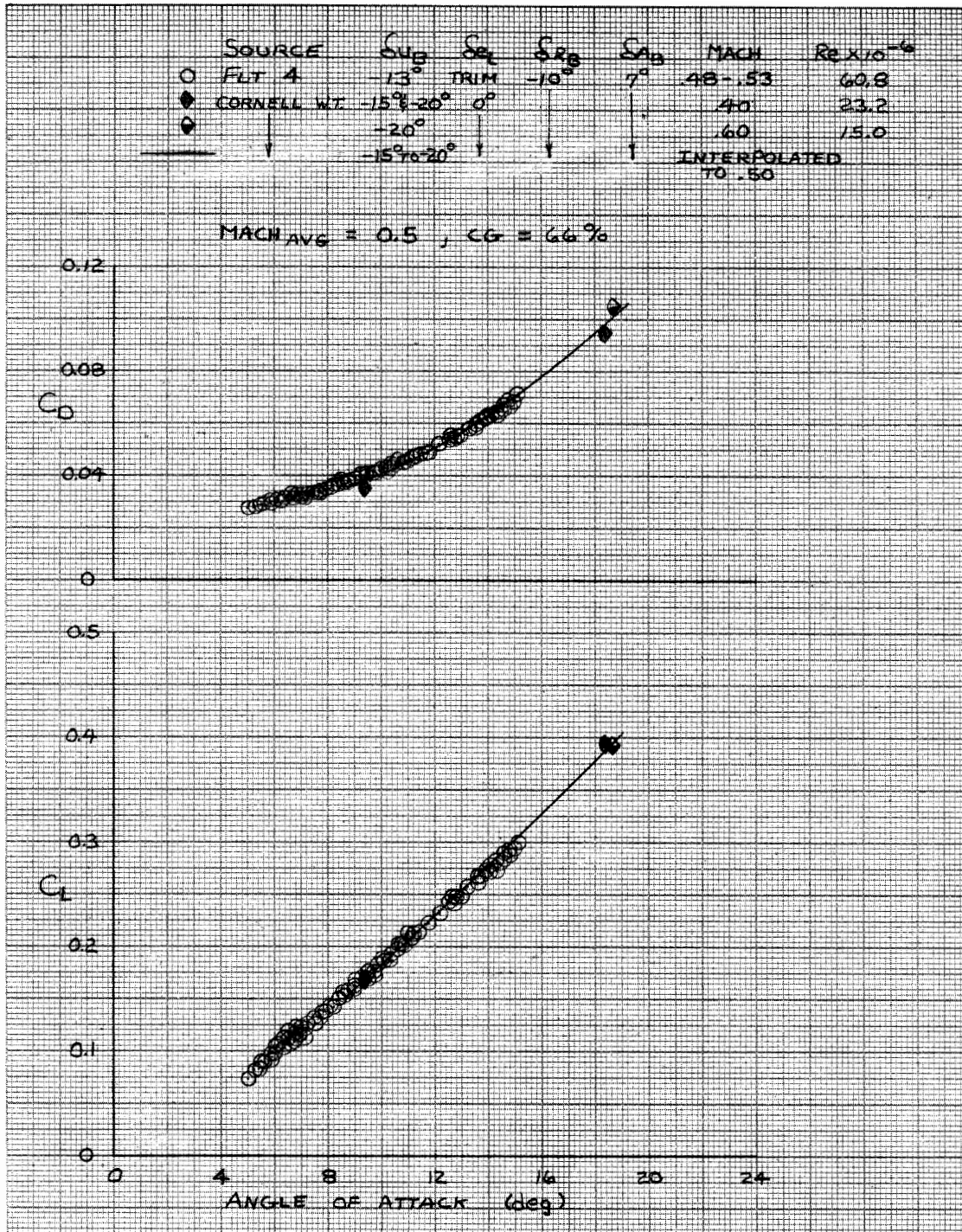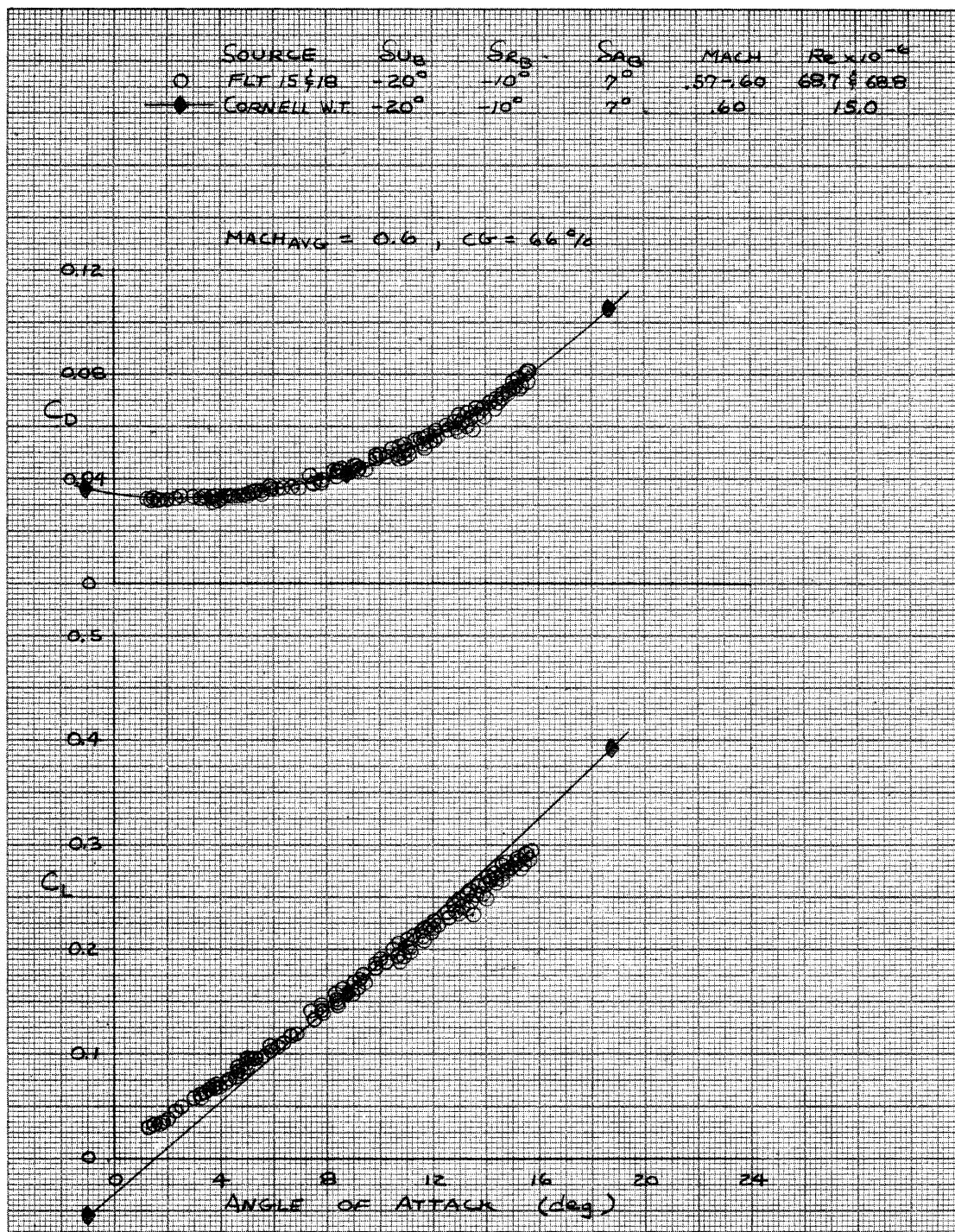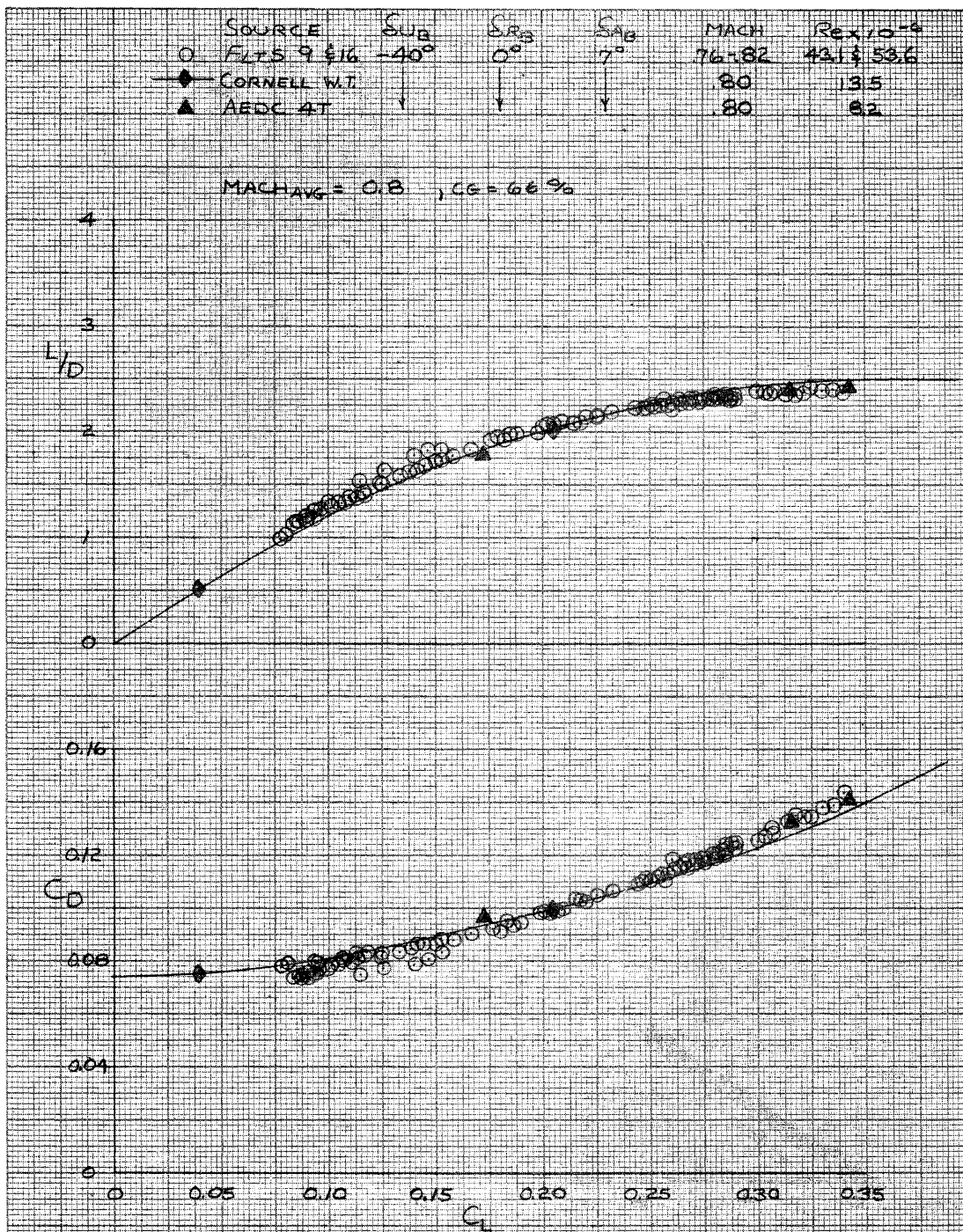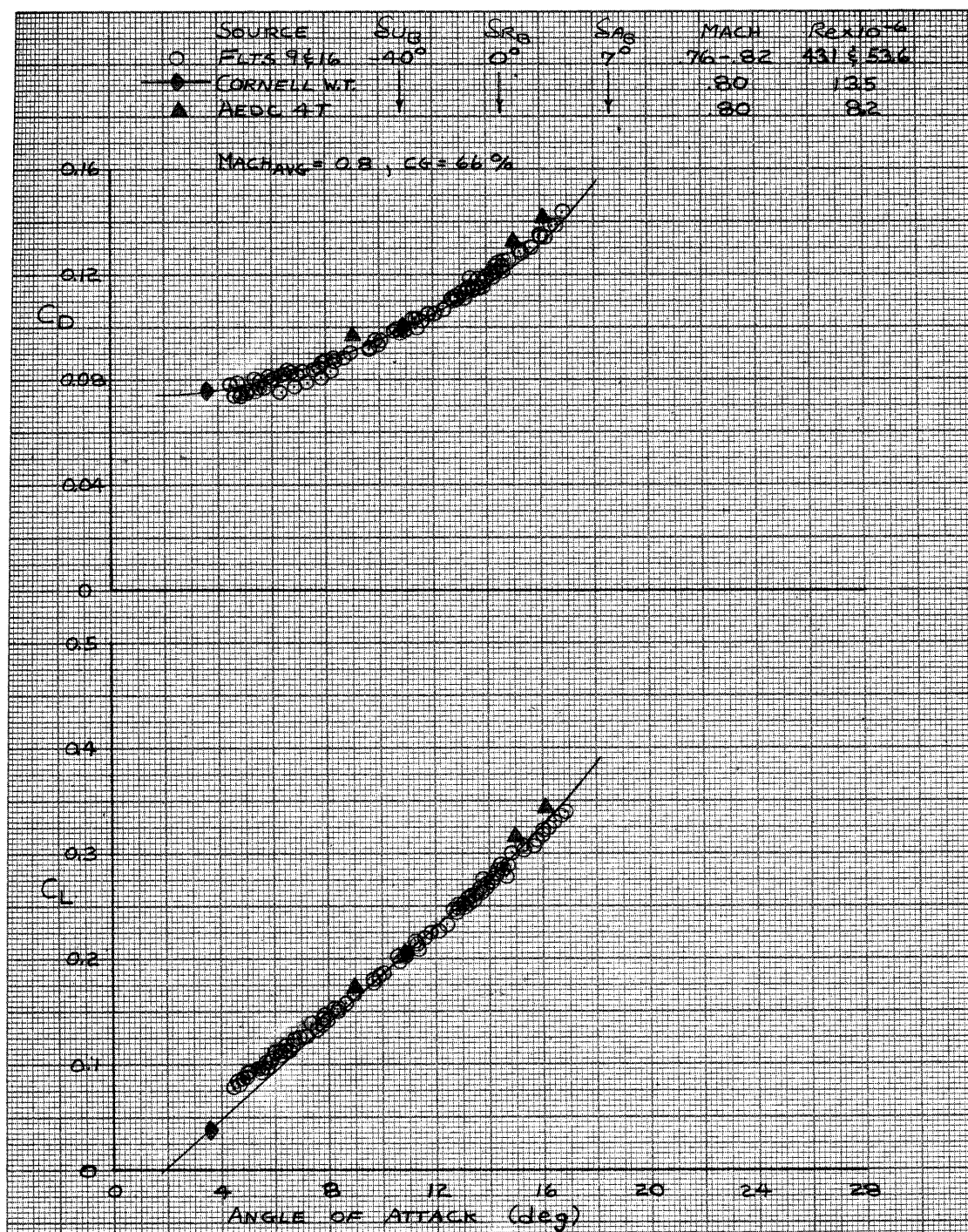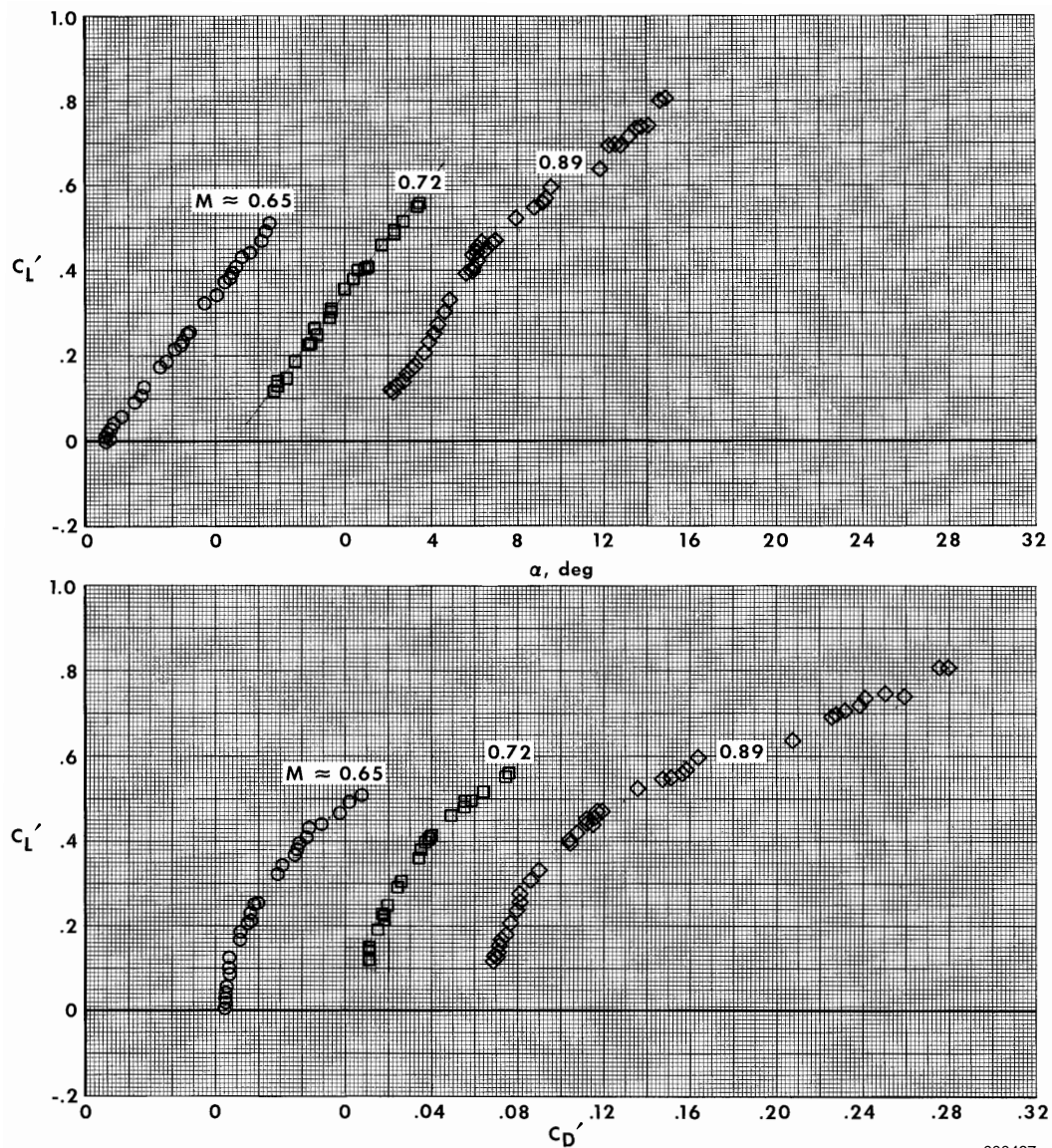
(a). Concluded.

Figure A-5. Continued.

(b) X-24B vehicle trim performance data for $M = 0.5$ and $\delta U_B = -20°$.

Figure A-5. Continued.

Source	δ_{UB}	δ_{RB}	δ_{AB}	MACH	$Re \times 10^{-6}$
○ FLT 5	-20°	-10°	7°	.46-.51	54.1
◆ CORNELL W.T.				.40	23.2
◇				.60	15.0
——					INTERPOLATED TO .50

$MACH_{AVG} = 0.5$, $CG = 66\%$

(b). Concluded.

Figure A-5. Continued.

000527

71
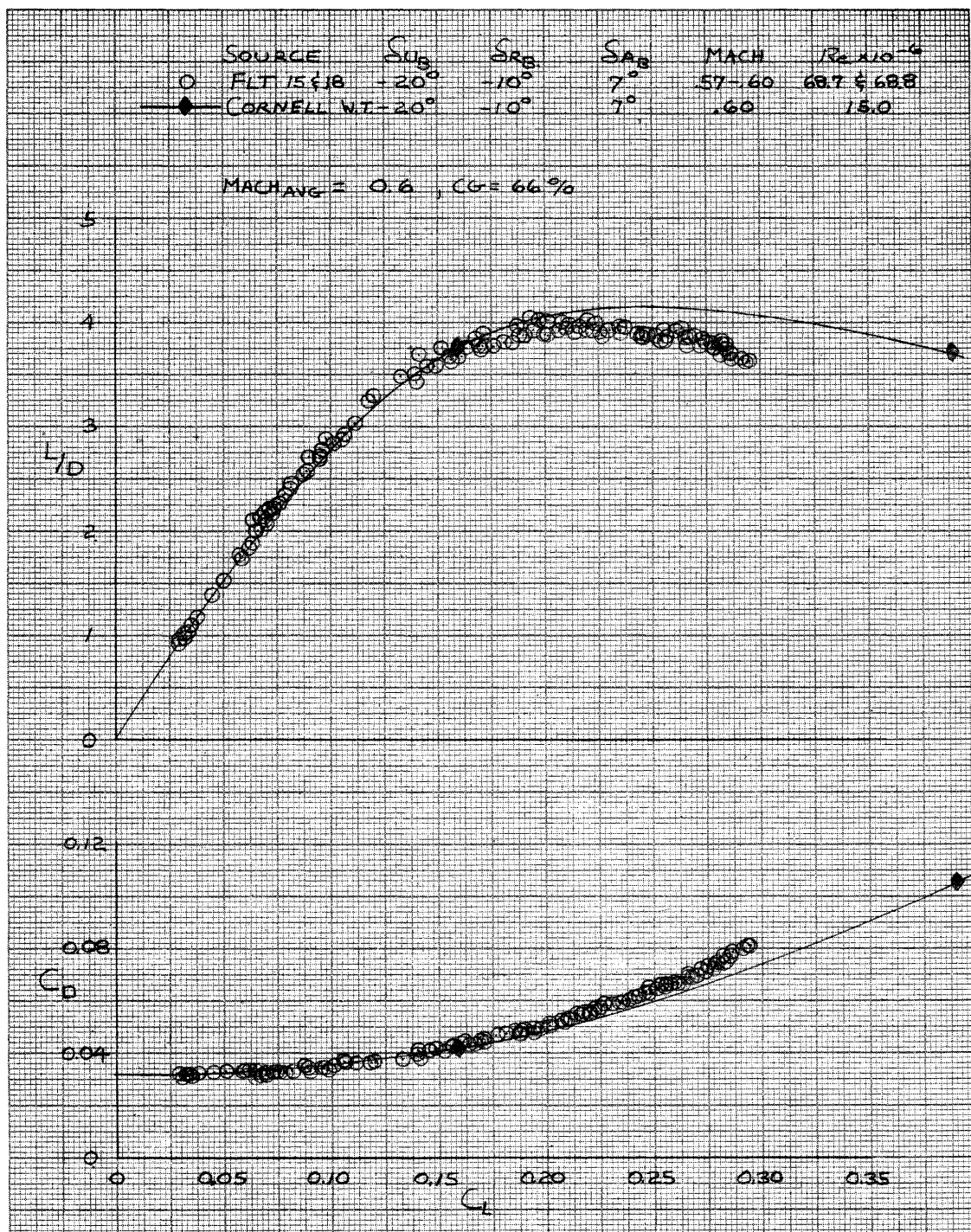
(c) X-24B vehicle trim performance data for $M = 0.6$ and $\delta U_B = -20°$.

Figure A-5. Continued.

(c). Concluded.

Figure A-5. Continued.

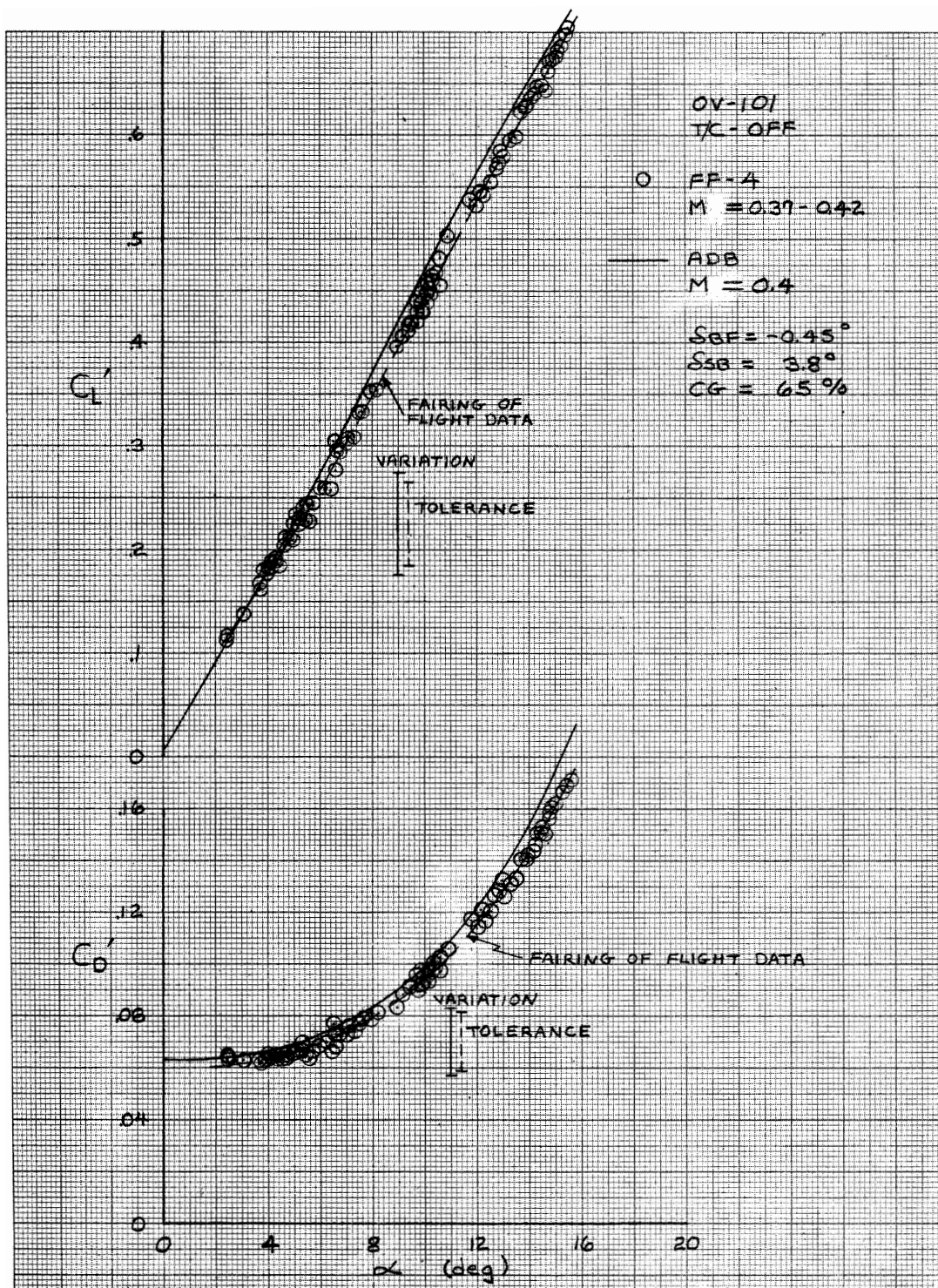(d) X-24B vehicle trim performance data for $M = 0.8$ and $\delta U_B = -40°$.

Figure A-5. Continued.

SOURCE	S_{UG}	S_{RB}	S_{AB}	MACH	$Re \times 10^{-6}$
○ FLTS 9 & 16	40°	0°	7°	76-82	431 & 536
◆ CORNELL W.T.				.80	135
▲ AEDC 4T				.80	82

$MACH_{AVG} = 0.8$; $CG = 66\%$

(d). Concluded.

Figure A-5. Concluded.

000529

Figure A-6. Photocopies of original published plots of lift-curves and drag polars for the X-15 vehicle from reference 21, page 29.

(a) Lift and drag data for *Enterprise* in unpowered flight at Mach 0.4, tailcone off.

Figure A-7. Photocopies of original published plots of lift-curves and drag polars for the Space Shuttle *Enterprise* from reference 23, pages 49 and 53.

OV-101
TK.-OFF

☐ FF-4, FF-5
M = 0.45 - 0.54

——— ADB
M = 0.50

$\delta_{BF} = -0.45°$
$\delta_{SB} = 3.8°$
C.G = 65 %
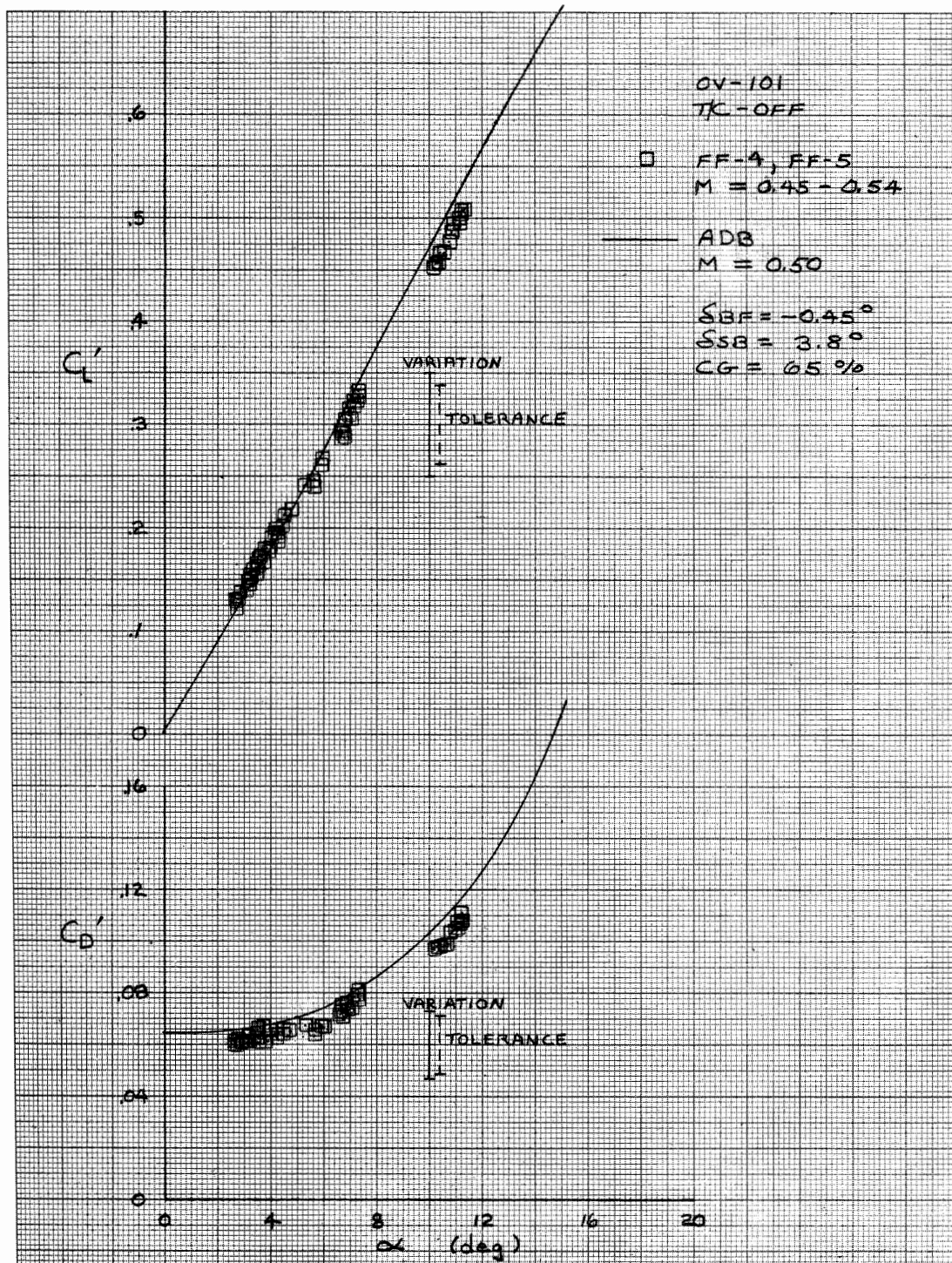
(b) Lift and drag data for *Enterprise* in unpowered flight at Mach 0.5, tailcone off.

Figure A-7. Concluded.

APPENDIX B

SOURCE DATA TRANSFORMED TO A COMMON FORMAT

Whereas appendix A provides the original "root-source" data for this report in a variety of formats as originally published, this appendix is offered as an alternate source that uses a common format for every vehicle. Readers likely will find the presentations of appendix B to be more convenient to use than appendix A. Appendix B was created by electronically scanning and replotting the root-source data of appendix A under a consistent set of formats for all seven vehicles and their various configurations. Because of the transmission process of fairing, tracing, scanning, and replotting, the data in appendix B may exhibit small differences from the root-source data, but these differences should be within the uncertainty of the original data (table 1).

The data plots presented here represent each of the seven subject vehicles for the flight conditions described in tables 2 and 3 of this report. These plots and figures are identified and indexed in table B-1.

Table B-1. Figure index.

| Vehicle | Parameter relationships [a] | | | |
	C_L, α	$L/D, \alpha$	C_L, C_D	$L/D, C_L$
M2-F1	B-1(a)	B-1(b)	B-1(c)	B-1(d)
M2-F2	B-2(a)	B-2(b)	B-2(c)	B-2(d)
HL-10	B-3(a)	B-3(b)	B-3(c)	B-3(d)
X-24A	B-4(a)	B-4(b)	B-4(c)	B-4(d)
X-24B	B-5(a)	B-5(b)	B-5(c)	B-5(d)
X-15	B-6(a)	B-6(b)	B-6(c)	B-6(d)
Enterprise	B-7(a)	B-7(b)	B-7(c)	B-7(d)

[a] Each of the above noted figures, parts (a)–(d), represent coefficients or angles of attack as follows: C_L' or C_D' values are based on reference areas as originally published; C_L or C_D are based on the more representative reference area as explained on page 18 and defined in table 2; and $\alpha^* = \alpha - (\alpha \; at \; C_L = 0)$.

The data plots indexed in table B-1 are each devoted to an individual vehicle. Summary plots have been prepared that combine all seven vehicles on one plot, using one representative flight condition or configuration for vehicles with multiple flight conditions and configurations. Appendix C shows the summary plots, which may be useful for comparison.
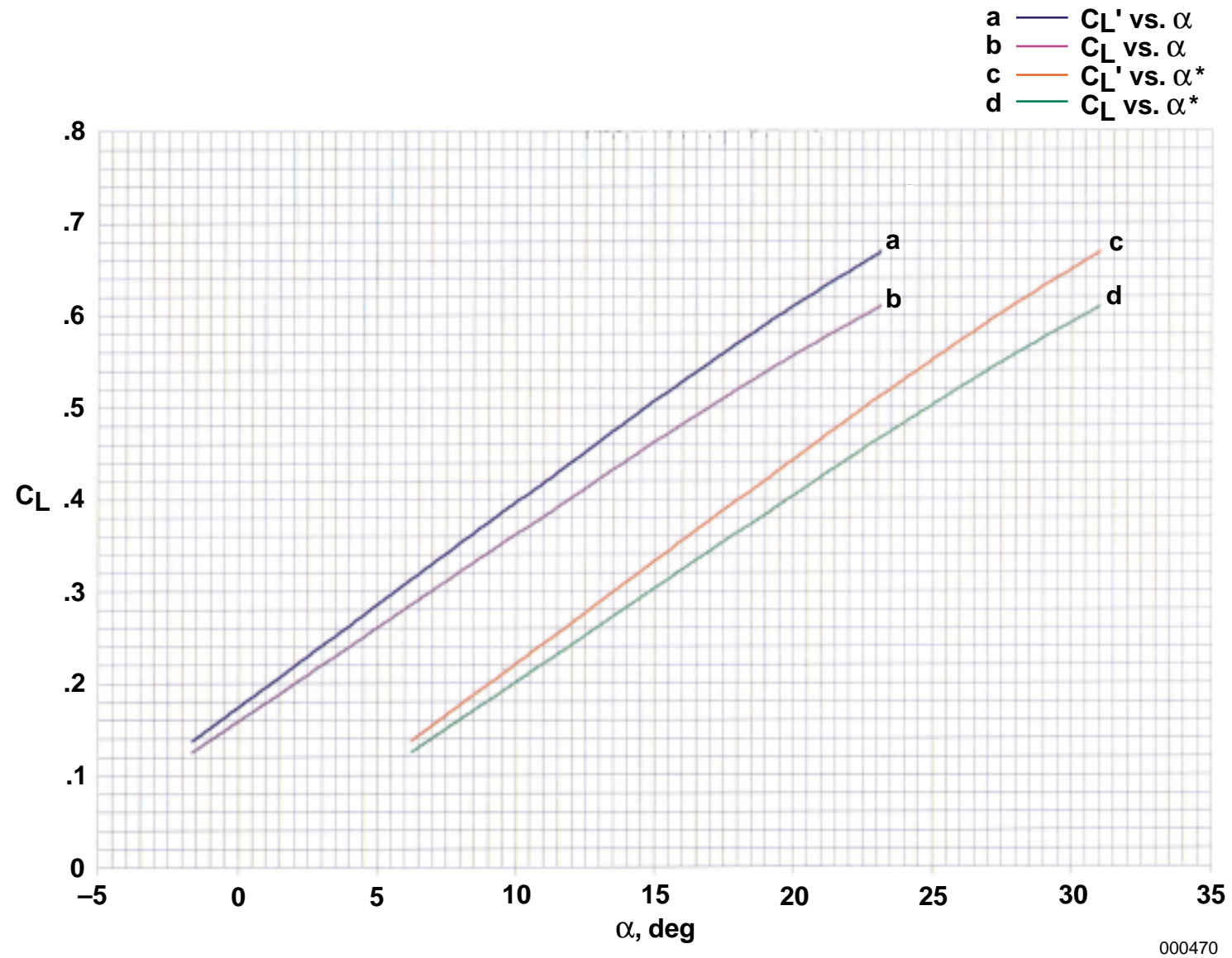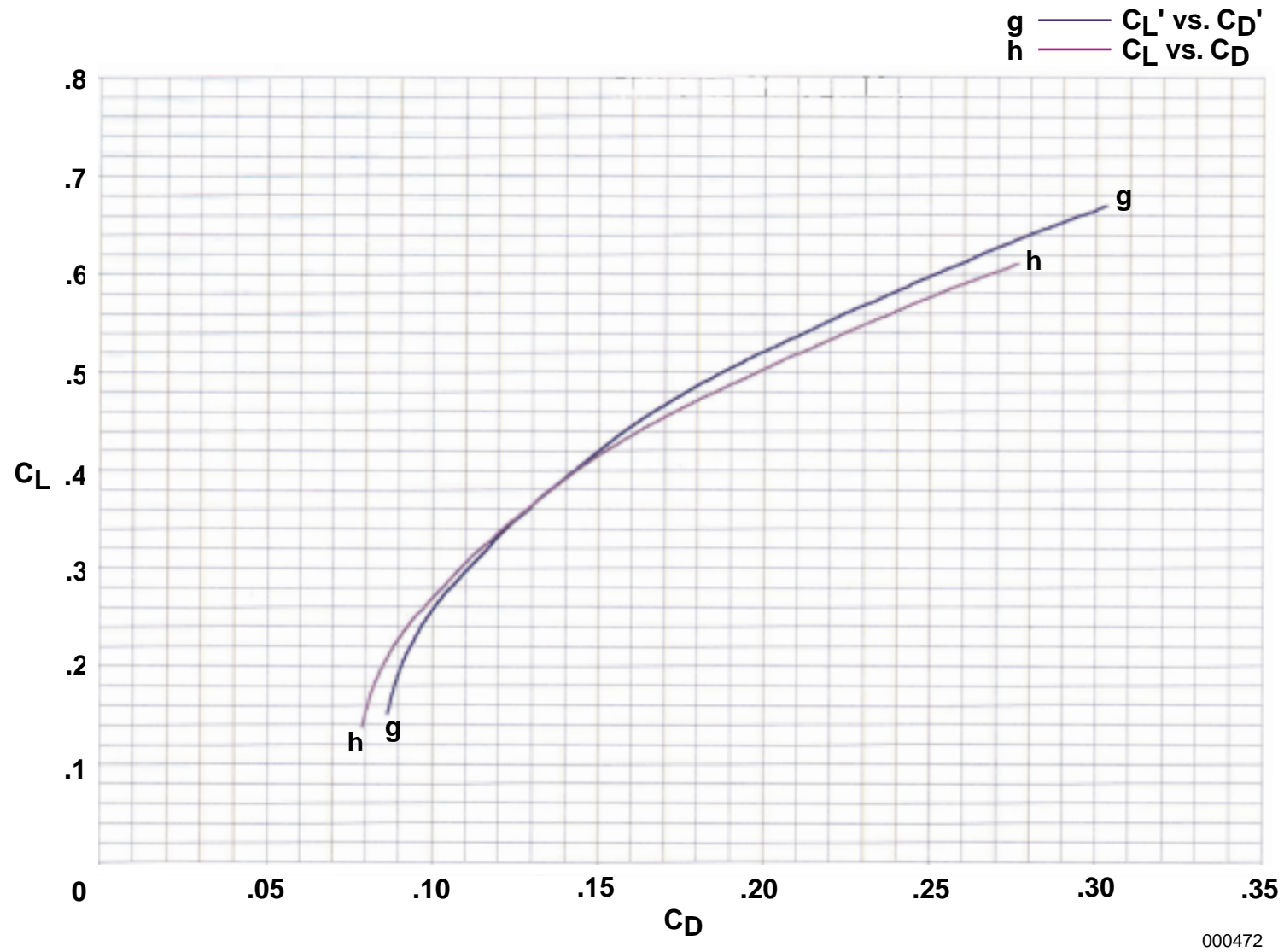
(a) C_L as a function of α.

Figure B-1. The relationship of basic performance components for the M2-F1 vehicle, derived from published reference as represented in appendix A, figure A-1.
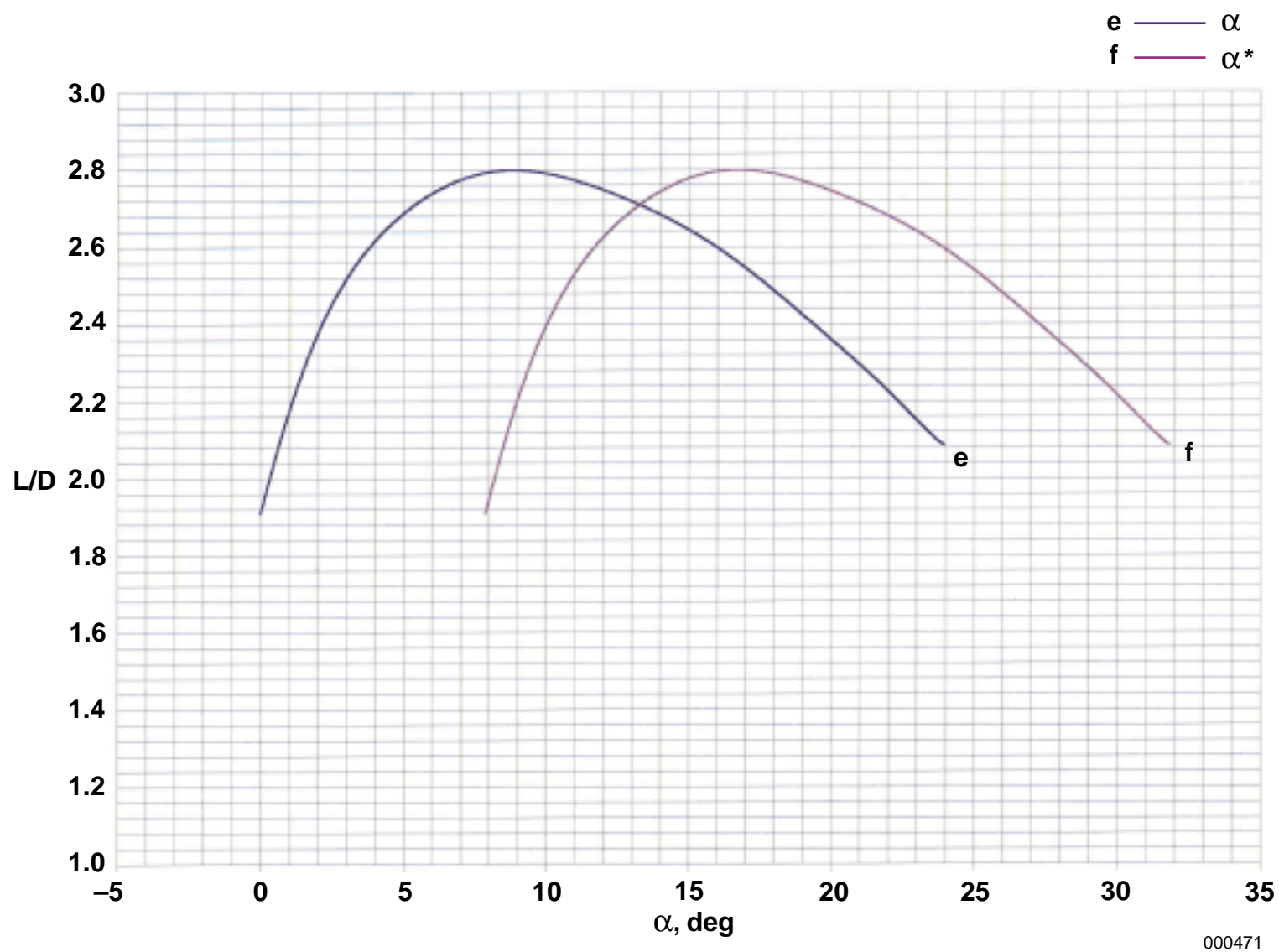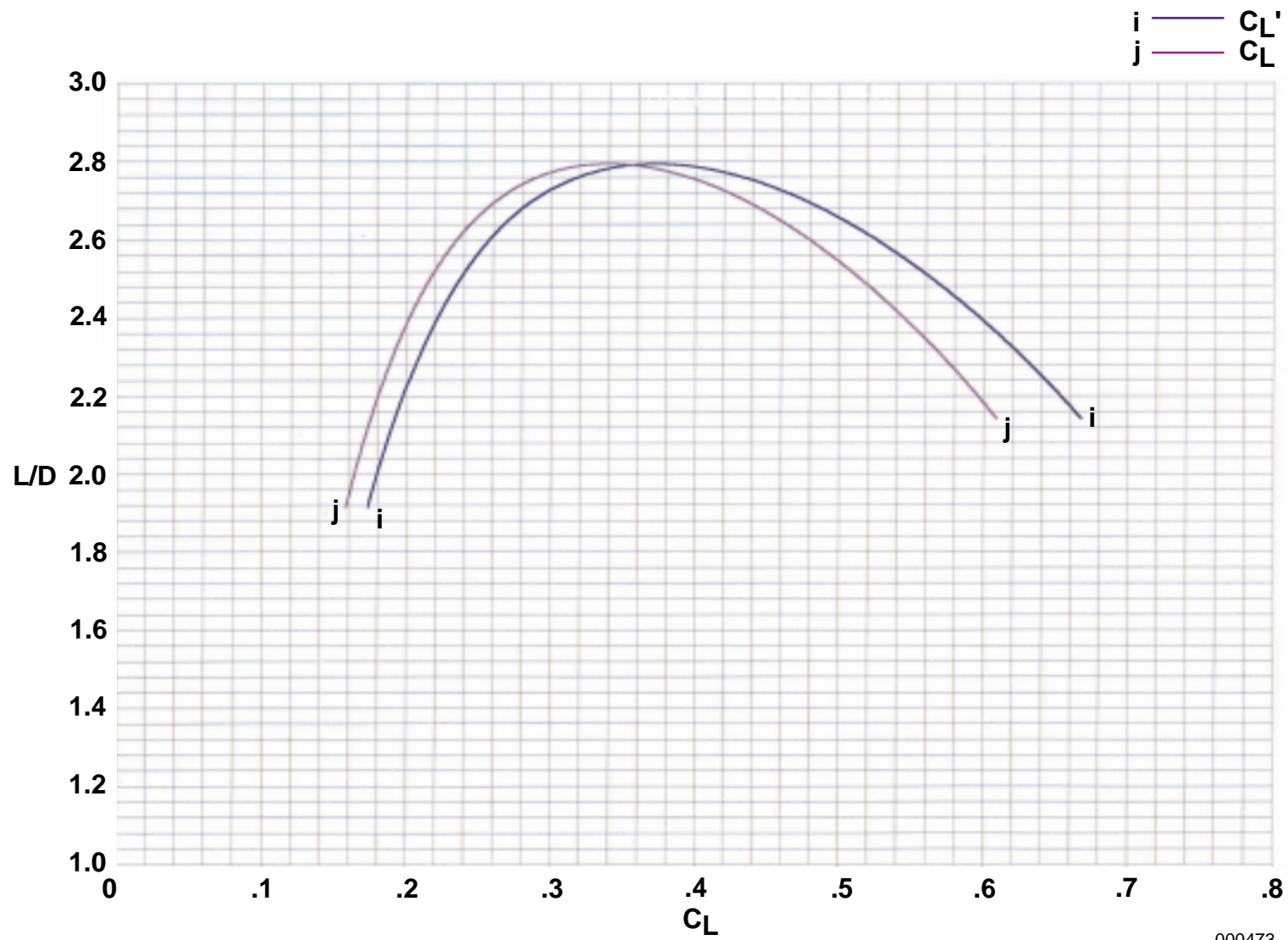
(b) L/D as a function of α.

Figure B-1. Continued.
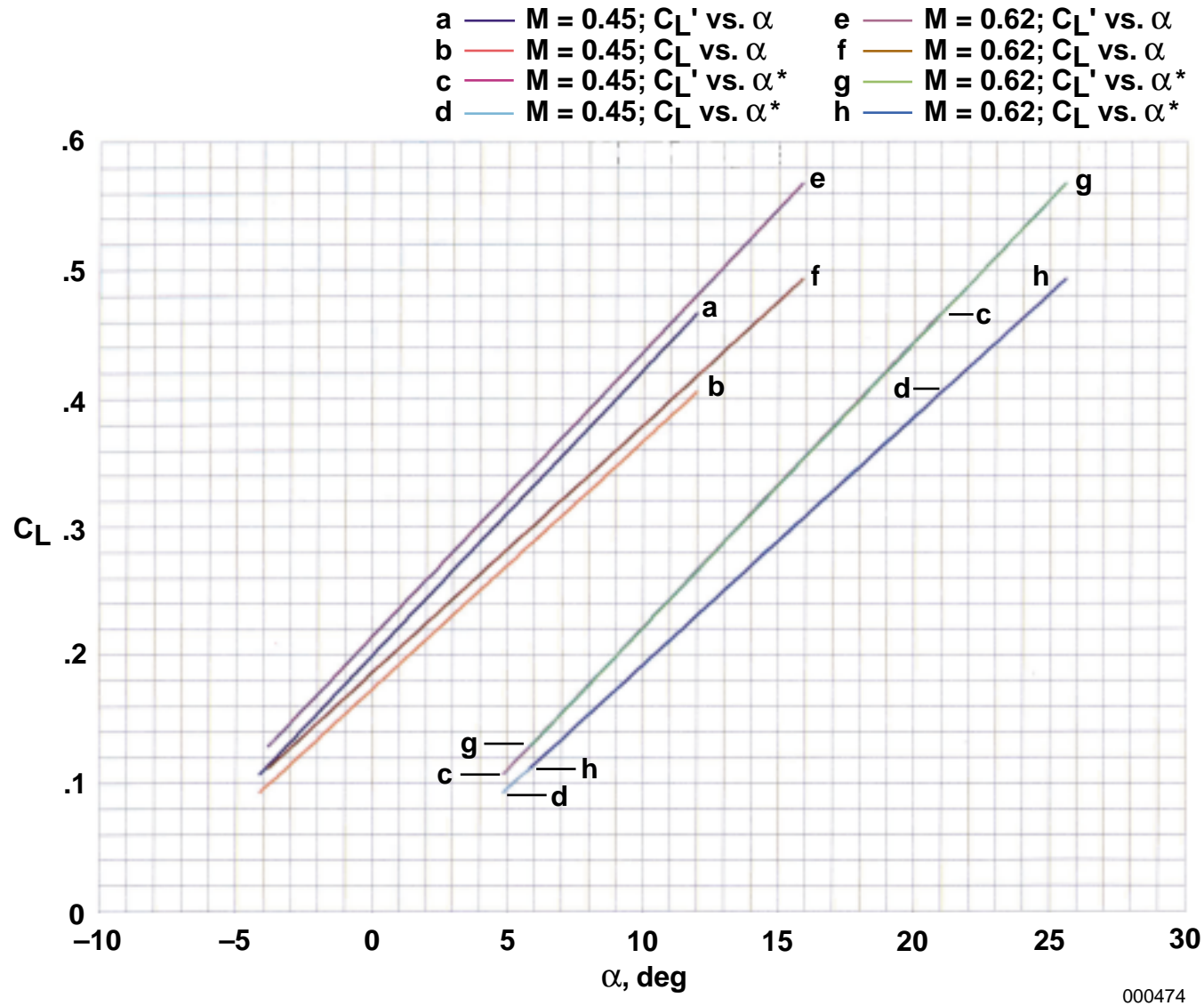
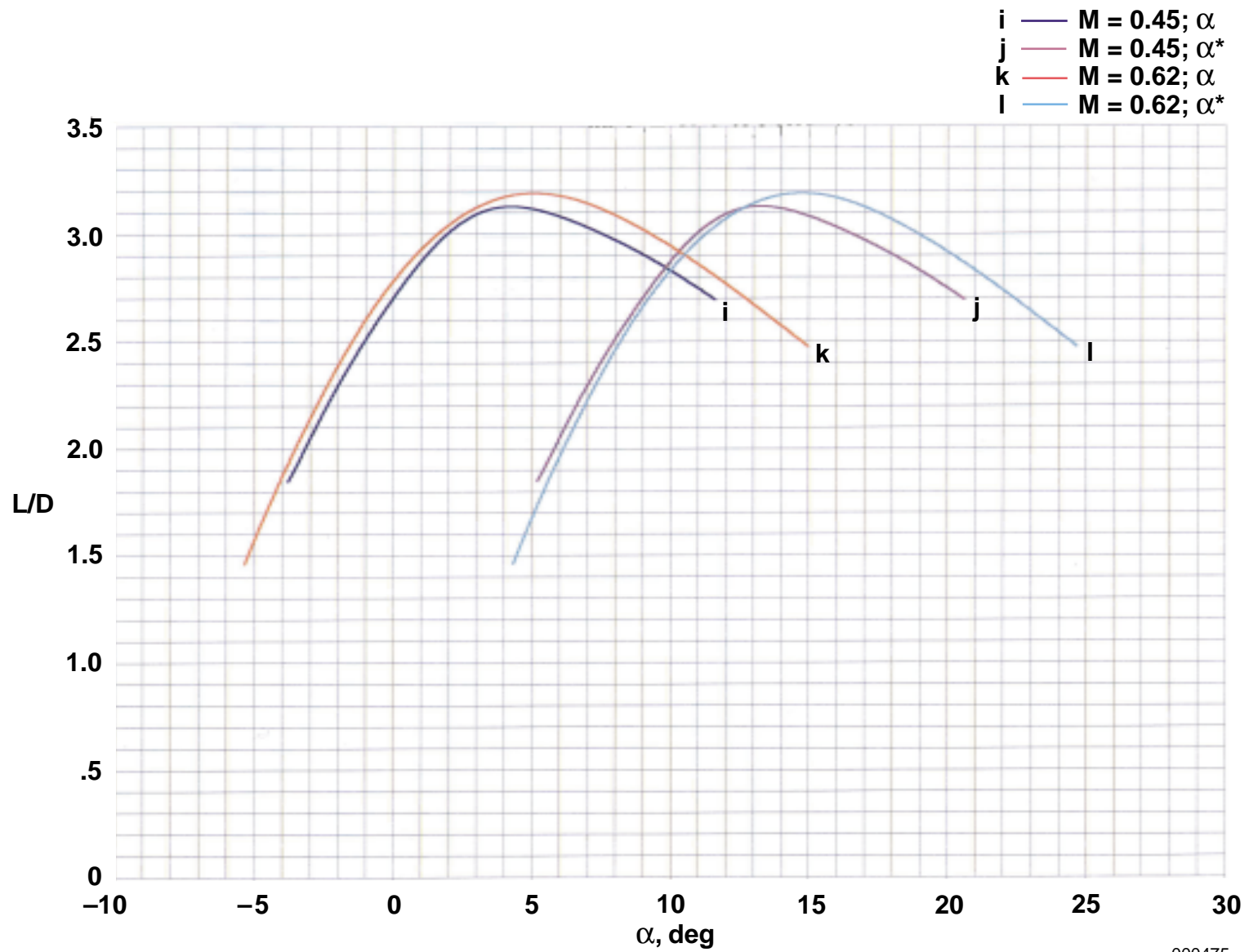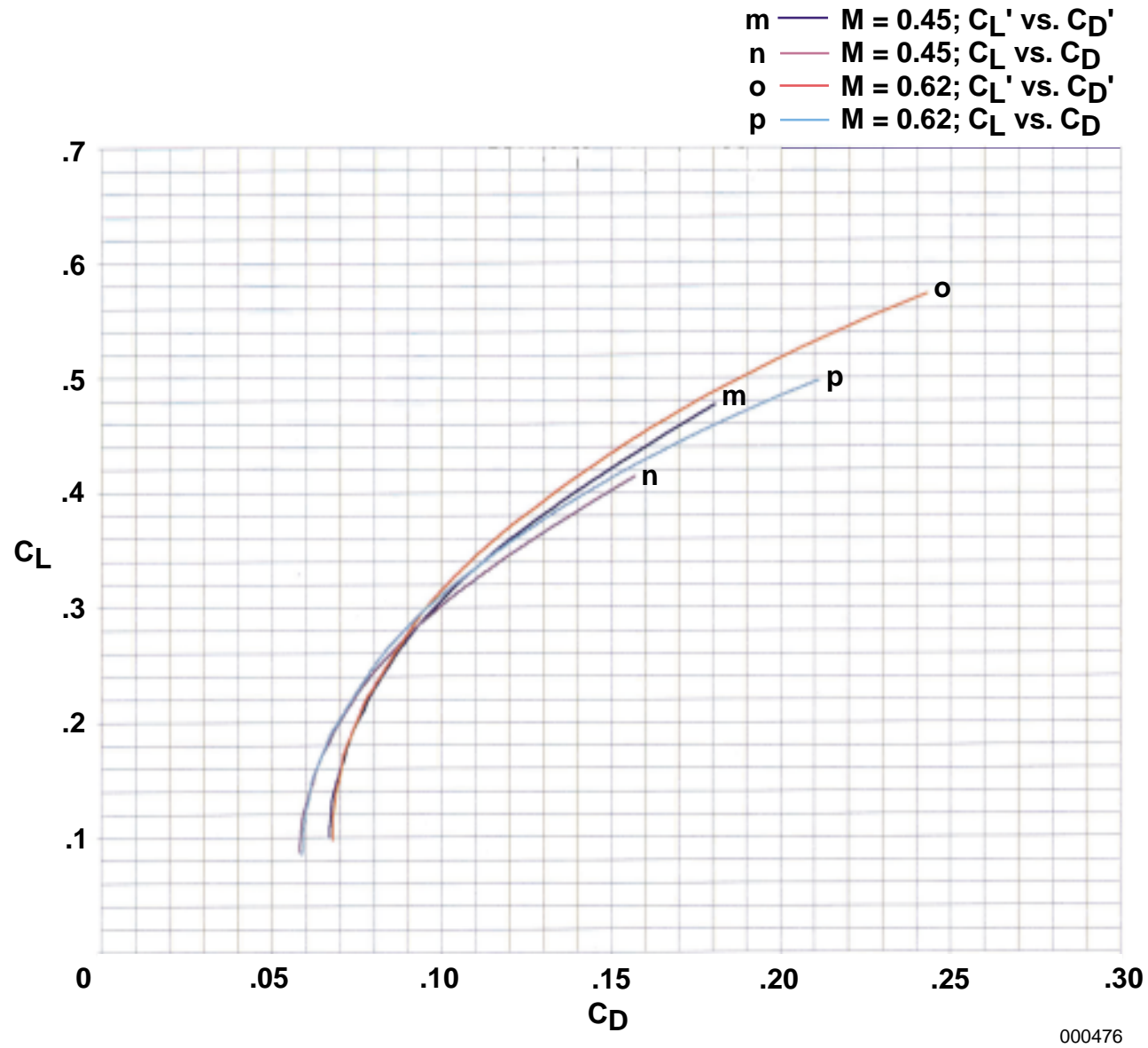(c) C_L as a function of C_D.

Figure B-1. Continued.

(d) L/D as a function of C_L.

Figure B-1. Concluded.

a	M = 0.45; C_L' vs. α	e — M = 0.62; C_L' vs. α
b	M = 0.45; C_L vs. α	f — M = 0.62; C_L vs. α
c	M = 0.45; C_L' vs. α^*	g — M = 0.62; C_L' vs. α^*
d	M = 0.45; C_L vs. α^*	h — M = 0.62; C_L vs. α^*

000474

(a) C_L as a function of α.

Figure B-2. The relationship of basic performance components for the M2-F2 vehicle, derived from published reference as represented in appendix A, figure A-2.
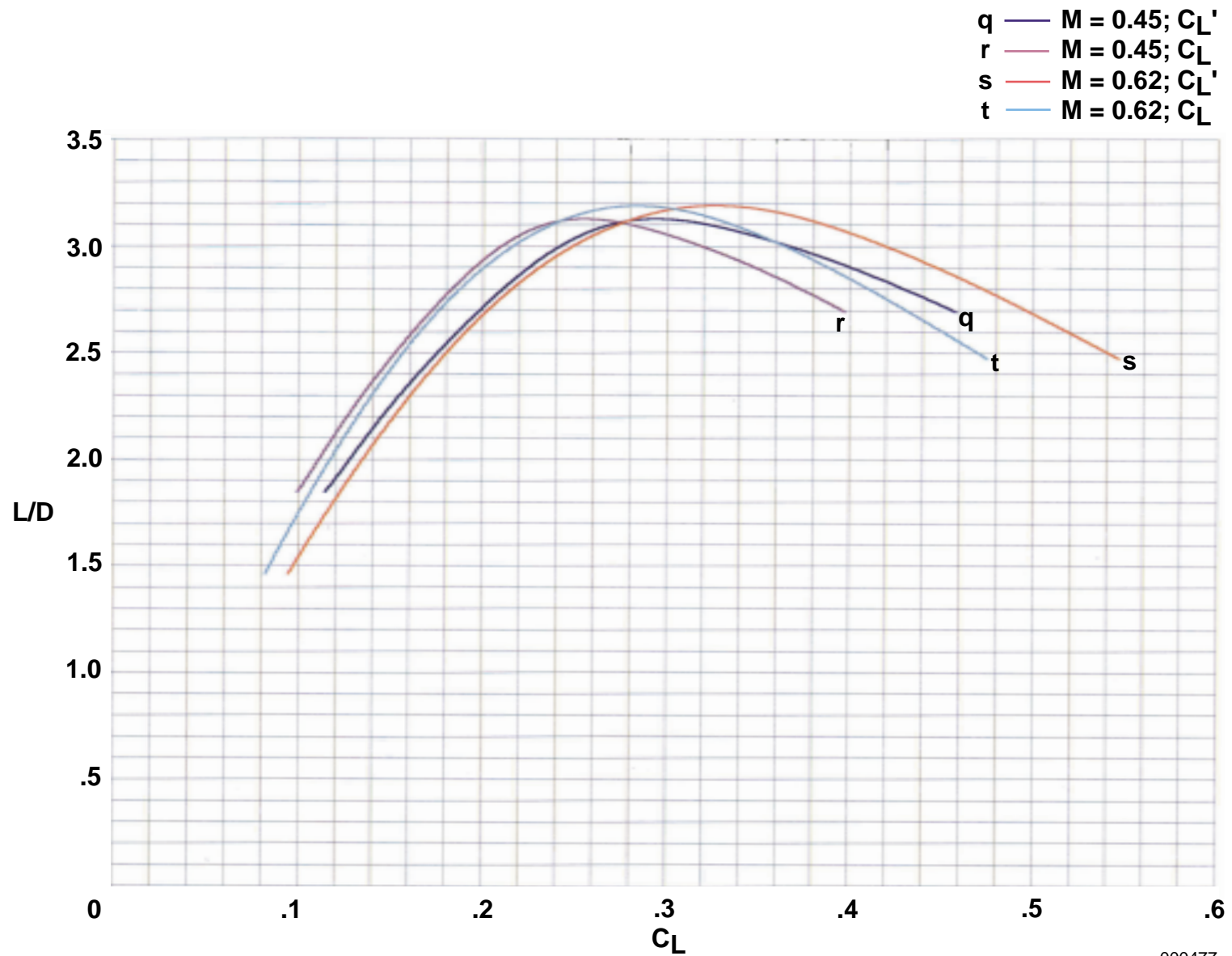
(b) L/D as a function of α.
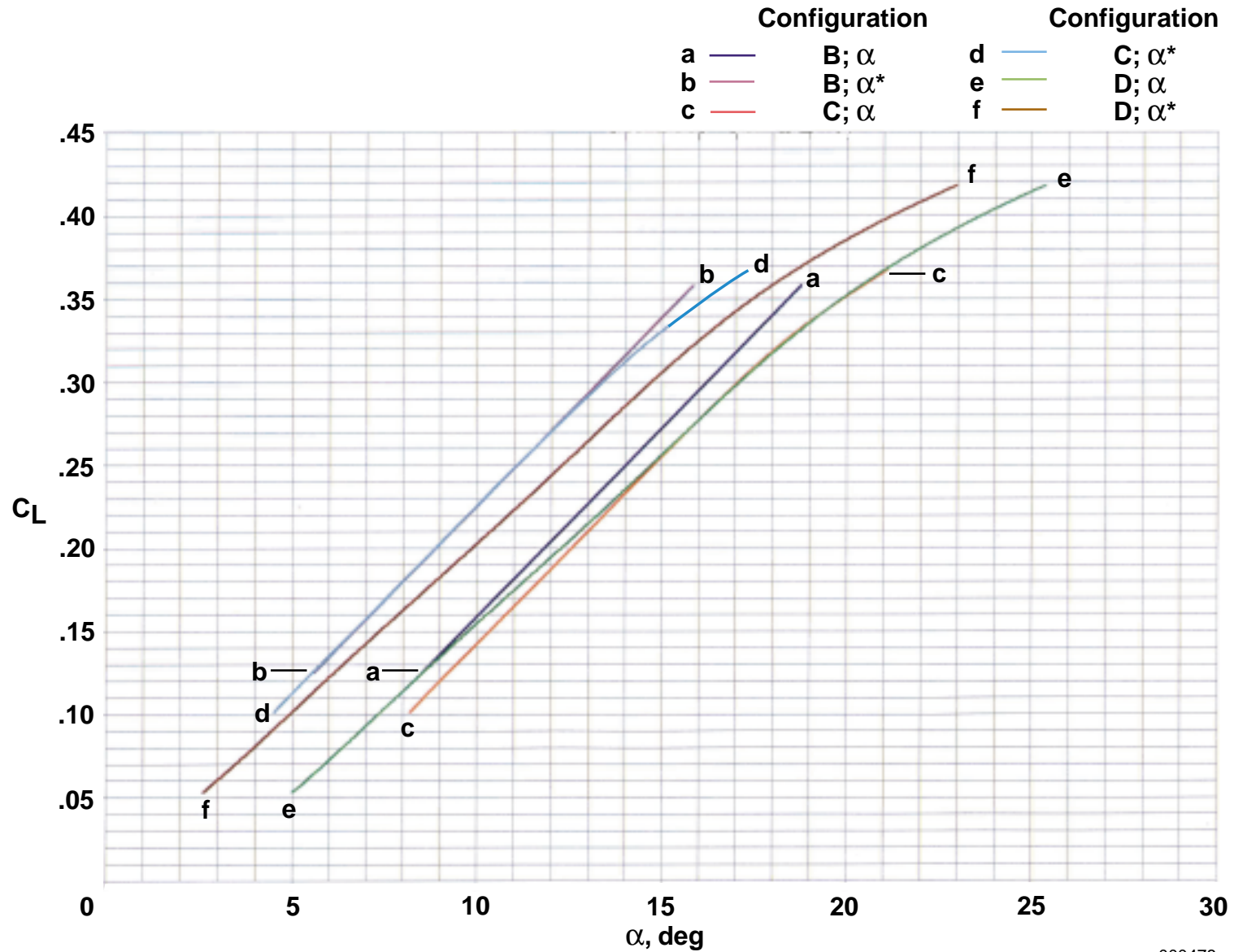
Figure B-2. Continued.

(c) C_L as a function of C_D.

Figure B-2. Continued.
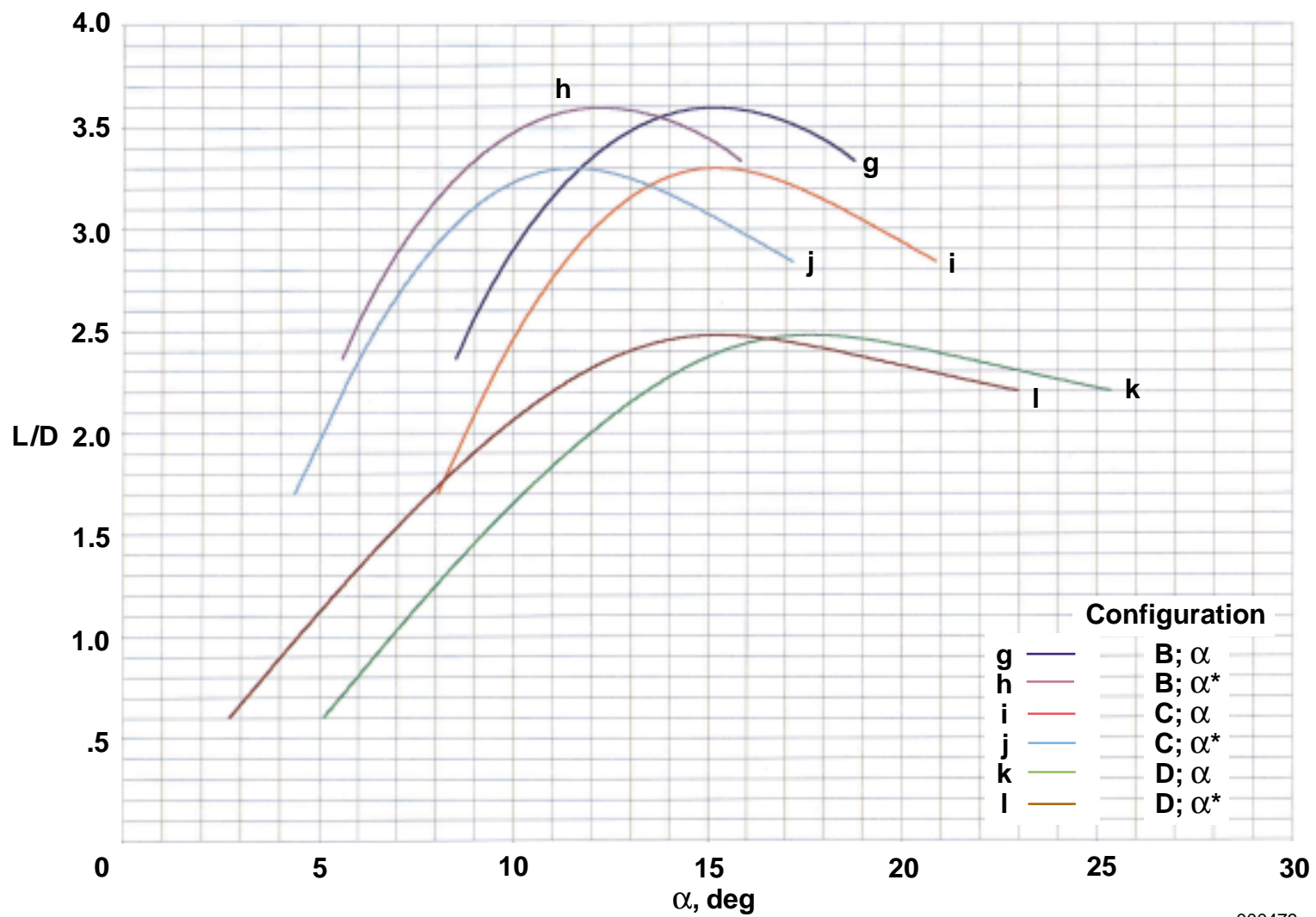
(d) L/D as a function of C_L.

Figure B-2. Concluded.
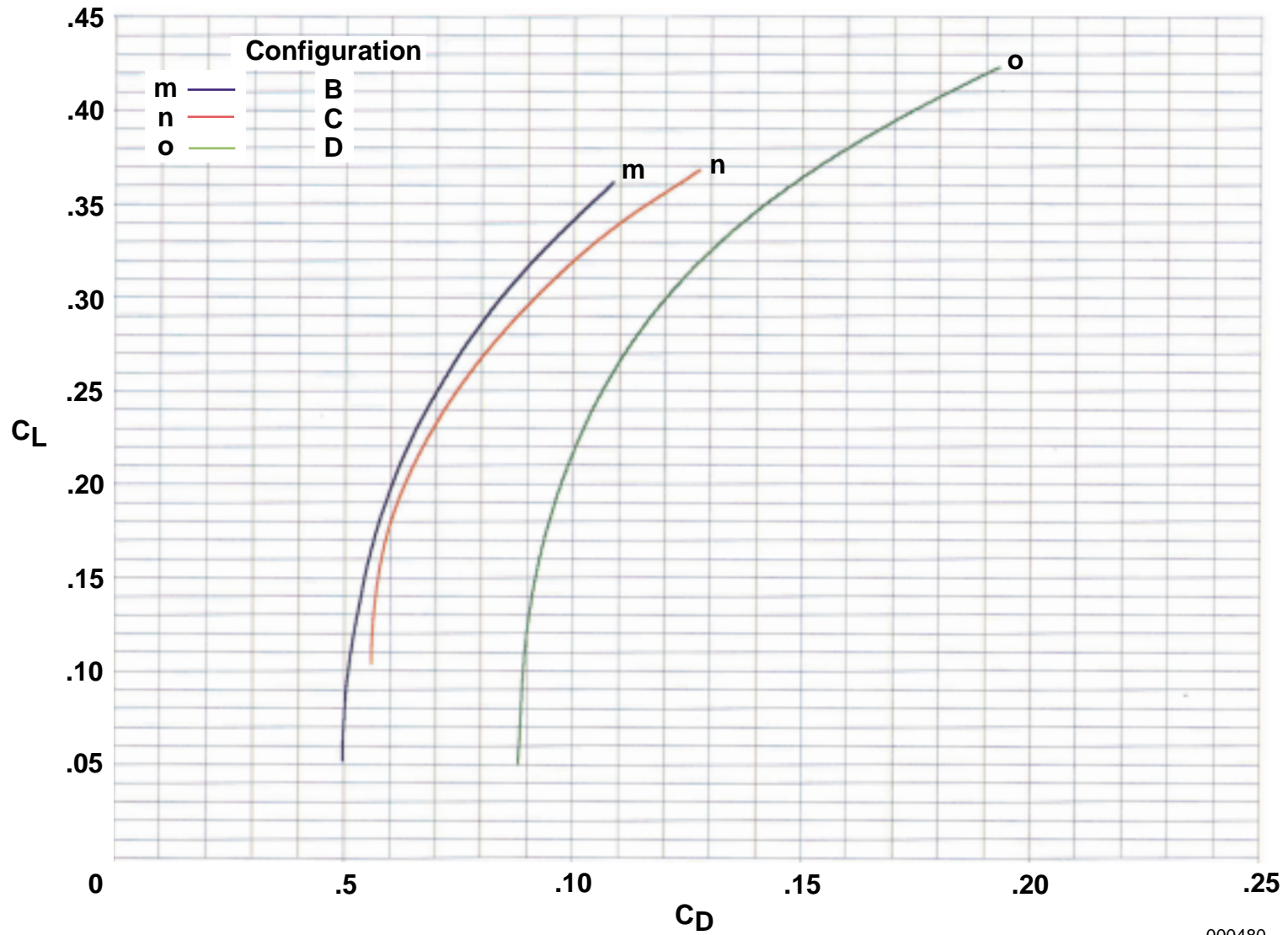
(a) C_L as a function of α.

Figure B-3. The relationship of basic performance components for the HL-10 vehicle, derived from published reference as represented in appendix A, figure A-3.
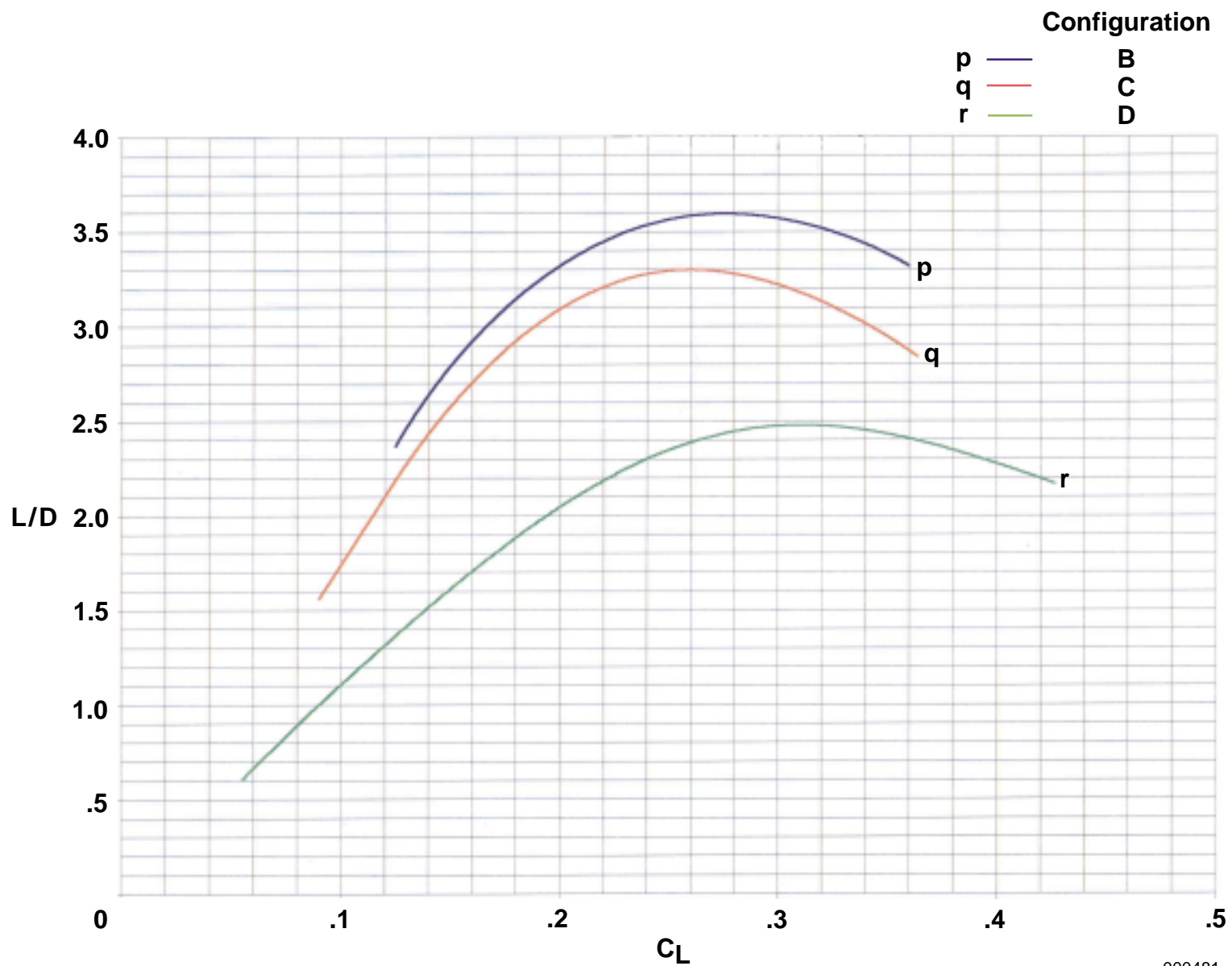
(b) L/D as a function of α.

Figure B-3. Continued.

(c) C_L as a function of C_D.
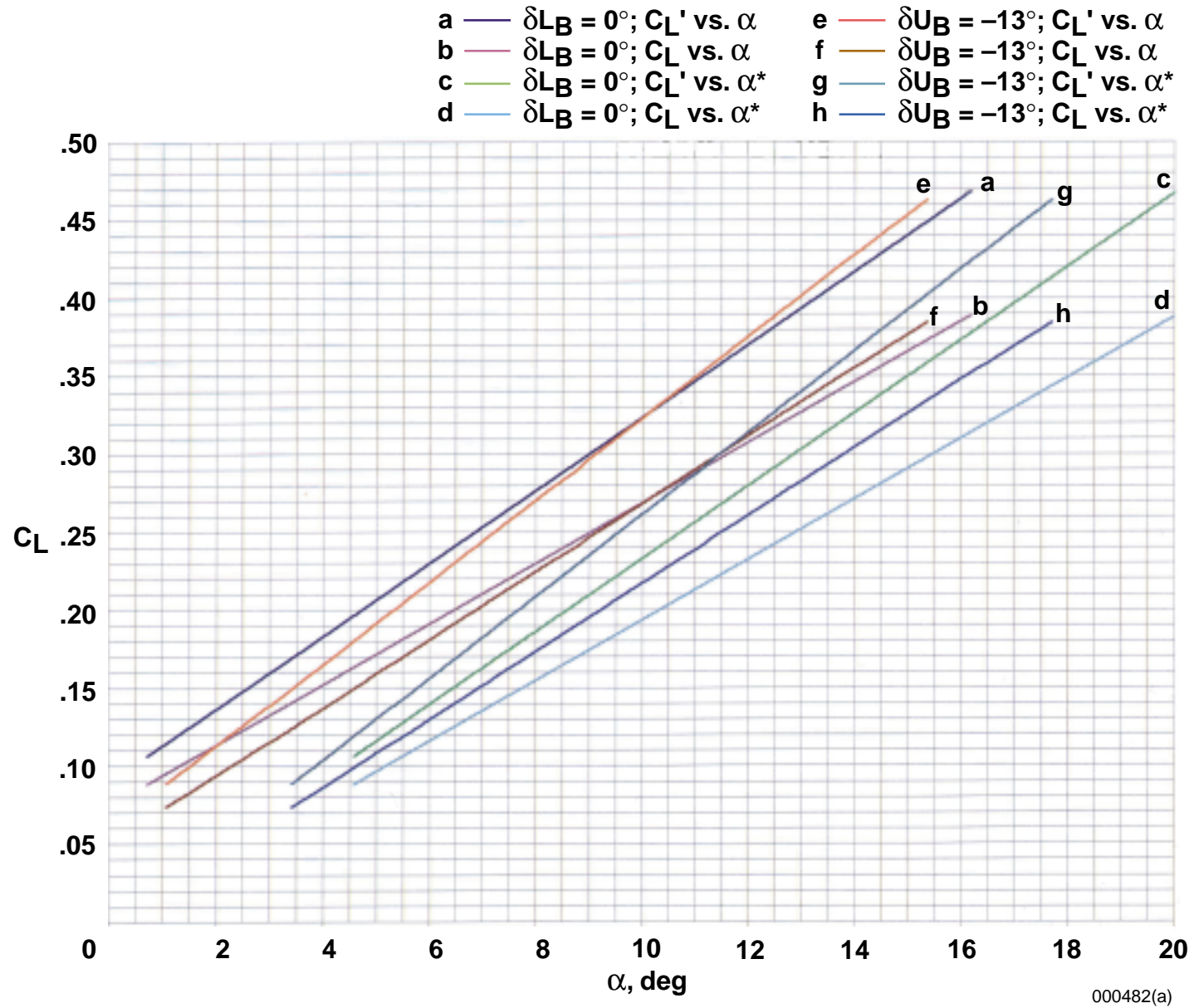
Figure B-3. Continued.

(d) L/D as a function of C_L.

Figure B-3. Concluded.

(a) C_L as a function of α.

Figure B-4. The relationship of basic performance components for the X-24A vehicle, derived from published reference as represented in appendix A, figure A-4.

(a). Concluded.

Figure B-4. Continued.

(b) L/D as a function of α.

Figure B-4. Continued.

(c) C_L as a function of C_D.

Figure B-4. Continued.

000484

(d) L/D as a function of C_L.

Figure B-4. Concluded.

Legend:
a — M = 0.5; $\delta U_B = -13°$; α
b — M = 0.5; $\delta U_B = -13°$; $\alpha*$
c — M = 0.5; $\delta U_B = -20°$; α
d — M = 0.5; $\delta U_B = -20°$; $\alpha*$

(a) C_L as a function of α.

000486(a)

Figure B-5. The relationship of basic performance components for the X-24B vehicle, derived from published reference as represented in appendix A, figure A-5.

(a). Concluded.

Figure B-5. Continued.

(b) L/D as a function of α.

Figure B-5. Continued.

(c) C_L as a function of C_D.

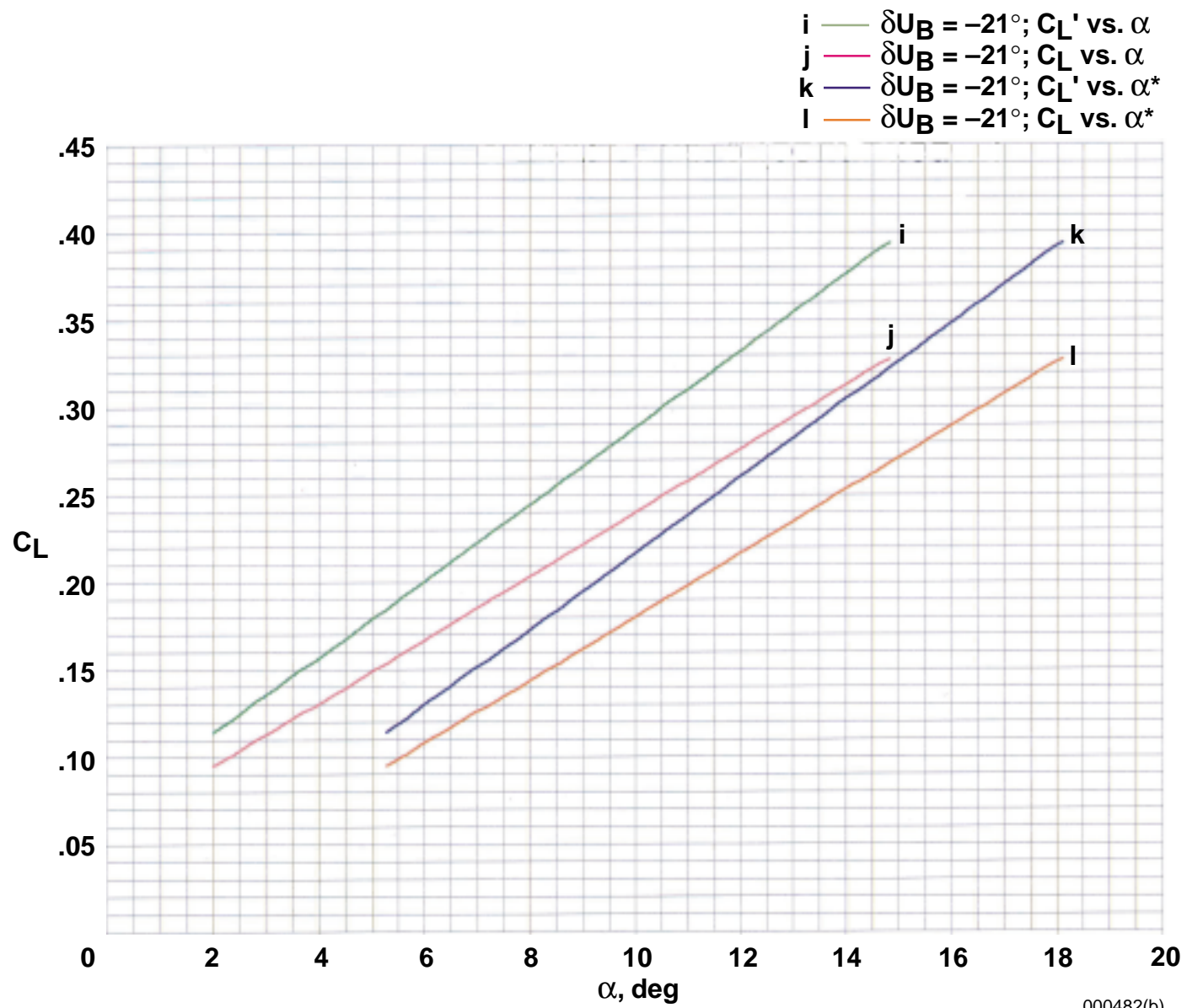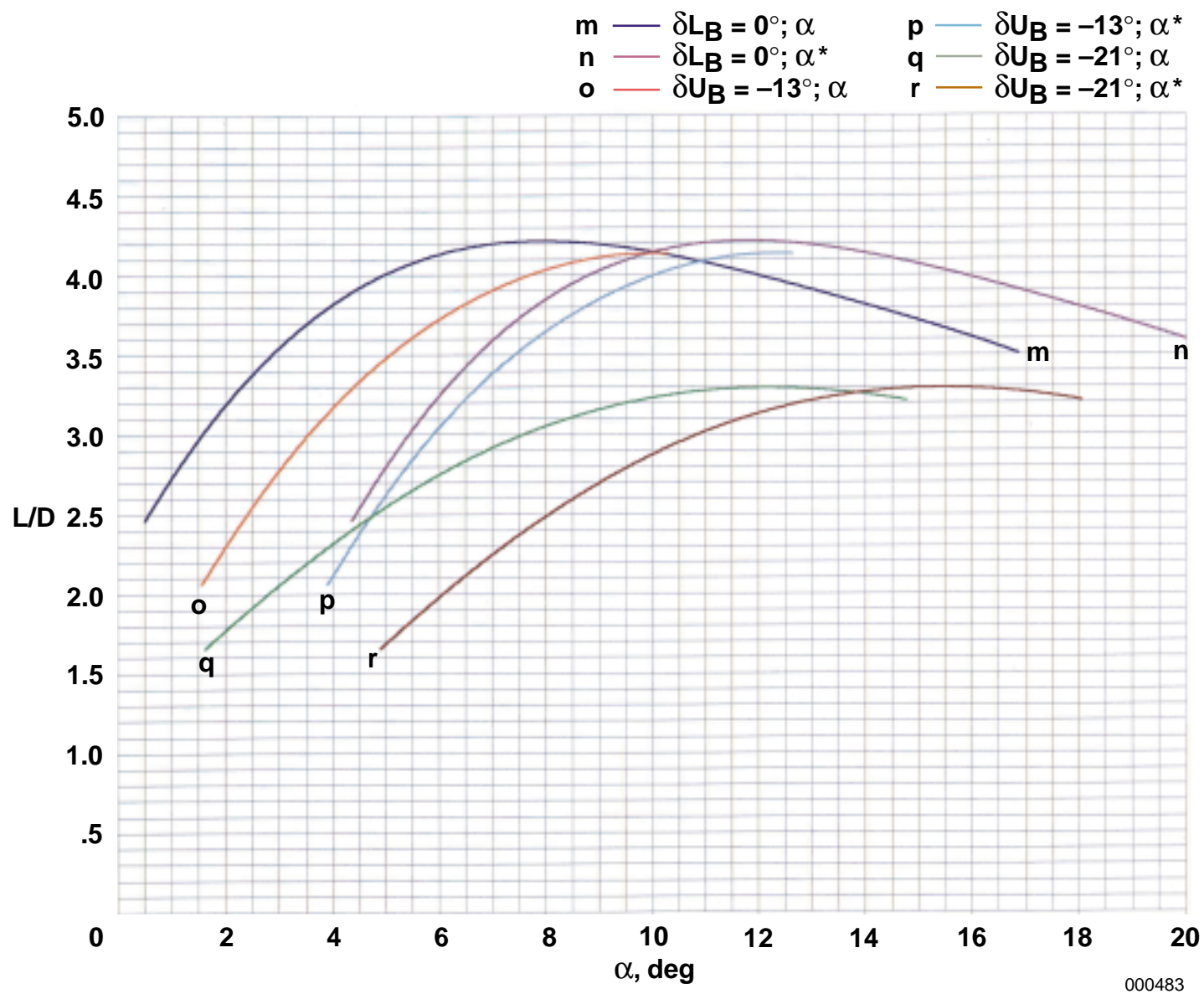Figure B-5. Continued.

(d) L/D as a function of C_L.

Figure B-5. Concluded.
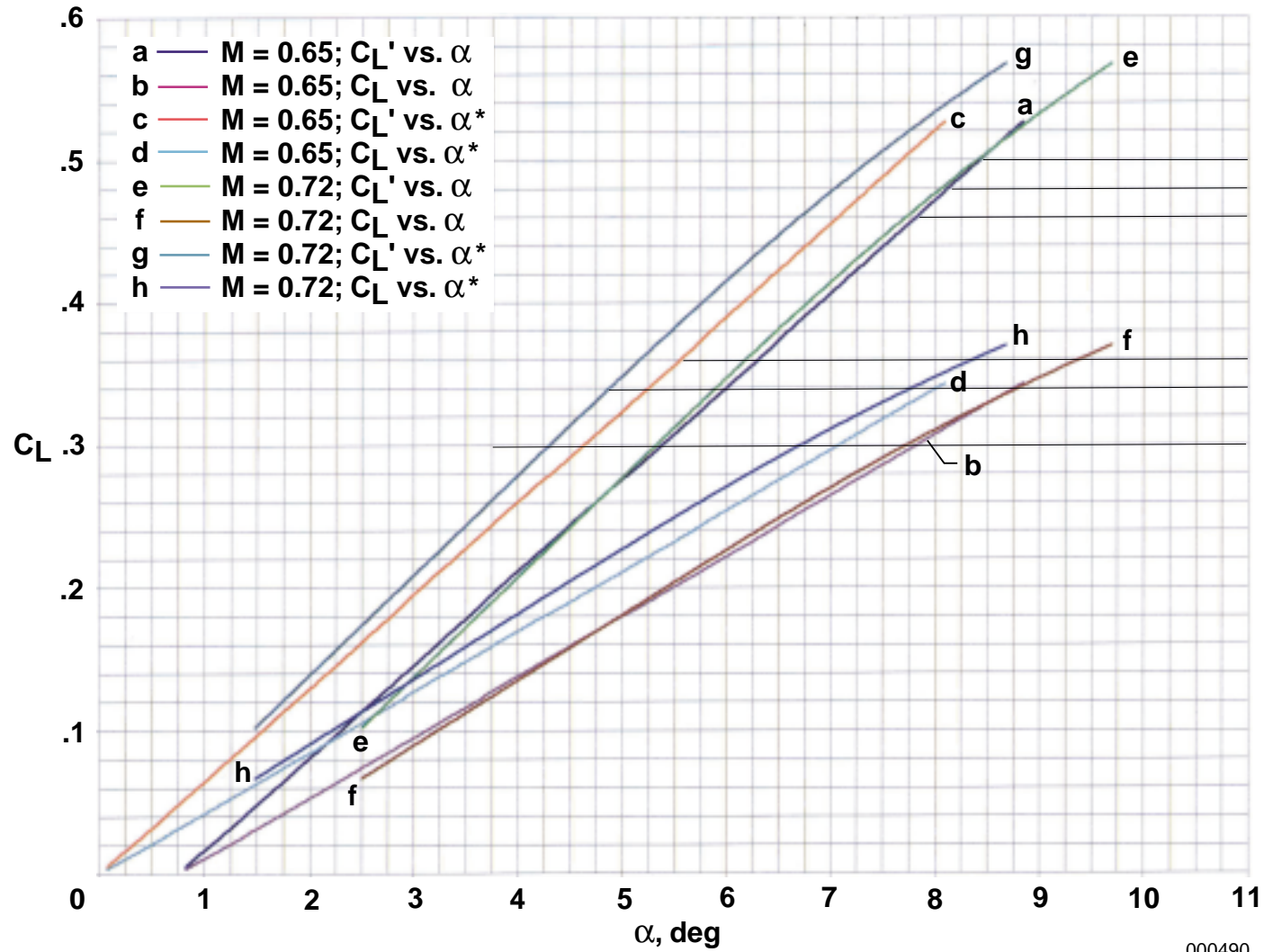
(a) C_L as a function of α.

Figure B-6. The relationship of basic performance components for the X-15 vehicle, derived from published reference as represented in appendix A, figure A-6.
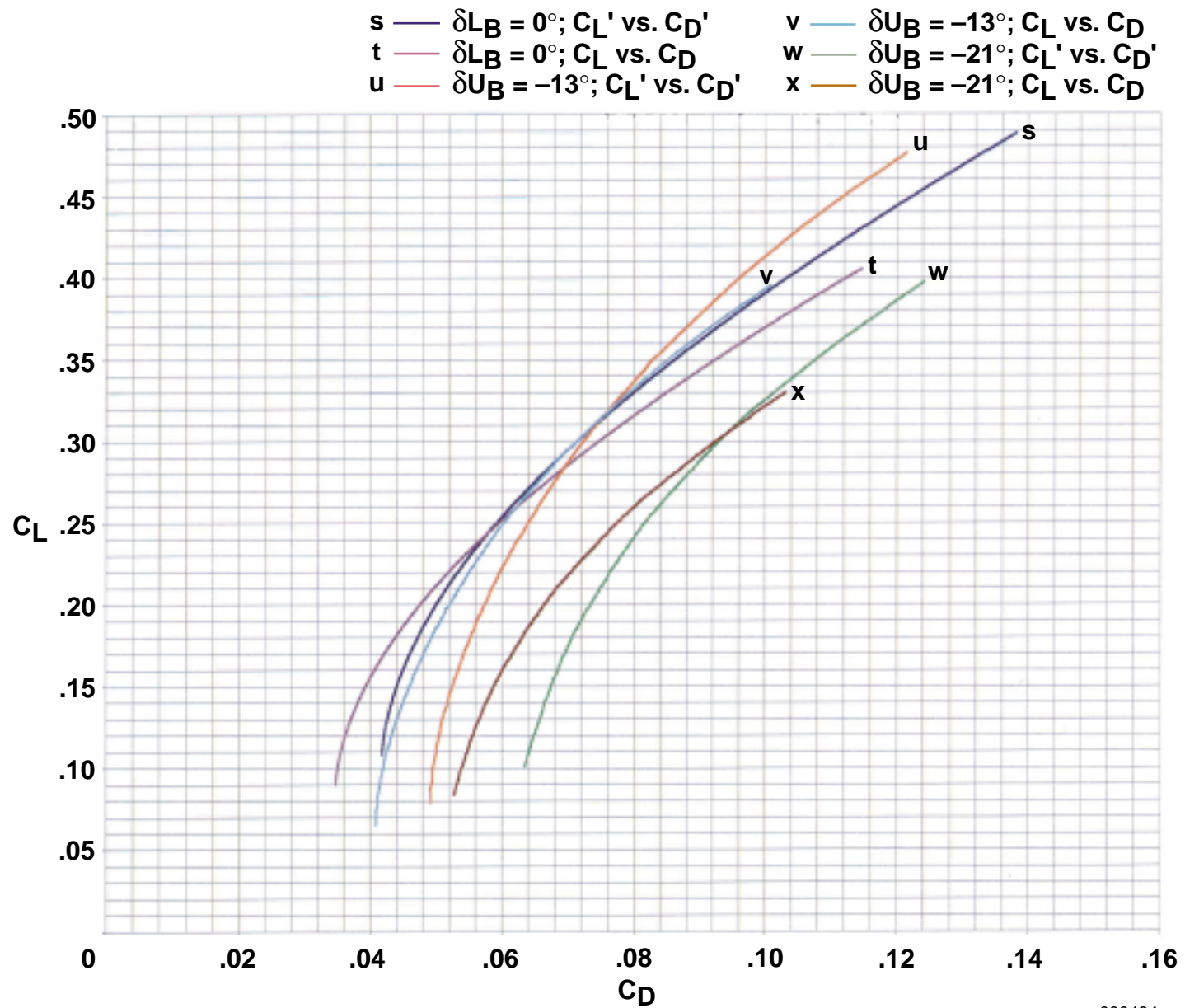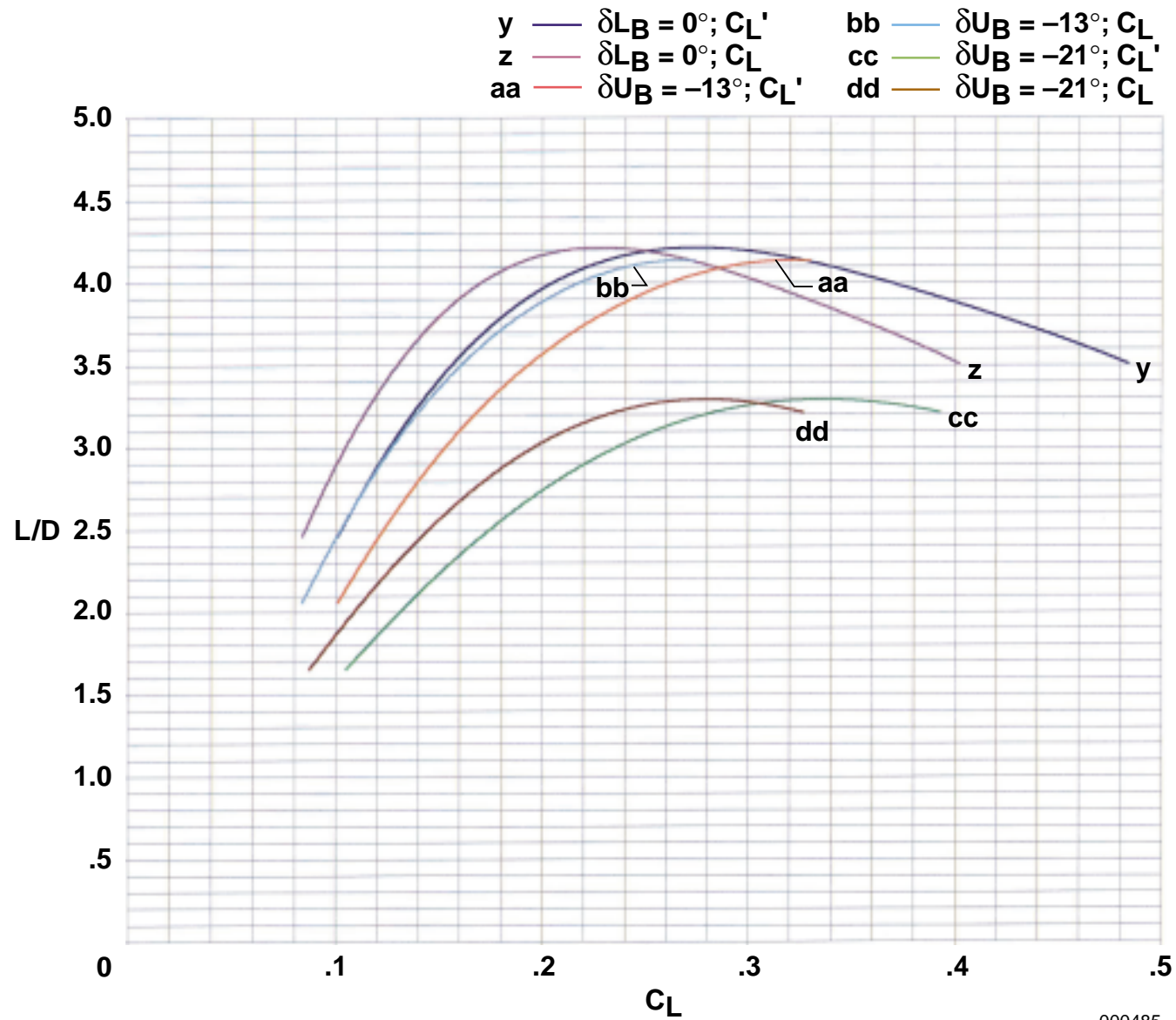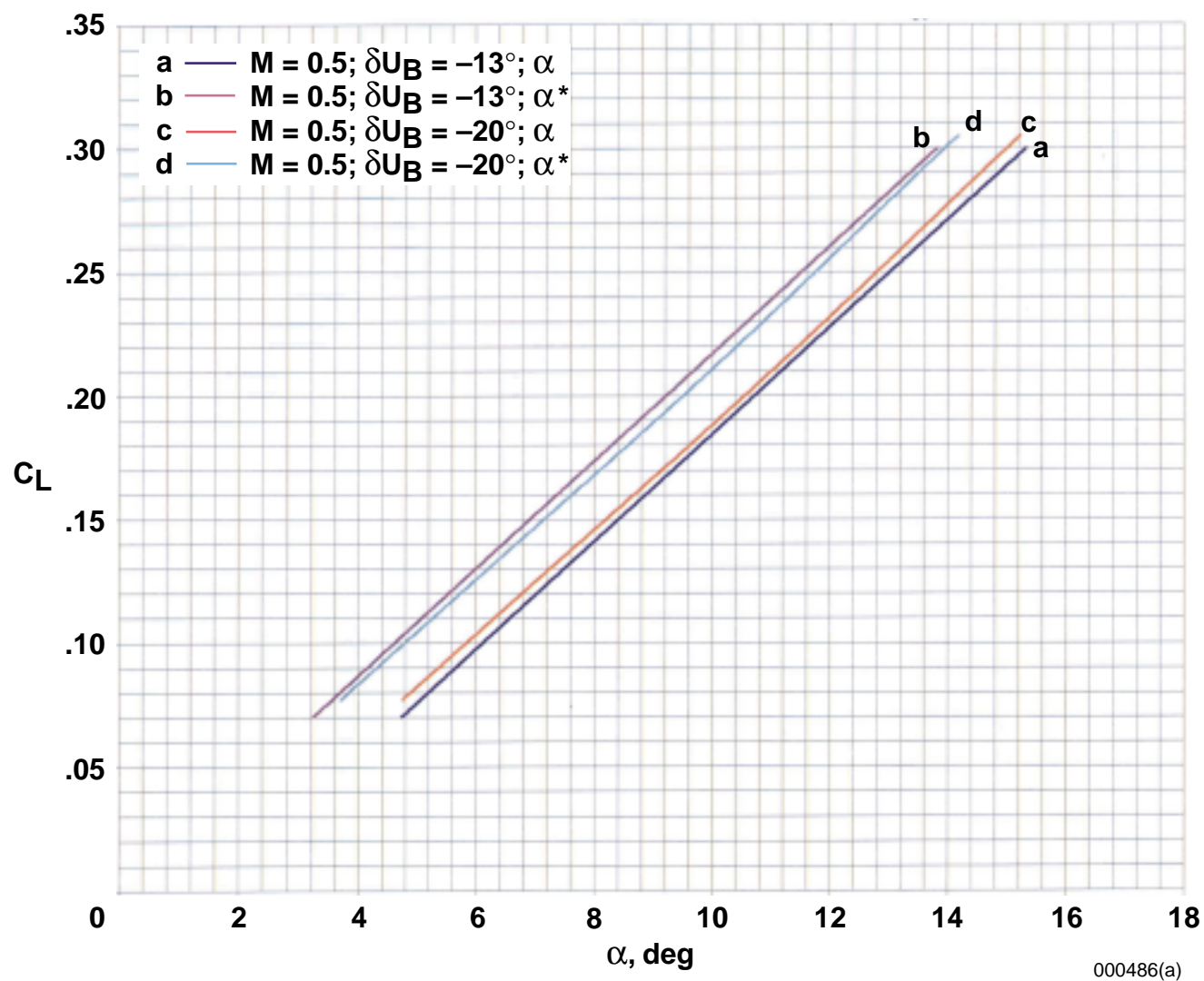
(b) L/D as a function of α.

Figure B-6. Continued.

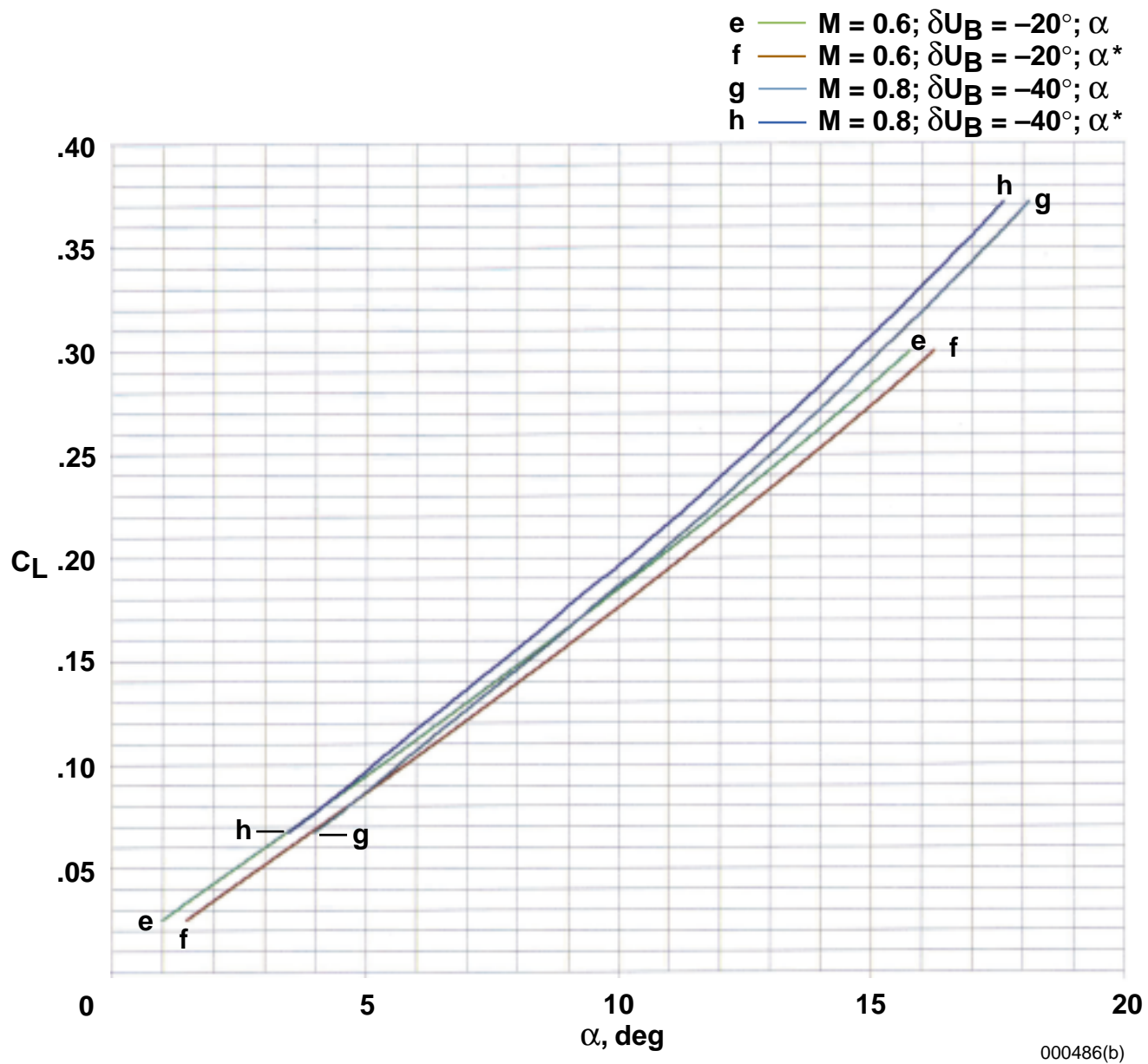(c) C_L as a function of C_D.

Figure B-6. Continued.

(d) L/D as a function of C_L.

Figure B-6. Concluded.
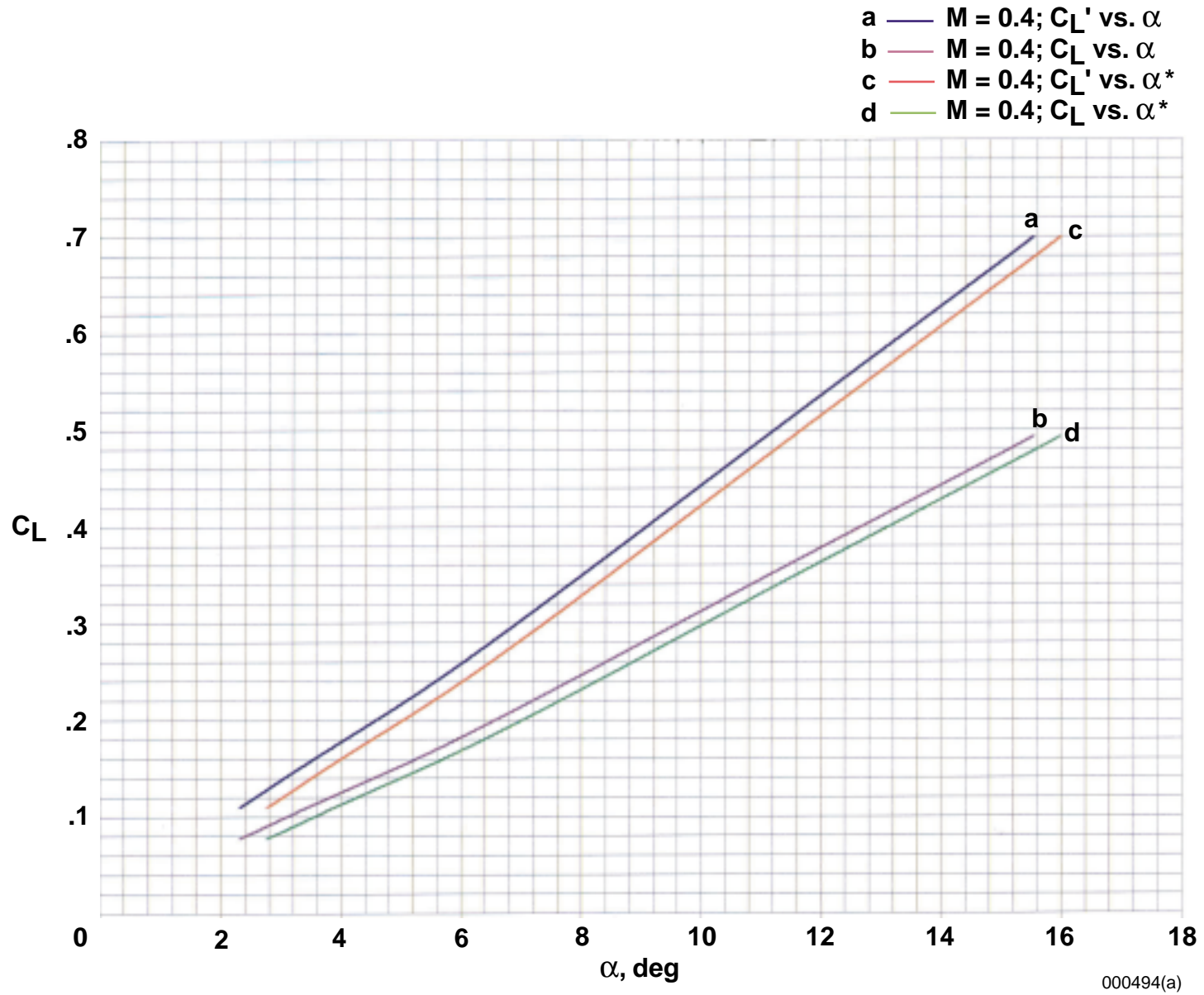
(a) C_L as a function of α.

Figure B-7. The relationship of basic performance components for the *Enterprise* vehicle, derived from published reference as represented in appendix A, figure A-7.

Legend:
- e — M = 0.5; C_L' vs. α
- f — M = 0.5; C_L vs. α
- g — M = 0.5; C_L' vs. $\alpha*$
- h — M = 0.5; C_L vs. $\alpha*$

Y-axis: C_L

X-axis: α, deg

000494(b)

(a). Concluded.

Figure B-7. Continued.
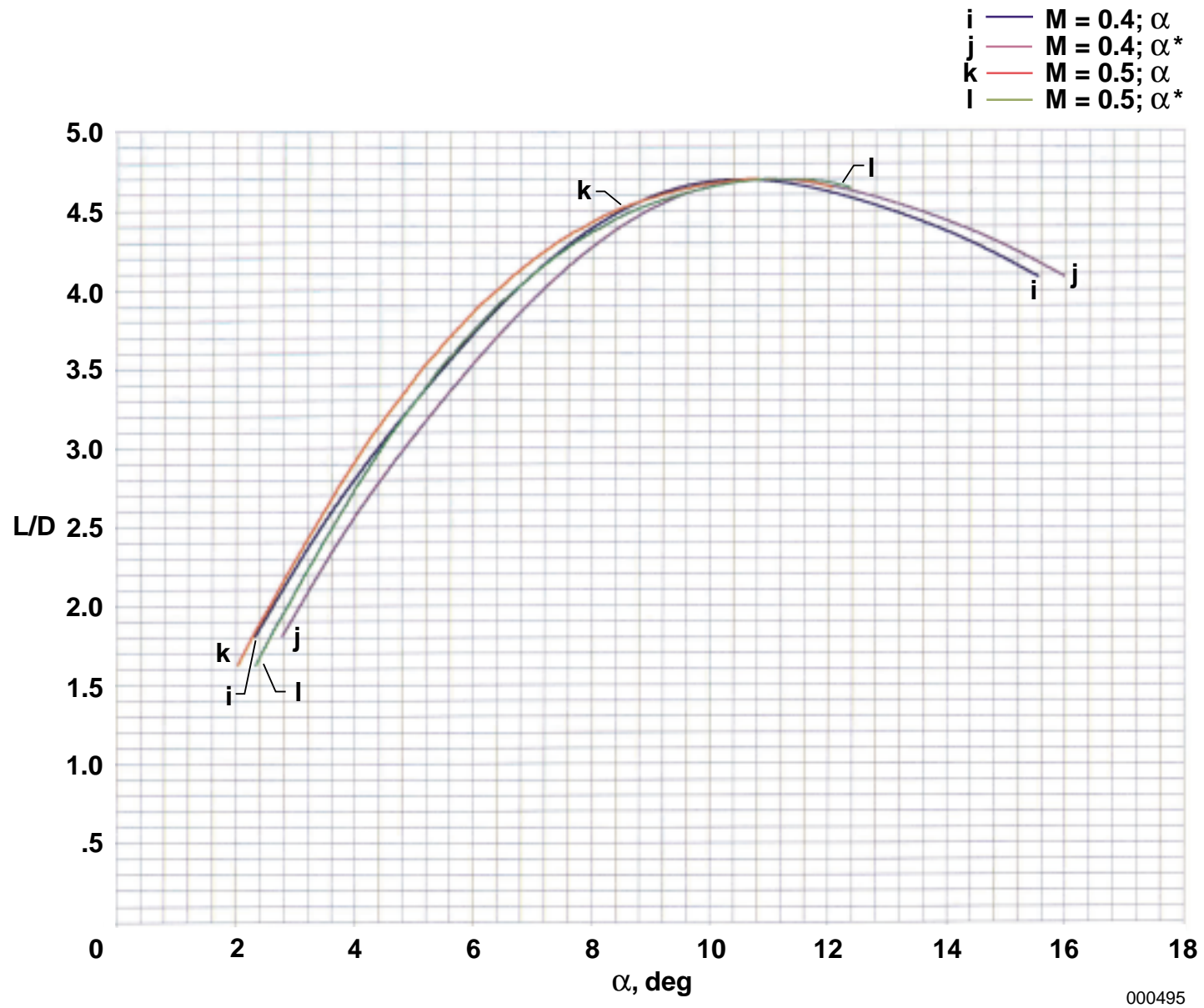
(b) L/D as a function of α.

Figure B-7. Continued.

(c) C_L as a function of C_D.

Figure B-7. Continued.
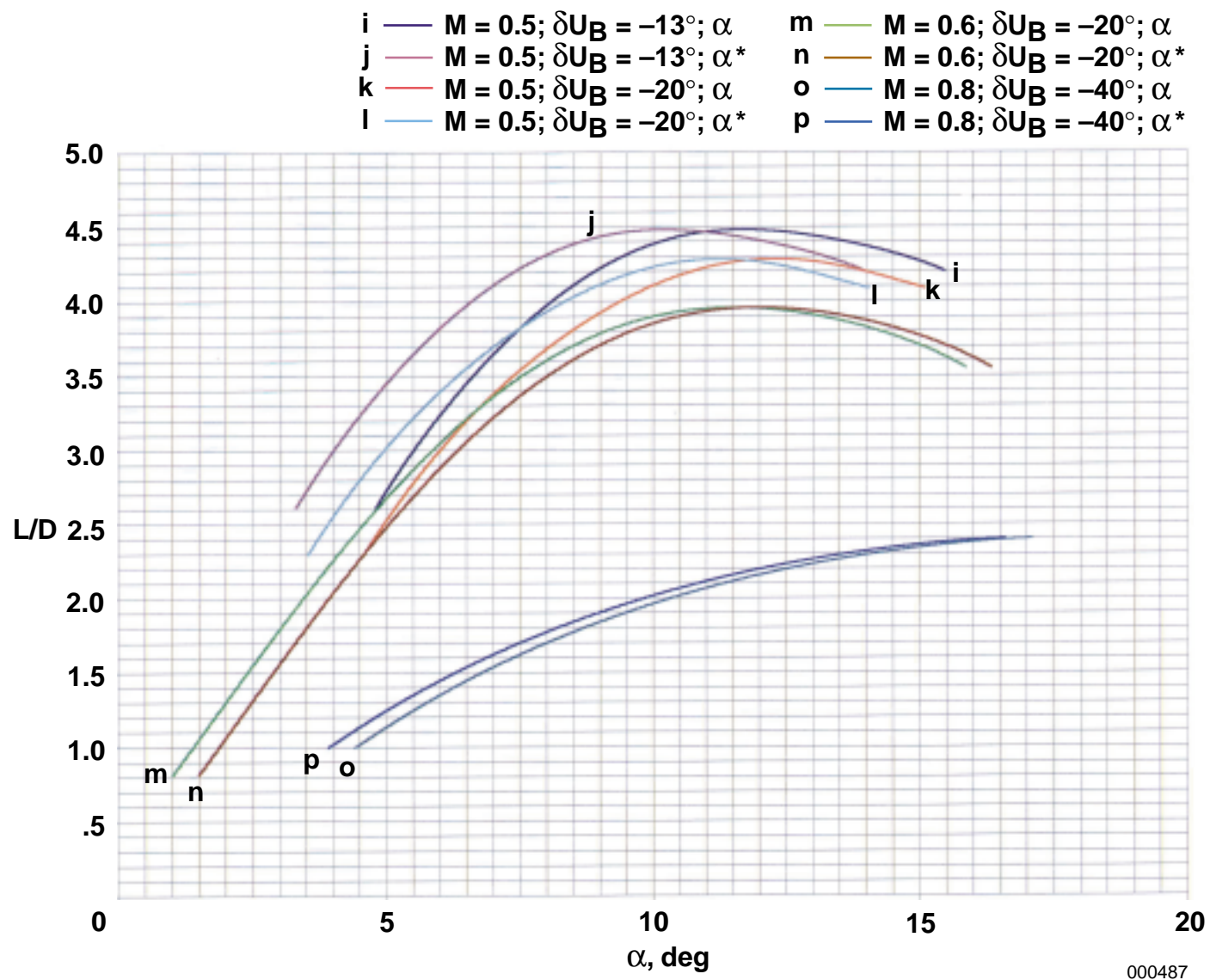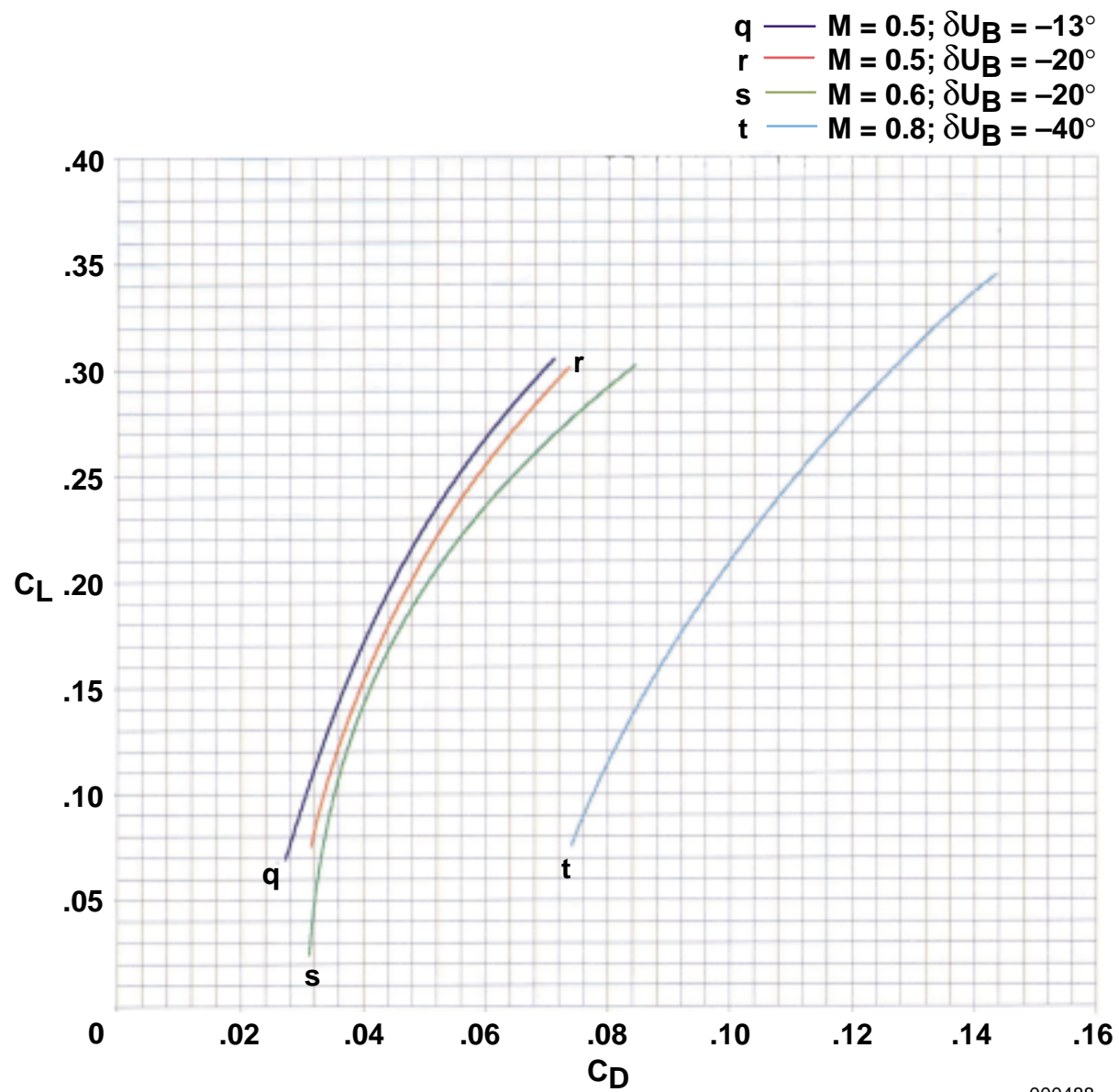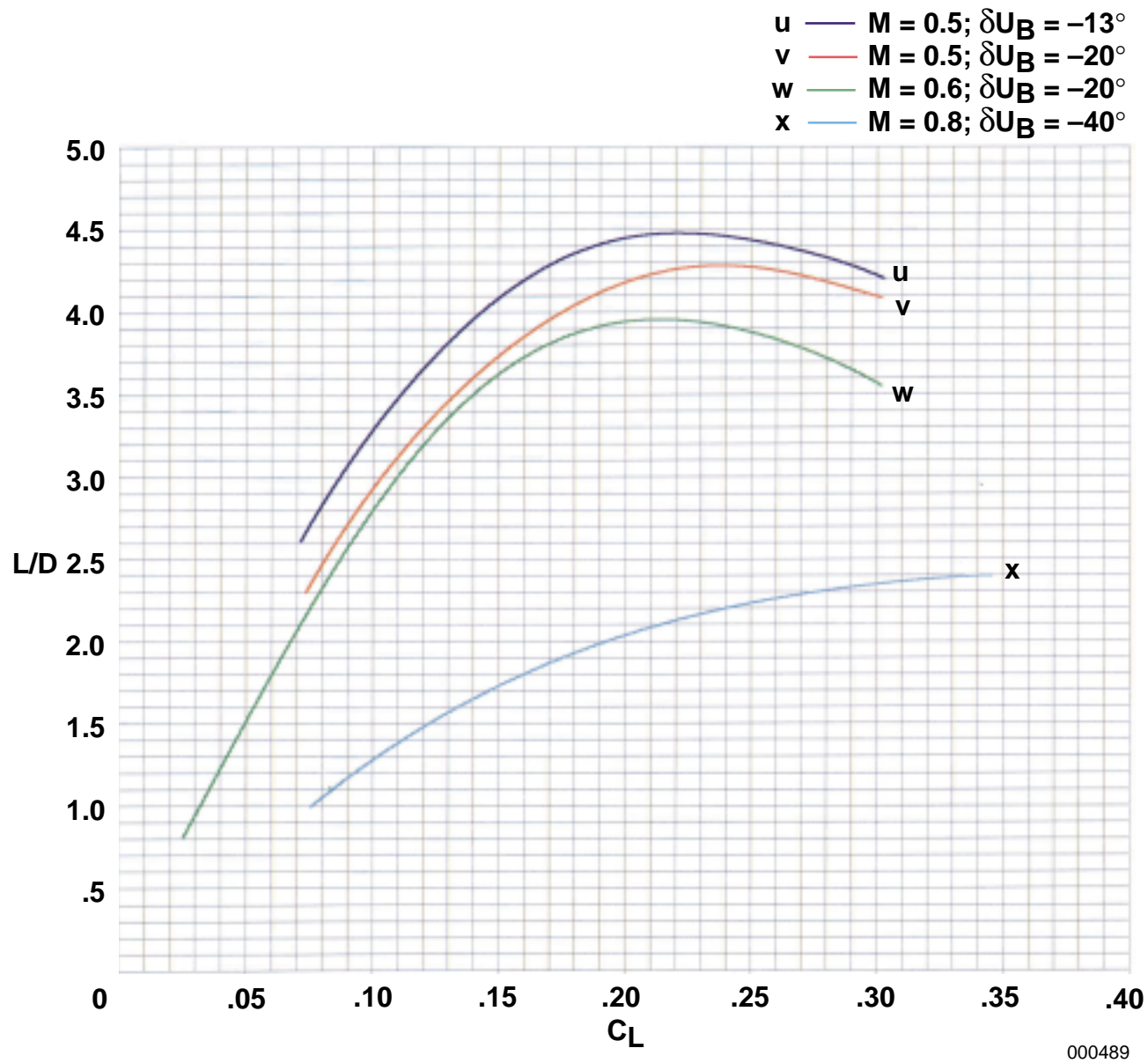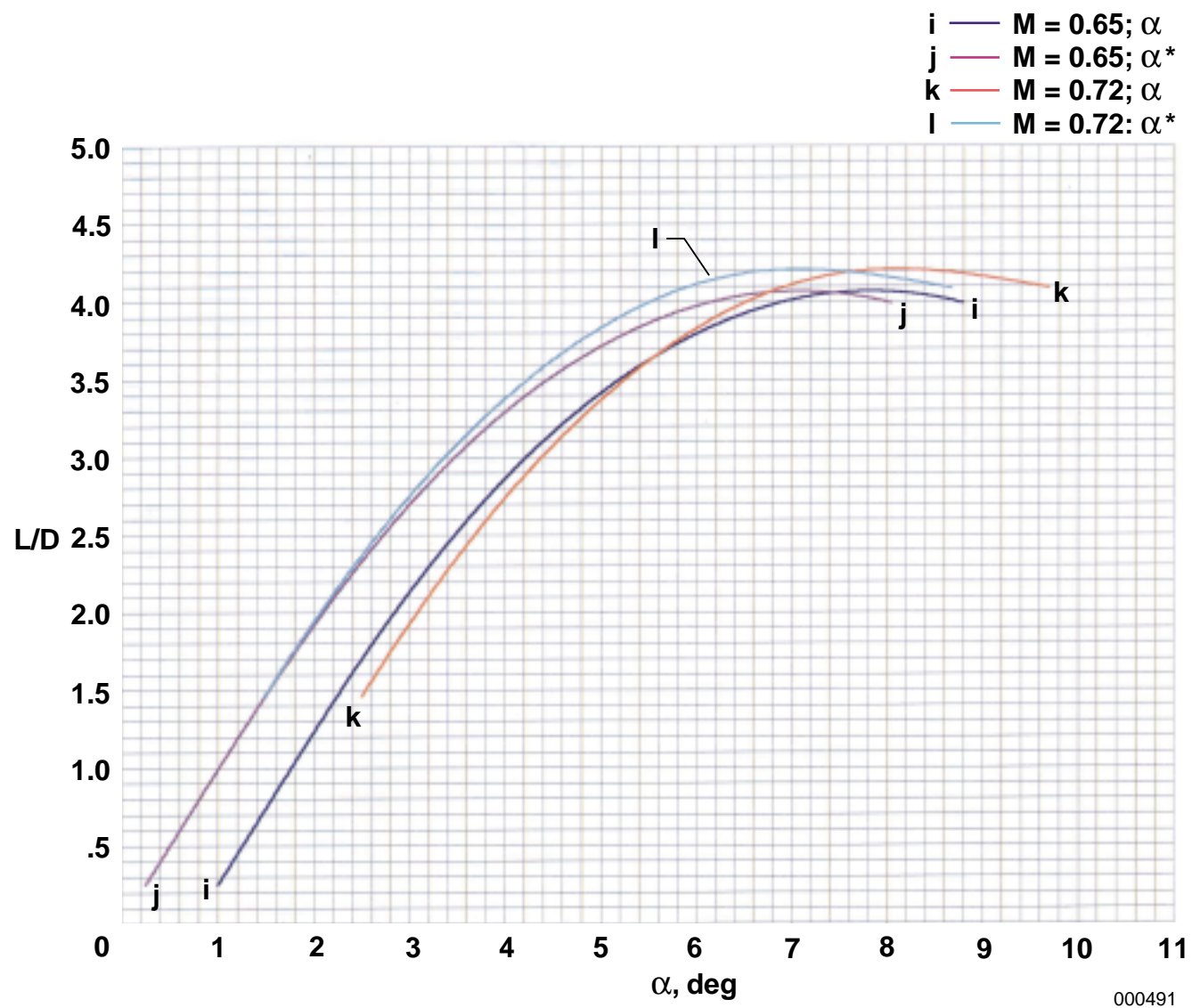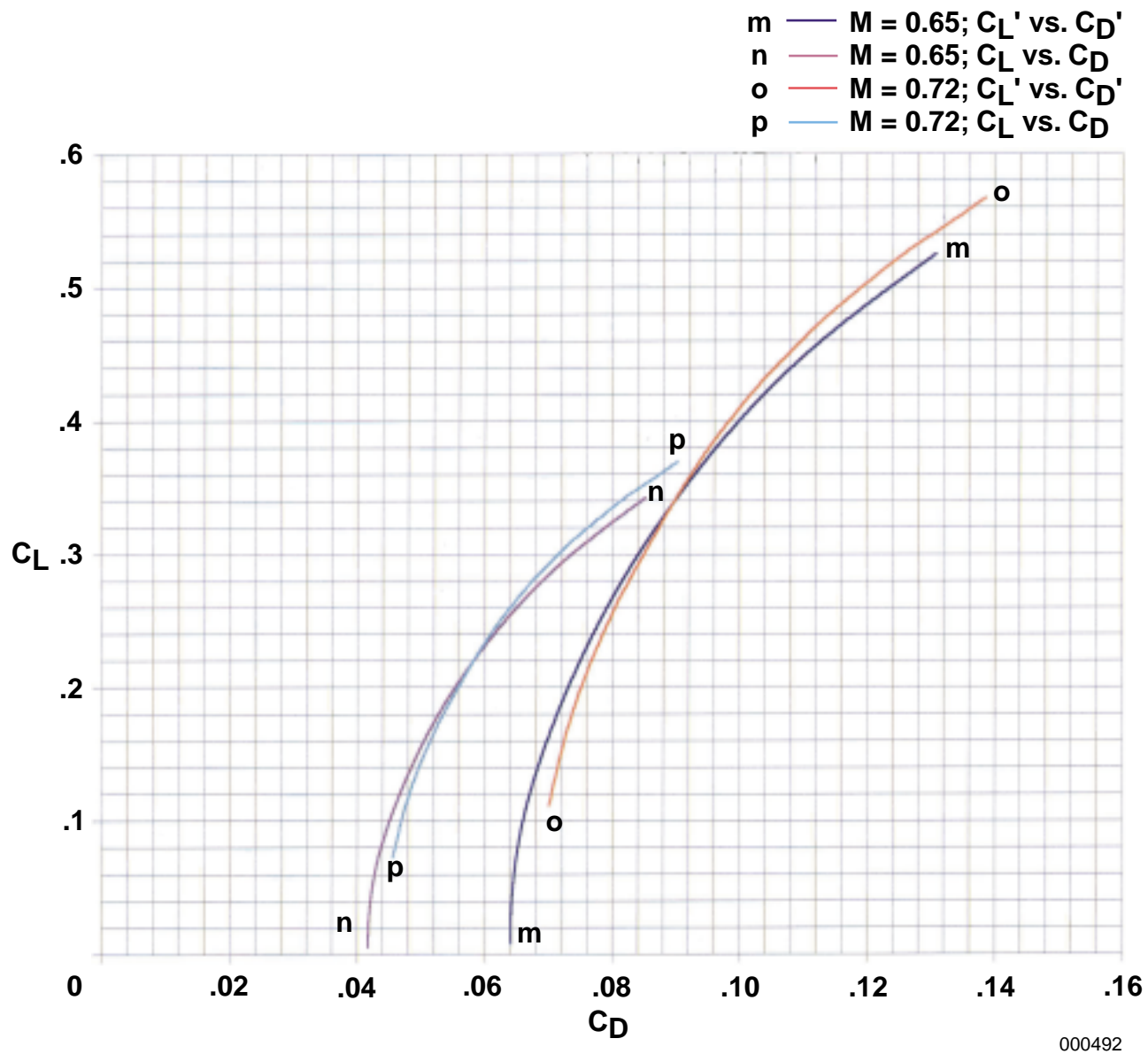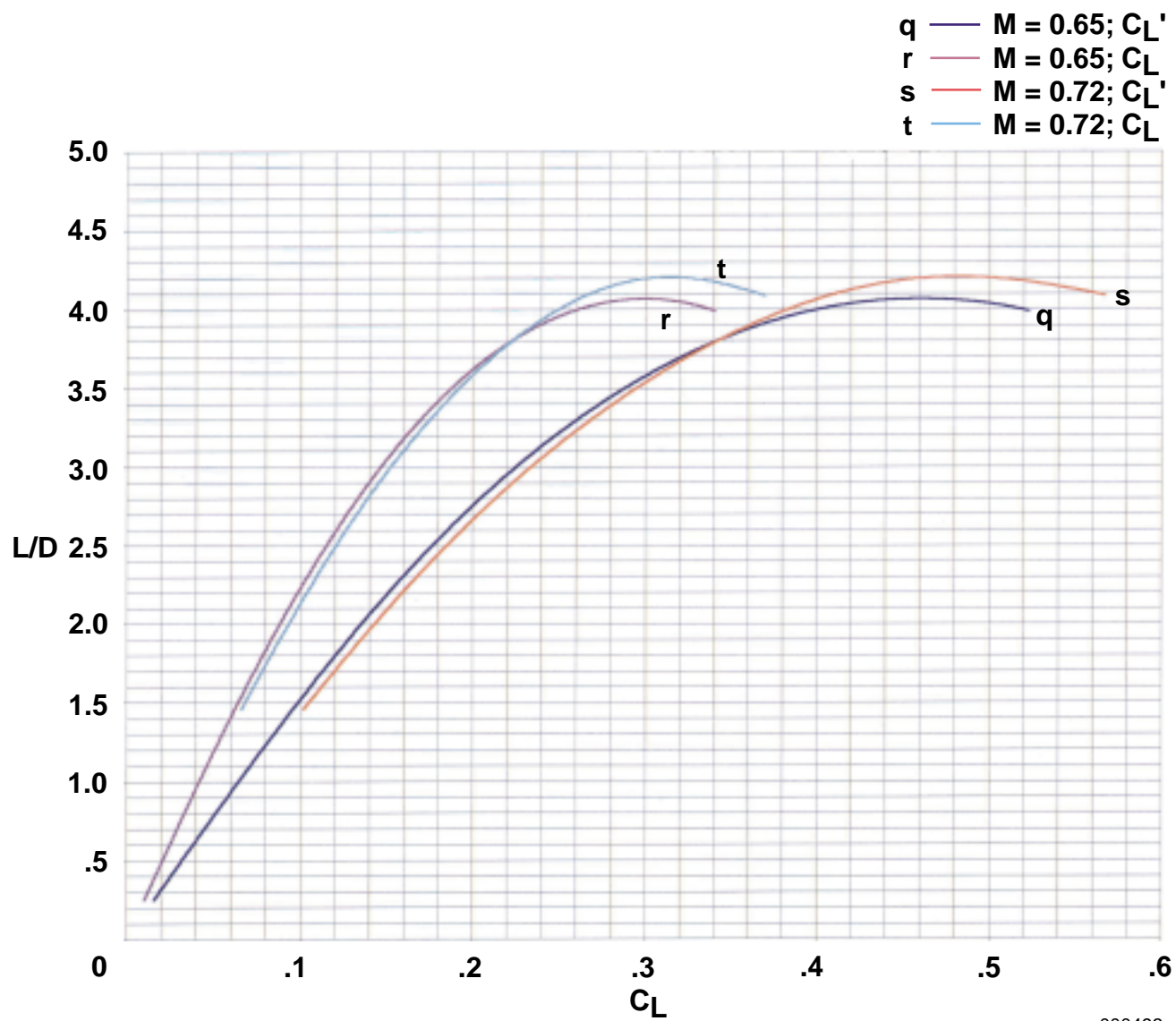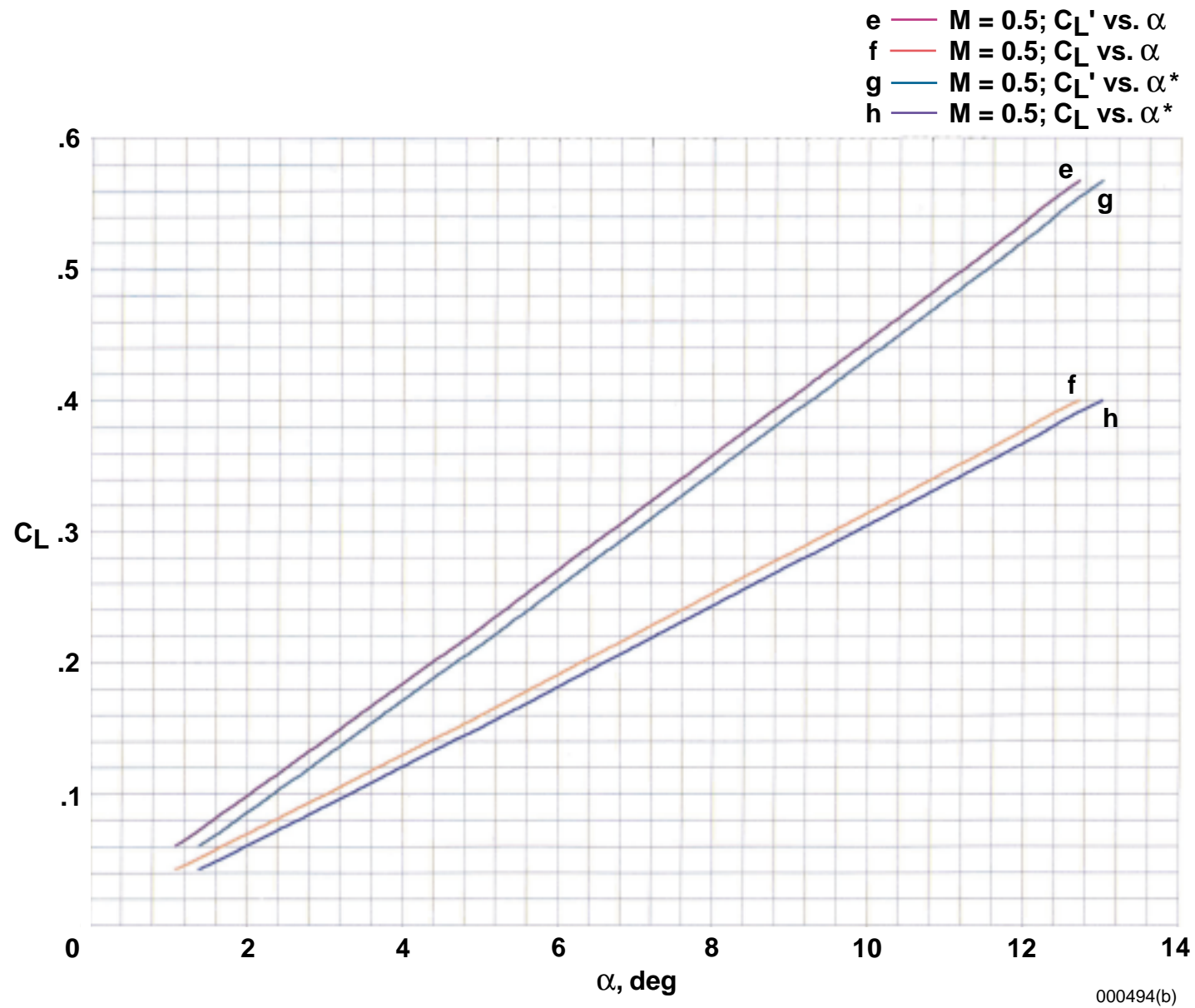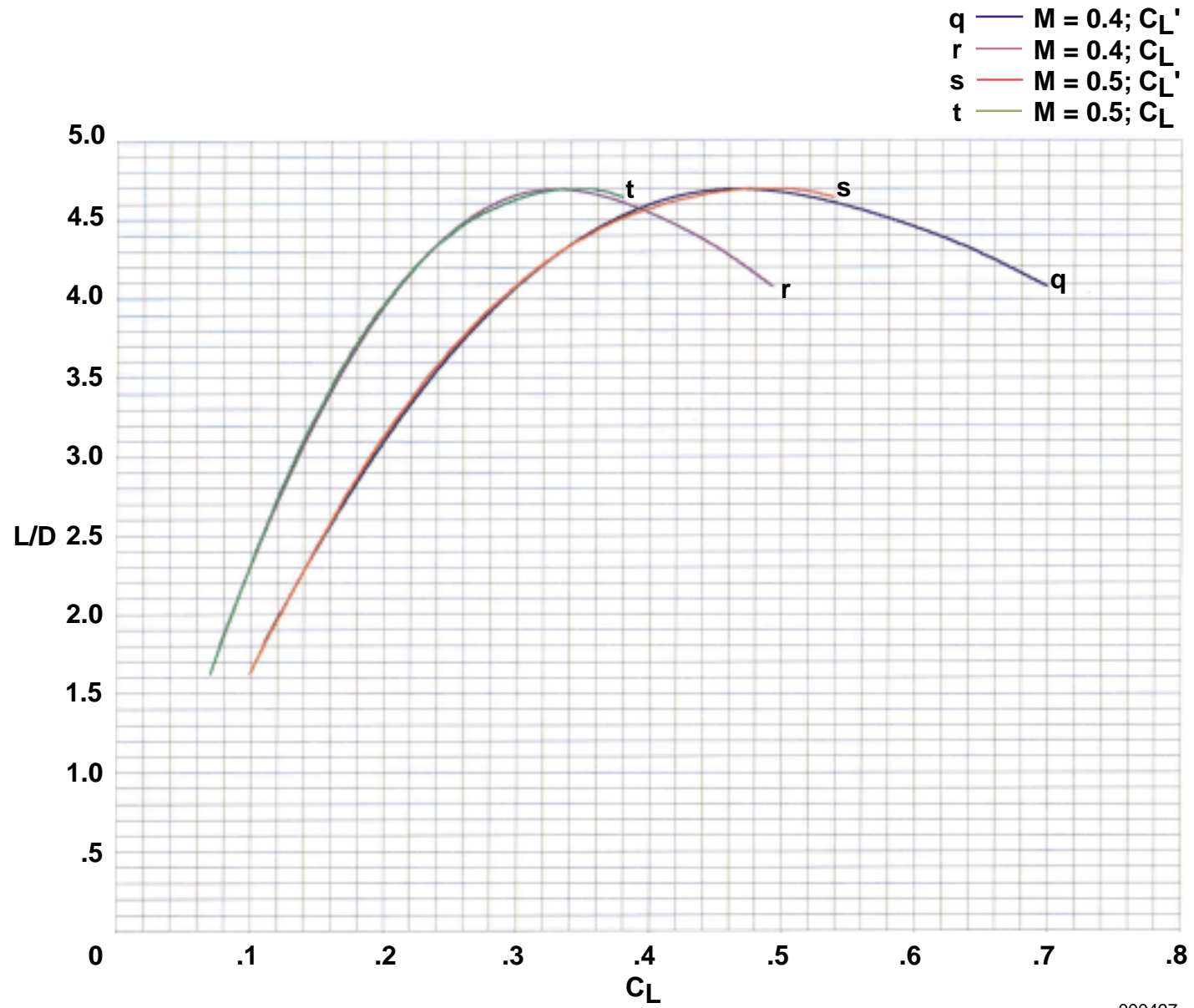
(d) L/D as a function of C_L.

Figure B-7. Concluded.

APPENDIX C

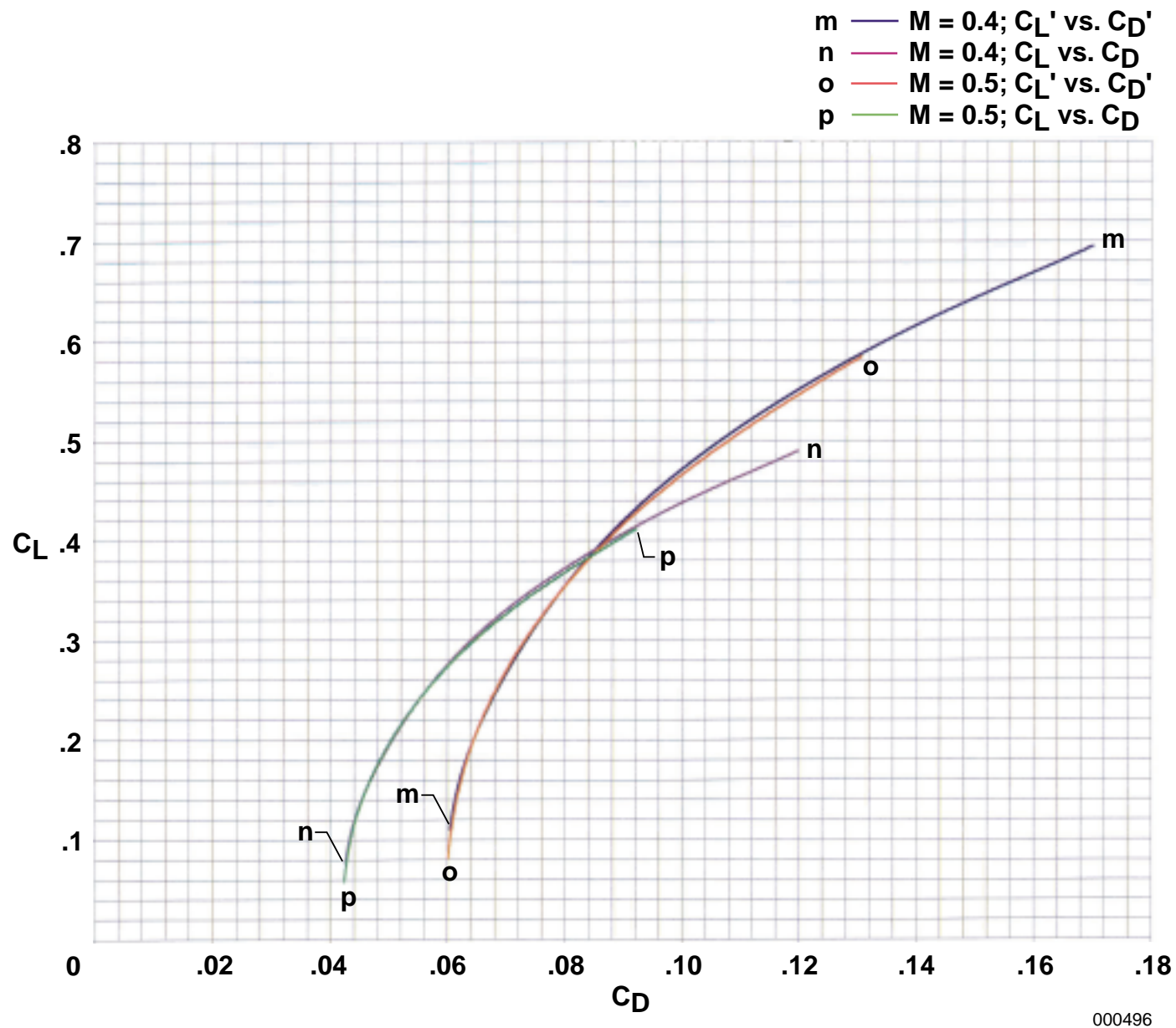# PARTIAL SUMMARY OF SOURCE DATA

As appendix B explains, the basic performance components as derived from the various reference sources have been replotted for each vehicle using a common format. Appendix B presents these replotted performance components; each plot contains results from only one of the seven subject vehicles. This appendix presents selected relationships from appendix B so that all seven vehicles may be compared in the same plot (that is, each plot will summarize the results for the several vehicles for a specific metric relationship). The product of this procedure is related to, but not the same as, the summary figures in the main text of this report (figs. 2 and 4–10). The appendix C presentations are limited to one flight condition for each vehicle to reduce confusion from additional overlapping curves. The choice of the specific flight condition for each vehicle for these comparisons was dependent on the reasoning shown in table C-1.

Table C-1. Reasons for flight conditions chosen.

Vehicle	Reason for choice of maneuver
M2-F1	Only one flight condition existed (gear drag included).
M2-F2	Flight condition providing highest lift-to-drag ratio was chosen.
HL-10	Flight condition providing highest lift-to-drag ratio was chosen.
X-24A	Upper flap bias deflection that was in common with X-24B vehicle maneuver was chosen.
X-24B	Upper flap bias deflection that was in common with X-24A vehicle maneuver was chosen.
X-15	Lower Mach number was chosen to reduce compressibility effects.
Enterprise	Condition having most complete "root-source" polar was chosen.

Table C-2 shows an index of the summary presentations. These summary figures have a dual purpose. First, for the raw, or unadjusted, components of the lift and drag coefficients, C_L and C_D, and angle of attack, α, considerable disorder exists for the array of data of the seven vehicles plotted together. Conversely, when more representative reference areas are applied and angle of attack is referenced from the zero-lift condition, the familial relationship of these vehicles (which are generically related by function) is more apparent. This tendency also may be seen in the various summary presentations in the main body of this report for other combinations of performance metrics and geometric features.

Table C-2. Summary figure index.

Metrics	Figure
C_L', α	C-1(a)
C_L, α	C-1(b)
C_L', α^*	C-1(c)
C_L, α^*	C-1(d)
C_D', α	C-2(a)
C_D, α	C-2(b)
C_D', α^*	C-2(c)
C_D, α^*	C-2(d)
C_L', C_D'	C-3(a)
C_L, C_D	C-3(b)
L/D, C_L'	C-4(a)
L/D, C_L	C-4(b)
L/D, α	C-5(a)
L/D, α^*	C-5(b)
C_L for maximum L/D, $C_{D_{min}}$	C-6
C_L for maximum L/D, A_b/S	C-6
α^* for maximum L/D, A_b/S	C-7

More specific commentary about some of the summary figures may be helpful. For example, the various curves in figure C-1(a) have a quite random pattern that suggests no apparent generic relationship. A more representative reference area, as defined in the "Lift-Curve Slope" subsection of the "Results and Discussion" section, is used to define the lift coefficient in figure C-1(b), which results in minimal apparent improvement. However, use of this more representative reference area is known to provide a more authentic presentation. Figure C-1(c) uses an α increment that is referenced to the zero-lift condition, which results in a presentation pattern that now features a fan shape oriented at the lower end toward the zero-zero coordinate. Figure C-1(d) uses this more representative reference area for C_L and the α increment above that for $C_L = 0$. This presentation is the most orderly and also the most authentic.

A close examination of figure C-1(d) may lead some readers to question why the lift-curve slope of the M2-F2 configuration with landing gear retracted should be slightly lower than that of the M2-F1 configuration with landing gear exposed. Although obvious control-surface differences may be a factor, note that the not-so-clean features of the M2-F1 vehicle may contribute positively to its lift-curve slope. Hoerner, in chapter 19 of reference 30, provides multiple data sources that show an increased crossflow lift component when crossflow drag is increased. The exposed M2-F1 landing gears (including openings in the fuselage to allow main gear flexing) certainly cause additional drag, which includes a crossflow

component. Note that, as stated in the main text discussions of figures 2 and 5, the outboard elevons do not appear to contribute to M2-F1 vehicle lift.

Figures C-2(a)–(d) provide successively improved evidence of familial relationships in a manner related to the successive improvements noted in the presentations of C_L with α. Note that although the low-angle-of-attack drag coefficients of the *Enterprise*, X-24A, and X-15 vehicles are nearly the same—when the more representative reference areas are used (figs. C-2(b) and C-2(d))—and the X-24B drag coefficient is even lower, conclusions based on relatively small differences in drag coefficient can be misleading. For example, note that for the flight conditions considered, $\delta U_B = -13°$, the corresponding parasite drag area values for the X-24A and X-24B vehicles show a lower value for the X-24A vehicle (table 3). Recall that parasite drag area, f, in ft^2 units is pounds of drag force for each lbf/ft^2 of dynamic pressure.

Figures C-4 and C-5 show summary relationships of the lift-to drag ratio, L/D, with a lifting parameter; lift coefficient; or α, respectively. A cursory examination of these presentations reveals that figure C-5(a) possesses great randomness, and the other three presentations are relatively unremarkable. A closer examination of figure C-5(b), where L/D is related to α^*, shows that for the lifting-body vehicles, the peak value of L/D for vehicles having the higher values (of those considered) successively occurs at the lower portion of the values of α^* range. This characteristic is worthy of further comment.

Figures C-4(b) and C-5(b) show that the values of C_L and α^* for which the peak L/D values occur are spread over a considerable range. However, these spread-out abscissa values for peak L/D can be shown to be orderly related to an important component of minimum drag.

The open symbols in figure C-6 show the C_L values for peak L/D as a function of $C_{D_{min}}$ for each vehicle. The tendency toward the C_L values for peak L/D to increase with the high $C_{D_{min}}$ values is inherent in the parabolic nature of lift-drag polars. Because the total drag coefficient at maximum L/D is twice the minimum drag coefficient for a true parabolic polar, an elevated minimum drag will cause the lift coefficient for maximum L/D to be elevated. This well-known relationship is expressed as follows (ref. 36, page 122):

$$C_L \text{ for } (L/D)_{max} = \sqrt{C_{D_{min}} \cdot \pi \cdot A \cdot \varepsilon}$$

The open symbols (fig. C-6) representing the lifting bodies show an orderly qualitative relationship; the two winged vehicles, the *Enterprise* and the X-15 vehicle, are set apart. A less orderly but related data pattern is apparent when the lift coefficient for peak L/D is considered as a function of base area, A_b, divided by the representative planform reference area, S (the solid symbols in figure C-6). Figure C-6 shows as a dashed line an approximation of the effect an increasing value of base area should have (thus increasing base drag) for a hypothetical vehicle based on the same equation from reference 36.

Figure C-7 shows the corresponding relationship of α^* required for peak L/D. The lifting-body data provide an orderly pattern; and the winged vehicles, not surprisingly, require lower angles of attack than do the lifting bodies to achieve maximum L/D. The higher angle of attack required by the *Enterprise*, as compared with the X-15 vehicle, is caused in part by its greater leading-edge sweep and consequent lower lift-curve slope (figs. 1(g)–(h) and table 2).

a — M2-F1
b — M2-F2 (M = 0.62, δ_{uf} = −11.5°)
c — HL-10 (Configuration B; M = 0.60, δ_{ef} = 0°)
d — X-24A (M = 0.50, δU_B = −13°)
e — X-24B (M = 0.50, δU_B = −13°)
f — X-15 (M = 0.65)
g — Enterprise (M = 0.40)

000498
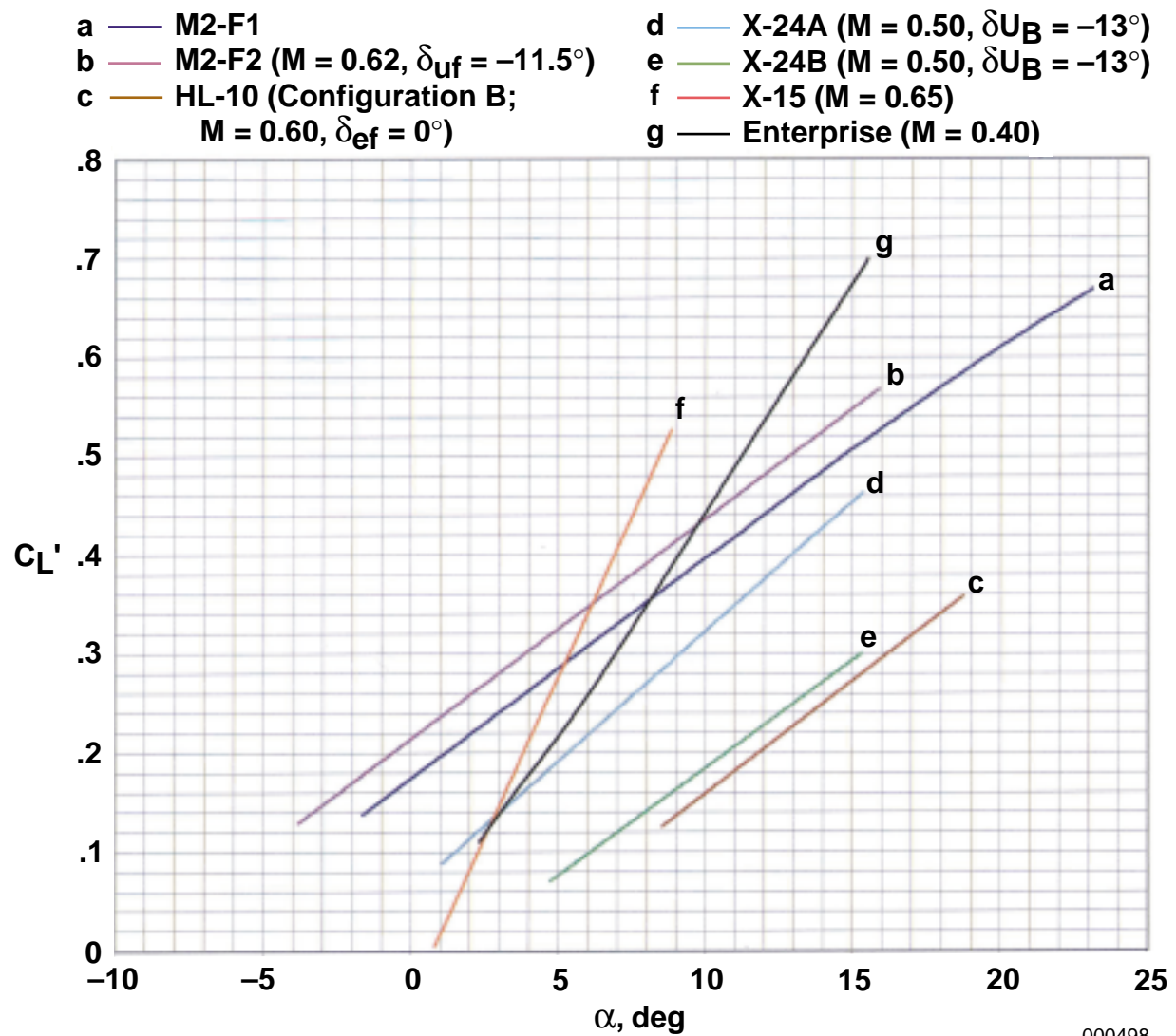
(a) C_L' as a function of α.

Figure C-1. The relationship of lift coefficient with angle of attack for the seven subject vehicles.
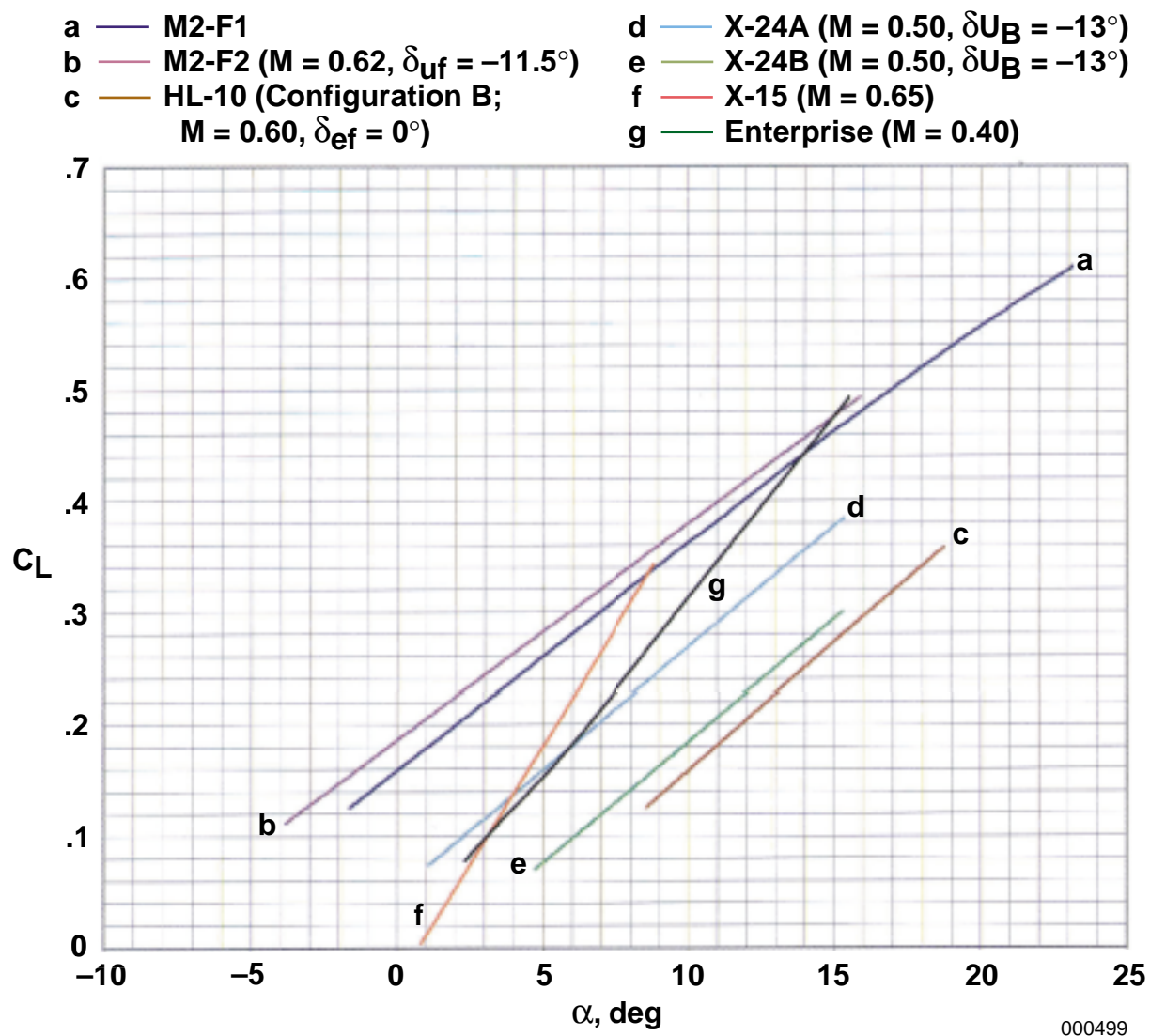
a — M2-F1
b — M2-F2 (M = 0.62, δ_{uf} = −11.5°)
c — HL-10 (Configuration B; M = 0.60, δ_{ef} = 0°)
d — X-24A (M = 0.50, δU_B = −13°)
e — X-24B (M = 0.50, δU_B = −13°)
f — X-15 (M = 0.65)
g — Enterprise (M = 0.40)

000499

(b) C_L as a function of α.

Figure C-1. Continued.

a —— **M2-F1**
b —— **M2-F2 (M = 0.62, δ_{uf} = −11.5°)**
c —— **HL-10 (Configuration B;**
         M = 0.60, δ_{ef} = 0°)
d —— **X-24A (M = 0.50, δU_B = −13°)**
e —— **X-24B (M = 0.50, δU_B = −13°)**
f —— **X-15 (M = 0.65)**
g —— **Enterprise (M = 0.40)**

(c) $C_L{}'$ as a function of α^*.

Figure C-1. Continued.

000500

116

(d) C_L as a function of α^*.

Figure C-1. Concluded.

117

a —— M2-F1
b —— M2-F2 (M = 0.62, δ_{uf} = −11.5°)
c —— HL-10 (Configuration B; M = 0.60, δ_{ef} = 0°)
d —— X-24A (M = 0.50, δ_{U_B} = −13°)
e —— X-24B (M = 0.50, δ_{U_B} = −13°)
f —— X-15 (M = 0.65)
g —— Enterprise (M = 0.40)

000502

(a) C_D' as a function of α.

Figure C-2. The relationship of drag coefficient with angle of attack for the seven subject vehicles.

a —— M2-F1
b —— M2-F2 (M = 0.62, δ_{uf} = −11.5°)
c —— HL-10 (Configuration B;
 M = 0.60, δ_{ef} = 0°)
d —— X-24A (M = 0.50, δU_B = −13°)
e —— X-24B (M = 0.50, δU_B = −13°)
f —— X-15 (M = 0.65)
g —— Enterprise (M = 0.40)

000503

(b) C_D as a function of α.

Figure C-2. Continued.

119

a ── M2-F1
b ── M2-F2 (M = 0.62, δ_{uf} = −11.5°)
c ── HL-10 (Configuration B; M = 0.60, δ_{ef} = 0°)
d ── X-24A (M = 0.50, δU_B = −13°)
e ── X-24B (M = 0.50, δU_B = −13°)
f ── X-15 (M = 0.65)
g ── Enterprise (M = 0.40)

Note: d and c coincide over most of α range
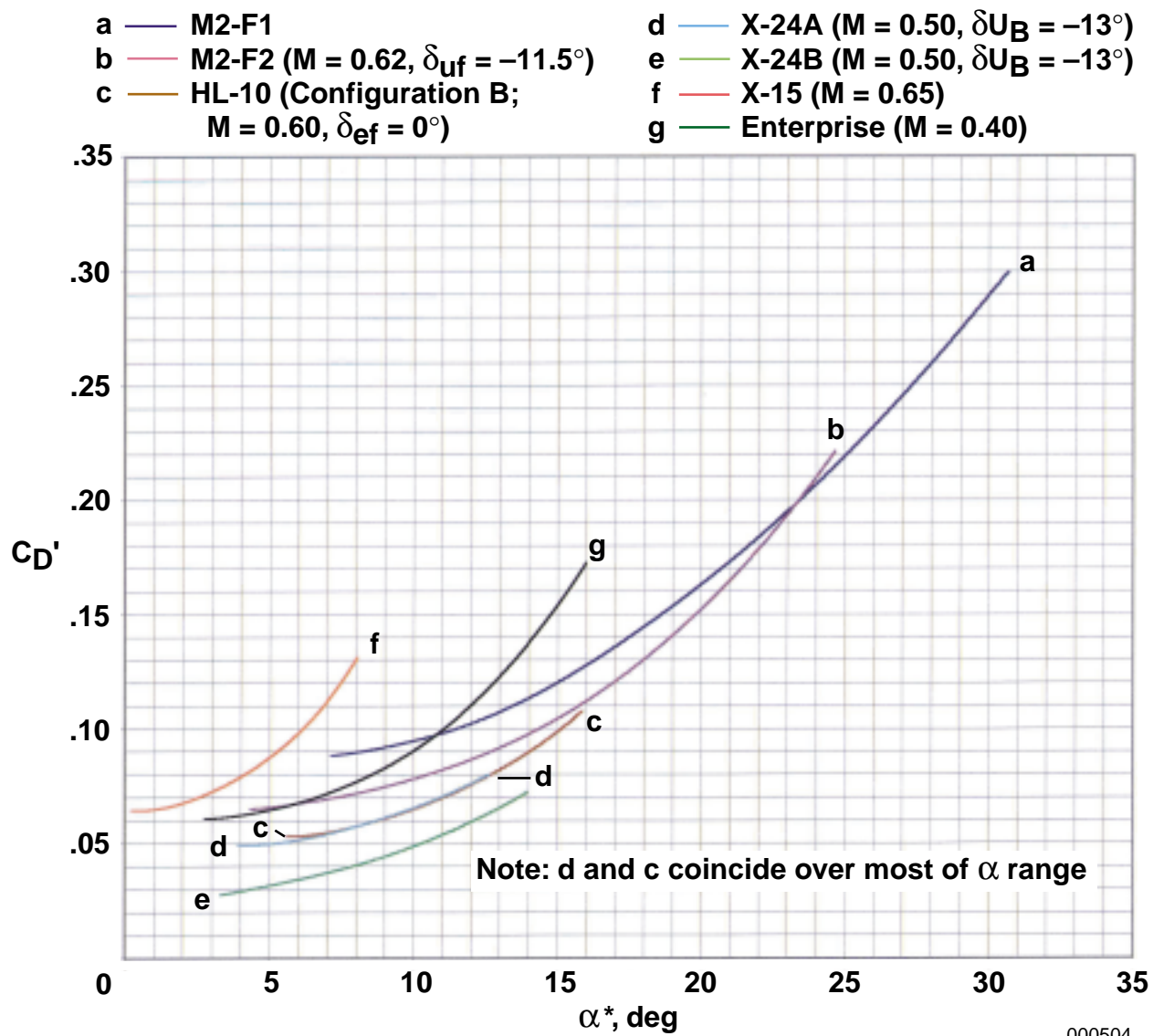
(c) $C_D{}'$ as a function of α^*.

Figure C-2. Continued.

000504
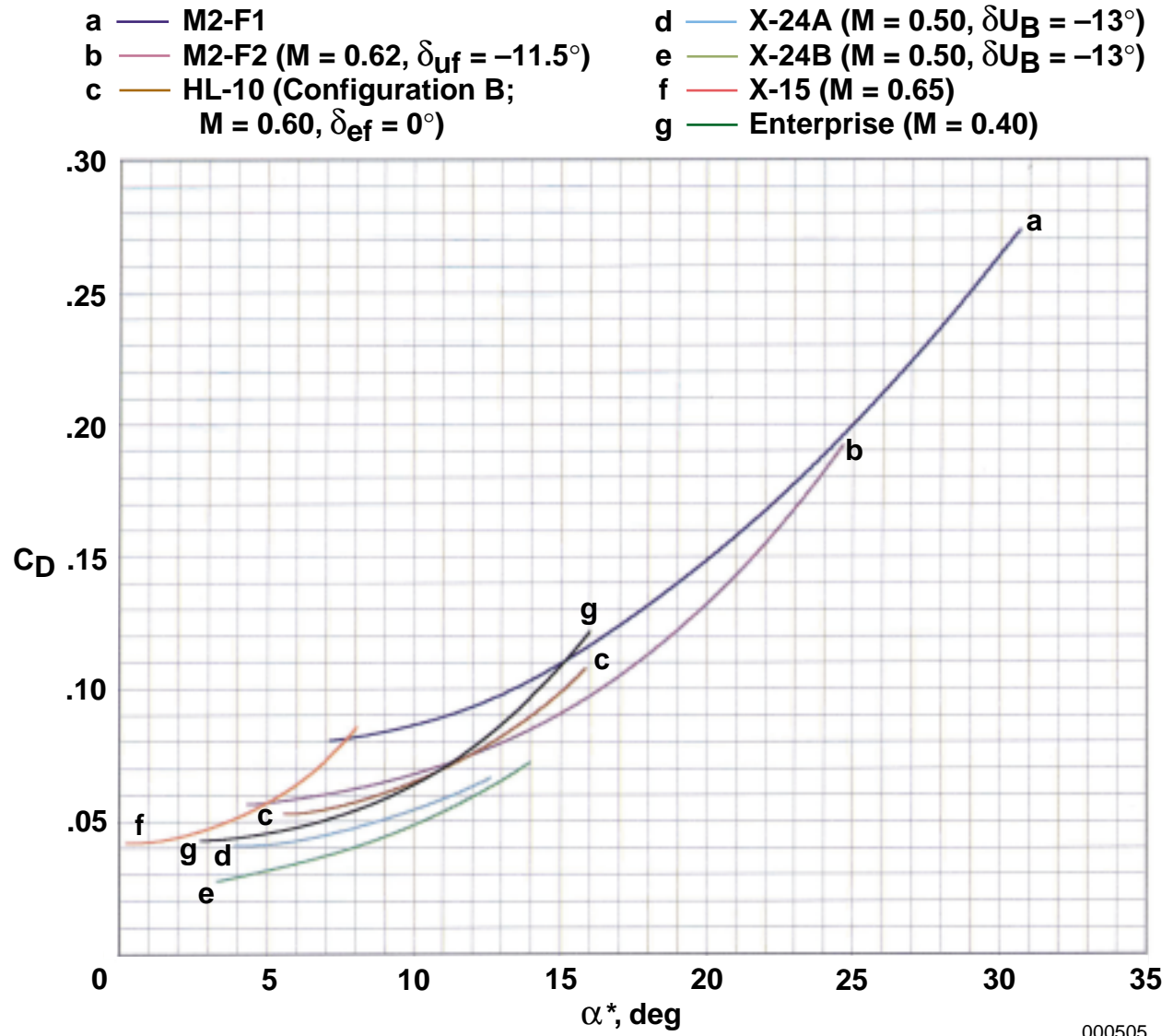
(d) C_D as a function of α^*.
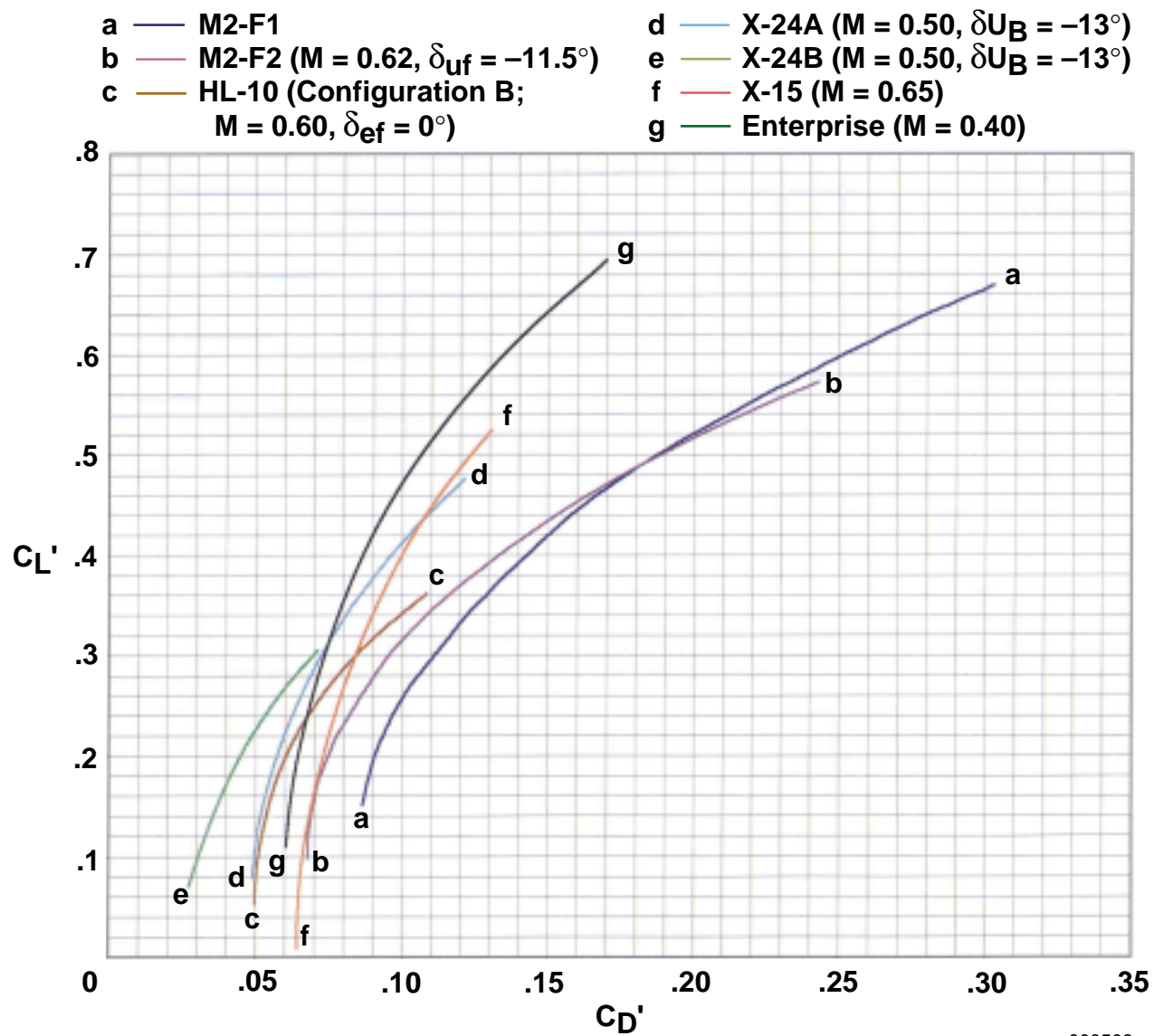
Figure C-2. Concluded.

(a) C_L' as a function of C_D'.

Figure C-3. The relationship of drag coefficient with lift coefficient for the seven subject vehicles.
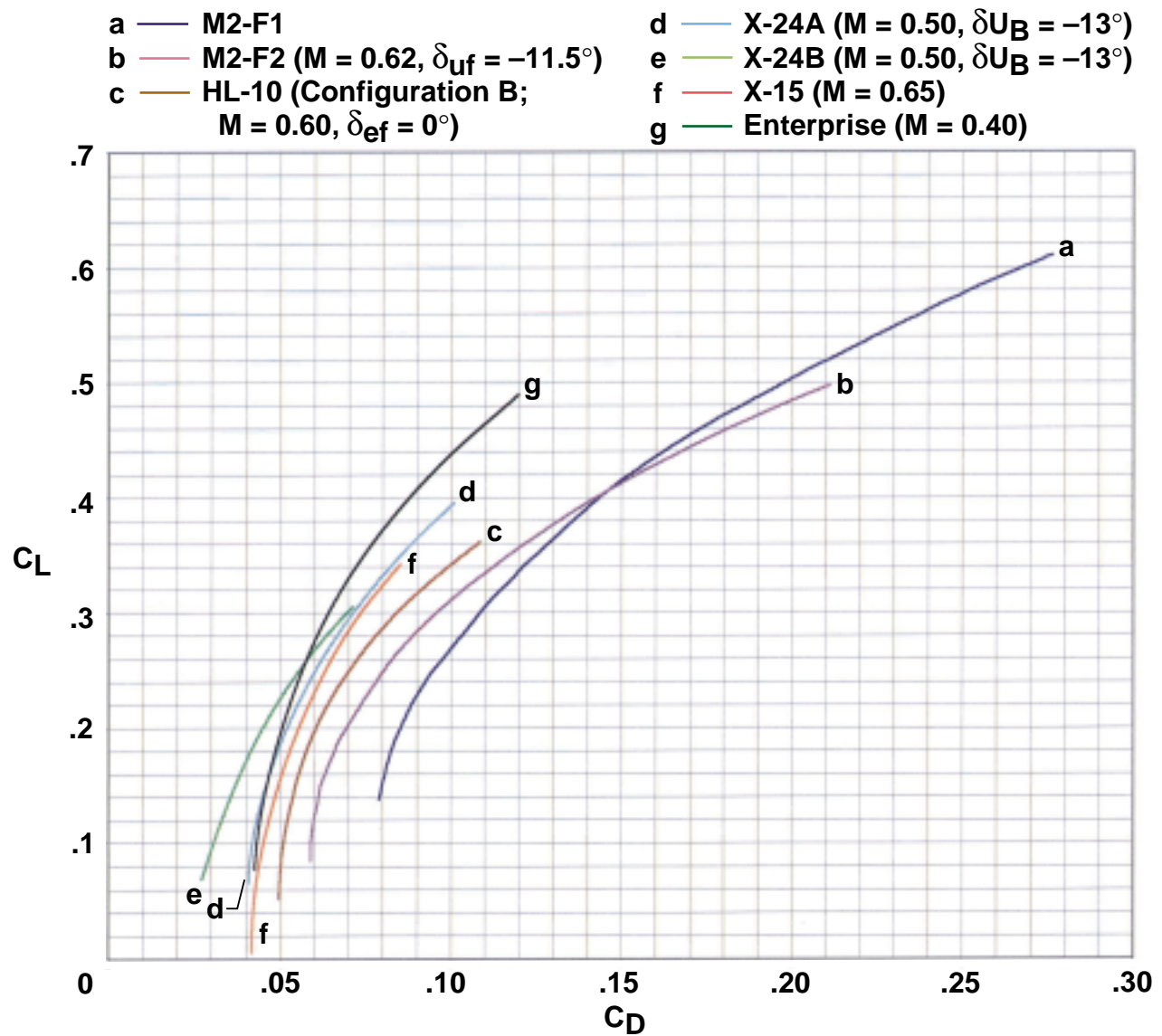
(b) C_L as a function of C_D.

Figure C-3. Concluded.
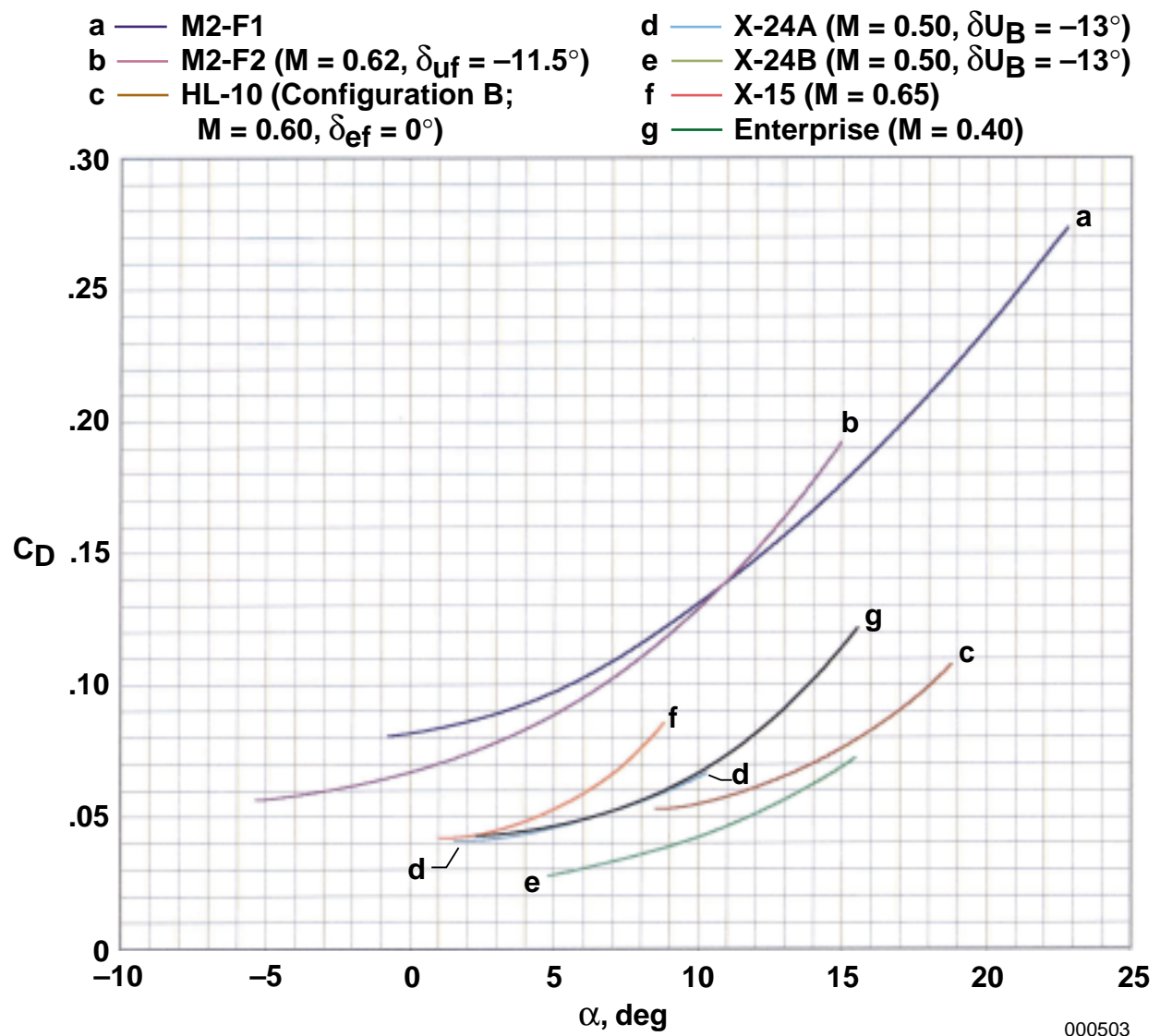
Legend:
- a — M2-F1
- b — M2-F2 (M = 0.62, $\delta_{uf} = -11.5°$)
- c — HL-10 (Configuration B; M = 0.60, $\delta_{ef} = 0°$)
- d — X-24A (M = 0.50, $\delta U_B = -13°$)
- e — X-24B (M = 0.50, $\delta U_B = -13°$)
- f — X-15 (M = 0.65)
- g — Enterprise (M = 0.40)
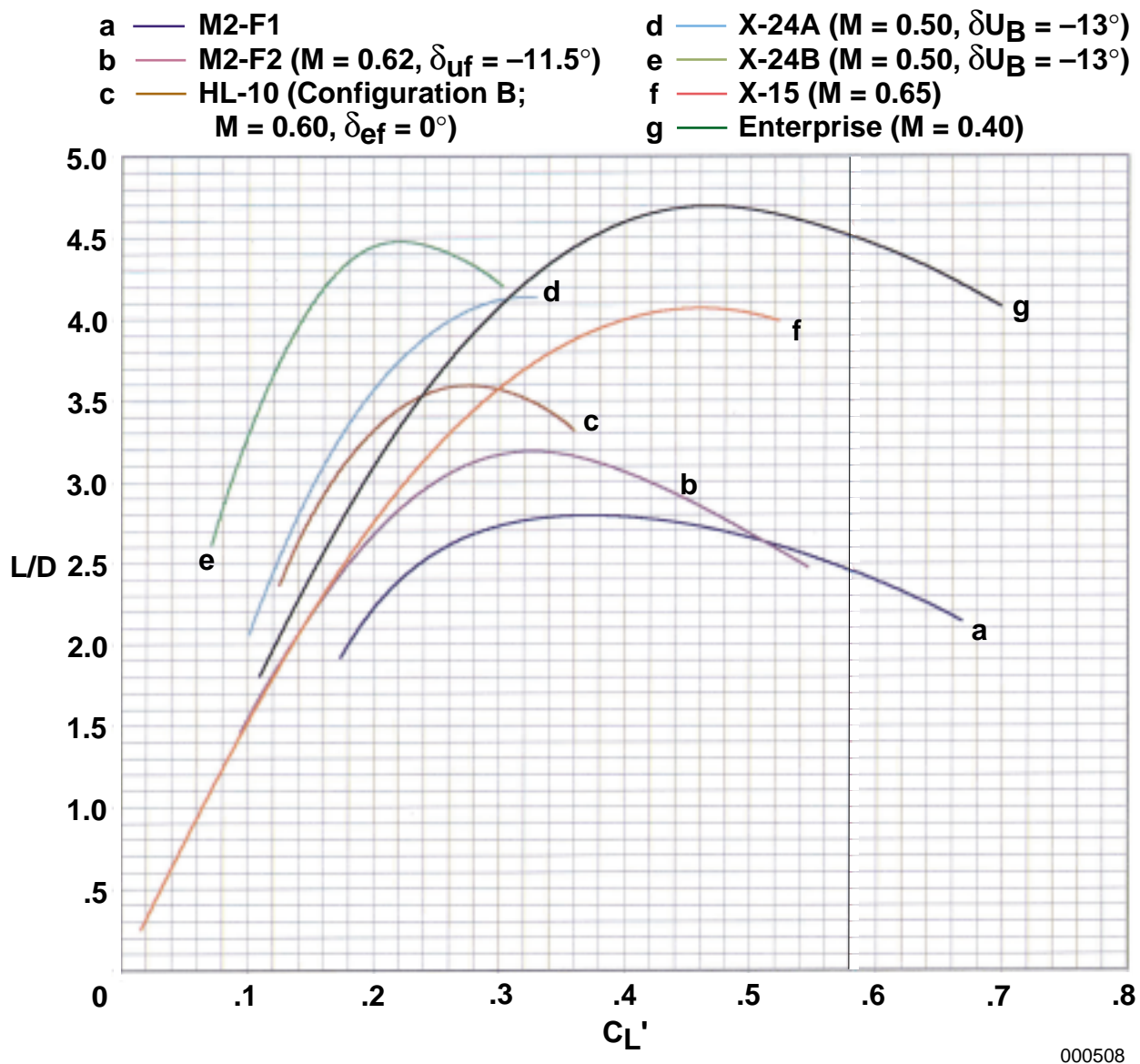
000508

(a) L/D as a function of $C_L{}'$.

Figure C-4. The relationship of the lift-to-drag ratio to lift coefficient for the seven subject vehicles.

a —— M2-F1
b —— M2-F2 (M = 0.62, δ_{uf} = −11.5°)
c —— HL-10 (Configuration B;
          M = 0.60, δ_{ef} = 0°)
d —— X-24A (M = 0.50, δU_B = −13°)
e —— X-24B (M = 0.50, δU_B = −13°)
f —— X-15 (M = 0.65)
g —— Enterprise (M = 0.40)
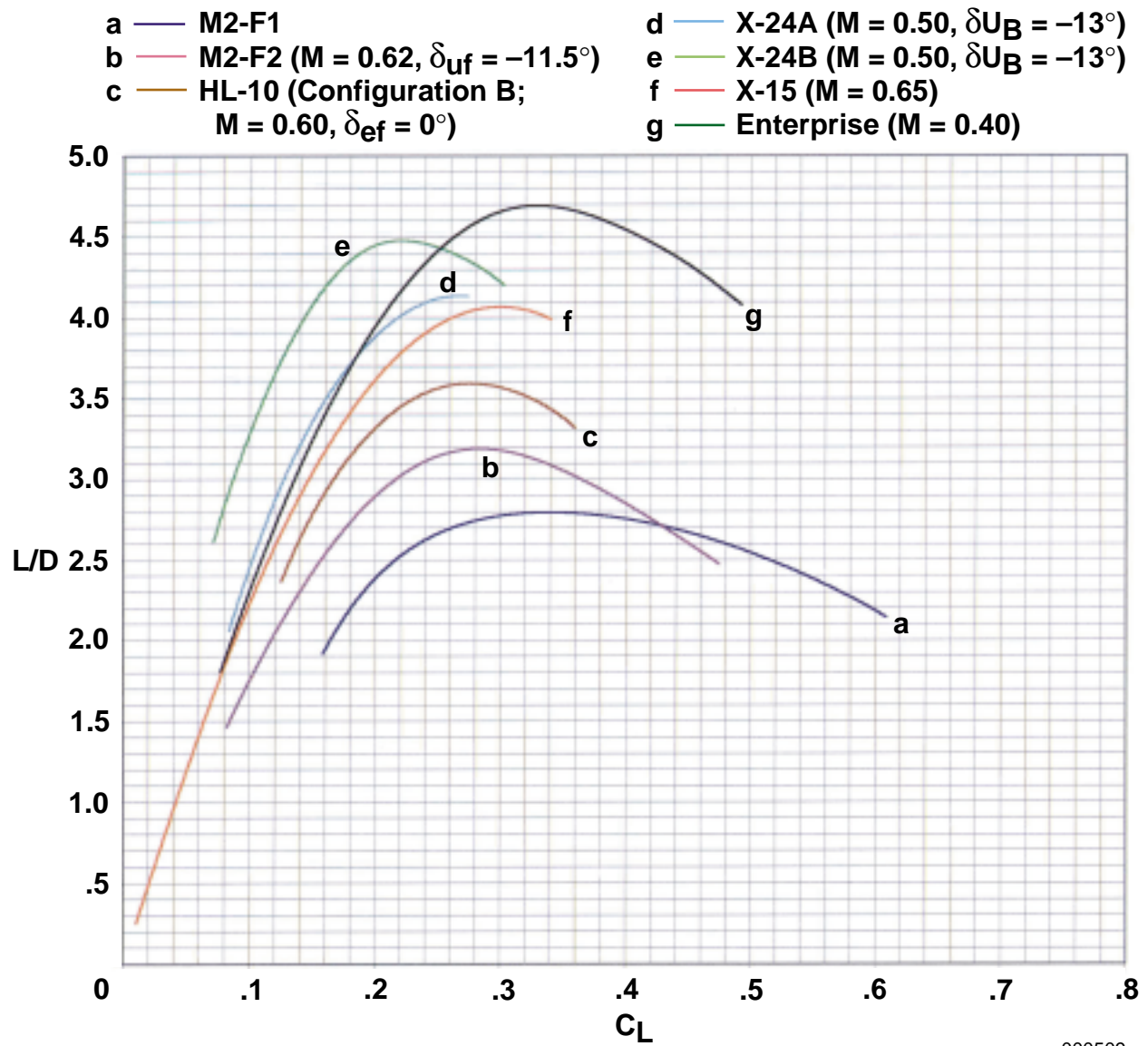
000509

(b) L/D as a function of C_L.

Figure C-4. Concluded.

125

Legend:
a — M2-F1
b — M2-F2 (M = 0.62, δ_{uf} = −11.5°)
c — HL-10 (Configuration B; M = 0.60, δ_{ef} = 0°)
d — X-24A (M = 0.50, δU_B = −13°)
e — X-24B (M = 0.50, δU_B = −13°)
f — X-15 (M = 0.65)
g — Enterprise (M = 0.40)
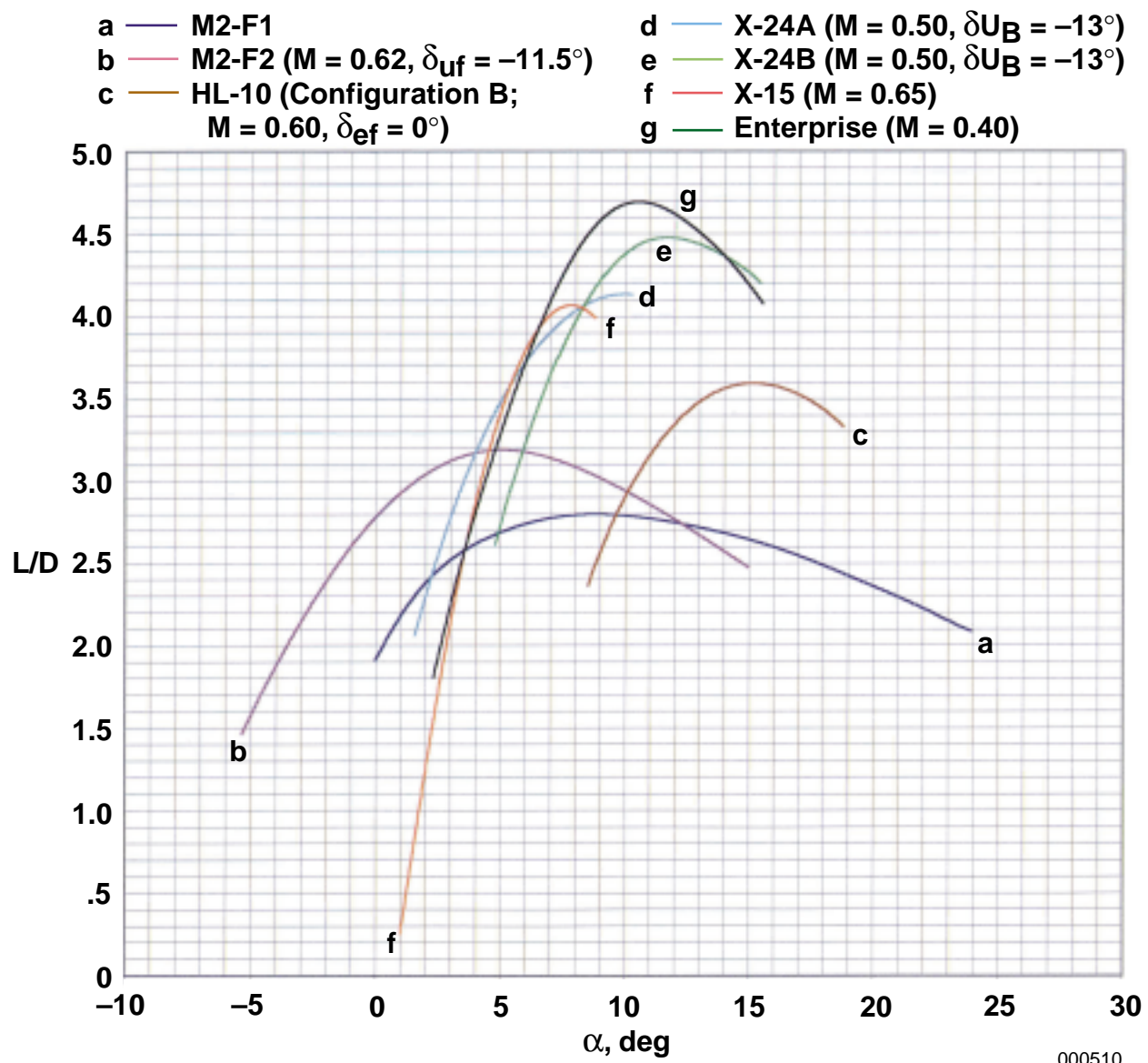
000510

(a) L/D as a function of α.

Figure C-5. The relationship of the lift-to-drag ratio to angle of attack for the seven subject vehicles.

a — M2-F1
b — M2-F2 (M = 0.62, δ_{uf} = −11.5°)
c — HL-10 (Configuration B; M = 0.60, δ_{ef} = 0°)
d — X-24A (M = 0.50, δU_B = −13°)
e — X-24B (M = 0.50, δU_B = −13°)
f — X-15 (M = 0.65)
g — Enterprise (M = 0.40)
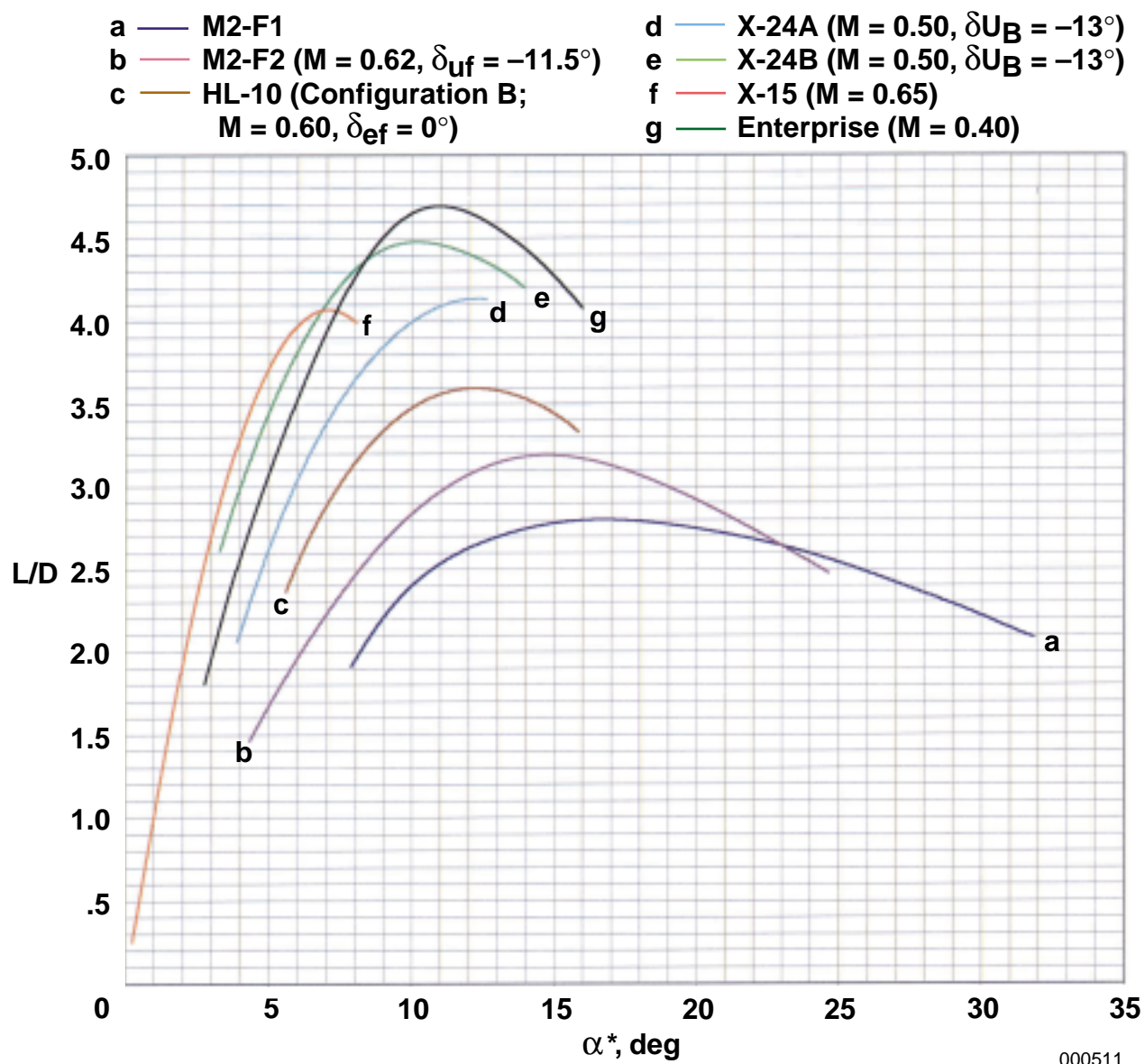
000511

(b) L/D as a function of α^*.

Figure C-5. Concluded.
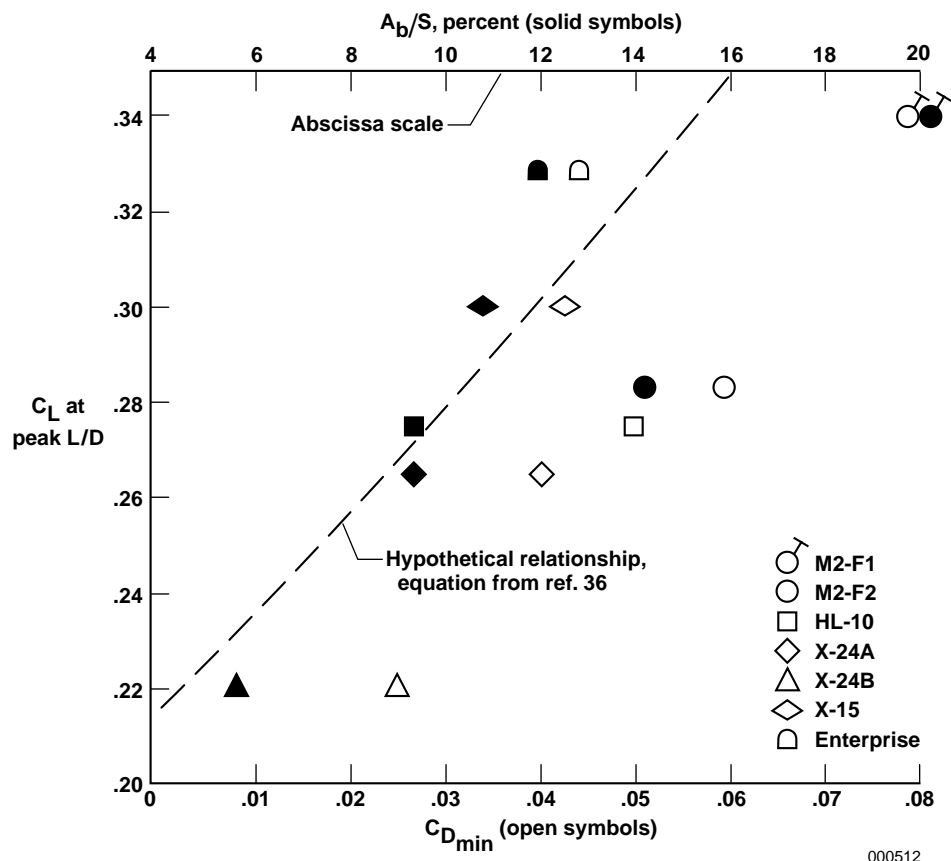
Figure C-6. The relationship of lift coefficient for peak *L/D* with minimum drag coefficient and the base area–to–reference area ratio.
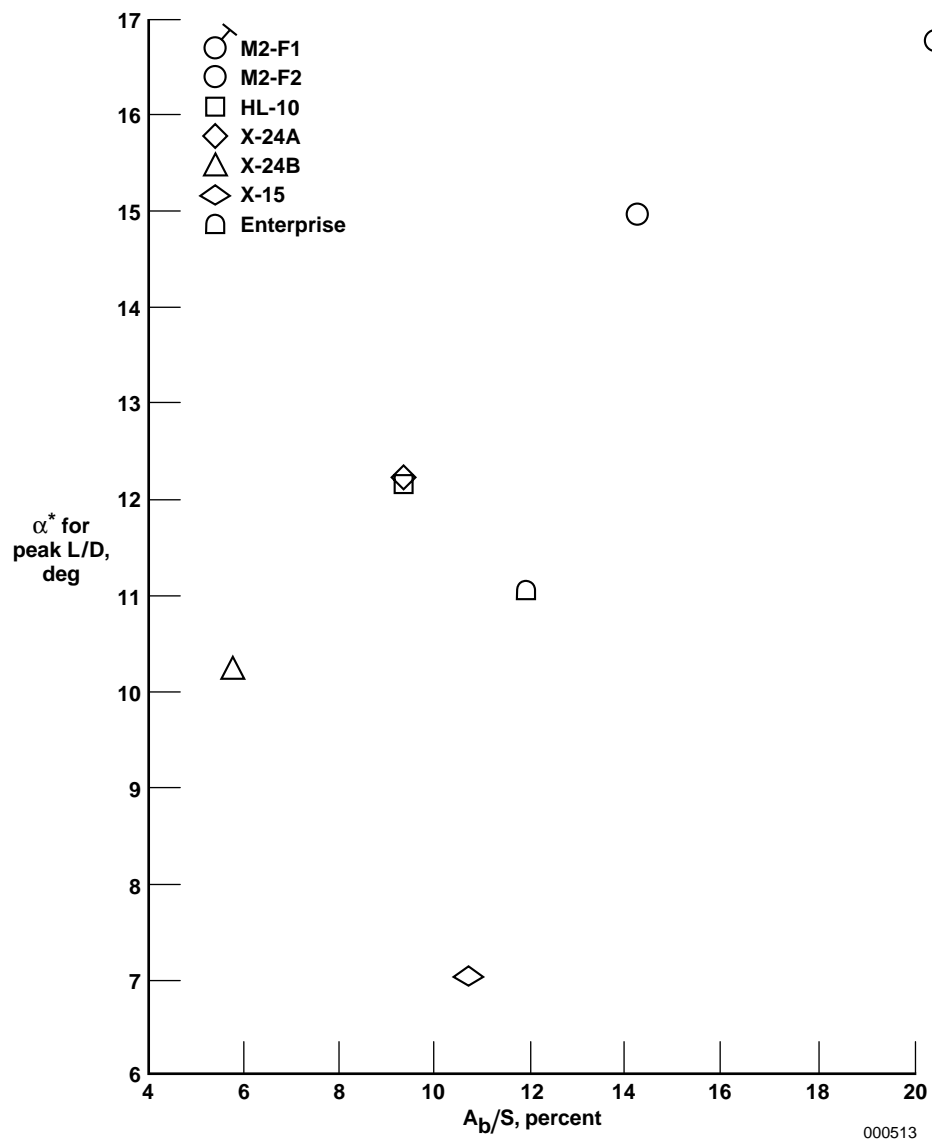
Figure C-7. The relationship of α^* for peak L/D with the ratio of base area to reference area S.

APPENDIX D

LOAD DISTRIBUTION AND COMPONENT INTERACTION

This appendix provides data and references that demonstrate the contribution of fuselage lift to total vehicle lift for winged vehicles. These data also support the rationale for the definition of a more representative reference area as mentioned on pages 18–19 and in the footnote on page 19. The lifting characteristics of a mated wing and fuselage are well-known to be a product of mutual interaction. Hoerner shows examples of these interactions in chapters 15 and 20 of reference 30. Reference 72 shows that wind-tunnel testing was ongoing and equations were being developed regarding these mutual interactions during the 1920's and 1930's. As airplane configurations evolved during the following decades, corresponding wind-tunnel testing continued regarding this matter.

In flight research, wing loading and horizontal tail loads sometimes were measured through the use of strain gages or detailed pressure distribution experiments. Total aircraft loads simultaneously were obtained through accelerometer measurements; fuselage lift then could be indirectly obtained by subtracting the wing and tail loads from the total aircraft loading. An early example of this approach has been reported for the X-1 airplane at subsonic speeds (ref. 73). Related data for flight through the speed of sound, as well as the results for subsonic flight in reference 73, are reported in reference 74, a compilation of papers presented at a joint Air Force–NACA conference regarding early X-1 flight results. The specific paper of concern in reference 74 is authored by Harold R. Goodman and begins on page 45. Figures 1 and 2 of the Goodman paper are reproduced here as figures D-1(a)–(b). Figure D-1(a) shows a schematic illustration of strain-gage locations for the gages used to sense wing-panel and horizontal tail loads. This system is the same as was used to obtain the data reported in reference 73.

Figure D-1(b) shows the resultant distribution of loads as shared by the wing panels, the horizontal tail, and the fuselage. The fuselage loads are deemed to be the difference between the overall aircraft loading (obtained from the normal component of aircraft acceleration) and the sum of the wing panel and horizontal tail loads. This indirect approach to defining the fuselage share of loads, seen here as approximately 18 percent for subsonic conditions, is reasonably accurate. However, for the purpose of this report, knowing the distribution of the fuselage load along the body length is also important.

Detailed pressure distribution measurements made from nose to base can provide the lift, or load, distribution for a fuselage in flight; however, such measurements are scarce. Two exceptions to this situation are the relatively detailed pressure measurements made on the X-1 no. 2 airplane later than references 73 and 74 (ref. 75), and the less comprehensive data from the X-15 airplane (refs. 76, 77).

Knapp et al. (ref. 75) have analyzed fuselage pressure data from 109 flush orifices distributed over the X-1 body. Their investigation covered fuselage angles of attack from 2° to 8° and Mach numbers from 0.78 to 1.02. Fuselage load distribution curves for 6° angle of attack are reproduced here in figure D-2. Although curves for four Mach numbers are shown (mid portion of figure D-2), emphasis will be directed to the lowest Mach number because the seven reentry vehicles of this report represent Mach numbers somewhat lower than 0.78. Obtaining fuselage load distribution data for a Mach number, more in accord with the Mach numbers representing the seven primary vehicles of this report, would be preferable. Nevertheless, the X-1 data for Mach 0.78 represent the lowest Mach number for which such detailed flight data are available. Although the fuselage normal forces of the X-1 aircraft are influenced by compressibility effects, the ratio of fuselage lift to total vehicle lift is relatively insensitive to Mach

number; hence, these data are believed adequate to support the concept to be discussed in the following paragraphs.

The curves of figure D-2 show the load variation over the entire length of the fuselage. The area under the solid curve (Mach 0.78) has been integrated from the nose apex to each of the four stations (indicated as A–D below the side-view drawing of the fuselage). Note the equation below the load distribution curves. Because the loading parameter $c_n\left(\dfrac{r}{R}\right)$ is the integrand, this integration process provides the total fuselage normal force coefficient, or the coefficient from the apex to any chosen station.

For the purposes of this report, the normal force coefficients for the fuselage forward of stations C and D are of the most interest. The integration to station C provides fuselage normal force coefficient to the station corresponding to the wing trailing edges extended to the fuselage centerline. The corresponding procedure to station D, of course, provides the normal force coefficient, C_{N_F}, for the entire fuselage. Note that when a common reference area is used (for example, the maximum fuselage cross-sectional area), the normal force coefficient generated by the fuselage forward of station C is very close to the coefficient for the complete fuselage (within 2 percent, see the table adjacent to the equation for C_{N_F} in figure D-2). Inspection of the two other subsonic curves suggests that this excess would also be true for those Mach numbers, and integration of the curve for Mach 1.0 shows that the fuselage surfaces forward of station C provide 95 percent of the total fuselage normal force at that condition.

The authors believe that this flight evidence of fuselage load distribution with respect to wing trailing-edge station is in accord with their application of Jones' postulation, "sections behind the section of maximum width develop no lift" (ref. 27, pgs. 59 and 63). The authors are aware that Jones was referring to more conventional lifting surfaces rather than trailing fuselage surfaces; however, borrowing his concept, which (although the "physics" may be different) appears to concur with evidence from the X-1 no. 2 flight vehicle, has been deemed to be appropriate here. Corresponding longitudinal lift distribution results previously have been described herein for the *Enterprise* (table 2), in which it was noted that the tailcone planform (which was aft of the wing trailing edge) did not provide an increase of the lift-curve slope.

In summary, both the X-1 airplane results (fig. D-2) and the tailcone data from the *Enterprise* indicate that a boat-tailed afterbody behind a wing is an ineffective source of lift. However, also examining the afterbody lift characteristics of streamline bodies that have no wings is of interest. Early inviscid theory predicted that for a complete (closed) streamline body of revolution, the tapered afterbody would experience "downloading" (that is, negative lift) that would cancel the lift generated by the forebody (refs. 30 and 72, vol. VI). In practice, however, viscous effects greatly diminish the tendency for the upper boat-tail surface pressures to be higher than the lower surface pressures, thus resulting in the forebody lifting forces exceeding the afterbody downward forces. This result provides a subsequent net lift for positive angles of attack.

An example of this result is provided from detailed pressure distribution measurements made on a 1/40-scale wind-tunnel model of the U. S. airship *Akron* (ref. 78). These data are from a body having a

fineness ratio of 5.9, approximately that of the X-1 fuselage, and were obtained at a Reynolds number of 17.3×10^6 (based upon length). Figure D-3 shows the longitudinal distribution of pressure. The circular symbols represent pressure measurements obtained from flush orifices along the upper surface centerline, and the square symbols represent the lower surface centerline. These pressures are for the base hull (that is, no simulated control car, engine nacelles, or tail surfaces). The more negative upper centerline pressure coefficients forward of $x/l \approx 0.38$ represent lifting; whereas between $x/l \approx 0.40$ and 0.95, downloading exists at the centerline. Note that the difference between the respective centerline pressures represents local loading only at and near the centerline element; the total normal load distribution requires accounting for the lateral elements (that is, the upper and lower pressure differences for surface elements between $\theta = 0°$ and $\theta = 180°$). The overall distribution of pressure shown in figure D-3 results in a net lifting force because viscous effects cause a significant reduction in the afterbody downloading as compared to inviscid theoretical predictions.

Figure D-4 shows analogous data for a relatively high-fineness-ratio body of revolution at Mach 0.7 and Mach 0.9 reproduced from reference 79. These data are presented in a similar format and represent a sting-supported prolate spheroid with a fineness ratio of 10. Considering both sets of data, the higher Reynolds number results from the *Akron* model and the lower Reynolds number (but higher speed) data for the prolate spheroid indicate relatively small negative loading for boat-tailed afterbodies as compared with the positive lift forces from the forebody. The data from these two wind-tunnel model experiments are rather typical for "closed" streamline bodies and are in qualitative agreement with the X-1 fuselage loading distribution results for subsonic flight conditions. These three sources of longitudinal loading characteristics for boat-tailed body shapes support the aforementioned definition of reference area as the planform of the forebody and the wing back to the projection of the wing trailing edges to the fuselage centerline.

Although several aircraft probably exist that have been instrumented with strain gages so that the wing-panel forces can be separated from the total normal forces, the authors are aware of only two aircraft where fuselage pressures have been measured for this purpose. Of these two, only the X-1 no. 2 airplane provides detailed fuselage load distribution data throughout the entire length of the fuselage. Note, however, that the X-15 airplane was instrumented well enough with strain gages, pressure distribution, and accelerometer measurements to establish that over one-half of the total vehicle normal force was provided by the fuselage at subsonic speeds (ref. 76). The flight data from the X-1 and X-15 aircraft demonstrate that the contribution of the fuselage to the total vehicle lift is significant.

Although the primary purpose of this appendix concerns loads and load distribution normal to the longitudinal axis of a body, including supporting data related to the longitudinal load, or drag, of the *Enterprise* with tailcone is deemed appropriate. A previous section of this report indicates that the tailcone of the *Enterprise* (of 1.3 fineness ratio) provided a 55-percent reduction of low-lift drag compared to the *Enterprise* with the blunt base. This substantial decrease in drag coefficient is in qualitative agreement with data from chapter 20 of reference 31; and said data are represented in figure D-5.
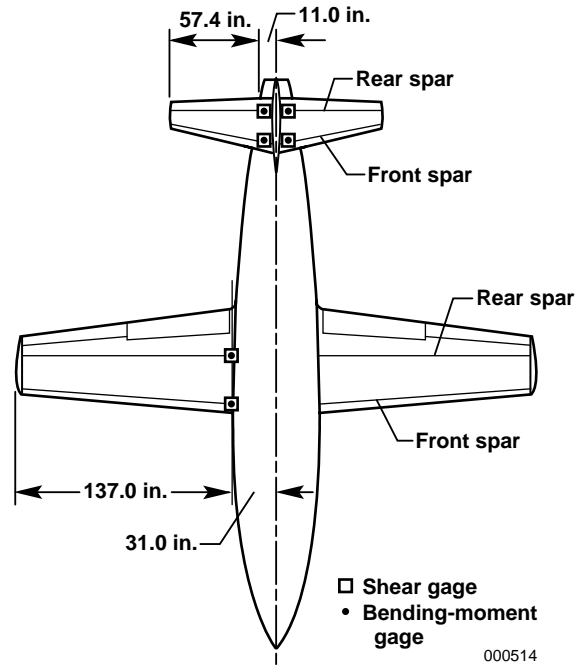
(a) Plan view of XS-1 airplane showing approximate location of strain-gage stations.
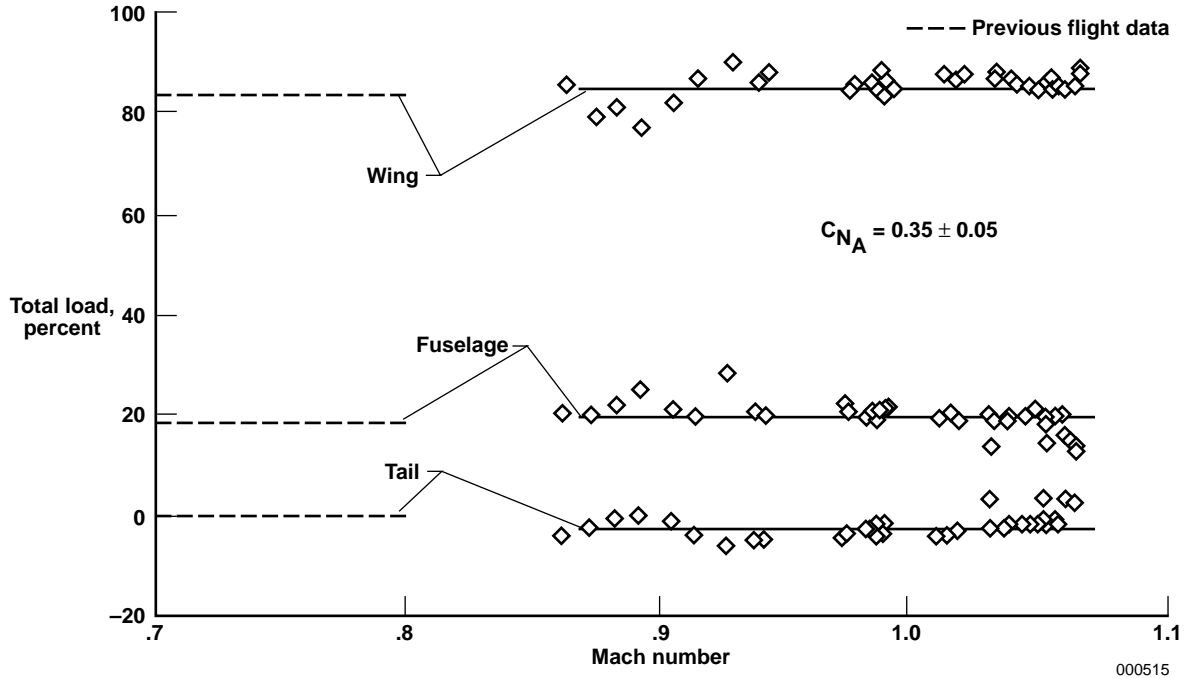
(b) Variation of wing, tail, and fuselage load in terms of percent of total airplane load with Mach number for $C_{N_A} = 0.35$ (10-percent–thick wing airplane).

Figure D-1. Flight-derived load distribution data for the X-1 number 2 airplane and illustration of strain-gage locations (ref. 74).
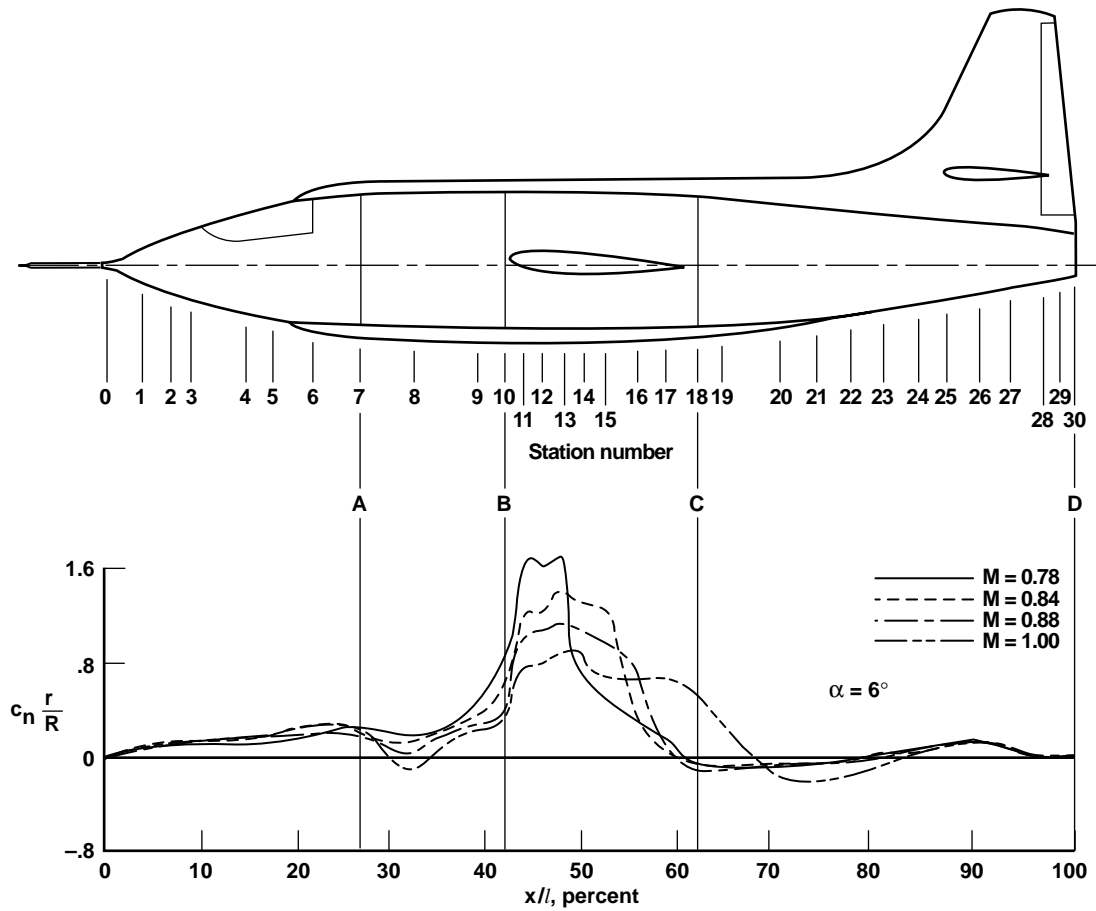
$$C_{N_F} = \frac{l}{\pi R} \int_0^1 c_n \frac{r}{R} \, d\left(\frac{x}{l}\right), \begin{cases} \text{Where reference area is} \\ \text{maximum fuselage cross} \\ \text{section = 16.48 ft}^2 \end{cases}$$

M = 0.78, α = 6°		
Integrated to station:	Planform area, ft^2	C_{N_F}
A	19.6	0.144
B	41.2	0.390
C	67.1	1.009
D	105.0	1.023

000516

Figure D-2. Flight-derived fuselage loading distribution for X-1 number 2 airplane (ref. 75).
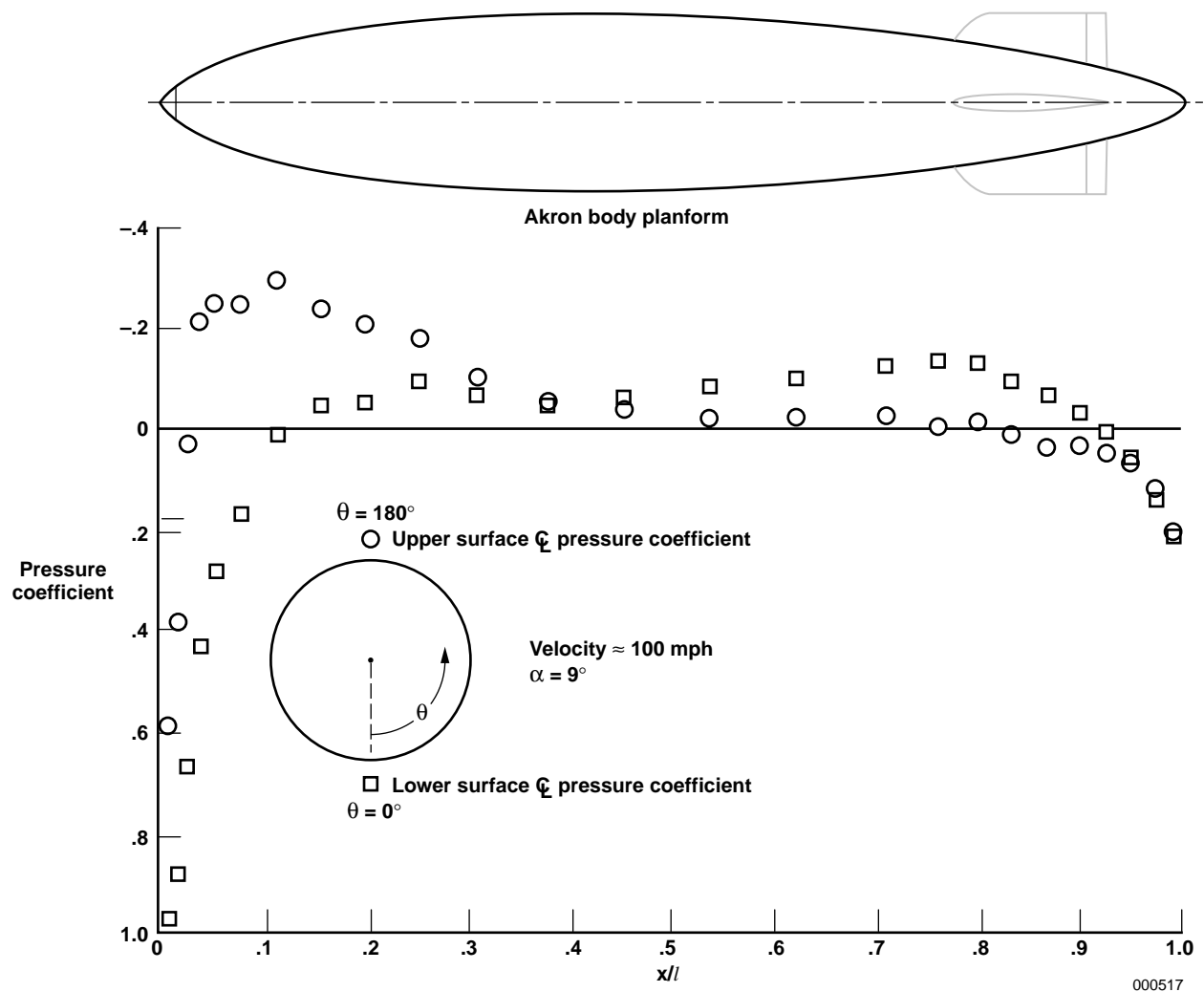
Figure D-3. Longitudinal distribution of pressure along the upper and lower surface centerlines of the base hull of a 1/40-scale model of the U. S. airship *Akron*. Reynolds number (based on length) = 17.3×10^6; fineness ratio ≈ 6.
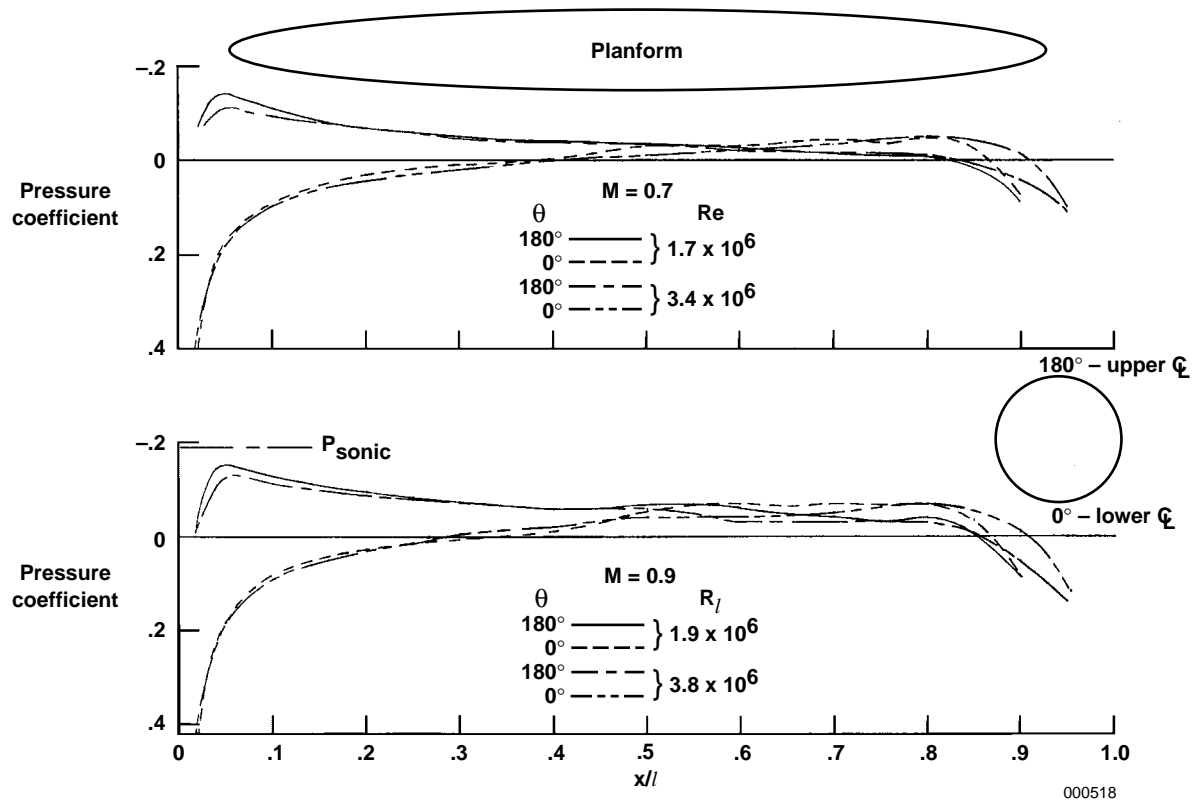
Figure D-4. Longitudinal distribution of pressure along the upper and lower surface centerlines of a prolate spheroid. Fineness ratio = 10; $\alpha = 10°$.
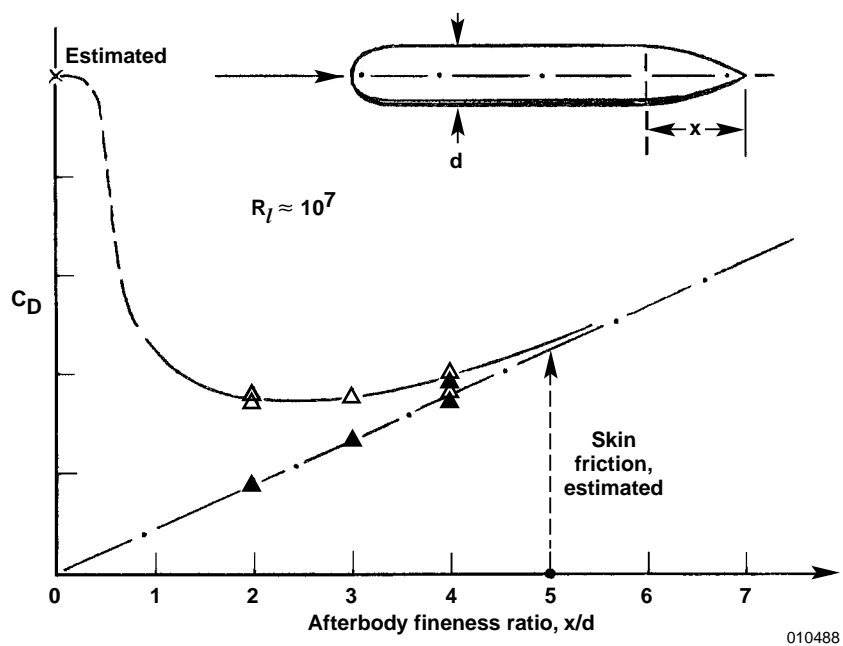
Figure D-5. Afterbody drag as a function of the length of a tailcone
when added to the cylindrical shape.

APPENDIX E

BASE PRESSURE COEFFICIENTS FROM THE M2-F3 VEHICLE

The M2-F2 vehicle obtained coasting lift and drag data, but no extant base pressure data have been found. The subsequent M2-F3 vehicle provided base pressure data from a few orifice locations that have not been previously published but were preserved in the files of NASA Dryden research engineer Louis L. Steers. Figure E-1 shows these base pressure coefficients, C_{P_b}, as a data band as a function of Mach number. The band is representative of the boundaries of the dynamic fluctuations in base pressure in the base region, and is to be expected unless pneumatic or electronic filtering is employed. The data used in this report are mean values of each band, which are then averaged for Mach 0.45 and Mach 0.62 for an upper flap deflection of $-11.5°$.

Figure E-1. Range (data band) of base pressure coefficient from M2-F3 vehicle during coasting flight.

APPENDIX F

ESTIMATION OF BASE PRESSURE COEFFICIENTS
FOR THE X-24A AND X-24B VEHICLES

Except for the X-24B vehicle datum at Mach 0.8, all other performance flight data for the X-24A and the X-24B vehicles have been published without corresponding base pressure data. Therefore, base pressure coefficients for these two vehicles 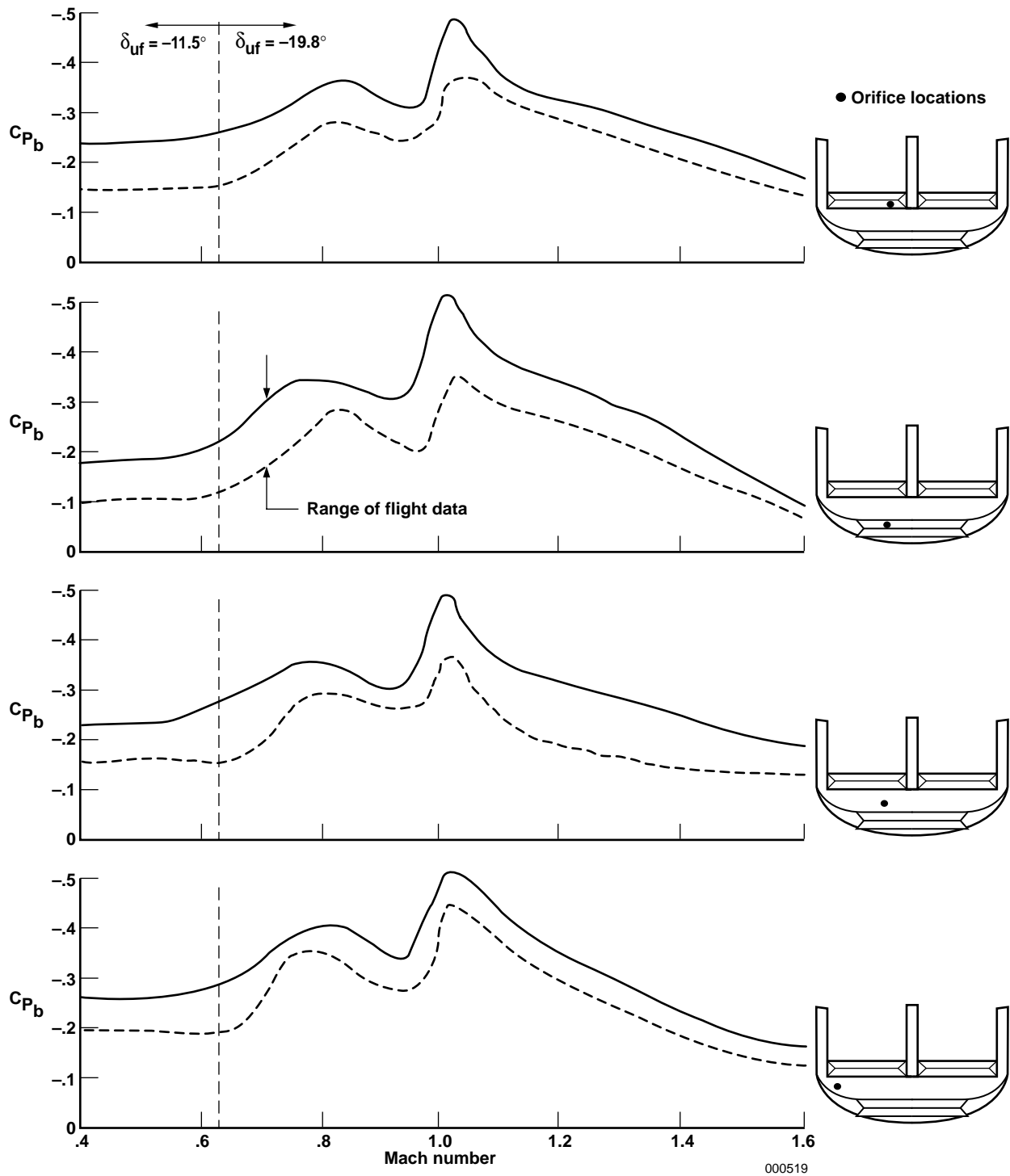have been estimated for all of the flight conditions reported here for Mach numbers less than 0.8. These estimates permit approximate forebody drag coefficients to be calculated for Mach numbers less than 0.8, as was mentioned in the introduction of the "Results and Discussion" section and the discussion of figure 7. All of these estimates depend on the above noted reference datum for base pressure obtained at Mach 0.8 from the X-24B vehicle (ref. 58).

Although these estimates are approximations, they are based on rational adjustments of the reference datum (taking into account compressibility effects and the influence of the wedge angle formed by the upper and lower flap deflections). Table F-1 shows the respective Mach numbers; flap deflections; and compressibility factor, $\left(\dfrac{1}{\sqrt{1-M^2}}\right)^{0.4}$, for all flight conditions of concern.

Table F-1. Physical conditions and compressibility factors.

| Vehicle | M | Body flap bias | | δw | $\dfrac{1}{\sqrt{1-M^2}}$ | $\left(\dfrac{1}{\sqrt{1-M^2}}\right)^{0.4}$ | Environment | C_{P_b} |
		Upper	Lower					
X-24B	0.8	–40°	28.0°	68.0°	1.667	1.227	Flight	–0.287
X-24B	0.5	–13°	6.0°	19.0°	1.155	1.059	Flight	To be estimated
X-24B	0.5	–20°	15.0°	35.0°	1.155	1.059	Flight	To be estimated
X-24B	0.6	–20°	14.5°	34.5°	1.250	1.093	Flight	To be estimated
X-24A	0.5	–9°	0.0°	9.0°	1.155	1.059	Flight	To be estimated
X-24A	0.5	–13°	9.0°	22.0°	1.155	1.059	Flight	To be estimated
X-24A	0.5	–21°	19.0°	40.0°	1.155	1.059	Flight	To be estimated
X-24A	0.2	–20°	20.0°	40.0°	1.021	1.008	Wind tunnel	To be estimated

Nine steps are required to obtain estimated base pressure coefficients for the X-24B vehicle at Mach numbers below 0.8 and wedge angles less than 68°. Two of the nine steps consist of adjustment of base pressure coefficient for the effects of Mach number by a modification of the Prandtl-Glauert rule. This same compressibility factor was used to adjust drag caused by flap deflection from Mach 0.5

conditions to Mach 0.8 conditions. Raymer and Jobe (refs. 34 and 80, respectively) each offer an equation for approximating Mach number effects on base pressure. After studying the base pressure data and the text of Hoerner regarding bodies and low-aspect-ratio wings (ref. 31), the decision was made to use the Prandtl-Glauert expression reduced to the 0.4 power, $\left(\dfrac{1}{\sqrt{1-M^2}}\right)^{0.4}$, as a compressibility factor. This revised expression is much closer to the compressibility effects predicted by Jobe than that of Raymer. Reference 51 was also considered as an advocate for a reduced power of the Prandtl-Glauert factor.

Figure F-1 shows the three alternative compressibility factors and the standard Prandtl-Glauert factor. The expressions of Raymer and Jobe have been normalized by dividing values at the elevated Mach numbers by a value of the expression representing incompressible conditions.

The step-by-step procedure for estimating the base pressure coefficients for the X-24B vehicle for the various wedge angles and Mach numbers less than 0.8 is as follows:

1. The base pressure coefficient for Mach 0.8 and a wedge angle of 68° is –0.287 (ref. 58). Application of the revised Prandtl-Glauert compressibility factor provides these base pressure coefficients for the same wedge angle at Mach numbers of 0.5 and 0.6.

M	δw	C_{P_b}	Source
0.8	68°	–0.287	Measured
0.6	68°	–0.256	Estimated
0.5	68°	–0.248	Estimated

2. Define the increment of drag caused by the 68° of total flap deflection at Mach 0.8. This increment is the sum of the drag caused by the windward surface and the leeward surface of the flaps (base drag increment).

From figure 14 of reference 15, an extrapolation of the drag coefficient as a function of wedge angle curve to 0° and 68° (at approximately Mach 0.5) provides an increment of drag coefficient of approximately 0.072 minus 0.036, which equals 0.036, based on the planform reference area of 330.5 ft². This figure from reference 15 is reproduced herein as figure F-2. The resulting increment of parasite drag area is:

$$\Delta f_{M\,=\,0.5} = 0.036 \times 330.5 \text{ ft}^2 = 11.9 \text{ ft}^2, \text{ caused by } 68° \text{ of } \delta w. \tag{F-1}$$

Adjusting from Mach 0.5 to Mach 0.8 for compressibility effects,

$$\Delta f_{M\,=\,0.8} = 11.9 \text{ ft}^2 \times \frac{1.227}{1.059} = 13.8 \text{ ft}^2 \tag{F-2}$$

Converting to a wetted area drag coefficient,

$$\Delta C_{F_{e,\,total}} = \frac{13.8 \text{ ft}^2}{948.4 \text{ ft}^2} = 0.01455 \text{ caused by } 68° \text{ of } \delta w \tag{F-3}$$

where the wetted area of the X-24B vehicle is 948.4 ft^2.

3. Define the lee-side drag of the flaps at Mach 0.8 and 68° of wedge angle. For this condition, the total base area is 38.05 ft^2. When the wedge angle is 0°, the base area is 10.95 ft^2. Therefore, the increment of base area caused by 68° of wedge angle is 27.10 ft^2.

Thus,

$$\Delta C_{F_{e,\,lee}} = \frac{|0.287| \times 27.10 \times 0.92}{948.4} = 0.00754 \tag{F-4}$$

where $C_{P_b} = -0.287$ at Mach 0.8, $\delta w = 68°$, and $c = 0.92$.

4. Define the windward-side drag of the flaps at Mach 0.8 and 68° of wedge angle,

$$\Delta C_{F_{e,\,windward}} = \Delta C_{F_{e,\,total}} - \Delta C_{F_{e,\,lee}} \tag{F-5}$$

or

$$\Delta C_{F_{e,\,windward}} = 0.01455 - 0.00754 = 0.00701 \tag{F-6}$$

5. Define X-24B forebody drag at Mach 0.8 for a wedge angle of 0°:

$$C_{F_{e,\,fore}} = C_{F_e} - \Delta C_{F_{e,\,windward}} - \Delta C_{F_{e,\,base}} \tag{F-7}$$

or

$$C_{F_{e,\,fore}} = 0.0245 - 0.00701 - \frac{|0.287| \times 38.05 \times 0.92}{948.4} = 0.0069 \tag{F-8}$$

6. Define base pressure coefficient for Mach 0.8 and a wedge angle of 0°. A revised version of Hoerner's three-dimensional equation will be used where $K = 0.095$ (that is, the average of 0.09 and 0.10).

$$|C_{P_b}| = \frac{0.095}{\left(\dfrac{0.0069 \times 948.4}{10.95}\right)^{0.5}} = 0.123 \tag{F-9}$$

7. Apply the revised Prandtl-Glauert factor to the base pressure coefficient for Mach 0.8 and 0° wedge angle (from step 6) and adjust base pressure coefficient to correspond for Mach 0.5 and Mach 0.6.

M	δw	$\left(\dfrac{1}{\sqrt{1-M^2}}\right)^{0.4}$	Estimates $\left\lvert C_{P_b} \right\rvert$
0.8	0°	1.227	0.123
0.6	0°	1.093	0.110
0.5	0°	1.059	0.106

8. Plot results of step 1 and step 7 at the respective wedge angles (fig. F-3) and add linear connecting lines.

9. "Pick off" base pressure coefficients from the relationships shown in figure F-3 for approximate values of Mach number and wedge angle. (These values are tabulated in the legend of figure F-3).

The same procedure is used for the X-24A vehicle for the appropriate Mach numbers and wedge angles. Two exceptions exist, however. Another curve has been included in figure F-3 that was not required for the X-24B vehicle because the X-24A vehicle was tested in the NASA Ames Research Center 40- by 80-ft low-speed wind tunnel at Mach 0.2. In addition, an accounting is made for the lower forebody drag of the X-24A vehicle as compared with the X-24B vehicle.

Although not immediately apparent from table 3 by examining the relative values of the minimum drag coefficient, $C_{D'_{min}}$, or the equivalent skin-friction coefficient, C_{F_e}; that the X-24A has the lower forebody drag is evident from the parasite drag areas, f, for comparable wedge angles. This lower forebody drag can only result in more negative base pressure coefficients for the X-24A vehicle than for the X-24B vehicle for comparable wedge angles. Therefore, based upon the relatively lower forebody drag of the X-24A vehicle, the X-24A base pressure coefficients derived from figure F-3 are adjusted by adding an increment of –0.005 to those represented by the curves for the appropriate Mach number and wedge angle. The resulting estimated base pressure coefficients for both the X-24A and X-24B vehicles are tabulated in the table (fig. F-3). The parenthetical base pressure coefficients shown in the table represent the values extracted from the constant Mach number curves of the figure. These curves represent relationships derived for the X-24B vehicle. In order to derive base pressure coefficient estimates applicable to the X-24A vehicle, the aforementioned increment of –0.005 is added to the parenthetical values, which results in the final estimated value for the X-24A vehicle shown without parentheses. The base pressure coefficients listed in the table are also tabulated in table 3 and influence or appear explicitly in figures 7–10 (value for Mach 0.2, wind tunnel, excluded).
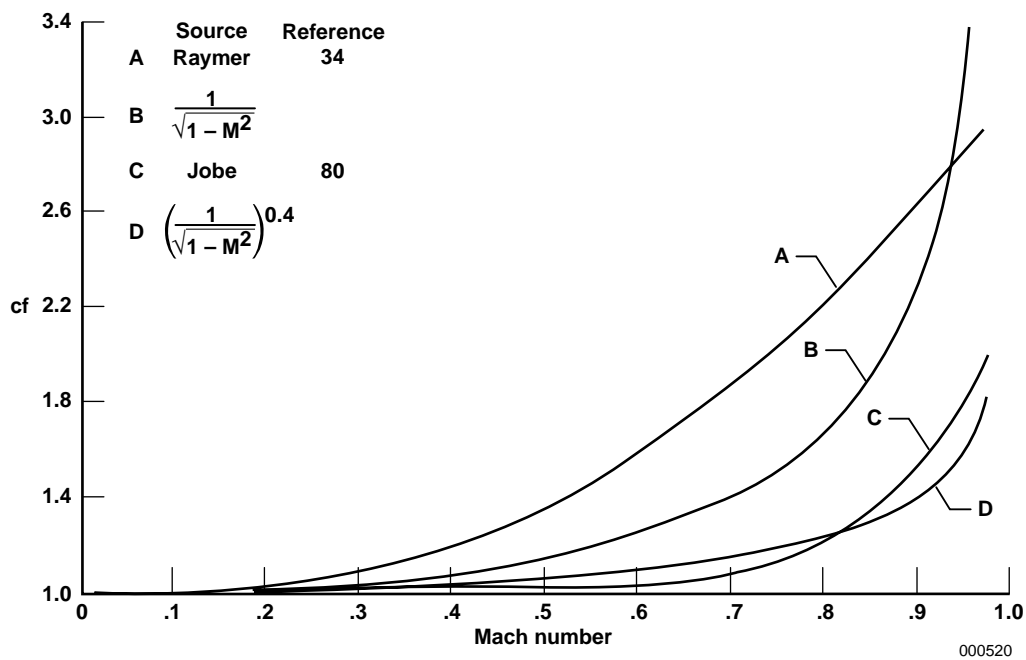
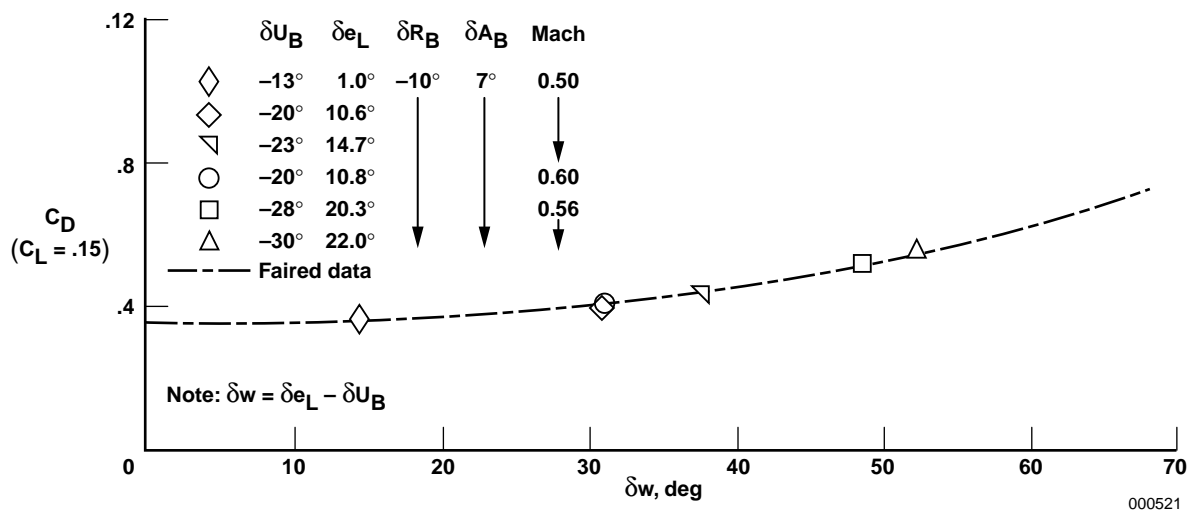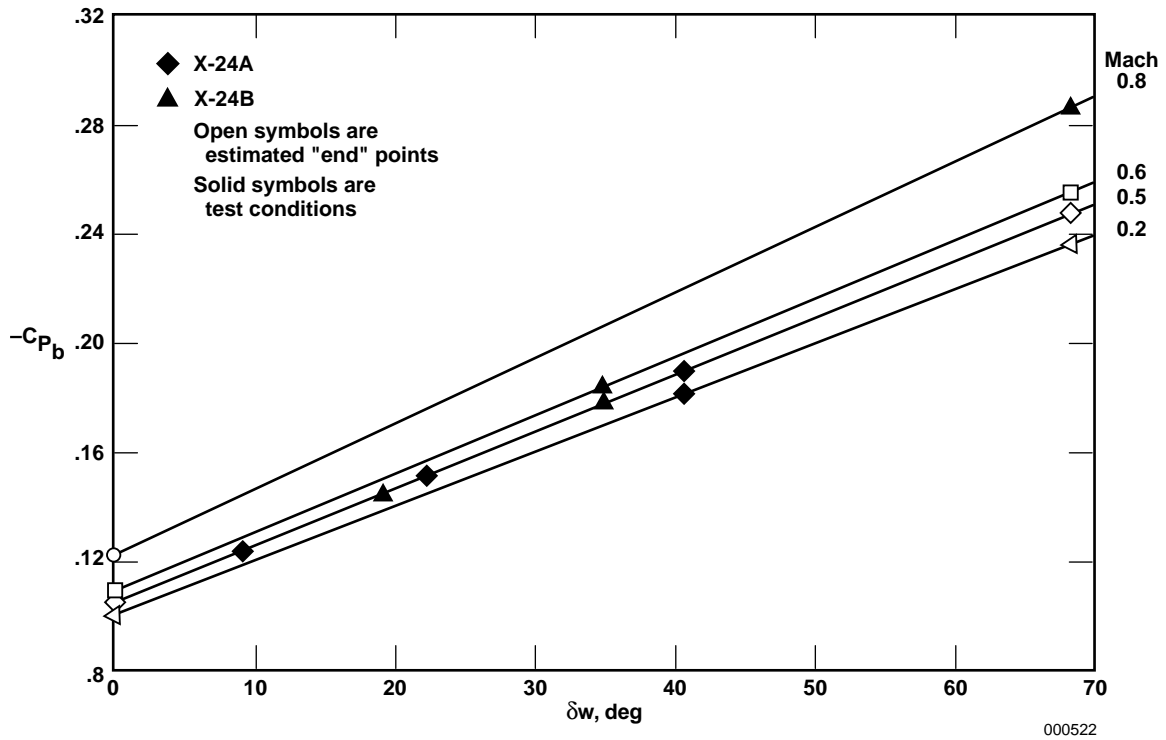Figure F-1. Comparison of compressibility factors.

Figure F-2. Drag coefficient as a function of wedge angle for X-24B vehicle (reference 15, page 37).

144

000522

Physical conditions and base pressure coefficients.

Vehicle	M	Body flap bias		δw	C_{P_b}		Source	Environment
		Upper	Lower					
X-24B	0.8	−40°	28.0°	68.0°	−0.287		Measured	Flight
X-24B	0.5	−13°	6.0°	19.0°	−0.145		Estimated	Flight
X-24B	0.5	−20°	15.0°	35.0°	−0.178		Estimated	Flight
X-24B	0.6	−20°	14.5°	34.5°	−0.184		Estimated	Flight
X-24A	0.5	−9°	0.0°	9.0°	−0.129	(−0.124)	Estimated	Flight
X-24A	0.5	−13°	9.0°	22.0°	−0.157	(−0.152)	Estimated	Flight
X-24A	0.5	−21°	19.0°	40.0°	−0.194	(−0.189)	Estimated	Flight
X-24A	0.2	−20°	20.0°	40.0°	−0.186	(−0.181)	Estimated	Wind Tunnel

Figure F-3. Estimated relationship of base pressure coefficient with Mach number and wedge angle for X-24A and X-24B vehicles.

REFERENCES

1. National Advisory Committee for Aeronautics, *NACA Conference on High-Speed Aerodynamics*: *A Compilation of the Papers Presented*, NASA TM-X-67369, 1958.

2. Faget, Maxime A., Benjamine J. Garland, and James J. Buglia, "Preliminary Studies of Manned Satellites—Wingless Configuration: Nonlifting," *NACA Conference on High-Speed Aerodynamics*: *A Compilation of the Papers Presented*, NASA TM-X-67369, 1958, pp. 19–33.

3. Wong, Thomas J., Charles A. Hermach, John O. Reller, Jr., and Bruce E. Tinling, "Preliminary Studies of Manned Satellites—Wingless Configurations: Lifting Body," *NACA Conference on High-Speed Aerodynamics*: *A Compilation of the Papers Presented*, NASA TM-X-67369, 1958, pp. 35–44.

4. Becker, John V., "Preliminary Studies of Manned Satellites—Winged Configurations," *NACA Conference on High-Speed Aerodynamics*: *A Compilation of the Papers Presented*, NASA TM-X-67369, 1958, pp. 45–57.

5. Chapman, Dean R., "Study of Motion and Heating for Entry Into Planetary Atmospheres," *NACA Conference on High-Speed Aerodynamics*: *A Compilation of the Papers Presented*, NASA TM-X-67369, 1958, pp. 1–17.

6. Love, Eugene S., "Introductory Considerations of Manned Reentry Orbital Vehicles," *Joint Conference on Lifting Manned Hypervelocity and Reentry Vehicles: A Compilation of the Papers Presented*, NASA TM-X-67563, 1960, pp. 39–54.

7. Dennis, David H. and George G. Edwards, "The Aerodynamic Characteristics of Some Lifting Bodies," *Joint Conference on Lifting Manned Hypervelocity and Reentry Vehicles: A Compilation of the Papers Presented*, NASA TM-X-67563, 1960, pp. 103–119.

8. Paulson, John W., Robert E. Shanks, and Joseph L. Johnson, "Low-Speed Flight Characteristics of Reentry Vehicles of the Glide-Landing Type," *Joint Conference on Lifting Manned Hypervelocity and Reentry Vehicles: A Compilation of the Papers Presented*, NASA TM-X-67563, 1960, pp. 329–344.

9. Reed, R. Dale with Darlene Lister, *Wingless Flight: The Lifting Body Story*, NASA SP-4220, 1997.

10. Horton, Victor W., Richard C. Eldredge, and Richard E. Klein, *Flight-Determined Low-Speed Lift and Drag Characteristics of the Lightweight M2-F1 Lifting Body*, NASA TN-D-3021, 1965.

11. Smith, Harriet J., *Evaluation of the Lateral-Directional Stability and Control Characteristics of the Lightweight M2-F1 Lifting Body at Low Speeds*, NASA TN-D-3022, 1965.

12. Pyle, Jon S. and Robert H. Swanson, *Lift and Drag Characteristics of the M2-F2 Lifting Body During Subsonic Gliding Flight*, NASA TM-X-1431, 1967.

13. Pyle, Jon S., *Lift and Drag Characteristics of the HL-10 Lifting Body During Subsonic Gliding Flight*, NASA TN-D-6263, 1971.

14. Ash, Lawrence G., *Flight Test and Wind Tunnel Performance Characteristics of the X-24A Lifting Body*, FTC-TD-71-8, June 1972.

15. United States Air Force, *Comparison of Flight Test and Wind Tunnel Performance Characteristics of the X-24B Research Aircraft*, AFFTC-TR-76-10, Apr. 1976.

16. *Flight Test Results Pertaining to the Space Shuttlecraft*, NASA TM-X-2101, 1970.

17. *Aerodynamics of Hypersonic Lifting Vehicles*, AGARD-CP-428, Apr. 1987.

18. Kempel, Robert W., Weneth D. Painter, and Milton O. Thompson, *Developing and Flight Testing the HL-10 Lifting Body: A Precursor to the Space Shuttle*, NASA RP-1332, 1994.

19. Matranga, Gene J., *Analysis of X-15 Landing Approach and Flare Characteristics Determined From the First 30 Flights*, NASA TN-D-1057, 1961.

20. Matranga, Gene J. and Neil A. Armstrong, *Approach and Landing Investigation at Lift-Drag Ratios of 2 to 4 Utilizing a Straight-Wing Fighter Airplane*, NASA TM-X-31, 1959.

21. Saltzman, Edwin J. and Darwin J. Garringer, *Summary of Full-Scale Lift and Drag Characteristics of the X-15 Airplane*, NASA TN-D-3343, 1966.

22. Thompson, Milton O., "Final Remarks and Future Plans," *Flight Test Results Pertaining to the Space Shuttlecraft,* NASA TM-X-2101, 1970, pp. 147–151.

23. United States Air Force, *AFFTC Evaluation of the Space Shuttle Orbiter and Carrier Aircraft: NASA Approach and Landing Test*, AFFTC-TR-78-14, May 1978.

24. Krienes, Klaus, *The Elliptic Wing Based on the Potential Theory*, NACA TM-971, 1941.

25. Helmbold, H. B., "Der unverwundene Ellipsenflugel als tragende Flache," *Jahrb*, 1942 der Deutschen Luftfahrtforschung, R. Oldenbourg (Munich), pp. I-111–I-113.

26. Polhamus, Edward C., *A Simple Method of Estimating the Subsonic Lift and Damping in Roll of Sweptback Wings*, NACA TN-1862, 1949.

27. Jones, Robert T., *Properties of Low-Aspect-Ratio Pointed Wings at Speeds Below and Above the Speed of Sound*, NACA Report 835, 1946.

28. Brown, Clinton E. and William H. Michael, Jr., *On Slender Delta Wings with Leading-Edge Separatio*n, NACA TN-3430, 1955.

29. Allen, H. Julian and Edward W. Perkins, *A Study of Effects of Viscosity on Flow Over Slender Inclined Bodies of Revolution*, NACA Report 1048, 1951.

30. Hoerner, Sighard F. and Henry V. Borst, *Fluid-Dynamic Lift: Practical Information on Aerodynamic and Hydrodynamic Lift*, published by Liselotte A. Hoerner, 1985.

31. Hoerner, Sighard F., *Fluid-Dynamic Drag: Practical Information on Aerodynamic Drag and Hydrodynamic Resistance,* published by the author, 1965.

32. Oswald, W. Bailey, *General Formulas and Charts for the Calculation of Airplane Performance*, NACA Report 408, 1932.

33. Wendt, R. E., "A Method of Airplane Performance Calculation Applicable to Any Polar," *Journal of the Aeronautical Sciences,* vol. 14, no. 4, Apr. 1947, pp. 243–250.

34. Raymer, Daniel P., *Aircraft Design: A Conceptual Approach*, AIAA Education Series, 1992.

35. Stinton, Darrol, *The Design of the Aeroplane*, Van Nostrand Rheinhold Company, New York, 1983.

36. Loftin, Laurence K., Jr., *Subsonic Aircraft: Evolution and the Matching of Size to Performance*, NASA RP-1060, 1980.

37. Perkins, Courtland D. and Robert E. Hage, *Airplane Performance Stability and Control*, John Wiley and Sons, New York, 1949.

38. Peterson, John B., Jr., *A Comparison of Experimental and Theoretical Results for the Compressible Turbulent-Boundary-Layer Skin Friction With Zero Pressure Gradient*, NASA TN-D-1795, 1963.

39. Bertram, Mitchel H., *Calculations of Compressible Average Turbulent Skin Friction*, NASA TR-R-123, 1962.

40. Saltzman, Edwin J., *Base Pressure Coefficients Obtained From the X-15 Airplane for Mach Numbers up to 6*, NASA TN-D-2420, 1964.

41. *Research-Airplane-Committee Report on Conference on the Progress of the X-15 Project: A Compilation of the Papers Presented*, NASA TM-X-57072, 1961.

42. Watts, Joe D. and Ronald P. Banas, *X-15 Structural Temperature Measurements and Calculations for Flights to Maximum Mach Numbers of Approximately 4, 5, and 6*, NASA TM-X-883, 1963.

43. Gord, P. R., *Measured and Calculated Structural Temperature Data From Two X-15 Airplane Flights With Extreme Aerodynamic Heating Conditions*, NASA TM-X-1358, 1967.

44. Pearson, Henry A. and Dorothy E. Beadle, *Flight Measurements by Various Methods of the Drag Characteristics of the XP-51 Airplane*, NACA MR-L6F12, 1946.

45. Beeler, De E., Donald R. Bellman, and Edwin J. Saltzman, *Flight Techniques for Determining Airplane Drag at High Mach Numbers,* NACA TN-3821, 1956.

46. Saltzman, Edwin J., K. Charles Wang, and Kenneth W. Iliff, "Flight-Determined Subsonic Lift and Drag Characteristics of Seven Lifting-Body and Wing-Body Reentry Vehicle Configurations With Truncated Bases," AIAA-99-0383, Jan. 1999.

47. Ware, George M., *Low-Subsonic-Speed Static Stability of Right-Triangular-Pyramid and Half-Cone Lifting Reentry Configuration*s, NASA TN-D-646, 1961.

48. Stivers, Louis S., Jr. and Lionel L. Levy, Jr., *Longitudinal Force and Moment Data at Mach Numbers From 0.60 to 1.40 for a Family of Elliptic Cones With Various Semiapex Angles*, NASA TN-D-1149, 1961.

49. Pyle, Jon S. and Lawrence C. Montoya, *Effect of Roughness of Simulated Ablated Material on Low-Speed Performance Characteristics of a Lifting-Body Vehicle*, NASA TM-X-1810, 1969.

50. Layton, Garrison P., Jr., *Interim Results of the Lifting-Body Flight-Test Program*, NASA TM-X-1827, 1969.

51. Gothert, B., *Plane and Three-Dimensional Flow at High Subsonic Speeds*, NACA TM-1105, 1946.

52. Diederich, Franklin W., *A Plan-Form Parameter for Correlating Certain Aerodynamic Characteristics of Swept Wings*, NACA TN-2335, 1951.

53. DeYoung, John and Charles W. Harper, "Theoretical Symmetric Span Loading at Subsonic Speeds for Wings Having Arbitrary Plan Form," *Thirty-fourth Annual Report of the National Advisory Committee for Aeronautics: 1948,* 1951, pp. 593–648.

54. Saltzman, Edwin J. and John W. Hicks, *In-Flight Lift-Drag Characteristics for a Forward-SweptWing Aircraft (and Comparisons With Contemporary Aircraft)*, NASA TP-3414, 1994.

55. Roskam, Jan, *Airplane Design, Part VI: Preliminary Calculation of Aerodynamic, Thrust and Power Characteristics*, Roskam Aviation and Engineering Corporation, Ottawa, Kansas, 1990.

56. Hoey, Robert G., *Flight Test Handling Qualities of the X-24A Lifting Body*, FTC-TD-71-11, Feb. 1973.

57. Nagy, Christopher J. and Paul W. Kirsten, *Handling Qualities and Stability Derivatives of the X-24B Research Aircraft*, AFFTC-TR-76-8, Mar. 1976.

58. United States Air Force, *Correlation of X-24B Flight and Wind Tunnel Pressure Data*, AFFDL-TR-78-93, Sept. 1978.

59. Butsko, J. E., W. V. Carter, and W. Herman, *Development of Subsonic Base Pressure Prediction Methods*, AFFDL-TR-65-157, vol. 1, Aug. 1965.

60. Kirsten, Paul W., David F. Richardson, and Charles M. Wilson, "Predicted and Flight Test Results of the Performance, Stability and Control of the Space Shuttle From Reentry to Landing," *Shuttle Performance: Lessons Learned*, NASA CP-2283, part 1, 1983, pp. 509–524.

61. Phillips, W. P., H. R. Compton, and J. T. Findlay, "Base Drag Determination for STS Flights 1–5," AIAA-83-2719, Nov. 1983.

62. Whitmore, Stephen A. and Timothy R. Moes, "A Base Drag Reduction Experiment on the X-33 Linear Aerospike SR-71 Experiment (LASRE) Flight Program," AIAA-99-0277, Jan. 1999.

63. Nash, J. F., *A Discussion of Two-Dimensional Turbulent Base Flows*, NPL Aero Report 1162, July 1965.

64. Pollock, N., *Some Effects of Base Geometry on Two Dimensional Base Drag at Subsonic and Transonic Speeds*, Australian Defence Scientific Service Aeronautical Research Laboratories, Aerodynamics Note 316, Oct. 1969.

65. Tanner, M., "Reduction of Base Drag," *Progressive Aerospace Science*, vol. 16, no. 4, 1975, pp. 369–384.

66. Tanner, M., "A Method for Reducing the Base Drag of Wings With Blunt Trailing Edge," *Aeronautical Quarterly*, vol. 23, no. 1, Feb. 1972, pp. 15–23.

67. Saltzman, Edwin J. and John Hintz, *Flight Evaluation of Splitter-Plate Effectiveness in Reducing Base Drag at Mach Numbers From 0.65 to 0.90*, NASA TM-X-1376, 1967.

68. Tanner, Mauri, "New Investigations for Reducing the Base Drag of Wings With a Blunt Trailing Edge," *Aerodynamic Drag,* AGARD-CP-124, Apr. 1973, pp. 12-1–12-9.

69. Pyle, Jon S. and Edwin J. Saltzman, "Review of Drag Measurements From Flight Tests of Manned Aircraft With Comparisons to Wind-Tunnel Predictions," *Aerodynamic Drag*, AGARD-CP-124, Apr. 1973, pp. 25-1–25-12.

70. Bearman, P. W., "Review—Bluff Body Flows Applicable to Vehicle Aerodynamics," *Journal of Fluids Engineering*, vol. 102, Sept. 1980, pp. 265–274.

71. Saltzman, Edwin J., *Preliminary Full-Scale Power-Off Drag of the X-15 Airplane for Mach Numbers From 0.7 to 3.1*, NASA TM-X-430, 1960.

72. Durand, William Frederick, editor, *Aerodynamic Theory:A General Review of Progress*, vol. IV and VI, Dover Publications, Inc., New York, 1976.

73. Beeler, De E. and John P. Mayer, *Measurements of the Wing and Tail Loads During the Acceptance Tests of Bell XS-1 Research Airplane*, NACA RM-L7L12, 1948.

74. *Air Force—NACA Conference on XS-1 Flight Research: A Compilation of the Papers Presented*, 1948.

75. Knapp, Ronald J., Gareth H. Jordan, and Wallace E. Johnson, *Fuselage Pressures Measured on the Bell X-1 Research Airplane in Transonic Flight*, NACA RM-L53I15, 1953.

76. Keener, Earl R. and Chris Pembo, *Aerodynamic Forces on Components of the X-15 Airplane*, NASA TM-X-712, 1962.

77. Pyle, Jon S., *Comparison of Flight Pressure Measurements With Wind-Tunnel Data and Theory for the Forward Fuselage of the X-15 Airplane at Mach Numbers From 0.8 to 6.0*, NASA TN-D-2241, 1964.

78. Freeman, Hugh B., *Pressure-Distribution Measurements on the Hull and Fins of a 1/40–Scale Model of the U.S. Airship "Akron,"* NACA Report No. 443, 1932.

79. Cole, Richard I., *Pressure Distributions on Bodies of Revolution at Subsonic and Transonic Speeds*, NACA RM-L52D30, 1952.

80. Jobe, Charles E., "*Prediction of Aerodynamic Drag*," AFWAL-TM-84-203, July 1984.

REPORT DOCUMENTATION PAGE

Form Approved
OMB No. 0704-0188

1. AGENCY USE ONLY (Leave blank)	2. REPORT DATE November 2002	3. REPORT TYPE AND DATES COVERED Technical Publication	
4. TITLE AND SUBTITLE Aerodynamic Assessment of Flight-Determined Subsonic Lift and Drag Characteristics of Seven Lifting-Body and Wing-Body Reentry Vehicle Configurations		**5. FUNDING NUMBERS** WU 529-50-04-00-RR-00-000	
6. AUTHOR(S) Edwin J. Saltzman, K. Charles Wang, and Kenneth W. Iliff			
7. PERFORMING ORGANIZATION NAME(S) AND ADDRESS(ES) NASA Dryden Flight Research Center P.O. Box 273 Edwards, California 93523-0273		**8. PERFORMING ORGANIZATION REPORT NUMBER** H-2397	
9. SPONSORING/MONITORING AGENCY NAME(S) AND ADDRESS(ES) National Aeronautics and Space Administration Washington, DC 20546-0001		**10. SPONSORING/MONITORING AGENCY REPORT NUMBER** NASA/TP-2002-209032	

11. SUPPLEMENTARY NOTES

12a. DISTRIBUTION/AVAILABILITY STATEMENT Unclassified—Unlimited Subject Category 02, 15 This report is available at http://www.dfrc.nasa.gov/DTRS/	12b. DISTRIBUTION CODE

13. ABSTRACT (Maximum 200 words)

This report examines subsonic flight–measured lift and drag characteristics of seven lifting-body and wing-body reentry vehicle configurations with truncated bases. The seven vehicles are the full-scale M2-F1, M2-F2, HL-10, X-24A, X-24B, and X-15 vehicles and the Space Shuttle *Enterprise*. Subsonic flight lift and drag data of the various vehicles are assembled under aerodynamic performance parameters and presented in several analytical and graphical formats. These formats are intended to unify the data and allow a greater understanding than individually studying the vehicles allows. Lift-curve slope data are studied with respect to aspect ratio and related to generic wind-tunnel model data and to theory for low-aspect-ratio planforms. The definition of reference area is critical for understanding and comparing the lift data. The drag components studied include minimum drag coefficient, lift-related drag, maximum lift-to-drag ratio, and, where available, base pressure coefficients. The influence of forebody drag on afterbody and base drag at low lift is shown to be related to Hoerner's compilation for body, airfoil, nacelle, and canopy drag. This feature may result in a reduced need of surface smoothness for vehicles with a large ratio of base area to wetted area. These analyses are intended to provide a useful analytical framework with which to compare and evaluate new vehicle configurations of the same generic family.

14. SUBJECT TERMS Aerodynamics, Lifting bodies, Reentry vehicles, Reusable launch vehicles			15. NUMBER OF PAGES 157
			16. PRICE CODE
17. SECURITY CLASSIFICATION OF REPORT Unclassified	18. SECURITY CLASSIFICATION OF THIS PAGE Unclassified	19. SECURITY CLASSIFICATION OF ABSTRACT Unclassified	20. LIMITATION OF ABSTRACT Unlimited